Imperial College London
Department of Physics

A UV Assisted Methodology for Functional Oxide Film Formation from Small Molecules

Jasvir Kaur Bhamrah Harley

Submitted in fulfilment of the requirements for the degree of
Doctor of Philosophy in Physics, Imperial College London and
the Diploma of Imperial College London, 2016

Declaration of Originality

I hereby declare that, excepting where specific reference is made to the work of others, this thesis is my original work and has been written by myself in its entirety.

This thesis has not previously been submitted, wholly or in part, for any degree at this or any other institution.

Dedication

To my son, Navdeep Lachlan Bhamrah Harley, for his infinite patience, unending faith and support and for inspiring me by always being excited about Science. You are awesome.

Acknowledgements

Funding for this doctorate was provided by the Engineering and Physical Sciences Research Council (EPSRC) and work was carried out in the Centre for Plastic Electronics and the Department of Materials, Imperial College London and in the Chemistry Department and London Centre for Nanotechnology at University College London.

My sincerest appreciation must go to Dr Sandrine Heutz who turned out to be the supervisor I needed. Thank you for your continual support, encouragement and thought-provoking discussions, not forgetting your tact which always kept me amused.

My thanks also go to Professors Mary P. Ryan and John de Mello for their complementary supervision and the Heutz group (in no particular order), Ryun, Jimmy, Hsiang-Han, Alex, Michele, Emma, Leo, Peter and Lucille, for their broad range of interests and expertise. Particular appreciation to Ryun for our collaborative efforts.

Thank you to Robert Palgrave at UCL and Ignacio J. Villar Garcia at Imperial for assistance with XPS, Richard Thorogate at the LCN for support with AFM and Richard Sweeney and Sarah Fearn at Imperial, primarily for magic and gossip respectively but also for help with XRD and SIMS.

Several people have made my PhD so much more enjoyable and should be mentioned: Jorge, Joby and Lisa at Imperial for their conviviality, sharing many good times with tea, cocktails and dinners, David and Gabriele at Queen Mary, David for his belief and both for more tea, cocktails and dinners and Sourpuss and Grumpyface for sharing my workspace so democratically.

Finally, much appreciation to my parents, Mohan Singh and Sudarshan Kaur Bhamrah and my sister, Prabhjit Kaur Matharu, who waited a long time and most of all to Ewan and Navdeep Bhamrah Harley who never had to help but always did.

Abstract

The development of organic electronics has progressed rapidly due to the demand for lower cost, large scale fabrication of devices using inexpensive materials with flexible substrates. The field has seen the discovery of many suitable organic substitutes for traditional electronic component materials, in particular, by polymers and small molecules. One class of materials, metal oxides, have yet to find organic alternatives capable of performing to standards required.

In this thesis, a non-toxic, room temperature method for functional oxide film formation from small molecules frequently employed as active layers in devices is explored to fully determine the mechanism by which the metal oxide is formed. Comparison of precursors, ZnPc (zinc phthalocyanine) and ZnTPP (zinc tetraphenylporphyrin), with contrasting morphology when deposited as thin films demonstrates the importance of the oxygen-assisted mechanism and its relation to grain boundaries. It is demonstrated that efficiency of oxide formation may be improved by choice of a crystalline precursor.

Heterostructures of ZnPc and PTCDA (3,4,9,10-perylenetetracarboxylic dianhydride), an archetypal organic semiconductor, are used as a model to determine the effect of the UV process for oxide production on underlying organic layers. We show that approximately half the precursor film reacts before the underlying layer is affected. The structures also reveal no effect of molecular orientation on the rate of oxide formation and templated films of ZnPc on PTCDA are correctly indexed for the first time. The use of PTCDA also confirms that inclusion of an oxygen-containing molecule can be employed as a method to increase the rate of film degradation.

Finally, nanosphere lithography of ZnPc films is combined with the UV assisted process to form regular arrays of hollow triangular nanostructures or pillars with the aim of creating structures suitable for photonic use.

Contents

List of Tables

List of Figures

Chapter 1

Introduction

First built in 1947, the transistor heralded the launch of modern semiconductor based electronics [22], creating ever smaller devices at lower cost but research efforts now also include organic materials, achieving major breakthroughs [23,24]. Lightweight and inexpensive, organic electronics has the potential to supersede silcon based electronics in many areas, in particular when considering large scale printing and flexiblility. Although a doped single crystal of silicon may have a mobility of $\sim$ 1000 cm^2/Vs [25], size limits its use to smaller applications with amorphous silicon fulfilling most other device requirements, with a much lower mobility of $\sim$ 1.0 cm^2/Vs [26], a value, however, within reach of organic semiconductors [24, 27]. Although organic materials, whether polymers or small molecules, have been developed to replace many active components in electronic devices, one class of inorganic materials critical for device function, for which adequate organic alternatives have not been found, is metal oxides.

Metal oxides fulfil many roles, exploiting their structural, conductive, photovoltaic, thermoelectric and multiferroic properties, requiring a range of synthesis and preparation methods to realise their use, whether as bulk crystals, nanowires or thin films. The opportunity therefore exists to develop methodologies for inclusion of metal oxides within traditional electronics with increasing demand for methods of functional oxide formation for plastic electronics. The primary goal of this thesis is to develop a unique process involving vacuum ultraviolet (VUV) light and oxygen for the creation of metal oxides, specifically zinc oxide, from small molecules

routinely employed in the active layers of organic electronic devices, in particular organic solar cells and organic light emitting diodes (OLEDs).

In this chapter, the field of Organic Electronics is briefly described and zinc oxide use highlighted. Current methods of oxide formation are compared and typical uses of ultraviolet light explored before elaborating on the process and materials involved in zinc oxide fabrication within this thesis.

Chapter 2 describes the experimental methodology used for sample preparation and characterisation techniques employed throughout this thesis.

Chapter 3 presents a thorough investigation of the effect of contrasting morphology on zinc oxide formation via the UV process with the aim of determining the mechanism of oxide formation. Grain boundaries are shown to have a significant positive effect on the rate of oxide formation by providing a route for oxygen assisted film degradation.

Chapter 4 employs heterostructures of metalorganic precursor and an archetypal molecular crystal as a model for multi-layer organic systems, such as might be encountered in an organic electronic device, to explore the impact of the UV process on layers underlying the precursor. In addition, the effect of molecular orientation and inclusion of an oxygen-containing layer is investigated, the latter more fully demonstrated by UV irradiation of a multilayer structure. We show that UV degradation and oxide formation proceed regardless of the molecular orientation of the precursor and that an underlying layer is affected only after 50% of the precursor film has reacted.

Chapter 5 combines nanosphere lithography and UV assisted zinc oxide formation for the first time, with the aim of creating patterned arrays of nanostructures for potential use as photonic structures. We report some success creating regular arrays and identify improvements which would result in structures with increased definition.

Chapter 6 summarises the findings from this thesis and outlines further work to progress beyond conclusions reached.

1.1 Organic Electronics

Modern technology relies on silicon based electronics but limitations involving the expense of manufacturing such inorganic materials on a larger scale have led to the development of organic electronics with the benefits of solution processing for printing and coating, easily synthesised molecules with tuneable properties, flexible, lightweight substrates and large area roll-to-roll manufacture. Although costs of electronics grade silicon have dropped recently due to increased manufacturing volume [28], this does not address the issues of weight and flexibility, thus the scope for lower cost organic based technologies meeting these demands exists. Economic assessments regarding the potential performance of organic based photovoltaics (OPV), for example, indicate that providing module lifetimes reach 5 years and efficiencies 7%, then OPV represents an economically viable investment [29].

Metal-free and copper phthalocyanines were two of the first organic molecules identified as possessing semiconducting properties in 1948 [30], followed by observation of photovoltaic (PV) activity using magnesium phthalocyanine [31] and the first organic heterojunction in 1986 using copper phthalocyanine [32]. Meanwhile 1987 saw the advent of the OLED [33] and developments in both fields broadened [34, 35] following the discovery of conducting polymers [36]. Polymer based solar cells generally contain blends of a conjugated polymer such as poly(3-hexylthiophene) (P3HT) and a C_{60}, fullerene derivative such as [6,6]-phenyl-C61-butyric acid methyl ester (PCBM) with efficiencies reported in excess of 10% [37]. However, progress using small molecules also continues apace, reaching efficiencies of 13.22% [38].

In addition to the active layer within a device, the electrode itself has a significant impact, being responsible for drawing or injecting charge and permitting the entry or emission of light. Traditionally, electrodes are invariably tin doped indium oxide (ITO), with a high light transmittance of over 80% in the visible range and resistivities below $\sim 1 \times 10^{-4}\,\Omega$cm [39]. ITO, however, suffers from brittleness and an increasing cost due to the scarcity of indium [40], already contributing significantly to the cost of a PV device [29]. Although ITO may be deposited on flexible substrates such as polyethylene terephthalate (PET), the resulting film is usually of lower quality due to the lower substrate deposition temperatures required [41]. Consequently,

alternatives to ITO have been sought.

Requirements of electrode materials for organic electronics include transparency in the visible range, low resistivity, processing methods and temperatures compatible with flexible substrates and active layers, stability and appropriate HOMO (highest occupied molecular orbital) and LUMO (lowest unoccupied molecular orbital) levels to enable efficient charge transport into and out of devices. Polymers such as poly(3,4-ethylenedioxythiopene) complexed with poly(styrene sulfonate) (PEDOT-PSS) have been successfully employed as electrode materials in electroluminescent devices and organic field effect transistors (OFETs) [42,43] but can suffer instability upon thermal and chemical stresses [40]. Individually, carbon nanotubes present high intrinsic mobilities of $\sim 10^5$ cm^2/Vs [44] and thin films have been used as electrodes for polymer/fullerene solar cells [45]. A major advantage would be solution based deposition following solubilisation of nanotubes, however, dispersion is a problem as carbon nanotubes aggregate easily due to a high Van der Waals interaction and progress is further hindered by the difficulty in obtaining carbon nanotubes in quantity, of a uniform size and with adequate purity.

Graphene is another material which has seen intensive research into potential applications since 2005 when room temperature mobilities of $\sim 10^4$ cm^2/Vs were reported [46]. Transmittance and sheet resistance for highly doped graphene both decrease with an increasing number of layers necessitating a compromise or the development of composite films. Alternatively, etching may be used to create a graphene grid with sufficient transparency [47] and deposition of graphene over a network of metal nanostructures can also achieve mobility and transparency requirements to some extent [48]. Solution processing of graphene functionalised by chemical oxidation may be used to deposit thin films, subsequently reduced to regain conductivity for use as electrodes [49]. Although ideal as a method to be industrialised for roll-to-toll processing, defects within sheets dramatically reduce conductivity.

Metal, with its high conductivity, offers yet another alternative to ITO. As metal is highly reflective, films used as electrodes must be extremely thin (< 10 nm) where transparency is required but at this point, surface roughness becomes an issue, resulting in scattering of charge carriers and decreased conductivity, with possible oxidation of such thin layers also a

concern [50, 51]. Alternatively, metallic nanostructures or a grid may be employed, allowing transmission of light between the gridlines or nanostructures [52, 53]. In the case of grids, the transmittance is limited by the finite width of gridlines and a trade-off must be made if using thinner lines, as resistance increases. Fabrication methods are often labour intensive and problematic as any defects adversely affect charge transport due to the narrow gridlines required for transparency [40]. Nanoimprint lithography simplifies manufacture but is more suitable for thicker lines [53].

The remaining group of alternatives to ITO is other metal oxides. Transparent conducting oxides (TCOs) include doped In_2O_3 (indium oxide) but also ZnO (zinc oxide) and SnO_2 (tin oxide), among others. These binary compounds may be doped with a range of impurites, summarised in table 1.1 [1], providing performance and stability superior to that of undoped metal oxide films where transport properties are a consequence of oxygen vacancies or interstitial metal atoms. Of these doped binary compounds, the most likely candidate to replace ITO is aluminium doped zinc oxide (AZO), thin films of which were shown to equal the resistivity of ITO for the first time in 1996 when prepared by pulsed laser deposition [54]. Furthermore, zinc oxide is abundant and inexpensive with no toxicity. The properties of AZO compare very favourably with those of ITO (table 1.2).

Table 1.1: TCOs and their dopants, suitable for use as transparent electrodes [1]

Method	Dopant or compound used
SnO_2	Sb, F, As, Nb, Ta
In_20_3	Sn, Ge, Mo, F, Ti, Zr, Hf, Nb, Ta, W, Te
ZnO	Al, Ga, B, In, Y, Sc, F, V, Si, Ge, Ti, Zr, Hf
CdO	In, Sn
$ZnO\text{-}SnO_2$	Zn_2SnO_4, $ZnSnO_3$
$ZnO\text{-}In_2O_3$	$Zn_2In_2O_5$, $Zn_3In_2O_6$
$In_2O_3\text{-}SnO_2$	$In_4Sn_3O_{12}$
$CdO\text{-}SnO_2$	Cd_2SnO_4, $CdSnO_3$
$CdO\text{-}In_2O_3$	$CdIn_2O_4$
$MgIn_2O_4$	
$GaInO_3$, $(Ga, In)_2O_3$	Sn, Ge
$CdSb_2O_6$	Y
$ZnO\text{-}In_2O_3\text{-}SnO_2$	$Zn_2IN_2O_5\text{-}In_4Sn_3O_{12}$
$CdO\text{-}In_2O_3\text{-}SnO_2$	$CdIn_2O_4\text{-}Cd_2SnO_4$
$ZnO\text{-}CdO\text{-}In_2O_3\text{-}SnO_2$	

Table 1.2: Properties of AZO and ITO [1]

	AZO	ITO
Resistivity (Ωcm)	10^{-5}	10^{-5}
Bandgap E_g(eV)	3.3	3.7
Refractive index	2	2
Work Function ϕ (eV)	4.6	4.8 - 5.0

In addition to their use as electrode materials, TCOs are used as charge transport layers in solar cells with ZnO as an electron transport layer in polymer solar cells [55] and transition metal oxide films, such as vanadium oxide (V_2O_5) and molybdenum oxide (MoO_3) as hole injection layers [56]. Furthermore, zinc oxide has been used as the channel layer in transparent thin film transistors [57] and as a buffer layer in OLEDS [58], making it one of the most useful of the metal oxides and deposition is possible via a range of methods. Hence, we have concentrated our efforts in this thesis on the fabrication of zinc oxide.

1.2 Manufacture of Zinc Oxide for Organic Electronics

Zinc oxide films may be fabricated by a variety of methods but not all are suitable for use with organic electronic devices or flexible substrates which will not generally withstand harsh solvents or high temperatures. Main deposition techniques are described below.

1.2.1 Magnetron Sputtering

The predominant deposition method, magnetron sputtering, takes place in an inert environment and is often used for ZnO deposition [59]. Ions are accelerated towards a metal oxide target, sputtering molecules, a portion of which adhere to the substrate. A magnetic field is applied, trapping electrons close to the target source in a helical path. Concentration of electrons in the vicinity of the oxide results in an enhanced deposition rate and both substrate and source may remain at room temperature, negating any necessity to raise the temperature of high melting point oxides for deposition and permitting use of low melting point substrates.

1.2.2 Pulsed Laser Deposition

Pulsed laser deposition (PLD) requires that both substrate and target are contained in a vacuum. A laser fired at the target creates a plasma plume, vaporising the metal oxide. The oxide vapour deposits as a film on the substrate with a higher quality than that achieved by magnetron sputtering as the quantity of material deposited in a single pulse is much higher, allowing higher levels of nucleation. PLD was used to deposit AZO films with resistivity comparable to that of ITO [60].

1.2.3 Chemical Vapour Deposition

When used for deposition of ZnO, this method generally involves reacting precursor molecules on the surface of a heated substrate or by thermal decomposition on the substrate. Molecules such as diethyl-zinc or dimethyl-zinc may be used but are highly reactive in air. Alternatively, zinc acetate has also been successfully employed [61]. The high temperatures involved prohibit the use of polymer substrates.

1.2.4 Spray Pyrolysis

Similar to chemical vapour deposition (CVD), spray pyrolysis involves the reaction of chemicals on the substrate. In this case, solutions of the chemicals are sprayed onto a heated substrate, releasing volatile by-products upon reaction and producing a metal oxide film [62]. Again, heated substrates are incompatible with the use of polymer materials.

1.2.5 Molecular Beam Epitaxy

In molecular beam epitaxy (MBE) both the substrate and sample are contained in a vacuum. The oxide is heated to sublimation and slowly, epitaxially deposits on the substrate. Metal sources may be used under oxygen radical irradiation to form the metal oxide on the substrate [63] and although sensitive substrates may be used, the source material must withstand heating.

1.2.6 Spin-Coating

Zinc oxide may be deposited using a sol-gel method and spin-coating which has the advantage of requiring no vacuum system. The sol-gel method for zinc oxide frequently uses zinc acetate as a precursor dissolved in a solvent with a stabiliser to form a colloidal solution. This solution is then poured onto a substrate which is spun at the rate necessary to form the required thickness prior to heating to remove the solvent [55, 64], limiting the substrates which may be used.

1.2.7 Electrodeposition

Electrodeposition is a simple and scaleable method, employing the substrate as a cathode and the metal whose oxide is to be deposited as the anode. The electrodes are placed in a solution such as a nitrate of the metal and a current passed through the solution through the electrodes. The metal oxide deposits on the cathode. Control of temperature, concentration, pH and potential allow the deposition of a variety of nanostructures and highly crystalline film [65].

1.3 UV assisted processing

Processing using UV light is already well-established in many fields due to the many benefits offered. Lamps are reliable with a consistent light output and a choice of wavelengths. The intensity is adjustable and the response time is very short. A major use is for disinfection or sterilisation allowing water reuse in industry, processing of sewage water and to create drinking water. As no chemicals are involved, water suffers no deterioration in taste or odour and for sewage, clearly improves these characteristics. As a method for cleaning and disinfection, UV light is extremely useful when applied to food packaging and food preparation surfaces where only a few seconds of irradiation are required with no chemicals involved. Lamps used for disinfection are usually mercury vapour lamps producing an emission line at 254 mn [66]. UVC radiation (10 - 280 nm) is particularly effective at killing bacteria by causing damage of DNA [67] and is even used to disinfect the water used as ballast to provide stability in large

ships.

Another major use is for curing and drying for coatings or printed ink and is of particular relevance to organic electronics where polymers are employed for UV-induced polymerisation in nanoimprint lithography, avoiding the need for thermal input and unsuitable solvents [68]. UV curing is also easily integrated into roll-to-roll processes, resulting in higher speed printing on flexible substrates [69]. The UV lamps require very little maintenance and processing produces minimal waste.

Of impact in this work is the use of UV light, in combination with oxygen for decomposition of organic molecules. Used with titanium dioxide, a photooxidative catalyst, UV light reacts with oxygen in the air to form highly reactive radicals and ozone which bind to volatile organic compounds, oxidising them for safe elimination and is employed in the removal of organic chemicals from industrial exhaust fumes [70, 71].

One of the broadest uses of UV light is for surface treatment which may be for electrode improvement by modification of work function [72, 73], UV hardening of photoresists for lithographic processes where temperatures might otherwise be too high [74] and increasing hydrophilicity and adhesion [75]. Many of these modification techniques use mercury vapour lamps [74]. A routine use of UV light for surface treatment is UV-ozone cleaning. Ideal as a technique to prepare substrates for subsequent deposition of films, ozone and reactive oxygen atoms created by the absorption of UV light by molecular oxygen are very strongly oxidising and remove any contaminants from the substrate surface [76].

UV sources are available in a variety of forms, each producing a different frequency or range of frequencies and each with their own benefits. One of the most popular is the low pressure mercury vapour lamp, a gas discharge lamp which produces light at several wavelength by passing an electric arc through vaporised mercury. UV light is produced at wavelengths of 185 and 254 nm. These lamps are commonly used for germicidal purposes. Mercury lamps do not emit UV light immediately as the mercury must first be vaporised then ionised. Lamps usually contain argon which is ionised as soon as the lamp is switched on, creating an arc which may then gradually heat up the mercury so that it vaporises. Gas discharge lamps may contain other

gases such as neon, helium or sodium, each producing light at a different range of wavelengths. UV LEDs have recently found uses for UV curing, photocatalytic applications and are being developed as UV sources for disinfection [77, 78]. As they do not contain mercury and require no specialist waste disposal, their appeal is obvious.

The source used here is a xenon excimer lamp which relies on emission of UV light from the excited state of a pair of weakly bound molecules which do not have a bound ground state under normal conditions as the ground state is repulsive, such as He_2^*, Ne_2^*, Ar_2^*, Ar_2^*, Kr_2^*, and Xe_2^* as well as the halides ArF^*, KrF^*, $XeCl^*$and XeF^* [79]. The light produced is incoherent and quasimonochromatic and for xenon, UV light is produced at 172 nm. Two concentric quartz tubes with metal electrodes on their outer surfaces are separated by xenon with the outermost electrode perforated to allow the escape of UV light (figure 1.1). A high voltage applied between the two electrodes results in microdischarges of a few hundred amperes per square cm appearing as long narrow filaments of charge. The electrons from these discharges collide with the xenon atoms to produce two excited atomic states (equation 1.1). Although both are formed, it is only the first excited state, Xe^*, which produces the excimer directly via a three body collision with two other xenon atons (equation 1.2) [79]. Finally, the excimer returns to its ground state, radiating UV light at 172 nm and disintegrating to two xenon atoms (equation 1.3). Soon after their development, excimer lamps found use in material deposition by photon-assisted cleavage of precursors to deposit metals or semiconductors, for surface modification, in particular of polymers and in pollution control [7].

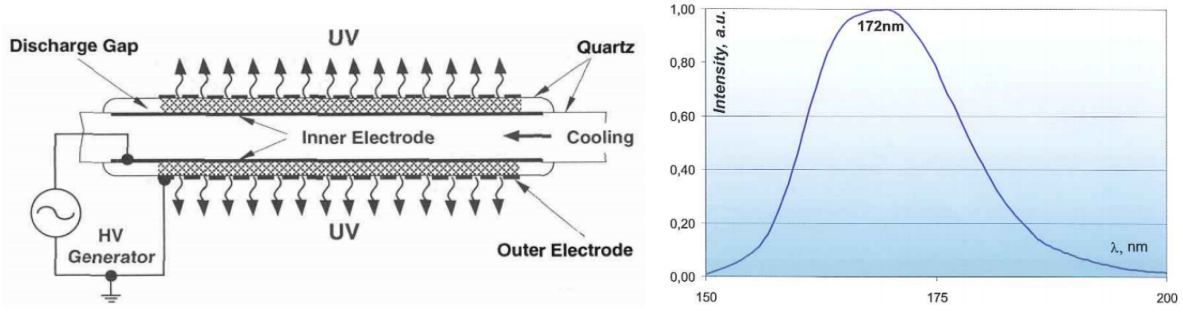

(a) (b)

Figure 1.1: (a) Cylindrical excimer lamp configuration, reproduced from [7] and (b) Light intensity produced by a Bluelight compact excimer system, reproduced from [8]

$$\mathrm{e} + \mathrm{Xe} \longrightarrow \mathrm{e} + \mathrm{Xe}^{*} \tag{1.1}$$

$$\longrightarrow \mathrm{e} + \mathrm{Xe}^{**}$$

$$\mathrm{Xe}^{*} + \mathrm{Xe} + \mathrm{Xe} \longrightarrow \mathrm{Xe}_2^{*} + \mathrm{Xe} \tag{1.2}$$

$$\mathrm{Xe}_2^{*} \longrightarrow 2\mathrm{Xe} + h\nu \tag{1.3}$$

1.4 Molecular Materials

The process explored in this thesis was first reported in 2000 when cobalt phthalocyanine films irradiated by light with an energy of 7.21 eV were found to form cobalt oxide with removal of organic fragments [80]. Investigations on manganese phthalocyanine in 2009 came to the same conclusion [81]. Here, we develop the process further as a methodology for functional oxide film formation, in particular for zinc oxide. This work therefore involves zinc phthalocyanine (ZnPc), a similar precursor, zinc tetraphenylporphyrin (ZnTPP) for comparison and as part of a multi-layer system, 3,4,9,10-perylenetetracarboxylic dianhydride (PTCDA), all of which will be described here.

1.4.1 Phthalocyanines

Phthalocyanines are a class of blue-green coloured polyaromatic compounds, structurally related to the porphyrin macrocycle ring system [82], the name originating from the Greek terms *naphtha* (mineral oil) and *cyanine* (dark blue). Phthalocyanines are used extensively for a range of applications, including dyes, solar cells [32, 83], transistors [84], OLEDs [85, 86], spintronics [87] and chemical sensors [88] and all contain the phthalocyanato anion, $C_{32}H_{16}N_8^{2-}$ (Pc^{2-}) bound to either hydrogen (H_2Pc), metal ions such as Cu^{2+}, $Mn^{2+}$and Zn^{2+} (MPc) or groups of atoms in the central cavity. The molecule remains planar for hydrogen and small metal atoms but acquires a pyramidal structure with larger ions, for example, vanadyl phthalocya-

nine (VOPc).

Structure

The phthalocyanine macrocycle comprises four isoindole units, resulting in a 2-d π-conjugated system responsible for intense electronic absorption in the visible region and an isotropic conductivity in a direction orthogonal to the molecular plane when stacked (figure 1.2) [12]. The high electronic interaction between the Pc and the metal atom results in a charge distribution where a metal ion such as Zn^{2+} manifests rather more as $Zn^{0.5+}$- $Zn^{0.9+}$, creating high thermal and chemical stability of the metal-phthalocyanine complex [89].

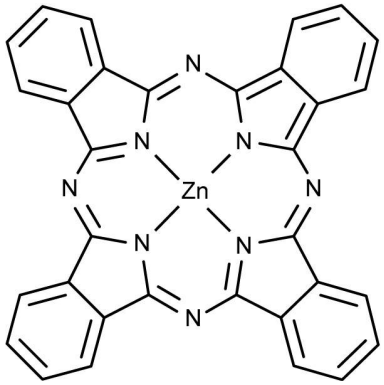

Figure 1.2: Molecular structure of zinc phthalocyanine

Planar phthalocyanines are generally considered isomorphic, with at least 15 different polymorphs described in the literature [3, 90]. For our purposes, zinc phthalocyanine may be considered to adopt the same structures as copper phthalocyanine (CuPc) [91]. The metastable α polymorph forms at room temperature and belongs to the $C2/c$ space group [92], crystallising in a monoclinic system. The stable β polymorph forms on annealing or when deposition occurs at higher temperatures and takes a monoclinic structure, crystallising in the $P2_1/a$ space group [92]. The CuPc α polymorph was considered for a long time to be the same as platinum phthalocyanine (PtPc) and the metal-free phthalocyanine, forming a herringbone arrangement when crystallising in the monoclinic system [2], however, Hoshino found in 2003 that the CuPc α polymorph is not isomorphic with the α polymorphs of either H_2Pc or PtPc and instead formed a slipped stack arrangement [3]. Structural information for both modifications is sum-

marised in table 1.3. The two polymorphs and x-ray diffraction identification are explored further in chapter 3.

Table 1.3: Structural information for the α polymorph of CuPc, as determined by Ashida [2] and Hoshino [3]

	ZnPc - Ashida [2]	ZnPc - Hoshino [3]
Space Group	C2/c	P2$_1$/a
Cell lengths (Å)	**a** 25.92, **b** 3.79, **c** 23.92	**a** 12.886, **b** 3.769, **c** 12.061
Cell angles (°)	$\boldsymbol{\alpha}$ 90, $\boldsymbol{\beta}$ 90.4, $\boldsymbol{\gamma}$ 90	$\boldsymbol{\alpha}$ 90.22, $\boldsymbol{\beta}$ 90.62, $\boldsymbol{\gamma}$ 90.32
Cell Volume (Å^3)	2349.77	582.275

Although planar metal phthalocyanines form films epitaxially when deposited on substrates such as copper and molybdenum sulphide [93, 94], when using weakly interacting substrates at room temperature, such as those used in this work, the film form in the α structure. Hence, only results reported for non-interacting substrates are considered. Films are composed of spherical microcrystallites, approximately 28 nm in size (figure 1.3), arranged with the (200) plane parallel to the substrate but depart from this orientation as film thickness exceeds 100 nm and crystallite size increases [95].

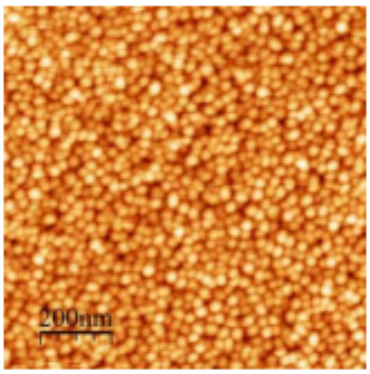

Figure 1.3: AFM image of a 27 nm film of iron phthalocyanine on sapphire substrates grown at 25°C [9]

Electronic Spectroscopic Properties

The electronic absorption spectra of phthalocyanines has been studied extensively, although ZnPc is reported less frequently than CuPc. The vapour, solution and thin film spectra show a

progressive increase in intermolecular interactions. Figure 1.4a compares the absorption spectra of CuPc in solution and as a thin film. The contribution of intermolecular interactions results in a broadening of the peaks from the momomer characteristics observed in solution and has been explained as a consequence of a dimer model with exciton dipole-dipole interactions resulting in the splitting of peaks in absorption spectra [10]. This effect is repeated in the vapour-phase and thin film absorption spectra of ZnPc (figures 1.4b,c) with distinct broadening of the sharp peaks seen at approximately 440 and 660 nm in the vapour-phase.

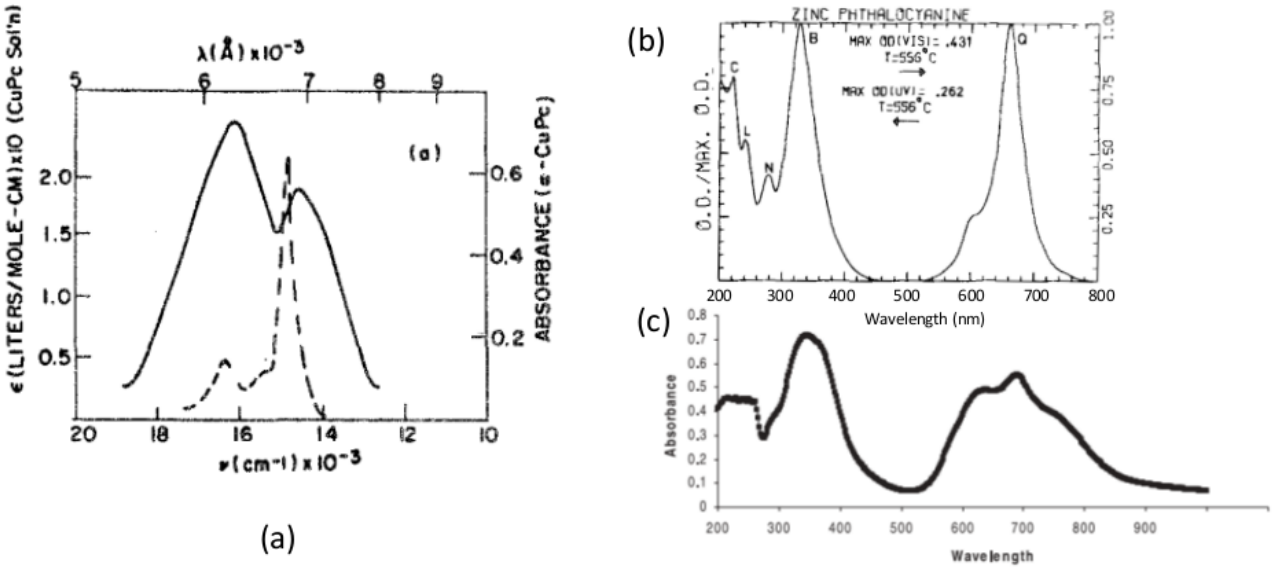

Figure 1.4: (a) Electronic absorption spectra of CuPc in 1-chloronaphthalene (dashed line) and an evaporated film of α-CuPc adapted from [10], (b) vapour-phase absorption spectrum of ZnPc adapted from [11] and (c) absorption spectrum for a flash evaporated ZnPc film reproduced from [12]

Figure 1.5 shows the absorption spectrum of ZnPc film with the Q and B (*Soret*) bands indicated at approximately 500 - 900 nm and 200 - 400 nm, which have been attributed to an a_{1u} to e_g transition, and an a_{2u} to e_g and a b_{2u} to e_g transition, respectively [12]. Not visible within this range is an additional absorption band, the C band with a peak at 212 nm [96]. The B band has been observed as a doublet with peaks at at 335 nm and 354 nm and a shoulder at 287 nm [97] and corresponds to a transition from the HOMO-1 energy level to the LUMO energy level. Additional peaks have also been reported just above the *Soret* band at 335 nm [96] and 354 nm [97]. There is some dispute as to whether the origin of the lower energy peak in the Q band (705 nm) is excitonic in nature and the higher energy peak (620.5

nm) due to a $\pi - \pi*$ transition on the Pc macrocycle [96] or whether the transitions arise as a result of Davydov splitting [98]. This is discussed further in section 3.2.3.

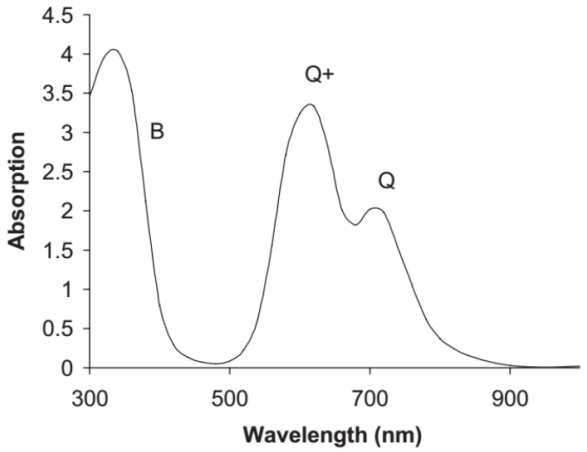

Figure 1.5: Thin film absorption spectrum of ZnPc, indicating the B and Q bands, reproduced from [13]

1.4.2 Porphyrins

Porphyrins are substituted porphins, many of which occur frequently in nature, for example, heme, which is the pigment in red blood cells and as chlorin, which occurs in chlorophyll used for photosynthesis. As with phthalocyanine, there are a range of metal tetraphenylporphyrins available, including Co, Fe, Ni, and Mn. Due to their absorption in the visible range, derivatives are used as the donors in solar cells [99] and as sensitisers for dye-sensitised solar cells [100]. A substituted porphin, zinc tetraphenylporphyrin (ZnTPP), is used in this work.

Structure

Although structurally similar to ZnPc, ZnTPP differs in its stacking ability as a result of the four phenyl rings attached to the main porphin macrocycle (figure 1.6a). These phenyl groups lie at an angle of approximately 60° to the core of the molecule [4] and as a consequence, ZnTPP forms amorphous films [101]. ZnTPP does, however, crystallise in the triclinic system when unsolvated crystals are dissolved in chloroform, filtered and layered with benzene, allowing crystals to deposit at the bottom several days later [4]. The highest intensity peak in the

x-ray powder diffraction data of ZnTPP indicates the (010) plane lies parallel to the substrate (figure 1.6b) but this is rarely seen in deposited films. Structural information is summarised in table 1.4 and the effect of structure on x-ray diffraction results is discussed in chapter 3.

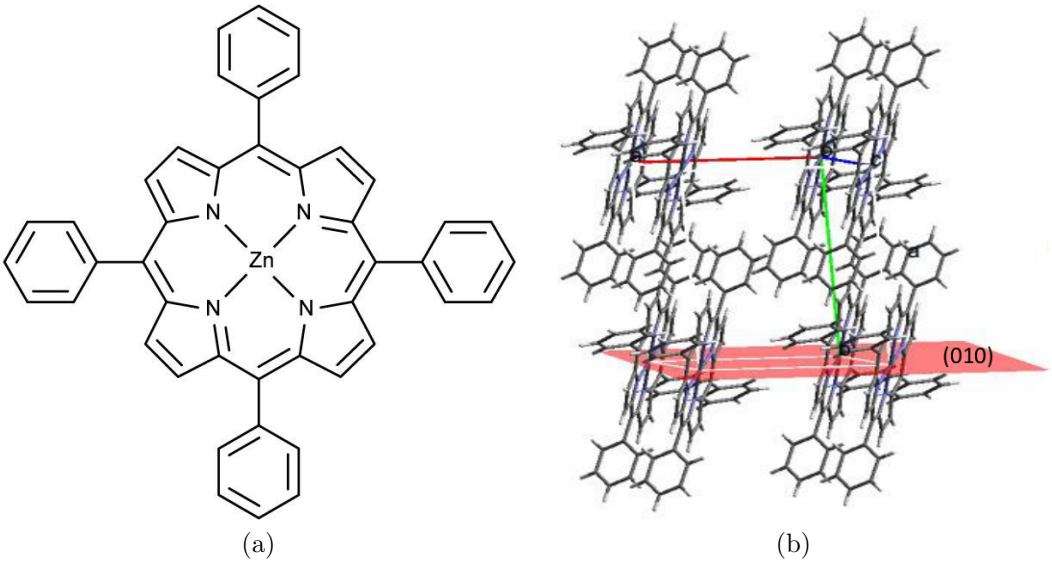

(a) (b)

Figure 1.6: (a) Molecular structure of zinc tetraphenylporphyrin and (b) arrangement of zinc tetraphenylporphyrin molecules in the triclinic system as determined by Scheidt [4], viewed along the (010) plane indicated in pink

Table 1.4: Structural information for zinc tetraphenylporphyrin as determined by Scheidt [4]

	ZnTPP - Scheidt [4]
Space Group	P -1
Cell lengths (Å)	**a** 10.382, **b** 12.421, **c** 6.443
Cell angles (°)	$\boldsymbol{\alpha}$ 98.30, $\boldsymbol{\beta}$ 101.15, $\boldsymbol{\gamma}$ 96.47
Cell Volume (Å^3)	798.131

Electronic Spectroscopic Properties

Absorption spectra of ZnTPP in the vapour phase, as a solution in water and a 50 µm film show an increasing splitting of peaks in the Q band as for ZnPc (figure 1.7). The highest wavelength peak in the thin film absorption spectrum (figure 1.7b) is attributed to the $\pi - \pi^*$ transition from the HOMO to the LUMO level (A_2u to E_g) and higher energy transitions from the HUMO-1 to the LUMO level [102].

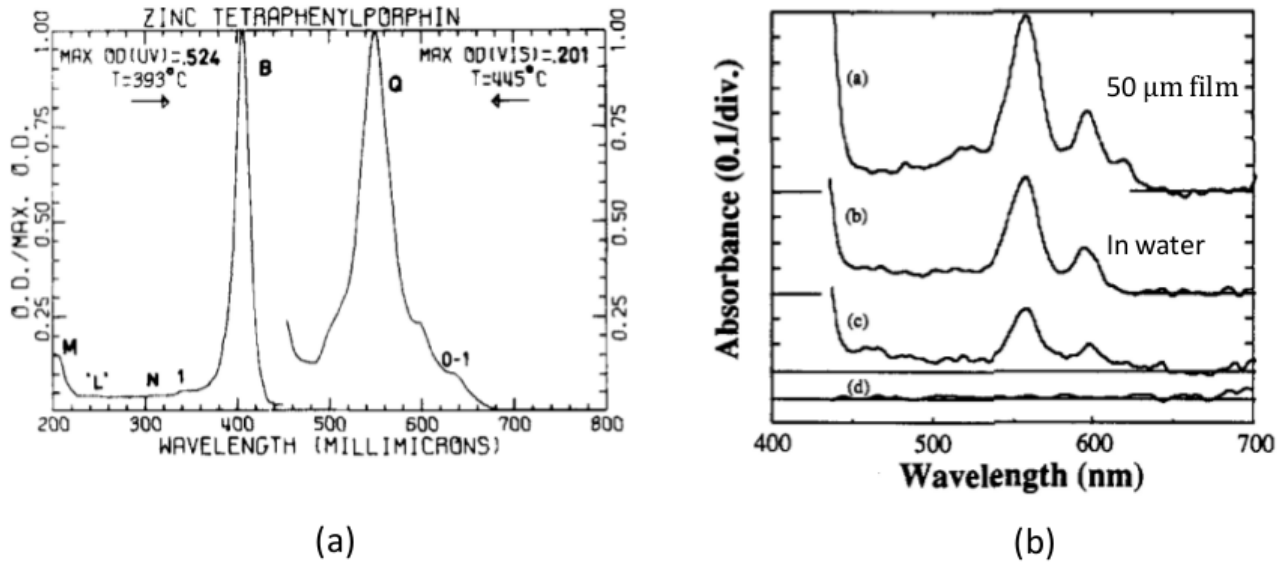

Figure 1.7: Electronic absorption spectra of ZnTPP (a) in the vapour phase [14] (b) as a 50 µm film and in water, adapted from [15]

1.4.3 3,4,9,10-Perylenetetracarboxylic Dianhydride (PTCDA)

3,4,9,10-Perylenetetracarboxylic dianhydride (PTCDA) is a commercial red pigment but has been investigated extensively as a result of its regular stacking and small intermolecular distance which make it an ideal model for organic semiconductor systems. Its mobility has led to its use as an electron acceptor in solar cells, for hole injection in OLEDs and has been investigated as the channel material for field effect transistors, distinguishing between electron flow along the molecular planes and hole transport orthogonal to the molecular plane [103–105].

Structure

PTCDA is a planar molecule based on perylene and exists as two polymorphs, α and β, both crystallising in the monoclinic system on weakly interacting substrates and both belonging to the $P2_1/c$ space group. In fact, the two structures are so similar, with intermolecular distances of 3.22 and 3.25Å, that until 1992, it was believed that only one modification existed [106]. The structural parameters are summarised in table 1.5.

Table 1.5: Structural information for the α and β polymorphs of PTCDA as determined by Tojo and Mizuguchi [5, 6]

	Alpha-PTCDA [5]	Beta-PTCDA [6]
Space Group	$P2_1/c$	$P2_1/c$
Cell lengths (Å)	**a** 3.703, **b** 12.013, **c** 17.161	**a** 3.74, **b** 18.95, **c** 10.75
Cell angles (°)	$\boldsymbol{\alpha}$ 90, $\boldsymbol{\beta}$ 93.26, $\boldsymbol{\gamma}$ 90	$\boldsymbol{\alpha}$ 90, $\boldsymbol{\beta}$ 96.0, $\boldsymbol{\gamma}$ 90
Cell Volume (Å^3)	762.157	757.711

While PTCDA forms films epitaxially on interacting substrates such as NaCl and KCl, on substrates such as glass and silicon with a native oxide layer, PTCDA forms films with its molecules arranged flat against the surface [106]. XRD scans of PTCDA on glass and silicon show that the molecules lie with the (10-2) plane parallel to the substrate with some adopting an orientation with the (110) plane parallel to the substrate [107].

Electronic Spectroscopic Properties

Several theories exist regarding the origin of transitions observed in the electronic absorption spectra (figure 1.8). Bulovic *et al.* consider the transition at 2.23 eV due to a charge transfer state and 4 higher energy peaks in the solution spectrum arising from transitions to different vibronic singlet states ($S_1[0 - \nu_n]$) (figure 1.8a) [16]. As the peak profiles were unaffected by concentration, these transitions were considered Frenkel-like with the electronic excitation mostly confined to the monomer and were broadened in the spectrum for a thin film (figure 1.8b). The spectrum is now considered to be composed of mixed molecular and charge transfer state transitions coupled to molecular vibrations with the entire absorption between 2 - 3 eV attributed to molecular $\pi - \pi^*$ transitions [108]. Absorption spectra for PTCDA are explored further in section 4.2.

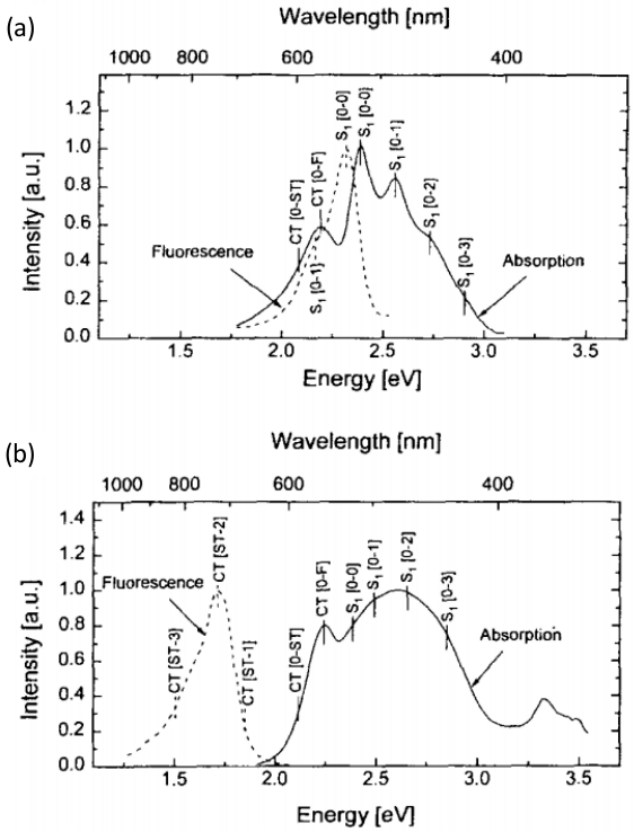

Figure 1.8: Electronic absorption spectra (solid line) and fluorescence spectra (dashed line) of PTCDA (a) in solution and (b) as a 1000Åfilm, adapted from [16]

Chapter 2

Experimental Details

In this chapter, the techniques used to prepare and irradiate samples is described, followed by a summary of characterisation techniques. Substrates were either quartz (10 x 10 x 1 mm, purchased from UQG Optics Ltd), glass (cut from transparent float glass slides purchased from VWR) or silicon with a native oxide layer (purchased from Virginia Semiconductor). Substrates were prepared for deposition by sonication for 10 minutes each in acetone then isopropanol before drying in a nitrogen stream and mounting on a substrate holder for film deposition. ZnTPP was of 98% purity supplied by Porphyrin Systems and ZnPc and PTCDA were supplied from Sigma-Aldrich with purity 97%.

2.1 Organic Molecular Beam Deposition (OMBD)

Organic Molecular Beam Deposition (OMBD) was used to deposit all films examined in this thesis. The main principle is deposition of films by sublimation of the source material in a high or ultra-high vacuum. Advantages are the high purity possible, consistent film growth with variable deposition rates and the option for co-deposition of material. In our case, purity is further ensured by placement of the OMBD system within a glovebox.

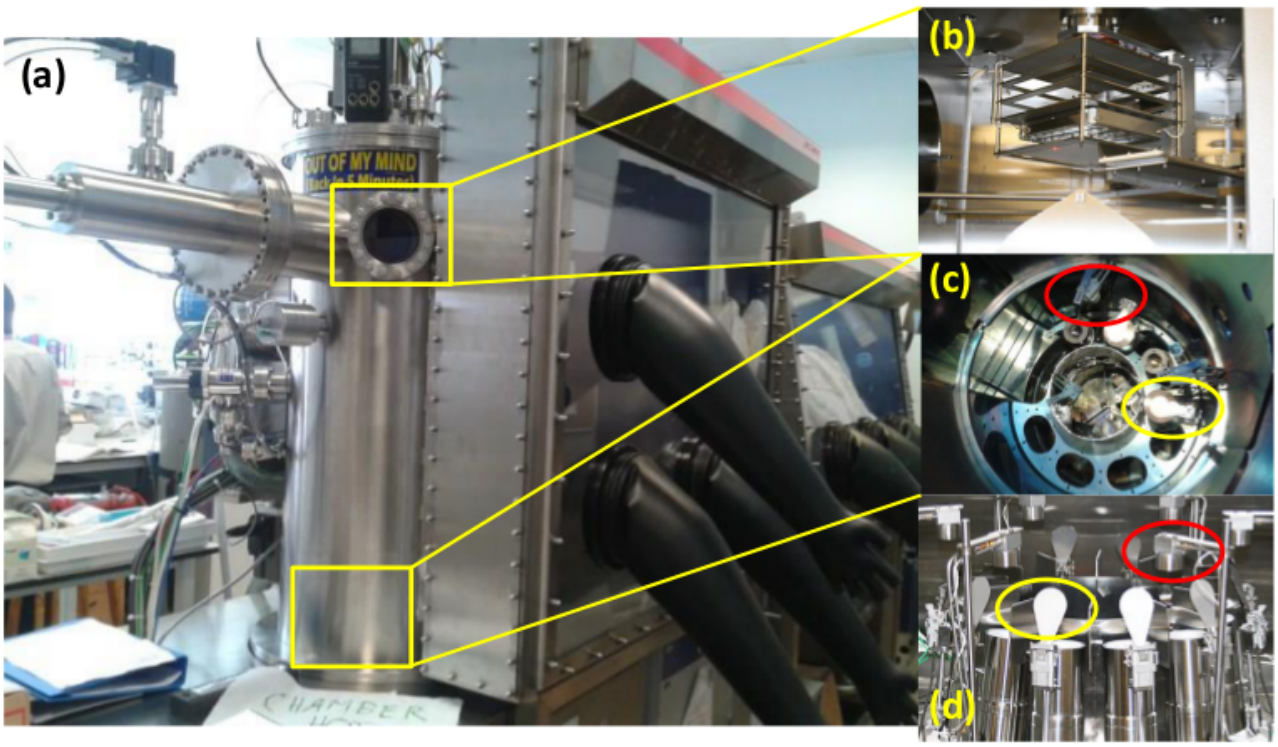

Figure 2.1: (a) The OMBD chamber and glovebox with (b) substrate holder at the top of the chamber, (c) top view of Knudsen cells situated at the bottom of the chamber and (d) side view of a set of Knudsen cells. Quartz crystal monitors are indicated by red ovals and shutters for the sources by yellow ovals. Images (b) and (d) are modified from images taken from the Kurt Lesker website

The OMBD system consists of a steel chamber capable of high and ultra-high vacuum achieved by a combination of roughing pumps, cryo pumps and in the case of ultra-high vacuum, ion pumps. The source material is placed in a ceramic crucible within a Knudsen cell at the base of the OMBD chamber (figure 2.1c) and substrates are mounted on a substrate plate and placed in a holder at the top of the chamber (figure 2.1b). The chamber used has the facility to deposit on several separate substrate plates in turn without breaking the vacuum. Once the required vacuum has been achieved (10^{-7}mbar here), the source within the Knudsen cell is heated by passing an adjustable current through tanatalum coils surrounding the crucible, allowing a variable rate for heating and monitored using a thermocouple attached to the crucible. Once the correct temperature is reached, the shutters covering the sources (indicated by yellow ovals in figure 2.1) open and the source material sublimes. The flux rate of sublimed particles is measured by quartz crystal monitors (QCM) placed close to the mouth of the cells. Deposition of material on quartz crystals alters their mass and consequently their resonant frequency,

allowing determination of the deposition rate. The deposition rate was maintained at 1Å/s for all films of thickness exceeding 30 nm. For thinner films, a rate of 0.1 Å/s was used by adjustment of source heating. Once a consistent rate is achieved, the shutter obscuring the substrates is removed and film deposition proceeds, monitored by a further QCM placed near the substrates. The substrate holder rotates thoughout deposition, ensuring a uniform film and may be heated if required. Films were deposited on substrated maintained at room temperature for this thesis.

Although the thickness of film determined by a QCM, T_{QCM}, may be used as an indication of material deposited, it is often necessary to measure the actual thickness, T_{True}, by other means. Here, films were scratched and the scratch profile measured by atomic force microscopy. This value is then used to adjust deposition parameters by use of a tooling factor to obtain a calibrated value, $TF_{calibrated}$, by adjustment of the initial value, $TF_{initial}$ (equation 2.1). A measurement of film thickness taken by this method is shown in section 3.2.3.

$$TF_{calibrated} = \frac{T_{true}}{T_{QCM}} TF_{initial} \tag{2.1}$$

2.2 Nanosphere Deposition

Chapter 5 gives a detailed description of the method used to form monolayers of polystyrene nanospheres and a brief comparison to other methods.

2.3 UV Irradiation

UV irradiation is carried out in a purpose built stainless steel vacuum chamber, of volume approximately 30 litres, fitted with a BlueLight Compact Excimer System, a xenon excimer lamp, capable of irradiance intensity 50mW/cm^2. Samples are mounted on an aluminium plate and placed at a distance of 8.5 cm from the lamp. The chamber is evacuated using a

rotary pump. Once a pressure of 10^{-1}mbar has been reached, nitrogen is let into the system to a pressure of 1.8 mbar via the gas inlet shown in figure 2.2. Once stable, oxygen flow is introduced until a total pressure of 3.0 mbar is reached, creating an environment with 40% oxygen.

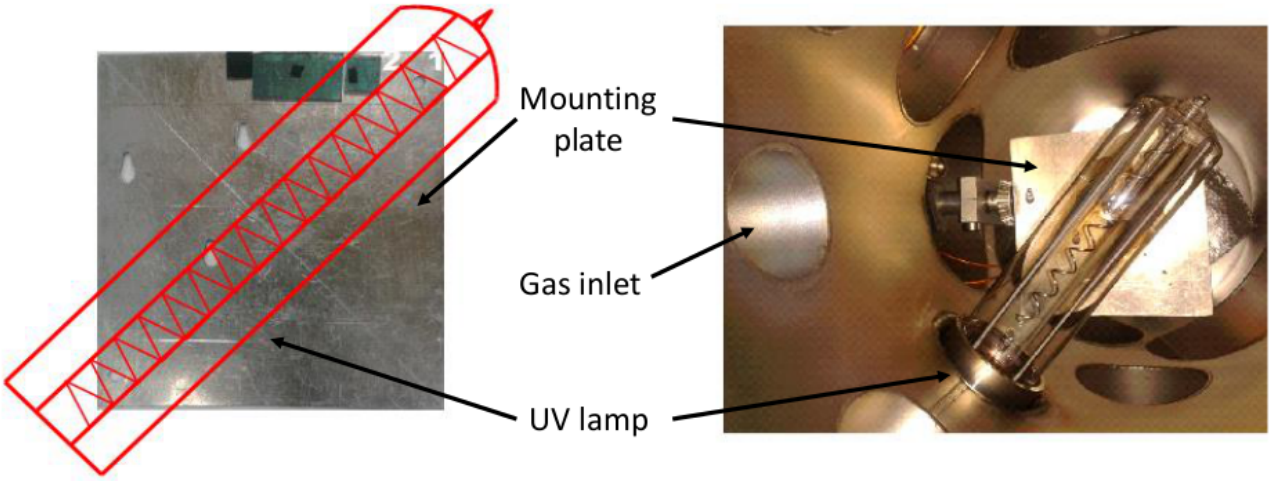

Figure 2.2: View of the sample plate for the UV chamber with a schematic of an excimer lamp drawn to indicate the position and a view of the interior of the UV chamber

The lamp was switched on for the duration required before reducing the oxygen flow to zero and switching off the lamp. Nitrogen was flushed through the chamber to remove any residual organic fragments and ozone before returning the chamber to atmospheric pressure. It was assumed that the flux of UV light would be represented by a simple model which yielded the light distribution shown in figure 2.3b, however, irradiation of ZnPc film for 90 minutes demonstrated a highly uneven flux across the sample holder (figure 2.3c). The thickness of ZnPc film remaining was determined as explained in section 3.2.3 and plotted in figure 2.3d. As the flux was not equal across the sample plate, samples for irradiation were always placed in the same position as indicated in figure 2.3a.

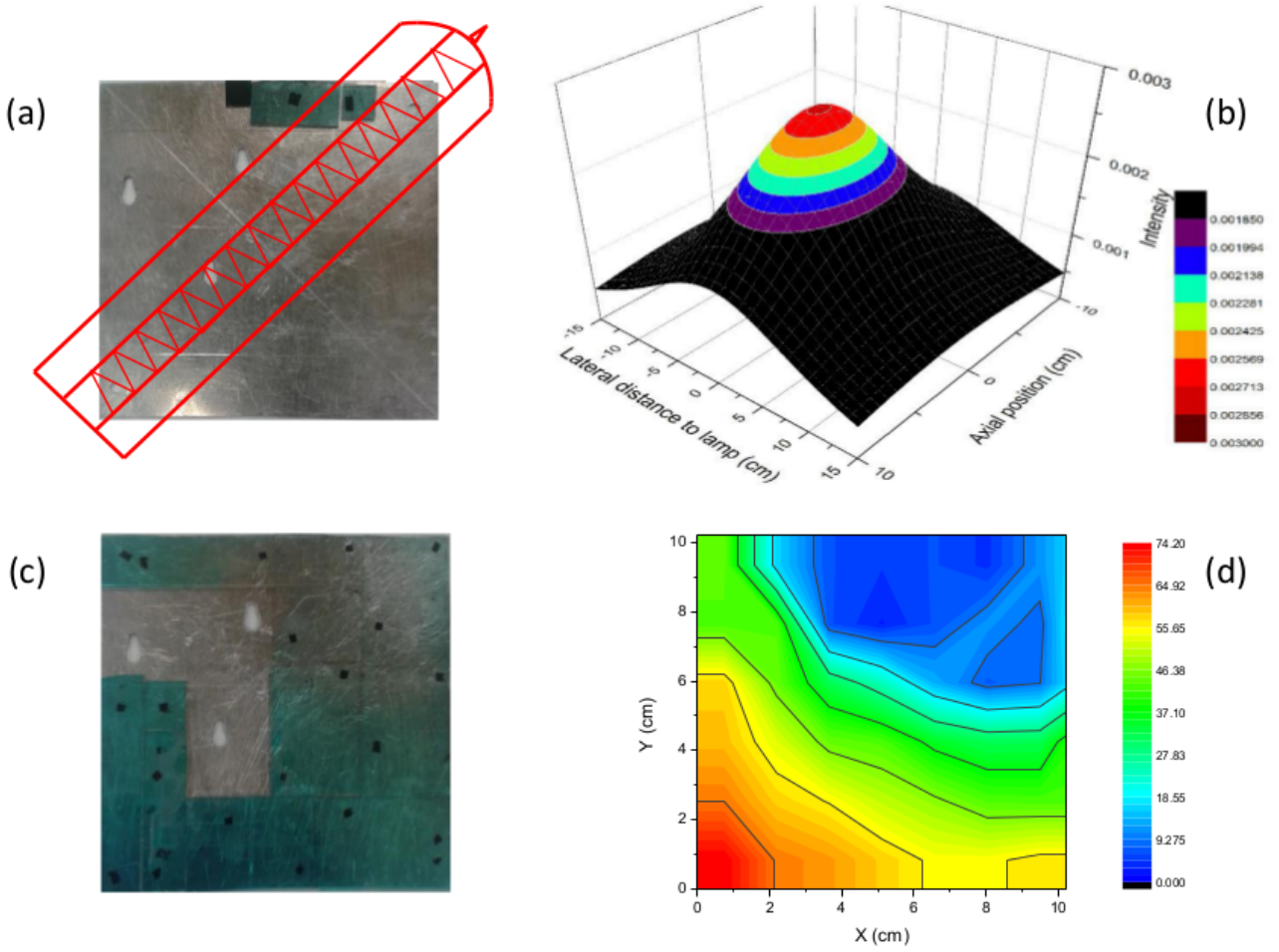

Figure 2.3: (a) Schematic of excimer lamp showing its position in relation to the sample plate with samples placed on one edge, (b) model of expected UV flux, (c) film samples of 100 nm ZnPc placed across the sample plate and irradiated for 90 minutes and (d) thickness of ZnPc remaining as a function of position on the sample plate. The films for (c) and (d) were deposited and irradiated and data taken by Lucille Chambon

2.4 Atomic Force Microscopy (AFM)

Atomic force microscopy is one of a range of scanning probe techniques and can provide 3-dimensional topographical information on a range of samples, regardless of substrate. The principle involves drawing a sharp tip attached to a cantilever of known force constant across the sample surface to create a map based on the tip-sample interaction. The two modes of operation are contact and tapping mode.

Proximity of the tip to the surface results in deflection of the cantilever due to repulsive forces

which decrease with distance. A laser reflected from the back of the cantilever is directed to a quadrant photodiode and any deflections are detected by changes in the intensity and direction of the reflected laser beam (figure 2.4). In the case of contact mode, the tip is held continually against the surface of the sample. Deflections detected are passed through an electronic feedback loop to a piezoelectric tube on which either the sample or cantilever is mounted and the height of the tube adjusted to maintain a constant deflection or constant force, ensuring the tip remains in contact with the surface.

While appropriate for samples resistant to damage, phthalocyanine films are somewhat softer and use of tapping mode is necessary. In this case, the tip is oscillated close to its resonant frequency so that it only touches the surface periodically, dramatically reducing lateral forces that would otherwise affect the film. The sample-tip interactions affect the frequency and amplitude of the oscillations, allowing modulation of either via the feedback process. The difference between the driving and resultant amplitudes is the phase and mapping of this gives information regarding variations in chemical composition of the surface.

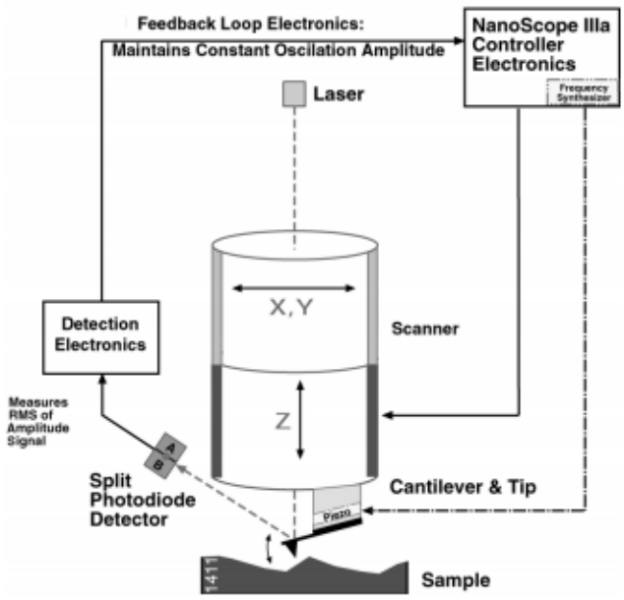

Figure 2.4: Schematic showing operation of AFM with the feedback electronics, reproduced from [17]

The microscope used here was a Veeco Dimension 3100 with NSC15/AIBS tips from Mikro-Masch with a force constant of 46 N/m, a frequency of 325 kHz and a radius of 8 nm.

2.5 X-Ray Diffractometry (XRD)

X-ray diffraction is a non-destructive technique giving information about the crystallographic order within a solid by analysis of x-rays scattered elastically by atomic electron clouds. A crystal contains atoms or groups of atoms (the basis or motif) arranged at each point in a regular three dimensional arrays (the lattice) such that each point in a lattice has the same surroundings as every other point in the array. The unit cell is the smallest building block of atoms which may be repeated translationally to produce the entire crystal leaving no holes. There are seven distinct unit cells associated with right-handed crystal axes systems defined by vectors $\vec{a}$, $\vec{b}$ and $\vec{c}$ with angles α, β and γ between the axes. Figure 2.5a shows a cubic unit cell with axis vectors and cell angles indicated. Variation of cell lengths and angles yields the seven crystal system and combination with lattice arrangements gives a total of 14 Bravais lattices.

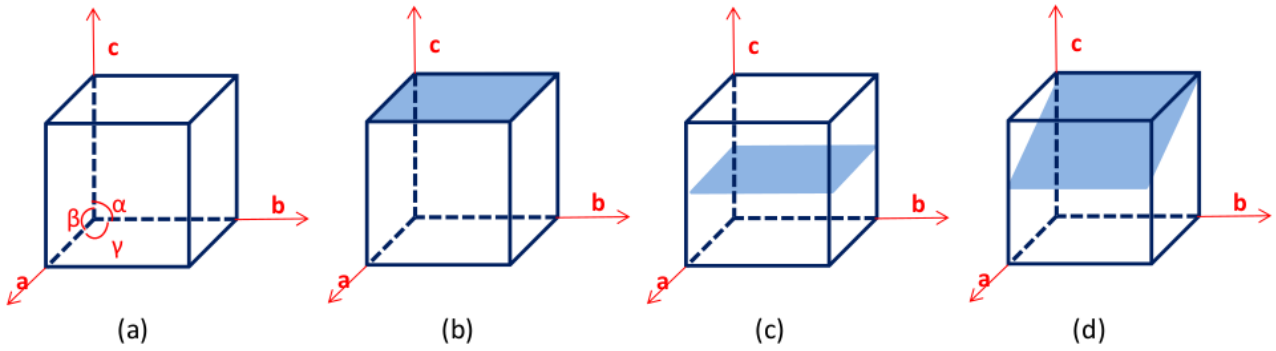

Figure 2.5: (a) A cubic cell with axis vectors and cell angles indicated, (b) the (001) plane, (c) the (002) plane and (d) the (102) plane

Directions and planes of atoms within these lattices may be described by Miller indices, written as $(h\,k\,l)$ and three planes are shown in figures 2.5b - d. It is planes such as these which are detected using XRD as repeated planes within a crystal will diffract x-rays at certain angles according to Bragg's law (equation 2.2) where n is the order of diffraction, λ the wavelength of x-ray used, d the distance between successive lattice planes and θ the angle of approaching radiation as shown in figure 2.6. Diffraction peaks are observed when the path difference, $2r = 2d\sin\theta$ and the planes separated by distance d are horizontally aligned, allowing determination of the orientation of crystallites. The technique, however, does require a minimum crystallite size of approximately 20 nm to produce diffraction peaks.

$$n\lambda = 2d\sin(\theta) \tag{2.2}$$

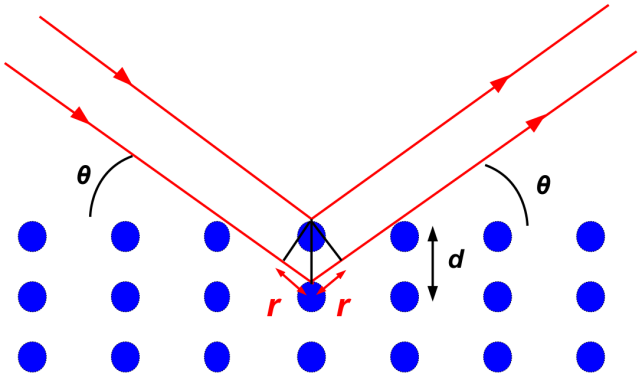

Figure 2.6: Schematic showing diffraction of x-ray at angle θ by a crystal

XRD data were collected using an XPert PRO PANalytical x-ray diffractometer with a Cu k_α x-ray source and diffraction patterns were taken between 5 66°, with a step size of 0.033 and a time per step of 40s.

2.6 UV-Visible Absorption Spectroscopy

Electronic absorption spectroscopy makes use of light to excite electrons in molecular electronic energy levels from the ground state to higher anti-bonding orbitals. Typically, a spectrometer has at least two lamps to provide light covering a range of wavelengths, for example, a deuterium lamp as the UV light source and a tungsten or tungsten/halogen lamp for light in the visible range. The light is passed through a monochromator to create a beam of light with a narrow bandwidth before being split into two separate beams. One passes through the sample to be measured and the other through a reference sample before reaching separate photodetectors. The light transmitted by the sample, I, and the intensity of the reference beam, I_o, are related to the absorbance, A, by equation 2.3, giving the percentage of light transmitted, the transmittance T in equation 2.4.

$$A = \log_{10}\left(\frac{I_0}{I}\right) \tag{2.3}$$

$$T = 100 \times \left(\frac{I}{I_0}\right) \tag{2.4}$$

The intensity of light absorbed is related to the amount of absorbing material present in the sample and is governed by the Beer-Lambert law (equation 2.5) relating the light absorbed at a given wavelength to the concentration, c, of the absorbing species, the optical path length, b and the molar extinction coefficient, ϵ, which depends on the wavelength. For thin films, equation 2.5 is modified to relate the absorbance to the absorption coefficient, α, and the thickness of the film, y (equation 2.6), giving the relation between light transmitted and film thickness as in equation 2.7

$$A = \epsilon bc \tag{2.5}$$

$$A = \alpha y \tag{2.6}$$

$$\frac{I_\lambda}{I_{0,\lambda}} = e^{-\alpha y} \tag{2.7}$$

The majority of absorption spectra were recorded using a Perkin Elmer Lambda 25 UV/VIS spectrometer. Reflectance measurements were recorded using an integrating sphere attached to a Varian Cary 5000 spectrometer. The sample and reference beams are carefully aligned before they enter the integrating sphere (figure 2.7). The inside of the sphere is coated with highly diffusive PTFE causing any light which enters the sphere to be redistributed so the sphere is uniformly lit. To measure reflectance, the sample is placed in the sample reflectance port (indicated in figure 2.7) and a reflectance standard coated with PTFE placed on the reference port. The detector will then be able to determine the difference between light reflected when the sample is present and when it is replaced by a second reference standard, measuring the total reflectance, a sum of diffuse and specular reflectance. To measure diffuse reflectance only,

a light trap is placed in the position where light would be specularly reflected from the sample (the specular exclusion port in the figure).

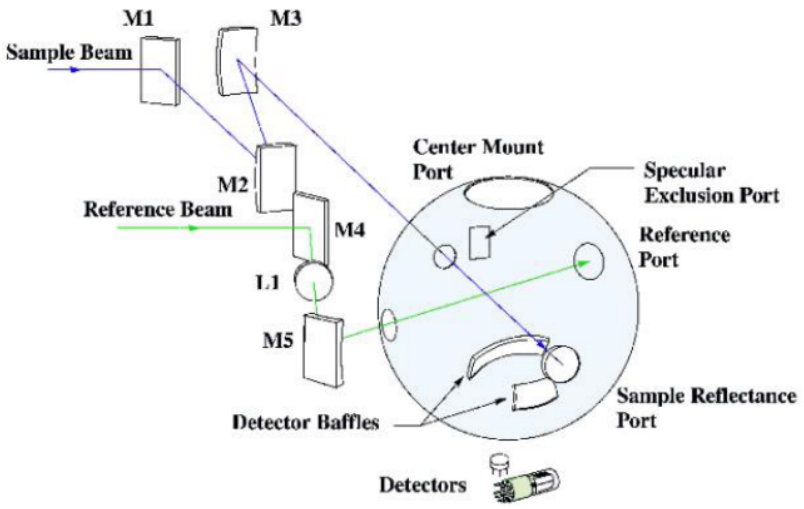

Figure 2.7: Schematic of the integrating sphere showing alignment of sample and reference beams and positions of the sample and detector. Reproduced from [18]

2.7 X-Ray Photoelectron Spectroscopy (XPS)

X-ray photoelectron spectroscopy uses x-ray photons to excite the electronic states of atoms near the surface of a sample placed in a vacuum of $\leqslant 10^{-8}$ mbar, resulting in the ejection of core electrons by the photoelectric effect. These electrons are separated according to kinetic energy by a hemispherical analyser and the intensity at each energy measured, giving information about the elemental composition and chemical state of elements in the sample. Although x-rays may penetrate deeply within a sample, XPS is a surface analysis technique sampling the outermost 10 nm of the surface due to limitations of the escape depth of ejected electrons. Any deeper than 10 nm and electrons are highly likely to suffer energy loss undergoing collisions before escaping from the surface. These electrons are detected but contribute to a background spectrum, having no well-defined energies.

Although photoelectric emission should result in well-defined peaks in a spectrum, for non-conducting samples, loss of electrons results in charging which will shift all peaks. This may be redressed by charge compensation. XPS

If a photon of energy $h\nu$ is absorbed by a core level electron which is subsequently emitted, the energy required for the electron to escape to the continuum, the binding energy E_B, depends on the atom and energy level it was ejected from and any neighbouring electronic influences such as bonds with other atoms. Furthermore, the electron must overcome the spectrometer work function, ϕ to escape. The relationship between the binding energy and the energy of the photon are related by the kinetic energy, E_K in equation 2.8.

$$E_B = h\nu - E_K - \phi \tag{2.8}$$

The binding energy, E_B, may be the difference between the energy states for an initial n-electron and final $n-1$-electron with no rearrangement of any other electrons (equation 2.9), in which case the binding energy is approximately equal to the negative of the orbital energy, ϵ_k (equation 2.10), according to Koopman's theorem.

$$E_B = E_f(n-1) - E_i(n) \tag{2.9}$$

$$E_B \approx -\epsilon_k \tag{2.10}$$

$$E_B = -\epsilon_k - E_r(k) \tag{2.11}$$

The difference between binding and orbital energy is due to a rearrangement of electrons to shield the hole created by electron emission and further relaxation of electrons in neighbouring atoms, known as the relaxation energy, $E_r(k)$ (equation 2.11). There are further corrections due to relativistic effects which may usually be neglected.

In addition to the peak corresponding to photoelectron emission, shifts in peak position may occur due to initial and final state effects producing shake-up and shake-off peaks. Shake up satellite peaks occur when a photoelectron loses energy to another electron within the same atom, promoting the second electron from a valence to a higher energy level. In aromatic-containing molecules, this corresponds to promoting an electron with a π to π^* transition

and has a discrete, well-defined energy. Therefore, carbon shake-up satellite peaks are always found at energy levels a few eV higher than that for the carbon 1s peak. Since the departing photoelectron lost energy when promoting an electron from π to π^*, it has an even lower kinetic energy than that of carbon 1s electrons, thus appearing as though it must have a higher binding energy than carbon 1s electrons. These are also known as l̈oss peaks änd are frequently seen in systems with aromatic structures, unsaturated bonds or transition metal ions.

In contrast to shake-up satellite peaks, a shake-off peak is the result of a photoelectron providing enough energy to a valence electron to actually ionise it. This peak can then have a range of energies as energy has been donated to the valence electron and the remaining kinetic energy is not discrete. The photoelectron will therefore have an lower kinetic energy on emission and thus be assigned a higher binding energy. This results in a broad feature which may not be easily distinguished from the background signal.

Another final state effect relevant here is splitting of peaks arising as a result of emission from p, d and f orbitals, known as spin-orbit splitting. After emission of an electron from one of these orbitals, two peaks will be detected with area ratios corresponding to the degeneracy of each spin state i.e. the number of different combinations of spin which will yield the total angular momentum, j. For example, if an electron is emitted from the $2p$ orbital, the principal quantum number $n = 2$ and the angular momentum quantum number $l = 1$. The spin angular momentum number $s \pm 1/2$, therefore the orbital angular momentum, $j = l + s$, may be $1/2$ or $3/2$. Thus there will be two peaks for the $2p$ binding energies with areas in a ratio of 1:2 for the $2p_{1/2}$ and $2p_{3/2}$ levels.

XPS spectra for this work were taken using an Escalab 220i-XL instrument at a base pressure $\leqslant 10^{-8}$ mbar with an Al k_α source producing x-rays of 1486.6 eV. The spot size was 400 µm

2.8 Secondary Ion Mass Spectrometry (SIMS)

Secondary ion mass spectrometry has the potential to provide highly accurate information regarding the elemental and molecular composition of a sample, both at the surface and within

depth by examination of fragments produced upon ion bombardment of the material. However, destruction of the sample is a drawback.

Samples are placed in an ultra-high vacuum ($\approx 10^{-10}$ mbar) and bombarded by a primary ion beam of ions with energies between 250 eV - 25 keV, such as O_2^+, Cs^+, Ar^+or cluster ions, for example, C_{60}^+. Sputtering of the surface results in the release of fragments. Approximately 1% of these are ionised, forming the secondary ion beam and the remainder are neutral. The ions are accelerated towards a mass spectrometer such as a time-of-flight mass spectrometer which allows simultaneous measurement of ion yields across the whole mass spectrum. The vast majority, 95%, of sputtered particles originate from the uppermost two layers of the sample but penetration of ions below this is increased as the angle the primary beam approaches at nears the normal to the sample. Ions penetrating further result in a collision cascade (figure 2.8) with the result that some atoms are embedded more deeply below the surface and some from deeper layers are sputtered, mixing layers and resulting in altered ion yields. Furthermore, the electronic state and bonding of atoms within a sample has a significant effect on the rate at which ions are sputtered.

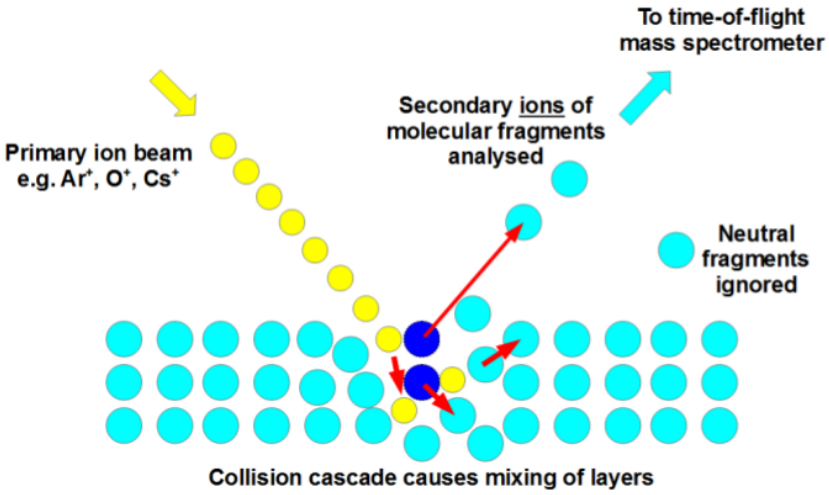

Figure 2.8: Schematic of the collision cascade inducing mixing of layers

SIMS may operate in two different modes, static and dynamic. The former requires that the probability of any site in the sample receiving a second ion impact to be less than one and will therefore give an accurate chemical map of the surface. Dynamic SIMS, however, allows

repeated impingement of ions and offers the potential for depth profiling. A sputter beam rasters across a sampling area to remove material, creating a crater, pausing to allow a pulsed analysis beam to generate ions. The most highly focused analysis beam is provided by liquid metal ion guns (LMIG), avoiding ion generation from the sloping crater walls which would severely affect the accuracy of results. Release of ionised fragments may result in charging of non-conductive samples, but this may be corrected by charge compensation using an electron flood gun, as for XPS.

Primary ion beams may be chosen to enhance ion yields. Oxygen, for example, interacts with metals in particular, producing the oxide from which the yield of the metal ion is artificially increased in comparison to from the metal. The yield of manganese ions increases from 0.0013 from the metal to 0.4 from the oxide [109]. An oxygen primary beam will enhance the yield of all positive ions to some extent. Similarly, Caesium may be used to increase the yield of negative ions.

An Ion TOF SIMS V was used with a sputter area of 300 x 300 µm and analysis area of 100 x 100 µm. An oxygen primary beam with energy 500 eV was used with a Bi_3^+ analysis beam. Data collection was at three shots per pixel.

2.9 Scanning Electron Microscopy (SEM)

A scanning electron microscope forms images from the interaction of the sample with an electron beam, producing secondary and backscattered electrons and x-rays. Electrons are produced thermionically under a high vacuum from a tungsten or lanthanum hexaboride cathode and accelerated by an anode, acquiring an energy of 10 - 40 keV. Focusing of the electron beam is achieved using electromagnetic condenser lenses and deflector plates or scan coils raster the beam over the sample area.

Secondary ions are produced from the surface by removal of valence electrons from sample atoms by the electron beam. Their energy is relatively low and they provide useful topographical data. Backscattered electrons, however, may originate from deeper within a sample and are the result

of direct inelastic collisions between the electrons and atoms in the sample and are directed backwards towards the beam source. As backscattering will depend on the mass of atoms within the sample, data from backscattered electrons gives higher mass contrast. Finally, Auger electrons may also be emitted when a core electron is expelled from an atom by an incoming electron. An electron from the outer shell drops down to fill the vacancy created by the departing core electron and transfers excess energy to yet another electron. If this electron is emitted from the atom, it is detected as an Auger electron, with an energy characteristic of the material. If an outer shell electron fills a vacancy and instead emits its excess energy as a photon, an x-ray will be detected. Many SEMs are equipped to give chemical and elemental data based on the characteristic energies produced.

A JEOL JSM-6010LA SEM was used to image films formed using nanosphere lithography with an accelerating voltage of 10 - 20 keV. Samples were coated with gold to avoid charging.

Chapter 3

Determining the Mechanism of Oxide Formation from Molecular Precursors

3.1 Introduction

Cobalt, copper and manganese phthalocyanine have been shown to form metal oxides when exposed to ultraviolet light (UV) in the presence of oxygen [80, 81]. As thin films in organic electronics, metal oxides have a wide range of uses. Zinc oxide (ZnO) is particularly useful as its resistivity of less than $10^{-3}\,\Omega$ cm [110] and large bandgap of over 3 eV makes it an attractive choice for applications in the visible and near UV region. ZnO as a transparent conducting oxide (TCO) has been successfully employed when doped with aluminium for OLEDs [111]; as the electron absorber in hybrid photovoltaic devices [112]; as a cathode interlayer in polymer solar cells, enhancing surface conductivity and electron mobility [113] and as the active channel in thin film transistors for display purposes [114]. In addition to zinc oxide, other metal oxides may also be produced from phthalocyanines by treatment with UV light with a potential for similar uses.

However, there are two possible reaction mechanisms contributing to the removal of precursor material and formation of metal oxide: photon assisted and oxygen assisted reactions. The first relies solely on the ability of incident photons to cleave molecular bonds and is therefore

only likely to happen if the energy of the incoming photon exceeds the energy of any of the bonds within the precursor molecule. The latter is a consequence of UV absorption by oxygen to form excited species which may not only attack phthalocyanine molecules at the surface of the film but also diffuse between grain boundaries to initiate a reaction below the surface. Determination of the relative importance of these two mechanisms is crucial in allowing us to optimise the process.

In the case of zinc phthalocyanine (ZnPc), the strongest bonds are the C-N, C=C and N-Zn bonds with energies in the regions of 6.7, 6.3 and 5.66 eV respectively [89, 115]. Bond energies are similar for zinc tetrapenylporphyrin (ZnTPP), with a slightly greater N-Zn energy of 6.32 eV [116]. All of these may conceivably be cleaved by photons of 7.2 eV, such as those produced by our source, a xenon excimer lamp emitting at 172 nm with a full width at half maximum (FWHM) of 14 nm [8].

UV irradiation in our 35 litre chamber is carried out at a distance of 8.5 cm from the lamp which has an output of 50 mW/cm^2, resulting in a radiation flux of 9.5 mW/cm^2 at the surface of the sample, approximating the flux to be cylindrically symmetrical and radially emitted from the axis of the lamp. The UV process is carried out at 3.0 mbar, with partial pressures of nitrogen and oxygen at 1.8 mbar and 1.2 mbar respectively. Both these gases may potentially absorb in the UV region. From this information and the universal gas law, we can determine the proportion of radiation absorbed by oxygen and nitrogen and calculate the fraction, $I_\lambda/I_{0,\lambda}$, which will reach the sample, using the Beer-Lambert Law (equation 2.7), where

$$\frac{I_\lambda}{I_{0,\lambda}} = e^{-\sigma_\lambda N l} \tag{3.1}$$

and:

σ_λ = Absorption cross section for $O_2 = 0.6 \times 10^{-18}\text{cm}^2$ [117]

or

σ_λ = Absorption cross section for $N_2 = \ll 0.6 \times 10^{-18}\text{cm}^2$ [117]

l = Distance between lamp and sample = 8.5 cm

N = Particle concentration

At wavelengths below 100 nm, molecular nitrogen is considered to have a much smaller absorption cross section than molecular oxygen, a view corroborated by the very small concentration of atomic nitrogen in the atmosphere compared to the concentration of atomic oxygen [117]. For our calculations, absorption cross sections for nitrogen were considered at values of 1% and 10% of that for oxygen. The results show that approximately 14% of the light produced by the lamp is absorbed by oxygen through a distance of 8.5 cm at an oxygen partial pressure of 1.2 mbar (figure 3.1). In the case of nitrogen, the impact is much lower with 2.2% of light being absorbed when $\sigma = 0.06 \times 10^{-18}$ cm^2. For $\sigma = 0.006 \times 10^{-18}$ cm^2, absorption by nitrogen is negligible at 0.2%.

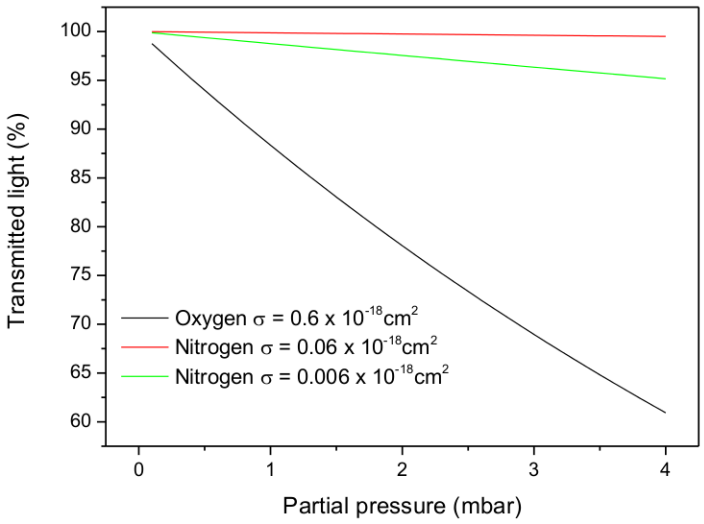

Figure 3.1: Attenuation of light through a distance of 8.5 cm from the xenon excimer lamp by oxygen and nitrogen

Therefore, photonic dissociation of bonds is indeed a plausible route to oxide formation and its impact will be greatest at the very surface of the precursor film where the light is incident. It is reasonable to assume that photon-assisted film removal would occur on a layer-by-layer basis. Absorption of 14% of the ultraviolet radiation by oxygen molecules suggests that excited oxygen species may also play a significant rôle.

When exposed to UV light at 172 nm, oxygen dissociates to form a ground state triplet atom $O(^3P)$ and an excited singlet atom $O(^1D)$ (equation 3.2a), the latter of which is highly reactive, oxidising nearby surfaces. An oxygen atom may also react with two further oxygen molecules to form vibrationally excited ozone, O_3*, via a three-body reaction (equation 3.2b) [118].

$$h\nu + O_2 \longrightarrow O(^1D) + O(^3P) \tag{3.2a}$$

$$O + O_2 + O_2 \longrightarrow O_3{}^* + O_2 \tag{3.2b}$$

Any of these excited species may interact with the precursor, propagating free radicals throughout the organic molecules, breaking bonds and facilitating the formation of carbon, nitrogen and zinc oxides. Crucially, these excited species will react with the phthalocyanine, not only at the surface, but also, by diffusing between crystallites at grain boundaries, to material below the surface. Since the proposed oxygen-assisted mechanism takes place at multiple sites including below the top of the film, it is unlikely to result in film removal increasing linearly with UV irradiation time.

Comparison of a precursor film irradiated with and without oxygen will demonstrate the necessity of oxygen in film degradation but not the mechanism by which oxide forms. In order to determine the relative importance of the two possible mechanisms, we can compare the rate at which two similar precursor films degrade, where one precursor forms a crystalline film and is therefore subject to both photon and oxygen assisted film removal and the other an amorphous

film, excluding the possibility of diffusion of excited oxygen species between grains.

Previous work has focused on phthalocyanines [119] and zinc phthalocyanine develops the process further for fabrication of zinc oxide films, whose crucial rôle, not only as a replacement for ITO, was described in chapter 1.1. Therefore, in addition to zinc phthalocyanine as a precursor, a similar molecule, zinc tetraphenylporphyrin (ZnTPP) which forms amorphous films due to the inclination of its phenyl rings, was also used (figure 3.2).

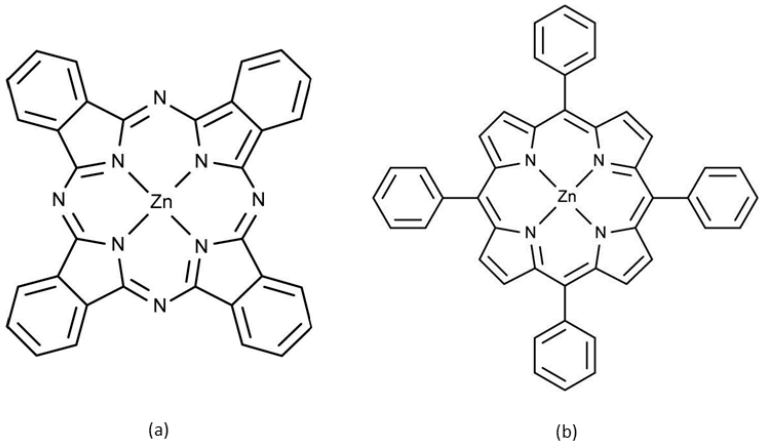

Figure 3.2: Precursors: (a) Zinc phthalocyanine and (b) zinc tetraphenylporphyrin

Having determined the absorption of UV light by oxygen and nitrogen, it now remains to establish the depth to which the radiation will penetrate precursor films as this will affect the mechanisms by which the film degrades and zinc oxide is formed. Referring again to the Beer-Lambert Law (equation 2.7), the penetration of radiation through solid films may be expressed in terms of the absorption coefficient, α, assuming the films are non-reflecting, where

$$I(y) = I_0 e^{-\alpha y} \tag{3.3}$$

and:

$$I(y) = \text{Intensity of light reaching depth } y \text{ in film}$$

$$I_0 = \text{Total light incident at surface of film}$$

$$y = \text{Depth inside film}$$

Light is produced by the excimer lamp at 172 nm (7.2 eV) which is beyond the range of much recent optical data for ZnPc [12, 96, 120], however, an approximate value from the literature is $\alpha \approx 3.6 \times 10^5$ cm^{-1} [121]. ZnTPP has no reported absorption data below 300 nm [122], therefore it is not possible to calculate the penetration of UV light within a thin film for ZnTPP. The depth of ZnPc through which 172 nm radiation penetrates is shown in figure 3.3 and suggests that photon assisted degradation of the ZnPc molecule may also be possible below, not only at, the surface. However, zinc oxide will only form if oxygen has diffused through to the body of the film and this may only happen preferentially at crystal boundaries in the first instance.

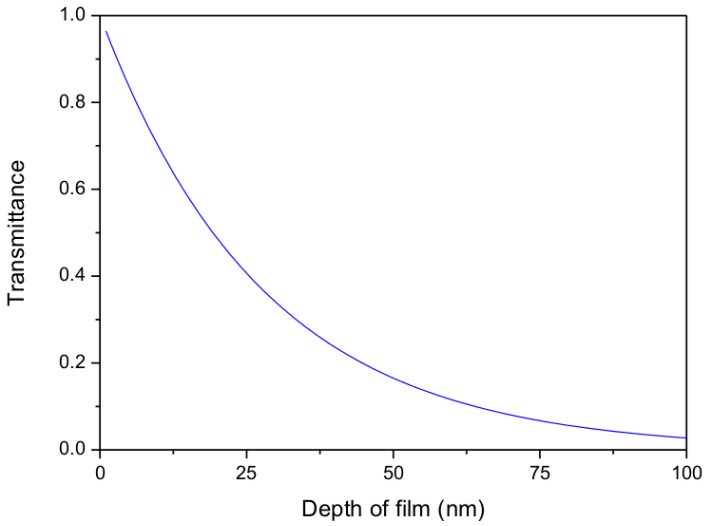

Figure 3.3: Penetration of light at 172 nm through ZnPc film

Consideration of the absorption spectra for ZnPc [96, 97] and ZnTPP [122] suggests that both films are likely to be absorbing in the VUV region. ZnPc exhibits a peak within the C band at 5.85 eV (212 nm) [97] in addition to a strong absorption between 6.8 (183 nm) and 8.0 eV (155 nm) and although there is little data at wavelengths below 300 nm for films of ZnTPP, vapour

phase absorption spectra record absorption at 200 nm at a level considerably lower than for the Q band or Soret peaks [14]. This implies that the penetration depth of UV light through ZnTPP would be higher than that for ZnPc and that the predominant route for reaction would be oxygen, rather than photon assisted.

As previously described in Section 1.4.1, when grown by OMBD at room temperature, ZnPc forms films in the α phase with a structure isomorphic to that of CuPc [92]. The unit cells occupy a volume of 582.3 $Å^3$ with one ZnPc molecule per unit cell if considering the structure reported by Hoshino *et al* [3] or 2349.8 $Å^3$ with four ZnPc molecules per unit cell for the structure reported by Ashida *et al* [2], the latter giving a volume of 587.5 $Å^3$ per ZnPc molecule. Both structures result in 1.7×10^{17} ZnPc molecules per cm^2 of 100 nm thick film. Assuming full conversion of ZnPc molecules to zinc oxide with complete removal of organic fragments, it is possible to estimate the expected yield of zinc oxide. Zinc oxide crystallises in a hexagonal structure with two atoms of zinc occupying each unit cell of volume 47.6 $Å^3$ [123]. Therefore, assuming the zinc oxide formed by the UV process crystallises in this structure, a 100 nm film of ZnPc would yield a zinc oxide film of thickness $\approx$ 4 nm. ZnTPP unit cells occupy a volume of 798.1 $Å^3$ with 1 ZnTPP molecule per unit cell [4], resulting in a maximum thickness of 3.0 nm. Electrodes utilising doped zinc oxide as a transparent conducting oxide require a thickness of approximately 300 - 800 nm [110, 124] but careful choice of precursor would allow an increased yield via the UV method. Furthermore, the oxide produced offers potential uses based on the change in optical properties effected (chapter 5). Unless otherwise stated, all molecular films were grown to 100 nm thickness.

3.2 Results: As-Deposited Films

3.2.1 Morphology - Atomic Force Microscopy

AFM images taken of ZnPc and ZnTPP films deposited on silicon clearly define the differing morphology. ZnPc forms crystallites approximately 40-50 nm in diameter with peak to trough

distances up to 17 nm giving an RMS roughness (R_q) of 4.6 nm (figure 3.4) whereas ZnTPP forms an amorphous film with a very low roughness of 0.41 nm and peak to trough distances never rising above 2 nm (figure 3.5). This contrasting morphology is expected to determine the relative importance of the photon assisted and oxygen assisted routes as a smooth film such as ZnTPP will not be subject to oxygen diffusion within the film, at least initially.

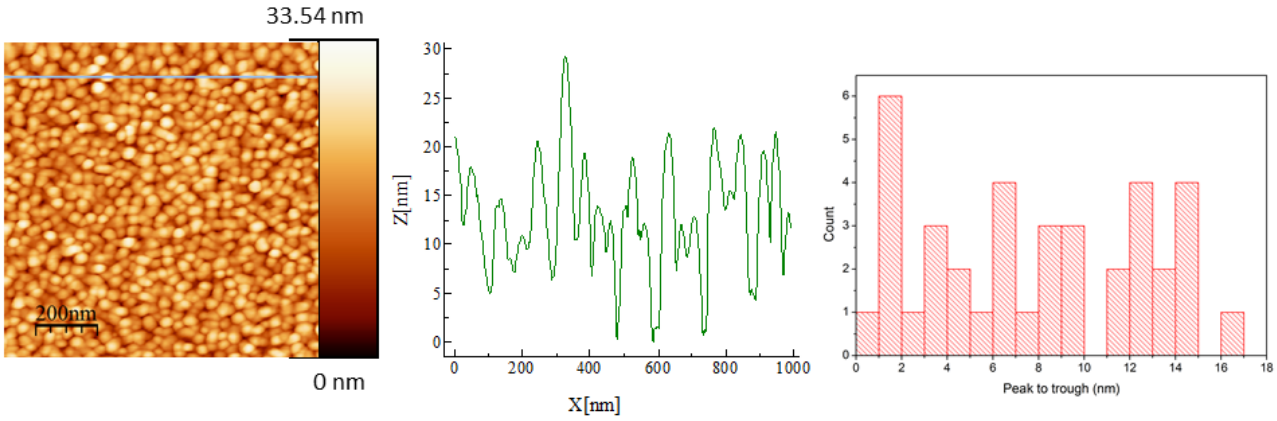

Figure 3.4: AFM image, line profile and peak to trough distances of 100 nm ZnPc, as-deposited, on silicon, RMS roughness of 4.6 nm

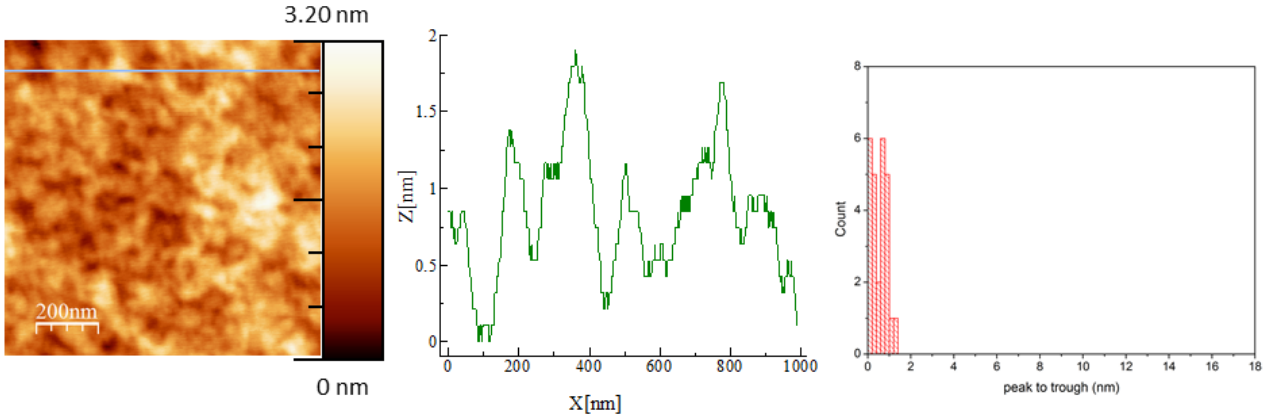

Figure 3.5: AFM image, line profile and peak to trough distances of 100 nm ZnTPP, as-deposited, on silicon, RMS roughness of 0.41 nm

3.2.2 X-Ray Diffraction

X-ray diffractograms of the as-deposited films were recorded and compared with published data. The XRD results for ZnPc show the film is crystalline with a broadened peak at $2\theta = 7.08°$ (figure 3.6a). The powder diffraction patterns of α-CuPc structures are commonly used

for planar metal phthalocyanines deposited at room temperature on non-interacting substrates. As ZnPc and CuPc are considered isomorphic, the structural data is a good approximation for ZnPc and are also shown in figure 3.6a [2], [3], [91].

Looking more closely at the 5 - 10° region (figure 3.6b), the peak seen in as-deposited ZnPc does not appear in either of the powder diffraction patterns determined by Hoshino [3] or Ashida [2]. The breadth of the peak suggests that diffraction may be taking place from both the (100) and (001) or (200) and (002) planes, therefore it is uncertain which molecular arrangement the molecules have taken.

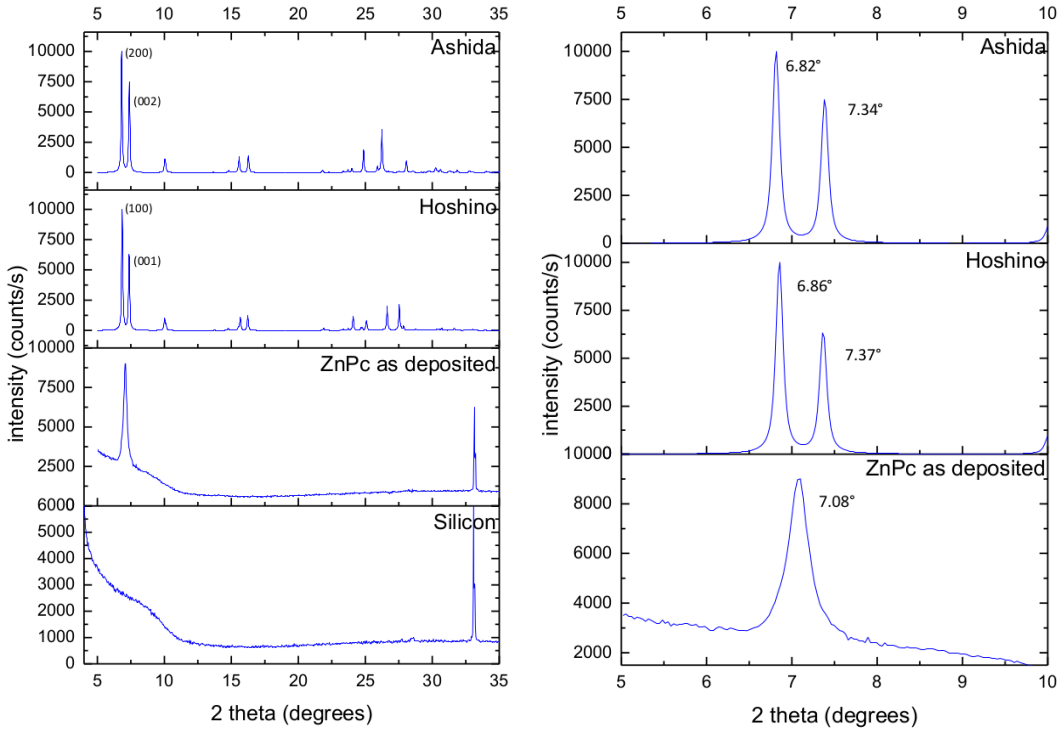

Figure 3.6: XRD scans of (a) 100 nm ZnPc as-deposited on silicon, the substrate and powder diffraction patterns for α CuPc from crystallographic data by Ashida [2] and Hoshino [3], (b) from 5 - 10° of 100 nm ZnPc as-deposited on silicon and powder diffraction patterns for α CuPc from crystallographic data by Ashida [2] and Hoshino [3]

The two possible molecular arrangements are shown in figure 3.7 and the diffracting planes parallel to the substrate, indicated by the solid black line. For each of these possible orientations, the phthalocyanine molecules lie approximately perpendicular to the substrate with the planes parallel to the silicon surface. Using Bragg's law, the peak at $2\theta = 7.08°$ gives an interplanar

distance, d, of 1.25 nm, which is close to the two longest cell lengths for both arrangements. Furthermore, the data agrees with ZnPc films deposited by thermal evaporation which have been shown to crystallise at room temperature with the (200) plane parallel to the substrate [125], corresponding to a single peak at 6.8° and $d = 1.3$ nm. There are many other polymorphs for phthalocyanines, including the stable β polymorph which does produce a peak at 7.04° for the (100) plane [126], however, this arrangement is achieved at higher deposition temperatures over 200°C and the films grown here were deposited at room temperature and are therefore unlikely to be comprised of this polymorph [127].

The silicon peaks at approximately 33° in XRD results from the silicon substrate and the as-deposited ZnPc (figure 3.6a) differed by 0.049°. If due to instrumental error, the shift at lower angles would be correspondingly smaller and thus not sufficient to explain the difference between the peak measured at 7.08° and those seen in published data. However, whichever α phase modification the ZnPc molecules have taken (figure 3.7), in neither configuration are they parallel to the substrate which may influence the method by which zinc oxide is formed.

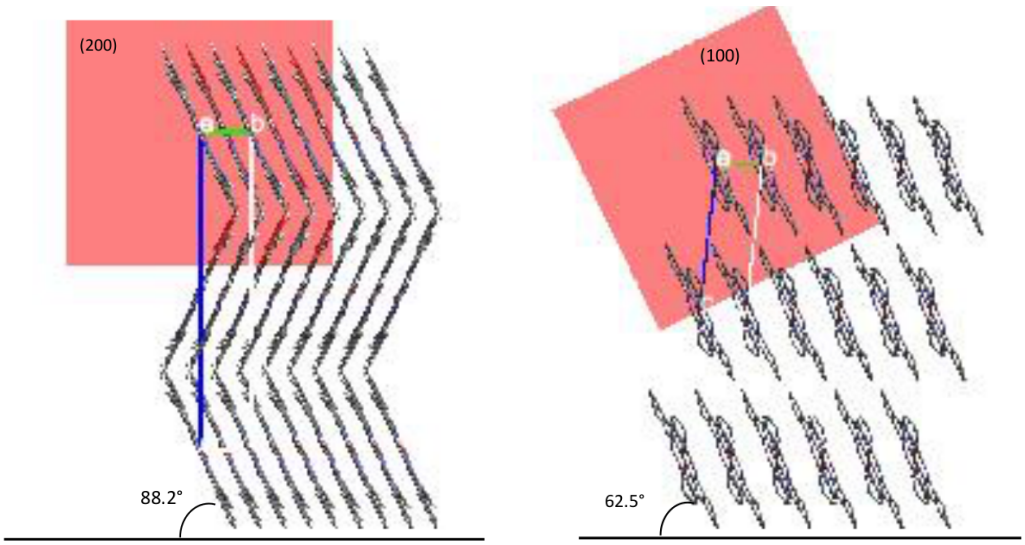

(a) (b)

Figure 3.7: Arrangement of phthalocyanine molecules in (a) the orientation determined by Ashida [2] and (b) the orientation determined by Hoshino [3], observed edge-on, along the diffraction planes (002) and (001) respectively, parallel to the substrate. The other diffracting planes, (200) and (100) are indicated in pink

Zinc tetraphenylporphyrin is known to crystallise in the triclinic system when unsolvated crys-

tals of ZnTPP are first dissolved in chloroform, filtered and benzene layered on the surface and left for 3 days. The triclinic crystals are then deposited on the bottom of the container [4]. The powder diffraction pattern reported from these data is shown in figure 3.8 with XRD data for 100 nm ZnTPP films grown here and the silicon substrate.

Peaks corresponding to diffracting planes, including the (010) and (100) planes are seen in the published powder diffraction pattern but there are no peaks visible in the data from our films. Therefore, the ZnTPP films are amorphous in nature, in agreement with the amorphous appearance seen in the AFM images (figure 3.5).

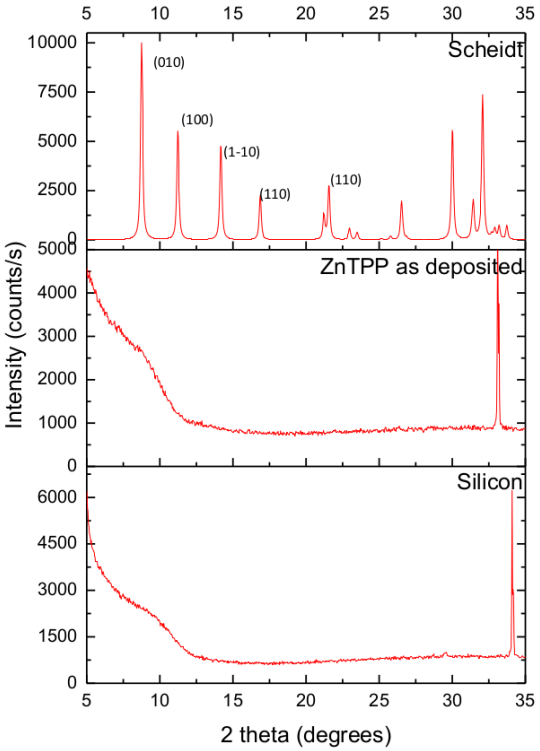

Figure 3.8: XRD scan of 100 nm ZnTPP as-deposited on silicon, the substrate and of the powder diffraction pattern for triclinic ZnTPP from crystallographic data by Scheidt [4]. The silicon peak has been shifted approximately 1° towards zero in the ZnTPP film which may be a result of instrumental error due to sample alignment.

3.2.3 UV-Visible Absorption Spectra

The optical absorption spectrum is useful for understanding the electronic structure and allowed transitions of phthalocyanines and tetraphenylporphyrins. Figure 3.9 shows the UV-visible absorption spectrum of ZnPc deposited on glass (corrected for substrate contribution).

Phthalocyanines exhibit optically allowed transitions in their spectra of which the Q band and the B (*Soret*) band are of the most interest [11]. The Q band and the B or *Soret* band are indicated in the figure with the transitions which result in the absorption seen. As the lowest energy transition, the peak at 706 nm in the Q band is the result of a transition from the highest occupied molecular orbital (HOMO) to the lowest unoccupied molecular orbital (LUMO), i.e. a $\pi - \pi*$ transition, with the higher energy peak at 621 nm due to coupling with vibrational modes within that transition. However, there are alternative interpretations of the Q band transitions which suggest that the peak at 706 nm is instead due to vibrational contributions [13]. Yet others attribute consider it an excitonic peak and the peak at 621 nm as the first $\pi - \pi*$ transition on the phthalocyanine macrocycle [96]. In addition, Yoshida advocates an interpretation based on Davydov splitting due to permitted transitions when considering the relative alignment of the monomer dipole moments in a dimer model for differing orientations of intermolecular interactions as opposed to vibrational components [98].

In our spectra, peak positions of the main Q band and B band at 621 and 332 nm respectively agree well with those documented in literature at 621 nm and 355 nm [96].

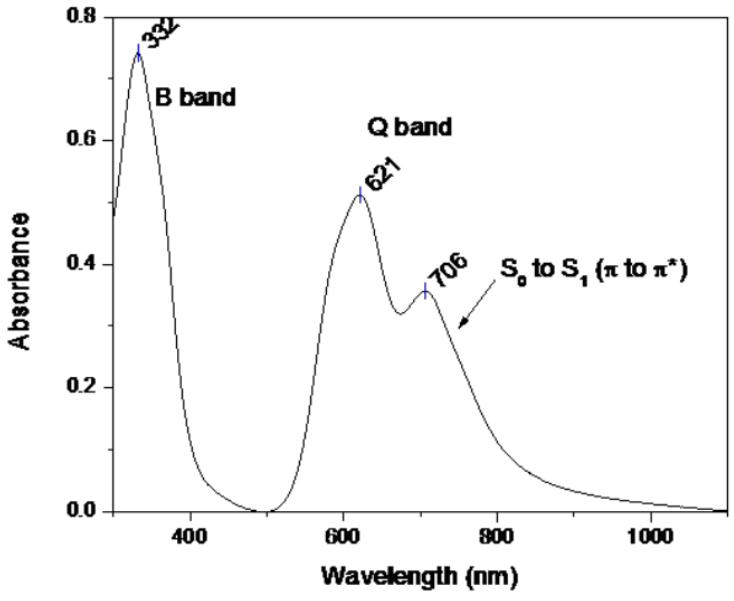

Figure 3.9: UV-visible absorption spectrum of 100 nm ZnPc as-deposited on glass, corrected for substrate

Similarly, the optical absorption spectrum of as-deposited ZnTPP on glass was recorded (fig-

ure 3.10) and corresponds well with values quoted in the literature for the β (Q) band at approximately 552 nm and the Soret (B) band at 432 nm with the S_0 to S_1 transition at approximately 640 nm [14, 122].

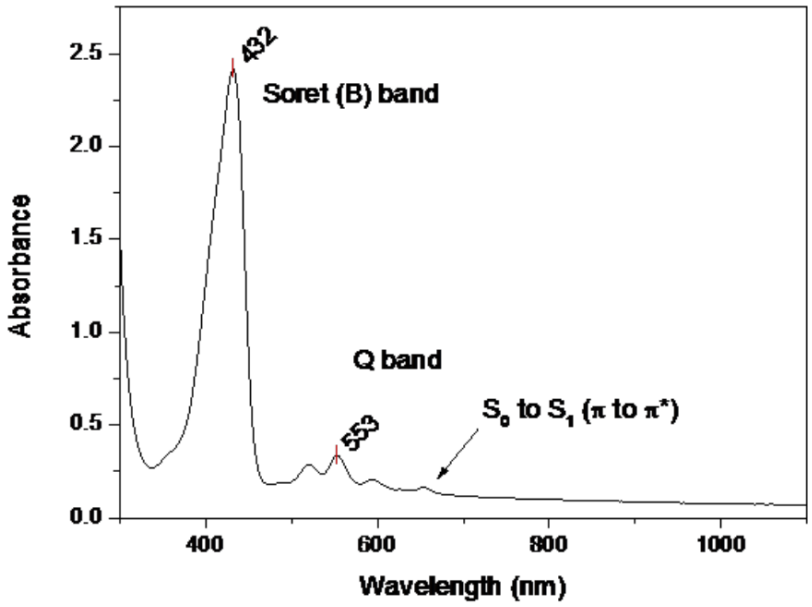

Figure 3.10: UV-visible absorption spectrum of 100 nm ZnTPP as-deposited on glass, corrected for substrate

As the Beer-Lambert law (equation 2.7) may be used to relate absorbance to the thickness of a film in the absence of reflectance, absorption spectroscopy presents a convenient method for measurement of the amount of precursor film remaining after UV treatment. To facilitate this, spectra were recorded from films of different thickness and the area under the Q band integrated to obtain a calibration curve for absorption spectra of both ZnPc and ZnTPP. As the Soret band comprises many transitions and the Q band involves two main electronic transitions, the latter presents a better region for integration.

To calibrate film thickness, any possible variation in integrated areas of equivalent films was determined. Samples were grown on substrates fixed across the whole of the OMBD substrate holder (figure 3.11a) and the variation in the area integrated under the Q bands of these films (figure 3.11b) used as the maximum possible error on the area of any future samples. The value for the error on areas under the Q band thus obtained was 1.7%.

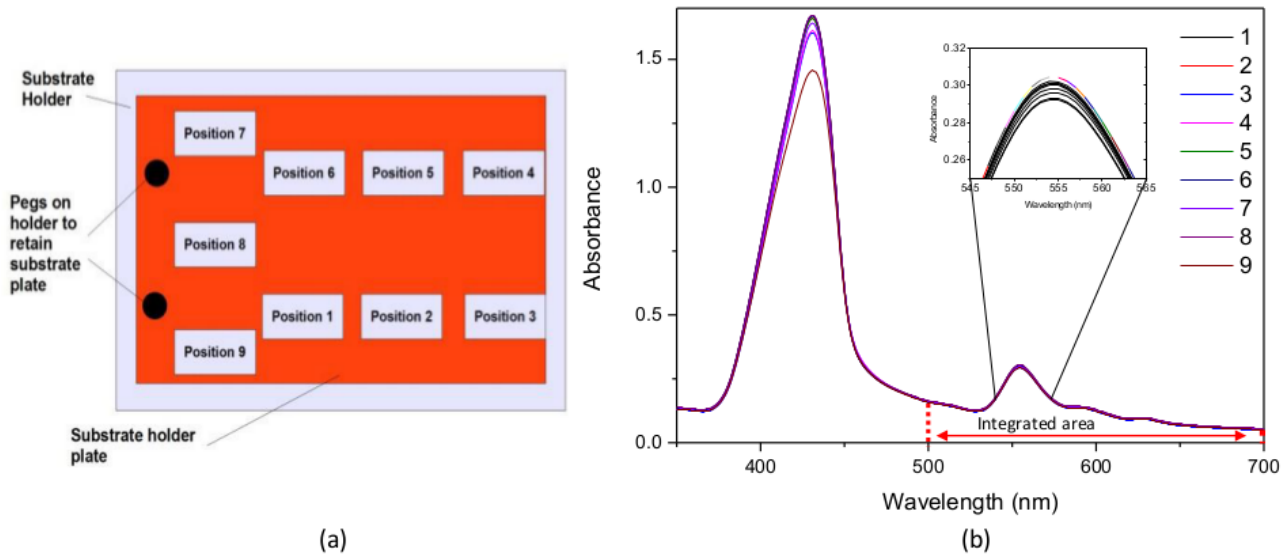

Figure 3.11: (a) Layout of samples on the OMBD substrate plate for thickness error estimation and (b) UV-vis spectra of ZnTPP films deposited at positions 1 - 9 on the OMBD substrate plate with area of integration indicated

Film thickness was determined by measurement of line profiles taken from AFM images of films which had been scratched to expose the substrate. Line profiles of the film shown in figure 3.12 yielded an average thickness of 99 ± 3 nm. This value was then used to modify the OMBD tooling factor ensuring that all subsequent thicknesses given by the quartz crystal monitors were accurate.

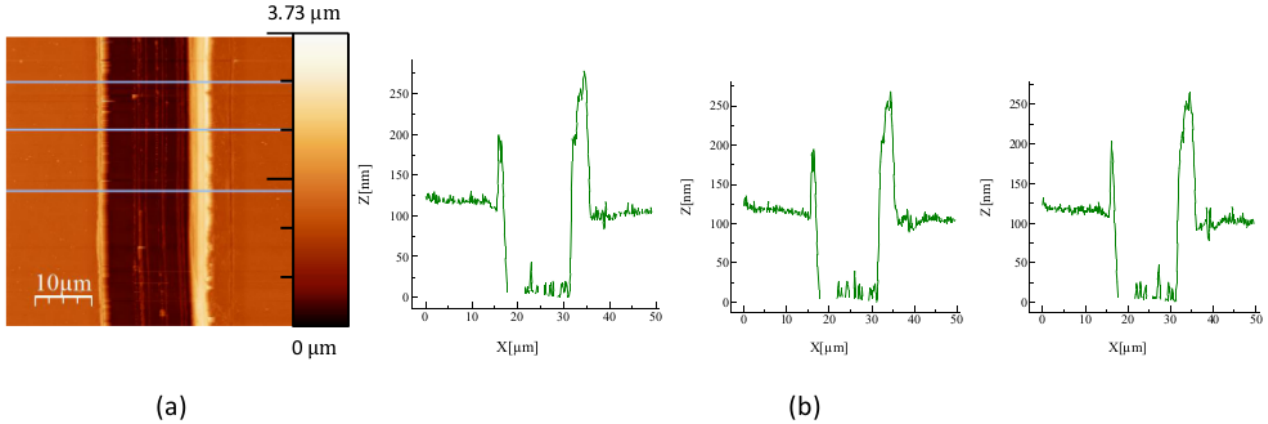

Figure 3.12: Determination of film thickness (a) AFM image of scratch on 100nm ZnPc film, (c) line profiles to determine depth. Peaks seen on either side of the scratch in the line profiles are due to build up of material when the film was marked.

Absorption spectra of 20 nm, 50 nm and 100 nm were taken and the area under the Q band

from 500 to 700 nm was integrated and used to generate a calibration curve, relating film thickness linearly to area (figure 3.13). This relationship was subsequently used to determine the percentage of ZnPc or ZnTPP film remaining on films which had been subjected to the UV process and as the system had been calibrated following thickness measurements, the error in thickness was neglected. For ZnPc, the area between 500 - 900 nm was taken as the Q band.

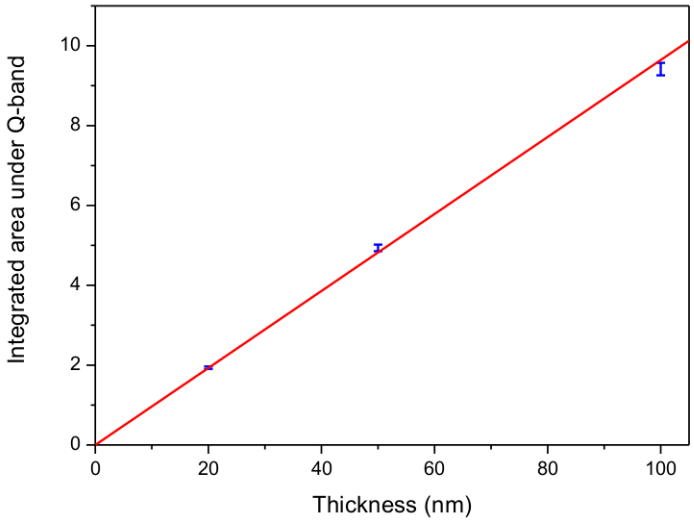

Figure 3.13: Area under the Q band plotted against against film thickness for ZnTPP

Finally, to verify the validity of this approach which considers absorbance only, reflectance spectra were taken of both ZnPc and ZnTPP using an integrating sphere. Absorbance is calculated using the transmittance of a sample (equation 2.3) and this clearly neglects any reflectance, attributing any decrease in the light detected through a sample to its absorption. Reflectance is a sum of two phenomena, diffuse and specular reflectance. The latter is generally considered mirror reflection and the angle of incidence is equal to the angle of reflection. Diffuse reflectance, however, occurs when a surface is rougher and light may be reflected in any direction. When using an integrating sphere, it is possible to measure either of these or both as the total reflectance and it was found that diffuse reflectance was negligible for both ZnPc and ZnTPP due to any imperfections in the surfaces of the films being of smaller order than the wavelength of light used (figure 3.14).

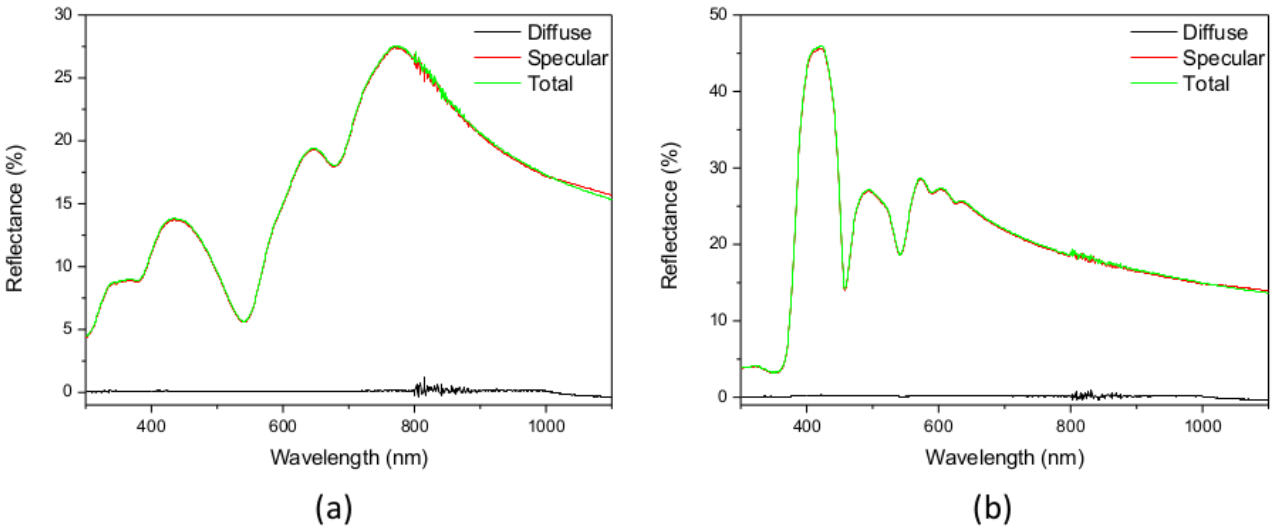

Figure 3.14: Diffuse, specular and total reflectance measured using an integrating sphere for (a) 100 nm ZnPc and (b) 100 nm ZnTPP

What is apparent from figure 3.14 is that reflectance is clearly not negligible and may have an effect on the absorbance calculated. For ZnTPP, in particular, reflectance reaches over 45% in the *Soret* band and should therefore be taken into account. To do so, absorptance must be compared to absorbance within the Q band to determine whether it is a valid approach to calculate the thickness of film by integration of the Q band when using absorbance only. Absorptance, A, is the fraction of incident radiant flux absorbed by a surface and is given by equation 3.4.

$$A = \frac{I_0 - T - R}{I_0} \tag{3.4}$$

For ZnPc (figure 3.15a), both absorbance and absorptance measurements result in very similar profiles. In contrast, the absorptance deviates considerably below 400 nm for ZnTPP (figure 3.15b). As this region does not affect Q band calculations, it is disregarded for our purposes. It is important to note that for both films, the profiles for absorptance and absorbance are very similar in the regions indicated used to determine the film thickness. Therefore, absorbance measurements will be used to determine thickness of film remaining and the validity of this approach verified again with a selection of irradiated films later (section 3.3.3).

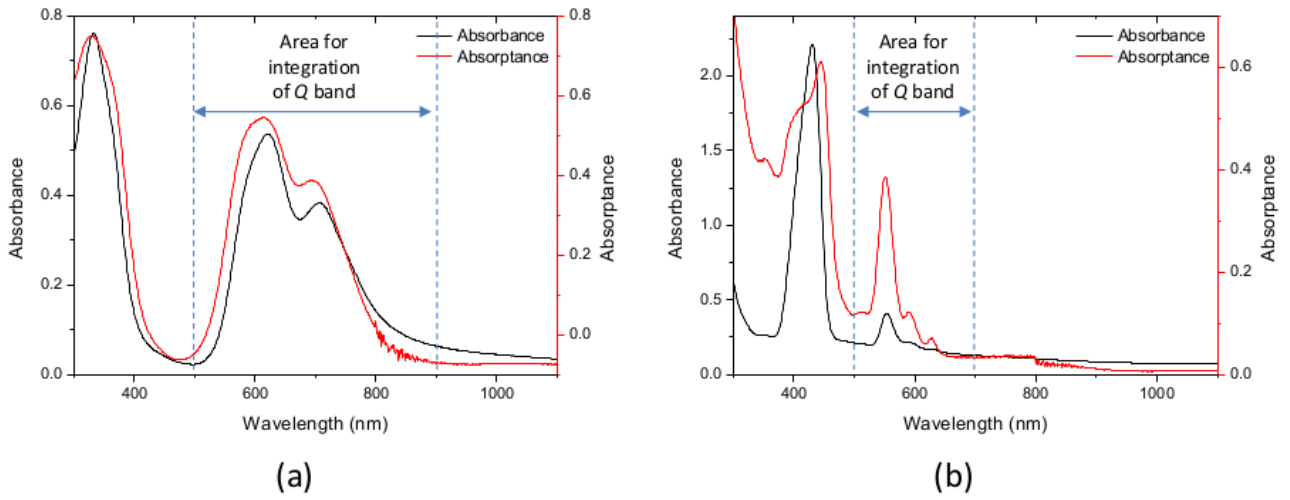

Figure 3.15: Absorbance and absorptance for (a) 100 nm ZnPc and (b) 100 nm ZnTPP with Q band regions indicated

3.2.4 X-Ray Photoelectron Spectroscopy

Zinc Phthalocyanine As-Deposited

X-ray photoelectron spectroscopy (XPS) spectra of 100 nm ZnPc deposited on silicon are shown in figure 3.16 and the peaks of interest are indicated in the survey spectrum (figure 3.16a). Data recorded for the survey spectrum yielded atomic ratios for C:N:Zn as 30:4:1 which gives approximately the correct C:Zn ratio expected from the chemical formula, $C_{32}H_{16}N_8Zn$, for ZnPc but there appears to be some depletion of nitrogen. A total of three passes were made for the survey spectrum and it is likely that additional passes would improve the ratio.

There are three peaks easily distinguished in the C 1s region (figure 3.16b). Of these, the peak of lowest binding energy, labelled C1 (284.3 eV), corresponds to the signal produced by the 24 aromatic carbons in a phthalocyanine molecule [128] and agrees with the value reported at 284.9 eV [129]. The peak with higher binding energy, C2 (285.7 eV) is identified as the peak published in the literature at 286.3 eV [129] and is attributable to the 8 carbon atoms bonded to nitrogen atoms within the pyrrole units [128].

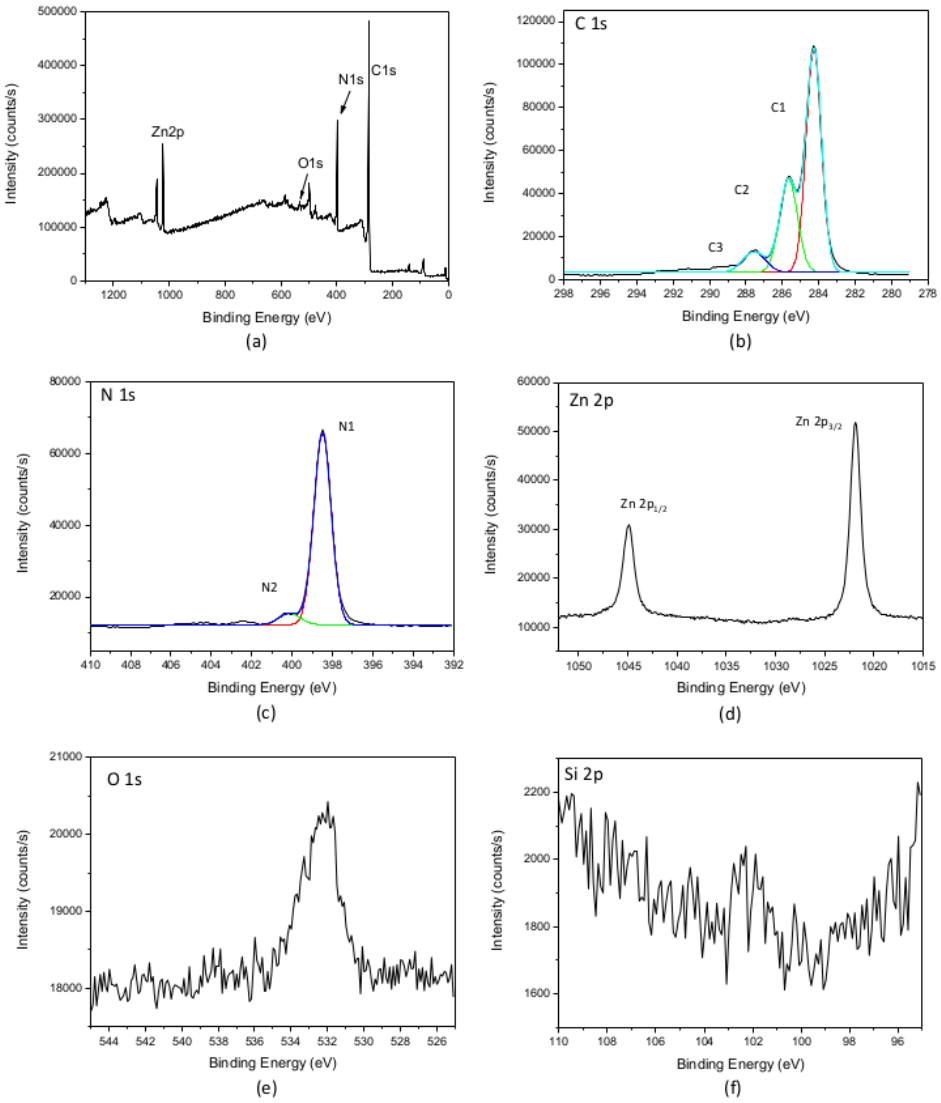

Figure 3.16: XPS spectra of ZnPc as-deposited: (a) survey spectrum, (b) carbon 1s, (c) nitrogen 1s, (d) zinc 2p, (e) oxygen 1s and (f) silicon 2p. Experimental spectra are shown in black.

The areas of C2 to C1 would therefore be expected to form a ratio in the region of 1/3, however, the experimental spectrum gives a ratio of 1/2. This may be due to surface contamination [128] as the samples were exposed to air prior to measurement. Furthermore, C1 and C2 are both likely to result in shake-up satellite peaks which occur when a departing photoelectron loses energy to the ion it leaves behind. The energy is transferred to a valence electron, promoting it from an occupied energy level to an unoccupied energy level and the reduced kinetic energy of the photoelectron is expressed as a peak with higher binding energy. C3 (287.6 eV) is the satellite peak formed by C2 photoelectrons, in approximate agreement with reported values of 288.3 eV [129, 130] but the satellite peak due to C1 appears very close to C2, making peak

resolution more difficult and increasing the C2/C1 area ratios as seen in the results for this sample [128]. The satellite peak C3 at 287.6 eV appears at a binding energy 1.9 eV higher than the main pyrrole peak in agreement with a satellite peak seen in ZnPc at 1.96 eV from its main peak, reported in the literature [130] and corresponds to energy lost to a $\pi - \pi*$ transition. Comparison with the peak energies in the Q band observed in the absorption spectrum (figure 3.9) suggests that the C3 satellite peak most likely corresponds directly to the HOMO - LUMO transition indicated by the absorption peak at 621 nm, equivalent to 2.0 eV. Binding energies measured for C1s peaks all fall slightly short of those published, however, the position of the satellite peak due to pyrrolic carbons with respect to the main pyrollic peak is in very close agreement and the overall peak shape matches that seen in literature, suggesting that the shift in binding energies observed is due to sample charging or an instrumental error. Indeed, this instrumental shift is reflected in the remaining spectra.

Zinc phthalocyanine contains two types of nitrogen atoms with subtly differing environments. Of these, four are in the pyrrole units and four are bridging atoms. The charges surrounding these two types are very similar, resulting in peaks which are not easily resolved [131], however, the nitrogen 1s spectrum obtained (figure 3.16c) shows a peak at 398.5 eV and a smaller shoulder at 400.1 eV with a difference, $\Delta E = 1.6$ eV, similar in magnitude to that produced by a shake-up satellite in the C1s spectrum. Furthermore, such second smaller peaks have been reported at binding energies of approximately 1.5 and 1.8 eV higher than the main peak in CuPc and interpreted as satellite peaks [128], [132], confirming that the N1s spectrum for ZnPc has a single peak accompanied by a satellite.

The Zn $2p_{3/2}$ and Zn $2p_{1/2}$ peaks appear at 1021.9 and 1044.9 eV respectively (figure 3.16(d)), with the $2p_{3/2}$ peak close to that measured at 1022.2 eV on copper substrates [131]. As the equivalent $2p_{3/2}$ peak in zinc oxide thin films appears at between 1021.72 - 1022.4 eV [133], [134] and as detection of zinc was no guarantee of oxide formation, the Zn 2p spectra were used purely for quantification and not for detailed chemical analysis after UV treatment.

The oxygen spectrum shows a poorly defined broad peak centred near 532.2 eV. Oxygen 1s peaks on copper phthalocyanine have been demonstrated to be largely due to adsorption of

water vapour [135]. As the ZnPc films were exposed to air prior to analysis, the presence of the oxygen peak may be attributed to the same contaminant. Although the vacuum within an XPS chamber will remove a proportion of surface water, it has clearly not been entirely eliminated. As the oxygen signal is a crucial indicator for the formation of zinc oxide, as-deposited films of ZnPc were briefly etched using an argon sputter beam within the XPS chamber and spectra remeasured to determine whether this would eliminate the problem of oxygen already present in the surface.

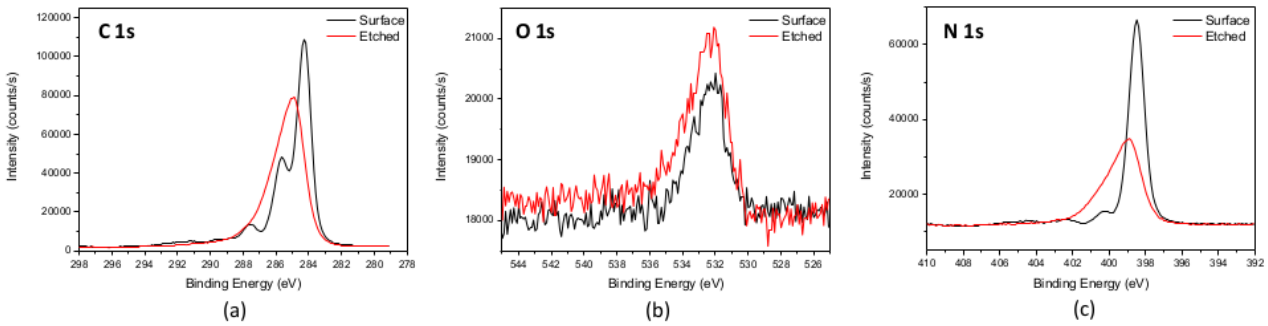

Figure 3.17: XPS spectra of ZnPc before and after etching: (a) carbon 1s, (b) oxygen 1s, (c) nitrogen 1s

The sample was etched for five seconds using an argon sputter beam with mid-current at 3 keV and key spectra are shown in figure 3.17. Despite the expectation that surface etching would remove adsorbed water, there has been no reduction in the O 1s signal (figure 3.17(b)) although there have been significant changes in the C 1s and N 1s spectra shown in figures 3.16(a) and (c) respectively. There is loss of resolution in both spectra and individual peaks attributable to the different bonds within the phthalocyanine molecule are no longer distinguishable. This suggests that damage to the molecule has occurred and that etching in the conditions associated with this XPS experiment is an inappropriate approach for this material. This is particularly true when investigating UV treated films as the surface will be most indicative of the degree of oxide formation.

Zinc Tetraphenylporphyrin As-Deposited

As deposited films of ZnTPP were similarly characterised using XPS (figure 3.18). The survey spectrum yielded atomic ratios of 19:2:1 for C:N:Zn. As the chemical formula for ZnTPP is $C_{44}H_{28}N_4Zn$, the C:N ratio is approximately correct, but there is a higher percentage composition of zinc than is expected which may be improved by further passes. As with ZnPc, there are two carbon 1s peaks, that due to aromatic carbons, C1, and that due to carbons bonded to nitrogen atoms, C2. C1 appears at 284.3 eV and C2 at 287.4 eV. Shake-up satellite peaks are also visible with that for C2 clearly identifiable at 291.3 eV (C3). As with ZnPc, the satellite for C1 lies in the same region as C2, making it difficult to resolve, although here, it is just possible to distinguish a peak for the satellite of C1 at 286.4 eV at $\Delta E_{C1} = 2.1$ eV from the main peak, shown in green in figure 3.18b. C3, the satellite for C2 lies at an energy $\Delta E_{C2} = 3.9$ eV higher than its main peak which would correspond to a transition in the Soret band of the absorption spectrum (figure 3.10) and appears at a higher binding energy than that of the satellite peak, C3 in ZnPc. The binding energy for the C1 peak agrees with that reported in the literature to within 0.3 eV [136] and satellites for the peak corresponding to pyrrolic carbon atoms have been reported at $\Delta E = 2.9$ eV from the main peak in copper tetraphenylporphyrin [128] suggesting that the peak C3 seen here is indeed a satellite as described.

The molecular structure of ZnTPP (figure 3.2) includes 36 carbon atoms of aromatic character which produce peak C1 and 8 which are bonded to nitrogen atoms, producing the higher energy peak, C2 which would be expected to produce a ratio for C2:C1 of 2/9. However, the spectrum shown in figure 3.18b yields a ratio of C2:C1 of 2/44 indicating that either the peaks have been fitted incorrectly or that C1 is a composite peak including peaks attibutable to those bound to nitrogen. The latter seems likely as the FWHM for the C1 peak is 1.43 eV compared to the FWHM for the C1 peak seen in ZnPc which is considerable smaller at 1.00 eV (figure 3.16b). This would then suggest that the peaks seen at 287.4 and 291.3 eV are satellite peaks as reported for copper tetraphenylporphyrin [128].

In contrast with the phthalocyanine, all nitrogen atoms in zinc tetraphenylporphyrin inhabit the same environment and therefore present a single peak at 398.2 eV (figure 3.18c) falling between

the binding energies reported in the literature for nitrogen at 397.8 eV [136] and 398.7 eV [137] with a satellite peak at a binding energy 3.0 eV higher than the main peak. As for the carbon 1s spectra, ΔE for the nitrogen satellite peaks of ZnTPP is higher than that for ZnPc.

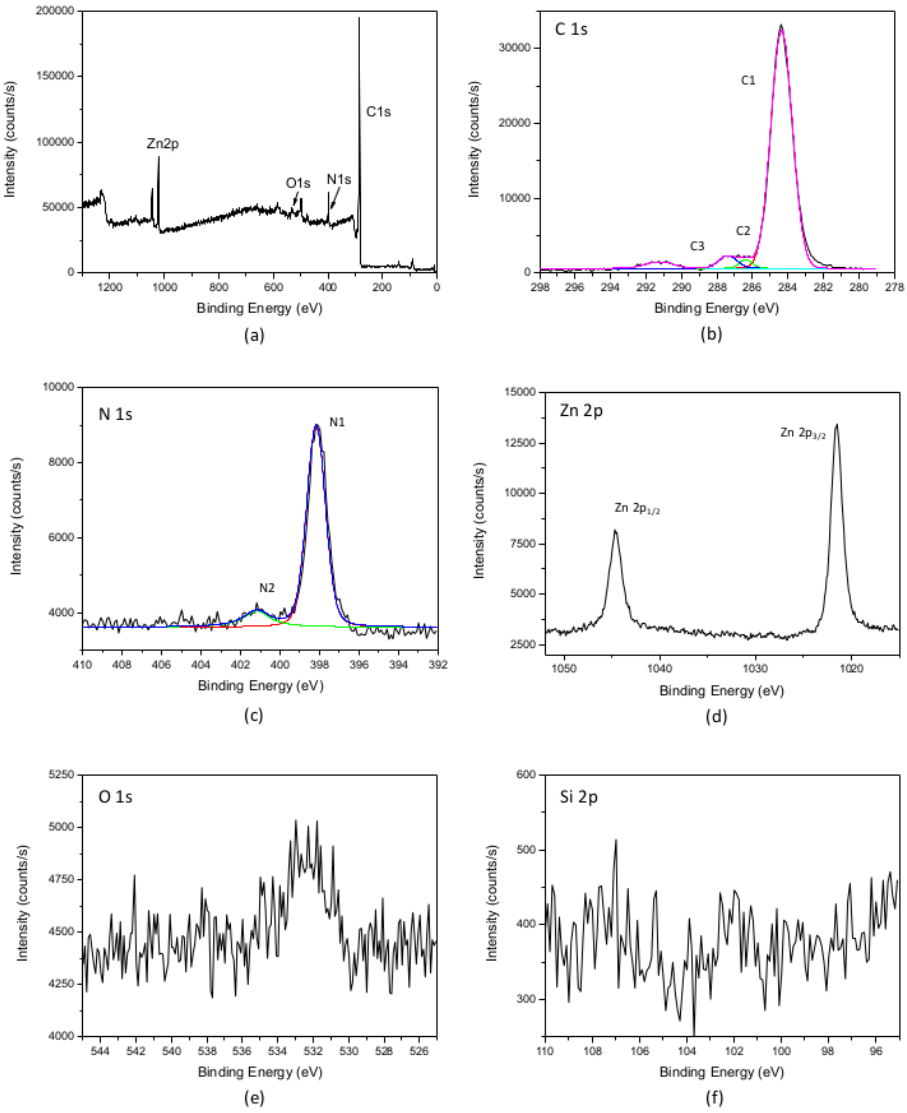

Figure 3.18: XPS spectra of ZnTPP as-deposited: (a) survey spectrum, (b) carbon 1s, (c) nitrogen 1s, (d) zinc 2p, (e) oxygen 1s and (f) silicon 2p. Experimental spectra are shown in black.

As with ZnPc, the oxygen 1s spectrum contains only one peak which is again poorly defined and centred around 532.3 eV (figure 3.18e), suggesting adsorption of water vapour. Negligible silicon was present at the surface of both ZnPc (figure 3.16f) and ZnTPP (figure 3.18f) as expected since in neither case was the substrate exposed and silicon would only be present as a contaminant encountered through handling procedures.

For both ZnPc and ZnTPP, the carbon 1s signal is well-defined with a high intensity, therefore, the XPS spectrum of carbon may be used to monitor removal of the organic fragments formed as UV degradation of the precursor progresses. Similarly, formation of zinc oxide may be estimated by the increase in the intensity of the oxygen 1s peak. Measured experimental values of binding energy and those from literature are summarised in table 3.1.

Table 3.1: Binding energies (eV) for ZnPc, CuPc, ZnTPP and ZnO from the literature and experimental results

Sample	Zn 2p	C 1s	C 1s Satellites	N 1s	N 1s Satellites	O 1s
ZnPc on indium antimonide [129]		284.9 286.3	286.7 288.3	399.1	401	
ZnPc on zinc sulphide [130]		285.07 286.43	286.92 288.39			
ZnPc [131]	1022.2					
CuPc on metal [132]		284.8		399		
CuPc on copper [128]		284.8 286.2	288.5	399.2	400.7	
ZnPc (experimental)	1021.9 1044.9	284.3 285.7	287.6	398.5	400.1	
ZnTPP on silver [137]	1022			398.7		
ZnTPP on gold [136]	1021.5	284.0		397.8		
ZnTPP on copper [131]	1022.2			398.6		
ZnTPP (experimental)	1022.3 1045.4	284.3 287.4	286.4 291.3	398.1	401.1	
ZnO from zinc acetate [134]	1021.22 1044.85					529.32
ZnO crystal [133]	1022.4					531.3

3.2.5 Secondary Ion Mass Spectrometry

SIMS depth profiles were taken of as-deposited films of ZnPc and ZnTPP on silicon using an O_2^+ primary sputter beam at 500 eV over an area of 300 µm x 300 µm. Positive fragments were analysed using a Bi_3^+ beam within a sampling area of 100 µm x 100 µm and at three shots per pixel. No electron floodgun was required for charge compensation.

Zinc Phthalocyanine As-Deposited

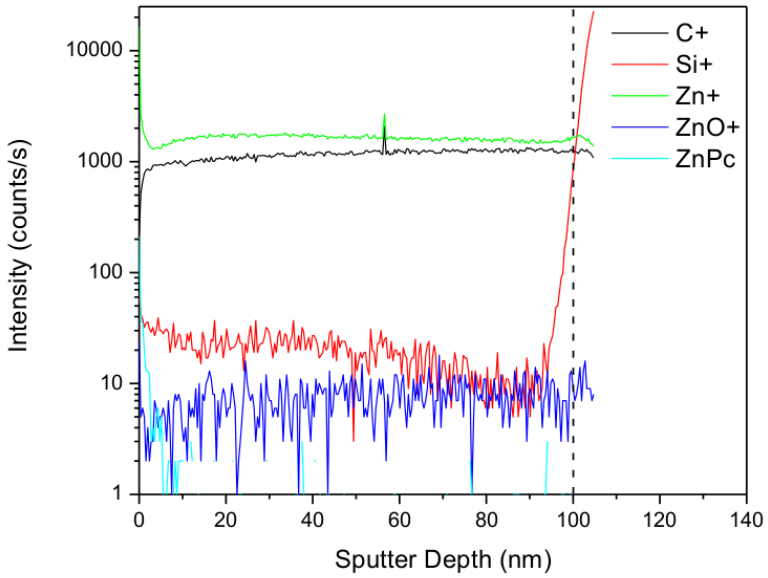

Figure 3.19: SIMS depth profile of ZnPc film, as-deposited

The depth profile of ZnPc is shown in figure 3.19. Carbon (C^+) and zinc (Zn^+) ions are detected with stable intensity throughout the depth of the film as would be expected. A small amount of ionised ZnPc is evident at the beginning of the depth profile but its intensity quickly reduces to zero due to repeated impact by primary ions, some of which penetrate below the surface, resulting in collision cascades which fragment the precursor molecule. Zinc oxide ions (ZnO^+) are present at an approximate intensity of 10 counts/s through the depth of as-deposited film. Oxygen is known to enhance the yield of positive ions such as Zn^+, however, due to interaction of the O_2^+ ion beam with the zinc in the film, not only is the yield of Zn^+ increased, but zinc oxide is formed, further enhancing the intensity of Zn^+ and also resulting in the detection

of ZnO^+ [138]. Silicon detected at the surface is likely to be due to handling and storage procedures as both the sample holders and gloves used contain silicon.

The steep increase in the silicon signal is a clear indication that the sputter beam has encountered the substrate. Further evidence of this is the slight increase in the yields of C^+ and Zn^+ ions. The density of silicon is approximately 2.33 g/cm^3 [139], considerably greater than that of ZnPc at 1.6 g/cm^3 [140]. Consequently, as sputtering progresses and atoms are embedded into layers below the level they originate from, there is a build up of C^+ and Zn^+ ions when the beam meets a material of higher density such as silicon. Further embedding of atoms is inhibited by the increased density and a peak in the intensities of C^+ and Zn^+ signals is observed. The position of the interface may be determined by examining the intensity of silicon and is often set at the point where the Si^+ intensity is half that of its maximum. Following this method for this depth profile would position the interface beyond the peak of C^+ and Zn^+ intensities which does not agree with the observed changes which have taken place and depend on the relative densities of material. In addition to a build up of ions at the interface, intensities of positive ions at the interface may be enhanced due to the interaction of the oxygen beam with the native silicon oxide layer on the substrate surface.

Depth profiles are recorded as the intensity of ions against sputter time. For as-deposited films, the thickness has been measured using either AFM or a profilometer as shown in section 3.2.3. Assuming the film is homogeneous throughout, conversion to sputter depth as shown in figure 3.19 is simply a matter of determining when the substrate has been reached in the SIMS profile which is clear from the steep increase in the intensity of Si^+ ions and the peak in C^+ and Zn^+ ions.

For as-deposited ZnTPP, the results are similar (figure 3.20). Once equilibrium has been reached, the intensities of C^+ and Zn^+ are stable, indicating homogeneous film deposition. The yield of C^+ ions is approximately 1000 counts/s as for ZnPc, however, the yield of Zn^+ ions is less than half that of ZnPc. One obvious explanation is the density of zinc atoms for each material. The chemical formulae are $C_{32}H_{16}N_8Zn$ for ZnPc and $C_{44}H_{28}N_4Zn$ for ZnTPP, giving ratios of Zn:C of 1/57 and 1/77 respectively. This alone would result in a reduced yield

of Zn^+ions. In addition, matrix effects are likely to contribute to the difference in yield and there is no reason they should be equal.

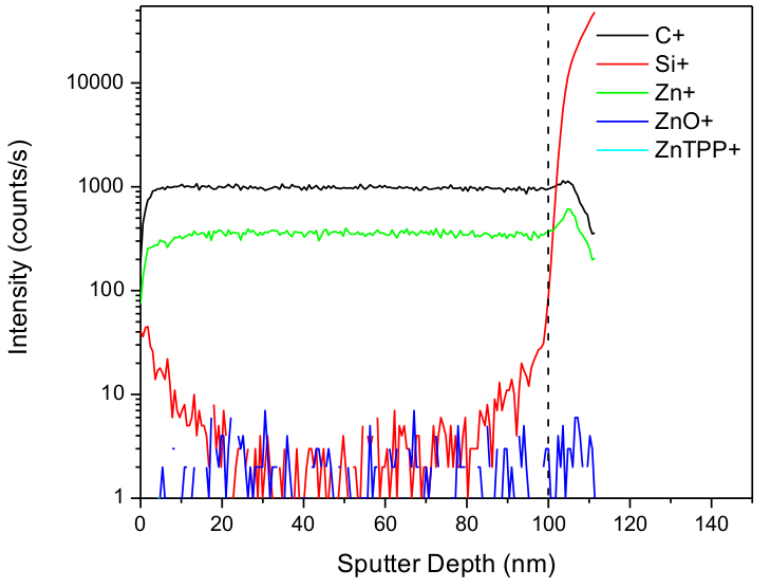

Figure 3.20: SIMS depth profile of ZnTPP film, as-deposited

As for ZnPc, the entire ZnTPP molecule does not survive ion sputtering and there is no detection of the molecular fragment at all. Although there should be no zinc oxide present in the film, ZnO^+ ions are also detected here due to interaction with the oxygen beam but at lower intensity than for ZnPc. The silicon interface is also easily defined in ZnTPP as the silicon intensity rises steeply, coinciding with a temporary peak in the C^+ and Zn^+ intensities. The interface has been indicated by a vertical dashed line and the data converted to show intensity as a function of depth as for ZnPc.

3.3 Results: UV Treated Films

Films grown by OMBD were placed on a sample holder in the vacuum chamber at a distance of 8.5 cm from the excimer lamp. The chamber was evacuated to a pressure of approximately 2×10^{-2} mbar and the pressure maintained for a minimum of 30 minutes before introducing nitrogen into the chamber allowing the pressure to reach 1.8 mbar. Once the pressure was stable, oxygen was also released into the chamber until a total pressure of 3.0 mbar was reached, giving

a partial pressure of oxygen of 1.2 mbar. The vacuum pump remained on, ensuring a continually renewed supply of nitrogen and oxygen. The UV lamp was operated for the period required, following which, the oxygen flow was reduced to zero and the nitrogen flow used to flush out any remaining organic fragments and ozone which might remain in the chamber before venting. Samples were removed for characterisation or for storage in a glovebox. One sample of ZnPc was irradiated for 90 minutes in standard conditions and one in 3.0 mbar of nitrogen only and their absorption spectra recorded to determine the necessity of oxygen to the process.

3.3.1 Morphology - Atomic Force Spectroscopy

Zinc Phthalocyanine Following UV Treatment

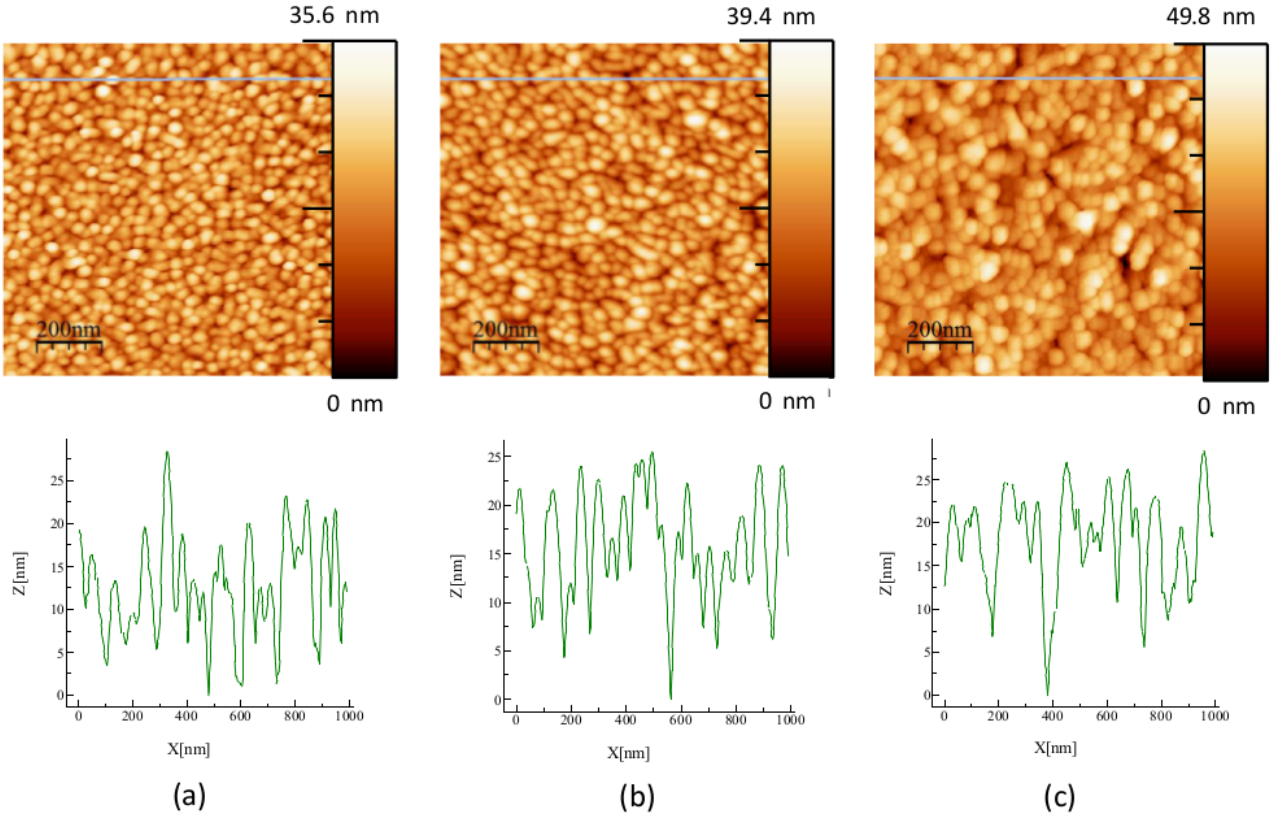

Figure 3.21: AFM images and line profiles of ZnPc after (a) 0, (b) 50 and (c) 90 minutes of UV treatment

During UV degradation, ZnPc largely retains its morphology and crystalline appearance (figure 3.21) with no significant change in peak to trough distance. There is a steady increase in

the size of features which is evident in the line profiles taken of ZnPc films after 50 and 90 minutes (figures 3.21b and c). This is accompanied by an increase in roughness (figure 3.22) from 2.6 nm to close to 6 nm. The change in roughness appears to follow a linear relationship with UV treatment time.

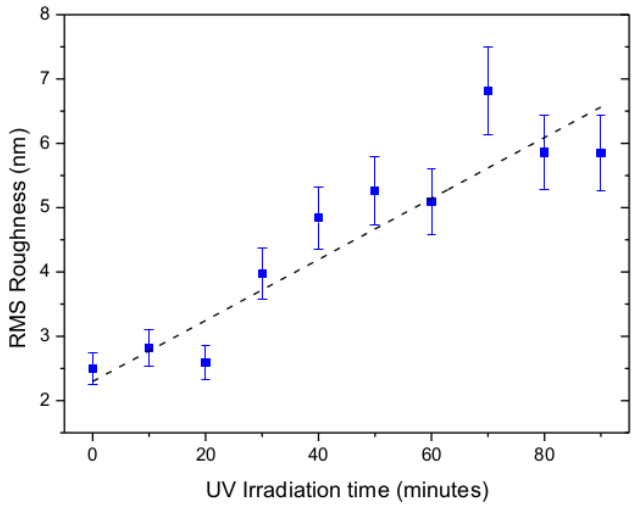

Figure 3.22: RMS roughness of ZnPc samples after UV treatment

Particle size analysis was carried out using Gwyddion Open Source software and a watershed algorithm with a drop size of 1% of the local minimum value, 10 steps and a threshold of 3 pixels^2. Segmentation was carried out with a drop size of 1% and 10 steps (figure 3.23). Data plotted in the histograms demonstrates an increase in the average particle size and in the distribution of particle sizes as the UV process takes place with particle radii ranging from 1 nm to 16 nm after 80 minutes, whereas the untreated film contained particles whose radii varied between 1 and 9 nm. This is easily seen from the AFM images (figure 3.21) where the as-deposited film has uniformly sized grains. The increasing size distribution leads to a gradual increase in R_q. The greater range of grain size in treated films may be due to a combination of factors including gradual erosion of grains to produce smaller particles, the formation of zinc oxide on the surface of particles which may prevent further reaction and possible diffusion of ZnPc molecules to form larger grains. In the case where a grain of ZnPc absorbs energy from an exited oxygen species or a photon but only some molecules fragment, there may be sufficient residual energy to allow molecules to diffuse laterally and recrystallise into larger grains. In addition, as some grains are eroded, others below which may be larger are exposed.

The table 3.2 summarises grain statistics for ZnPc, demonstrating clearly a reduction in particle number accompanied by an increasing average grain size. The approximate doubling of the variation from 50 to 80 minutes yielded by the grain analysis demonstrates a degree of unreliability in software generated results as the AFM images themselves do not portray such a high proportion of particles within the 1-2 nm range and this is reflected in the line profiles of the images themselves (figure 3.21) which also indicate a gradual increase in grain size. Hence, conclusions may not be drawn from the grain size analyses in isolation. Whether the grains are formed of ZnPc, a combination of oxidised precursor fragments, zinc oxide or a combination thereof may be determined by spectroscopic and chemical analysis in subsequent sections.

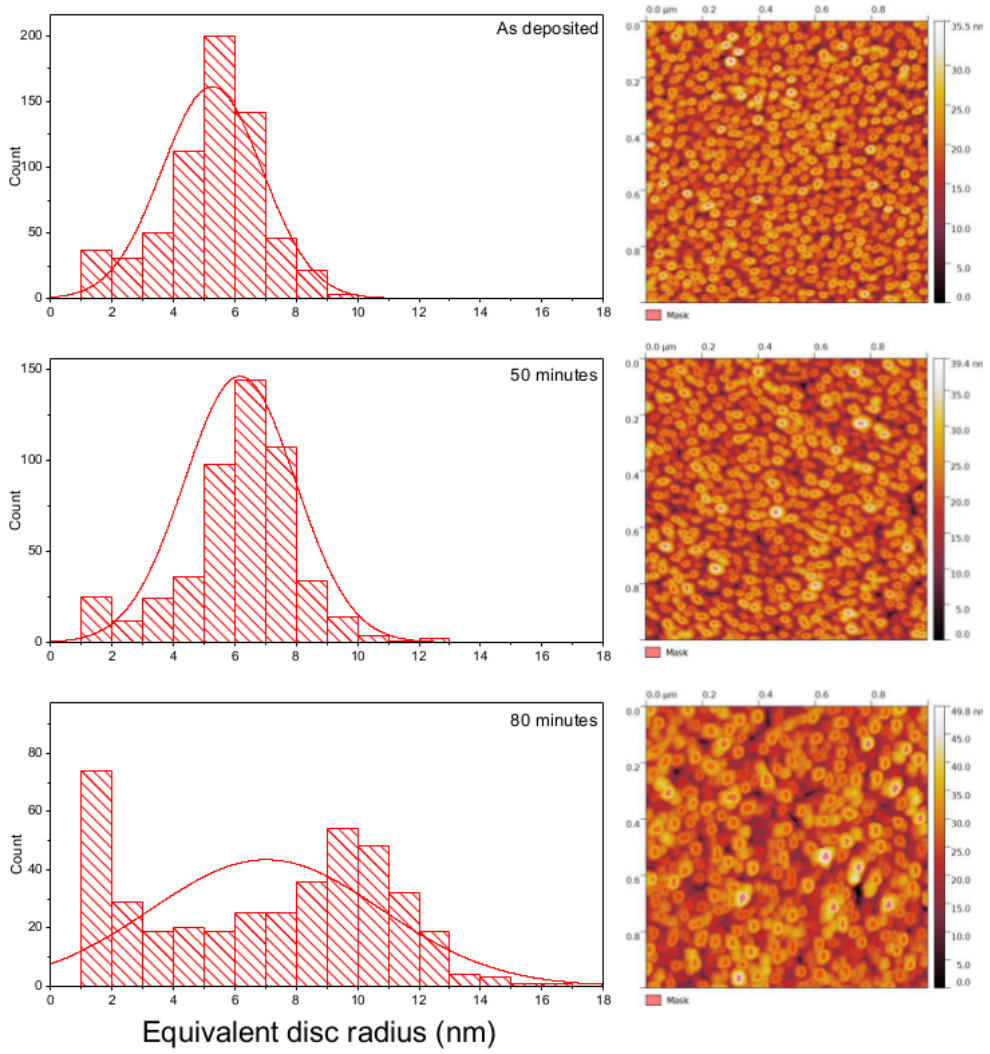

Figure 3.23: Grain size distribution for ZnPc films, as-deposited and after 50 and 80 minutes of UV treatment, with a distribution overlay and identified grains indicated in the AFM images

Table 3.2: Comparison of particle distribution for ZnPc

	As deposited	50 minutes	80 minutes
Number of particles	642	501	409
Average grain diameter (nm)	10.5	12.3	14.0
Standard deviation (nm)	1.6	1.8	3.8
Coefficient of variation (%)	15	15	27

Zinc Tetraphenyporphyrin Following UV Treatment

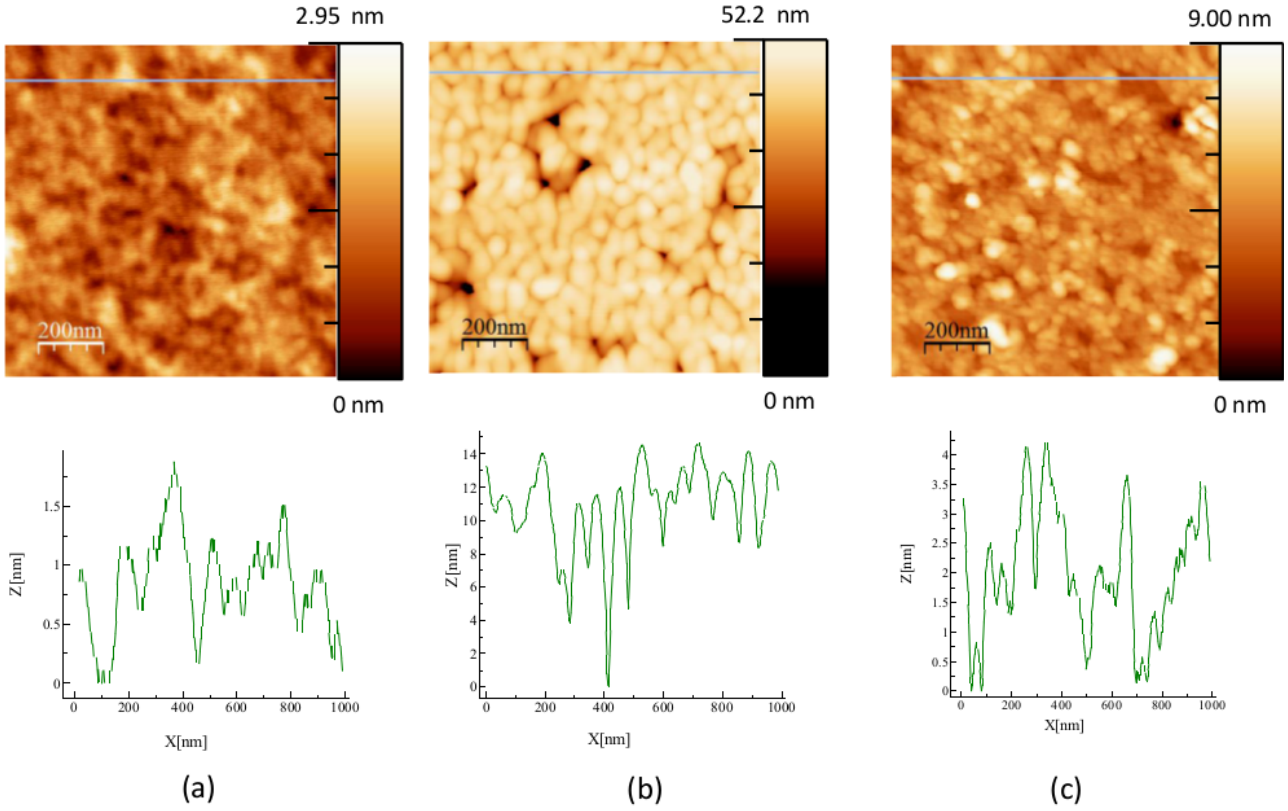

Figure 3.24: AFM images and line profiles of ZnTPP after (a) 0, (b) 90 and (c) 220 minutes of UV treatment

In contrast with ZnPc, the ZnTPP films underwent a dramatic change during UV treatment, clearly visible in the AFM images (figure 3.24). The as-deposited film lacked features with peak to trough distances averaging below 1 nm (figure 3.5) and a roughness, $R_q = 0.41$ nm. However, as photodegradation progressed, features formed at the 75 - 105 minute stage giving

the appearance of grains. Peak to trough distances increased to in excess of 10 nm at 90 minutes before decreasing to approximately 4 nm after 220 minutes, at which point there was little evidence of grainy features (figure 3.24c).

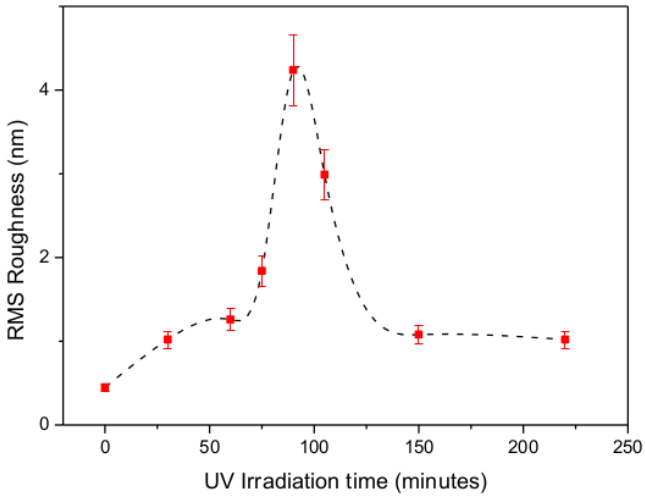

Figure 3.25: RMS roughness of ZnTPP samples after UV treatment

The appearance of grains was accompanied by an increase in roughness, peaking at over 4 nm after 90 minutes of treatment, coinciding with a peak in grain number density (figure 3.25). Whether the precursor is forming crystalline grains or this is an effect of roughening by photon and oxygen attack will be determined from the XRD results (3.3.2).

The same watershed algorithm applied to ZnPc was used to analyse grain distribution in ZnTPP films (figure 3.26). The disc radius histograms indicate the formation of larger features corresponding to the grain-like structures seen at 90 minutes and a high number of features below 5 nm in radius identifying imperfections as for as-deposited film. The algorithm applied with the parameters given will correctly analyse the distribution of convex or near-convex particles. The as-deposited film was amorphous with very little variation in height implying that any features detected are not crystalline structures, as the XRD results have confirmed (figure 3.8), but may be a result of film imperfections or impurities and therefore not convex features as required. Similarly, once fully degraded, the algorithm will not apply as the film again exhibits a low surface roughness. However, the particle analysis at 90 minutes does concur with not only the appearance of the AFM image but also with roughening caused by oxygen and UV attack.

The broad distribution of particle size contributes to the sudden increase in R_q. Roughening caused by oxygen and UV mechanisms will be further investigated in later sections by XRD and SIMS.

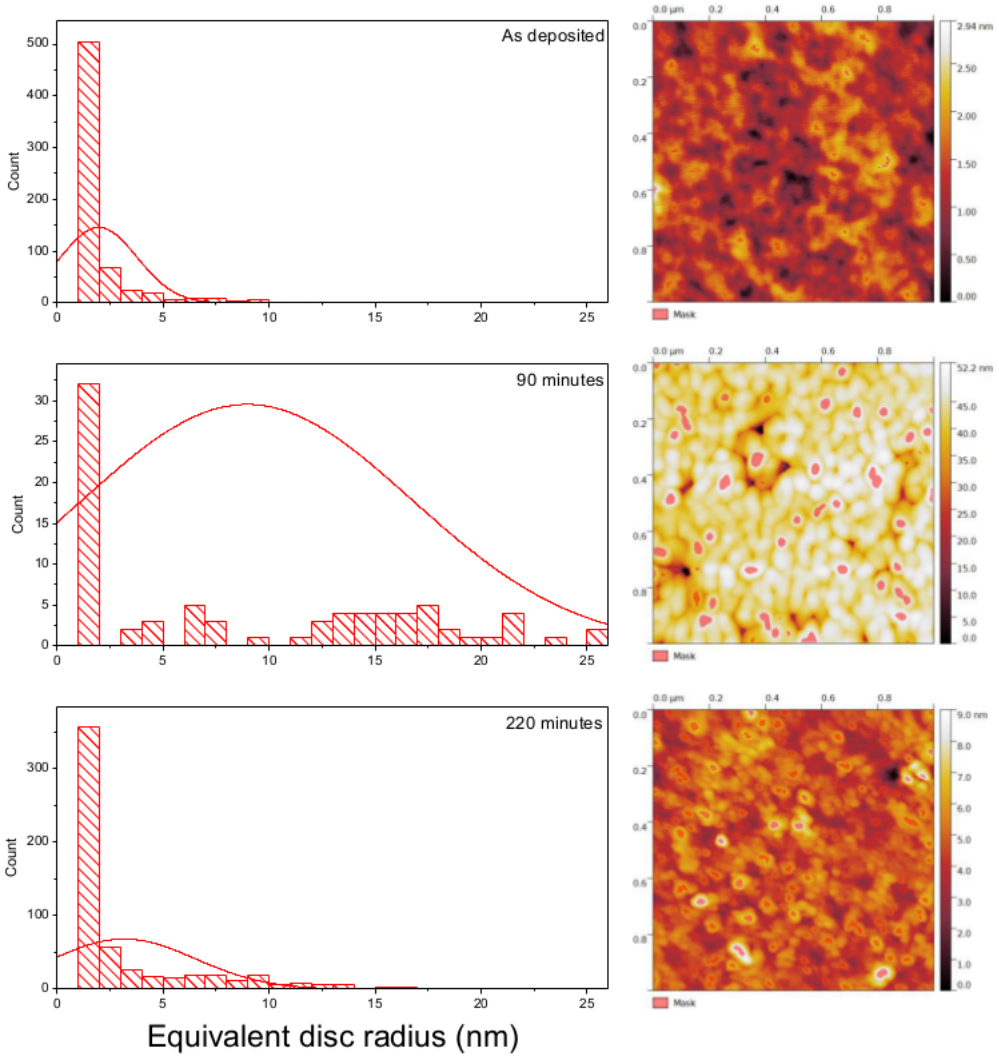

Figure 3.26: Grain size distribution for ZnTPP films, as-deposited and after 90 and 220 minutes of UV treatment, with a distribution overlay and identified grains indicated in the AFM images

3.3.2 X-Ray Diffraction of UV Treated Films

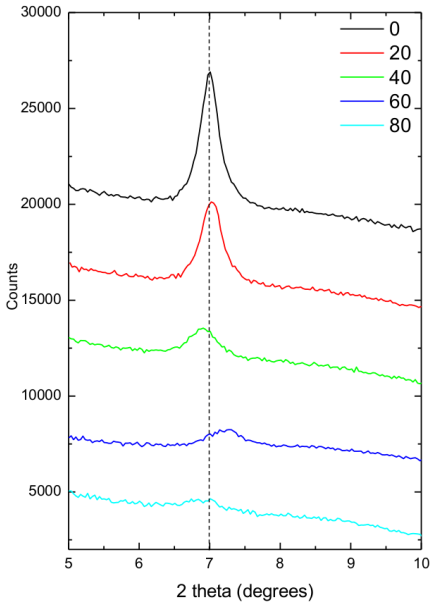

Figure 3.27: XRD scans for ZnPc on glass for 0, 20, 40 and 80 minutes of UV treatment. Scans are offset for clarity

XRD scans of ZnPc show a decrease in the peak intensity at 7° as the reaction proceeds and a slight positive shift of up to 0.2° at 60 minutes (figure 3.27). The peak at 60 minutes is close to the higher angle peak for the α modification when lying in the (002) (or (001)) plane [2, 3], but it is unlikely that ZnPc has undergone the 90° rotation which would be required to achieve such an orientation. Much more likely is an instrumental shift. As these samples were grown on glass, there is no silicon peak with which to calibrate the diffractograms, however, the reduction in peak intensity demonstrates a gradual loss of ZnPc crystalline structure with increasing UV irradiation time. The absorption spectra will determine whether any ZnPc molecules remain intact or whether the film has merely lost sufficient order that there are no diffracting planes.

As the deposited ZnTPP films were amorphous, there was no discernible change in the XRD scans as UV time was increased (figure 3.28). In both ZnPc and ZnTPP, there were no new peaks after UV treatment which might have indicated the formation of crystalline zinc oxide.

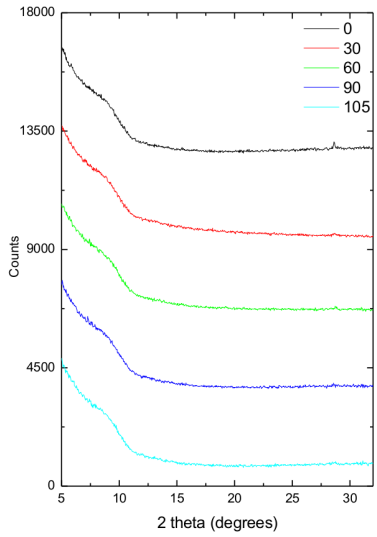

Figure 3.28: XRD scans for ZnTPP on glass for 0, 30, 60, 90 and 105 minutes of UV treatment. Scans are offset for clarity

There were no new peaks detected which might indicate the presence of zinc oxide. This is not unexpected as 100 nm films of ZnPc and ZnTPP are expected to form no more than 4 nm of zinc oxide. For detection by XRD, crystallite size must be in the order of 20 nm.

3.3.3 UV-Visible Absorption Spectra of UV Treated Films

Absorption spectra recorded for as-deposited ZnPc and ZnTPP films irradiated for 90 minutes in either standard conditions or nitrogen only show that oxygen is crucial to the reaction (figure 3.29). Using the principle stated in section 3.2.3, integration of the Q band (500 - 900 nm) gives an indication of the percentage of intact molecules remaining within film. In the case of the film exposed to UV light in standard conditions, less than 1% of the original film remains, whereas when irradiated in nitrogen only, 52% of the film remains. Therefore, although UV light will result in film degradation, oxygen is highly important to increase the rate at which the film degrades and will be necessary for the formation of oxide. Having established the necessity of oxygen to the reaction, comparison between ZnPc and ZnTPP may elucidate the mechanism by which the reaction proceeds.

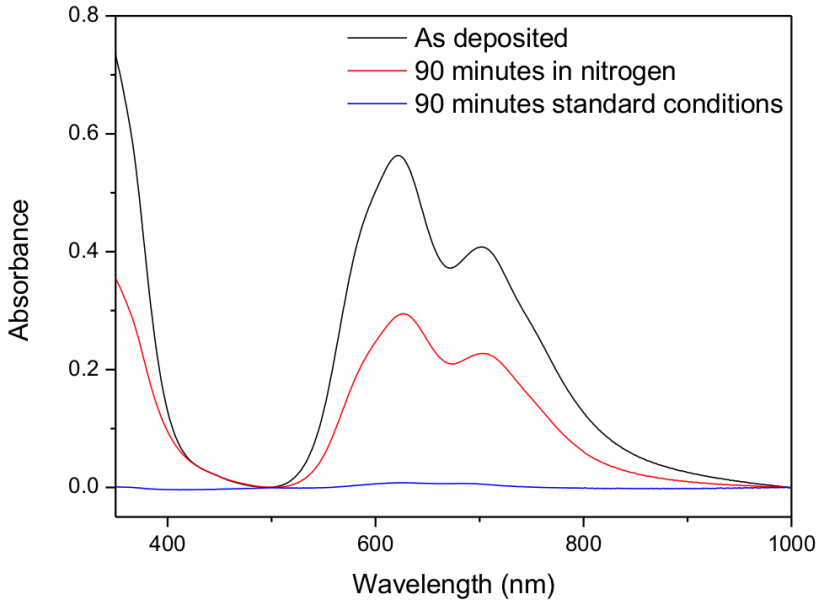

Figure 3.29: Absorption spectra of 100 nm ZnPc as-deposited and irradiated for 90 minutes, in standard conditions and in nitrogen only

Absorption spectra were recorded for both ZnPc (figure 3.30a) and ZnTPP (figure 3.31a) films to determine the rate at which precursor molecules were removed during UV treatment.

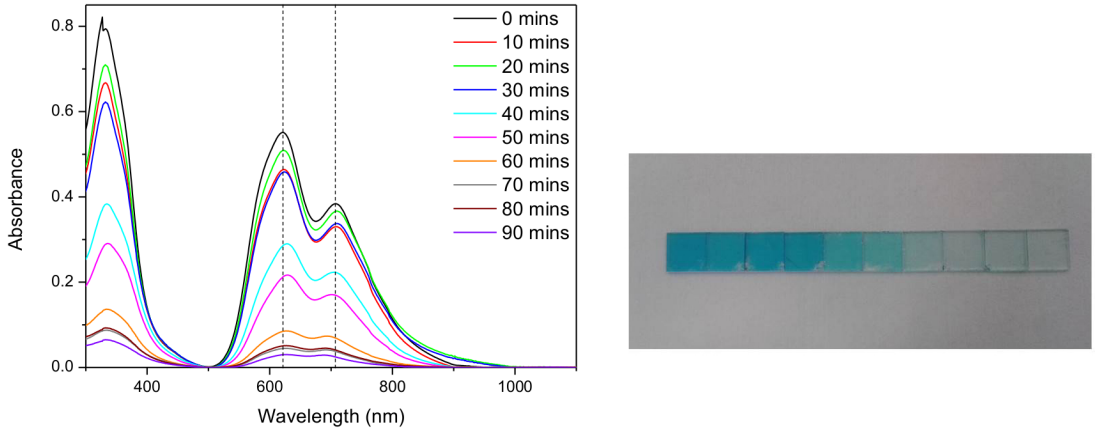

(a) (b)

Figure 3.30: (a) Absorption spectra of UV treated ZnPc films and (b) photograph of samples in increasing order of irradiation in UV light (samples typically of size 1 cm^2)

The results for ZnPc (figure 3.30) show that absorption by ZnPc decreases with increasing UV exposure and that the peak in the Q band at 621 nm begins to shift to higher wavelengths after 40 minutes but that the peak at 706 nm, corresponding to $\pi - \pi^*$ transitions remains at the same wavelength. The peaks in the Soret region also remain unshifted and the ZnPc has

been almost completely removed by 90 minutes. The change in the spectra is accompanied by a decrease in the blue colour of the film (figure 3.30b).

The absorption spectra for ZnTPP (figure 3.31a) also show decreasing absorption as UV exposure is increased with a simultaneous loss of colour from the film (figure 3.31b). The position of the highest peak in the Q band at 655 nm, attributed to HOMO - LUMO transitions is stable. The Soret peak at 432 nm is stable until 75 minutes of UV irradiation have elapsed, when the peak wavelength increases slightly. The asymmetry in the Soret peak is retained throughout and no absorption by ZnTPP is detected beyond 150 minutes.

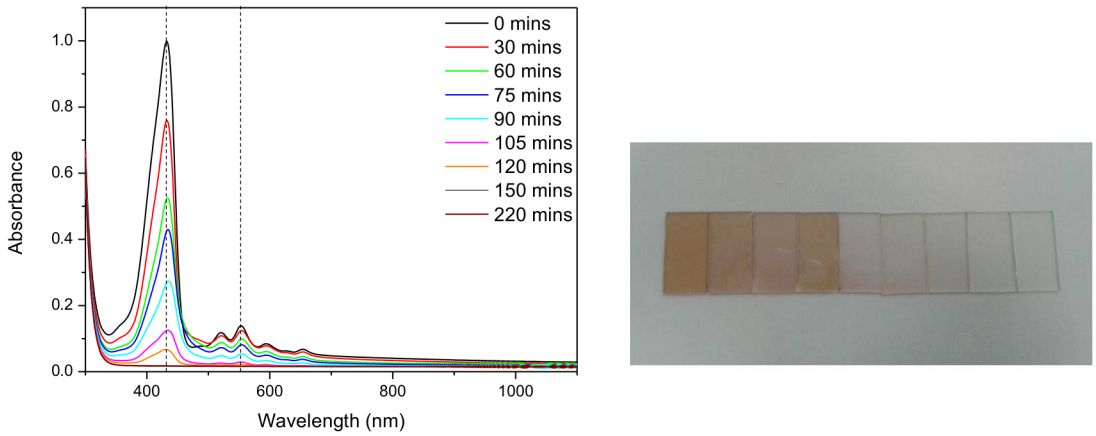

Figure 3.31: (a) Absorption spectra of UV treated ZnTPP films and (b) photograph of samples in increasing order of irradiation in UV light (samples typically of size 1 cm^2)

As stated in section 3.2.3, the area under the Q band may be used to determine the percentage of original film remaining. Integration of the Q band for ZnPc yielded a linear decrease in film thickness of 1.3 nm/minute (figure 3.32), concordant with the rate at which surface roughness increased (figure 3.22). Once the film has been irradiated for 70 minutes, the rate of film removal decreases. One possibility to consider is the formation on the surface of zinc oxide which absorbs UV light. The maximum thickness of zinc oxide expected to be produced is 4 nm and in the region of photon energies $E = 6.5$ eV, the absorption coefficient α, is approximately 8×10^4 $cm^{-1}$for highly oriented zinc oxide films [64]. Such a 4 nm film of zinc oxide would have a transmittance of 97% at 172 nm, therefore, the effect of UV absorption by zinc oxide produced is likely to have only a very small effect.

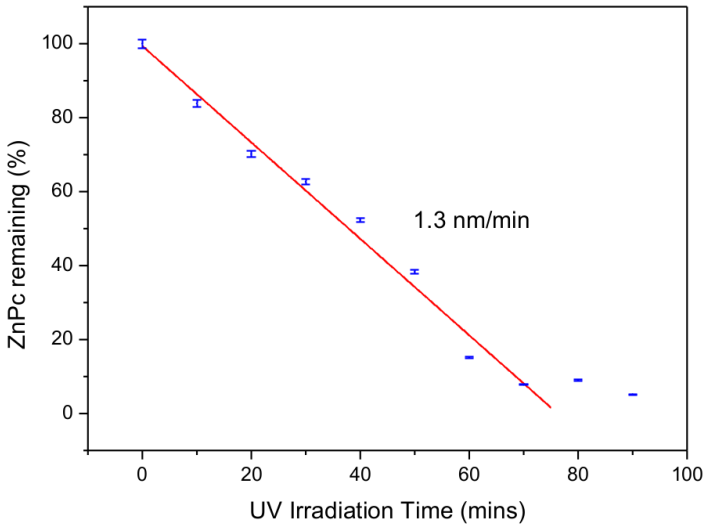

Figure 3.32: Percentage of ZnPc film remaining after UV treatment

Integration of the region under the Q band for ZnTPP revealed two different regimes for the film remaining as UV irradiation time increased (figure 3.33). The film removal rate was 0.3 nm/minute until 30 minutes after which there was an increase to 1.3 nm/minute until 105 minutes, at which point, the reaction rate decreased again, possibly for the same reasons as for ZnPc. During the period between 30 - 90 minutes, the rate for ZnTPP was the same as for ZnPc, suggesting that there may be different reaction mechanisms taking priority in ZnPc and ZnTPP but that once irradiation has exceeded 30 minutes in ZnTPP, the mechanisms act similarly for both materials.

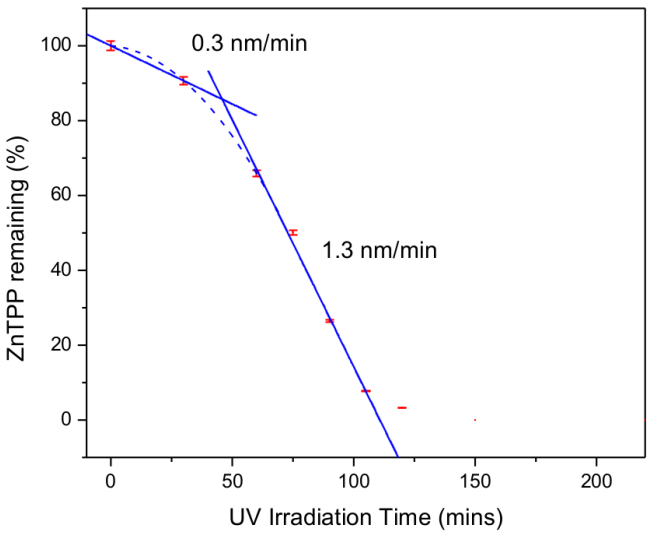

Figure 3.33: Percentage of ZnTPP film remaining after UV treatment

The aim of this project was to elucidate the reaction mechanism by comparison between crystalline and amorphous materials and determine the relative importance of the oxygen assisted and UV assisted routes. The results obtained from absorption spectra suggest that although initially these two routes exert different degrees of influence on the two films, after 30 minutes for ZnTPP, both films are subject to oxygen assisted and UV assisted degradation equally. This will be elaborated upon further in a later section (3.5)

It was suggested earlier that reflectance may be disregarded and absorbance used to calculate film thickness as shown (section 3.2.3). Reflectance measurements were taken of several irradiated ZnPc samples and absorbance and absorptance spectra compared and found to differ only slightly (figure 3.34). The major difference is that absorbance spectra are non-zero in the infra-red region. As reflectance measurements show, this is a direct result of calculating the flux absorbed from the transmittance, rather than taking account of reflectance (figure 3.14). The area under the Q band was integrated for both sets of spectra and values for irradiated films expressed as a percentage of as-deposited film to determine the error accrued by not accounting for reflectance (figure 3.35). It can be seen that the linear trend derived from absorbance spectra is repeated in absorptance measurements and values for film remaining are within 10% of each other, therefore, use of absorbance as a measure of film removal is a valid approach.

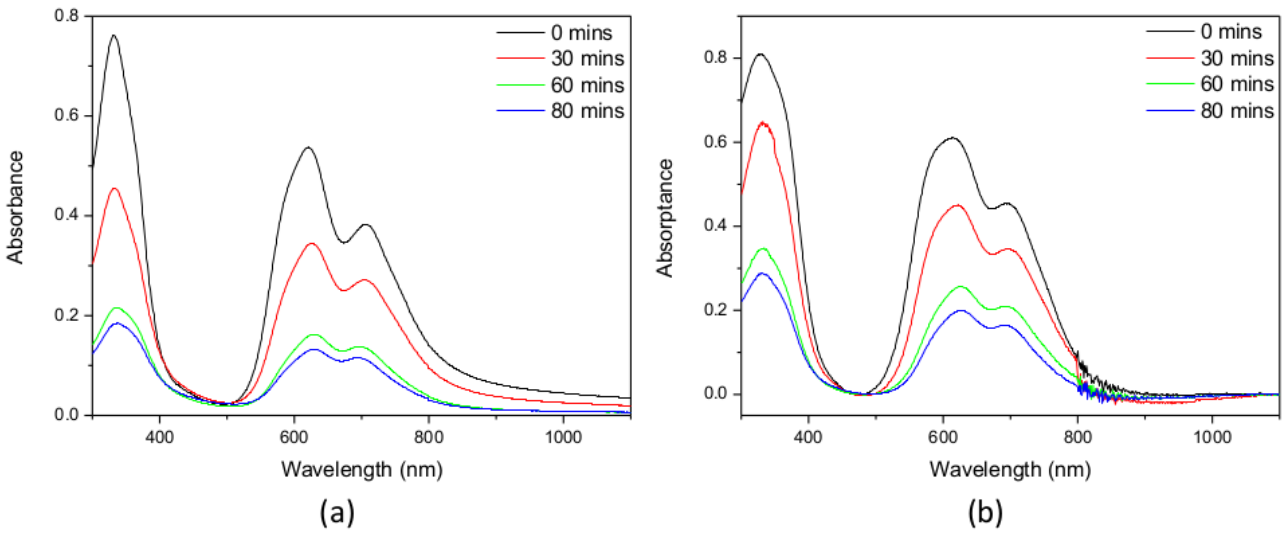

Figure 3.34: (a) Absorbance spectra and (b) absorptance spectra for as-deposited and irradiated ZnPc films

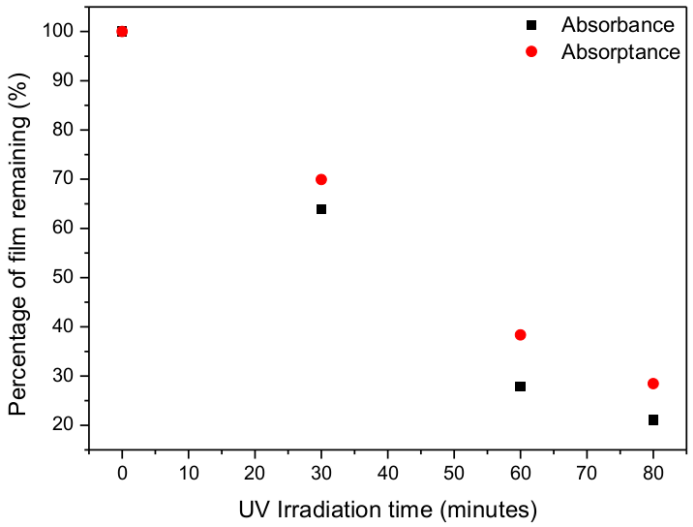

Figure 3.35: Percentage of ZnPc film remaining calculated by integration of the Q band of absorbance and absorptance

3.3.4 X-Ray Photoelectron Spectroscopy

XPS data was recorded for ZnPc and ZnTPP samples for increasing UV exposure times. The peaks were identified by comparison with literature (table 3.1).

Zinc Phthalocyanine Following UV Treatment

Relevant peaks for ZnPc are indicated in the survey spectra with individual XPS spectra shown for irradiation times of 0 - 90 minutes in 10 minute steps (figure 3.36).

Of the spectra, the silicon Si 2p spectrum is the simplest to analyse (figure 3.36b) as there is no silicon detected until the film has been irradiated for 90 minutes at which point the substrate has been exposed and a silicon peak is detected at approximately 100 eV. There is also a very small increase in intensity observable at 103.3 eV which may be attributed to the formation of silicon dioxide as the peak for Si 2p in bulk silicon dioxide has been reported at 103.9 eV with a FWHM of 2 eV [141].

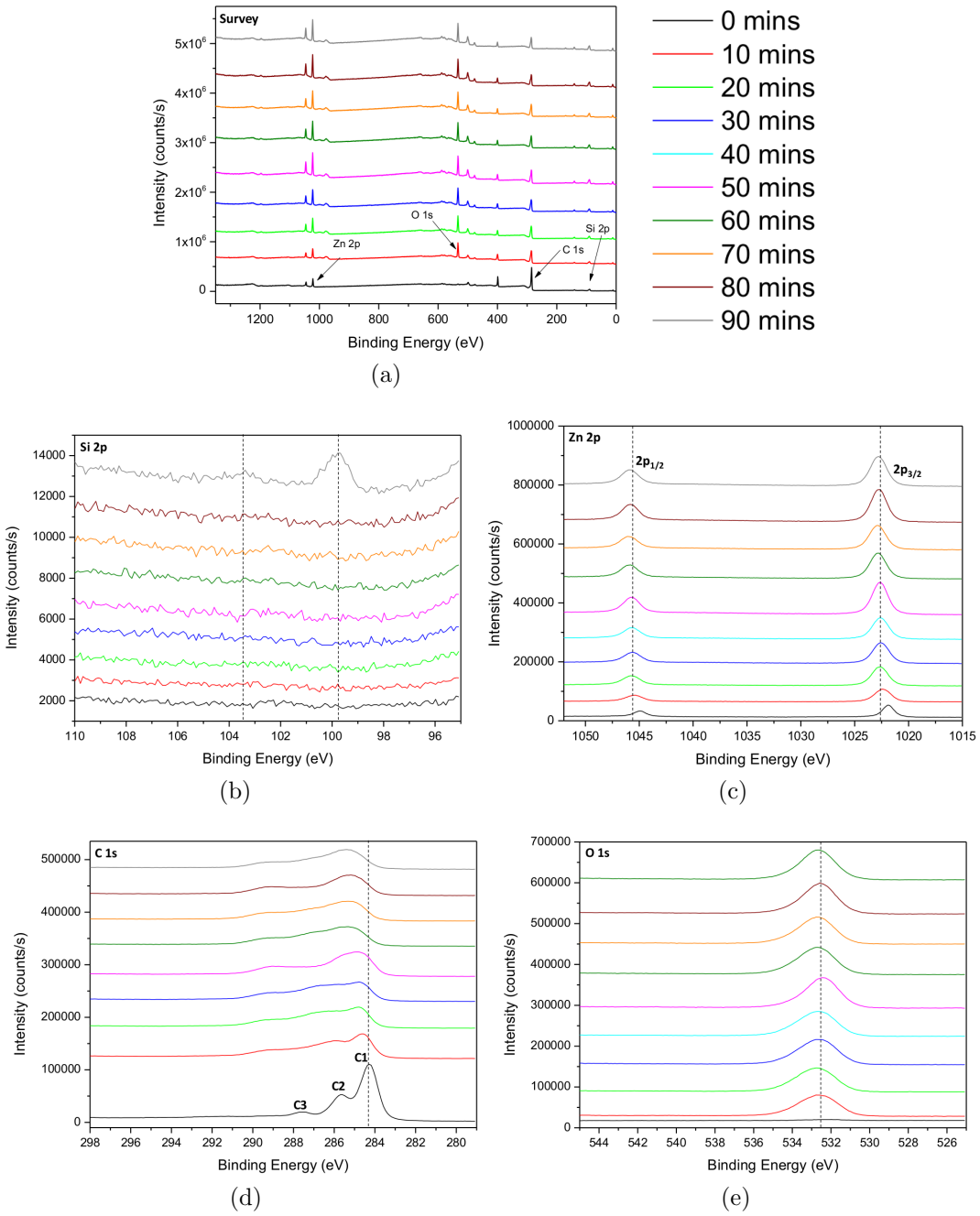

Figure 3.36: XPS spectra of UV treated ZnPc for (a) survey, (b) silicon, (c) zinc, (d) carbon and (e) oxygen at 10 minute intervals. The intensities are plotted as measured and are offset for presentation purposes

The spectra for Zn 2p binding energies (figure 3.36c) show a gradual increase in intensity for both the Zn $2p_{1/2}$ and Zn $2p_{3/2}$ peaks which may be explained by the removal of organic fragments that takes place during the UV process as zinc oxide is formed, resulting in a higher percentage composition for zinc. There is a slight shift of both peaks to a higher binding energy at 10 minutes irradiation with the position maintained throughout the remainder of the

samples. The energy separation between the Zn $2p_{1/2}$ and Zn $2p_{3/2}$ peaks remains constant throughout.

The results for carbon 1s initially repeat the results of etching a ZnPc film (figure 3.17) as there is a loss of resolution between carbon peaks arising from aromatic carbons and those bonded to nitrogen atoms (figure 3.36d). Furthermore, there is a shift of the highest peak from the original position of 284.3 eV to higher binding energies corresponding to a shift from aromatic bonds to aliphatic bonds. As the aromatic bonds are lost, the number of sp^2 hybridized orbitals decreases and sp^3 hybridised orbitals form which result in an increase of binding energy. Once the aromatic bonds break, whether initiated by photon or excited oxygen species, the reaction proceeds to the carbon-nitrogen bonds which had been identified in the as-deposited film at 285.7 eV (figure 3.16). After 10 minutes of irradiation, the carbon 1s peak has shifted to 284.6 eV, after 40 minutes, 284.8 eV and by 90 minutes to 285.4 eV. This gradual shift to higher binding energies and the change in the shape of the spectrum from three easily distinguished peaks to broader peaks less easily resolved would be a result of breaking of aromatic carbon bonds prior to attack on the pyrollic carbon bonds. This, together with information about molecular orientation obtained from XRD measurements gives some insight into the manner by which UV degradation takes place.

The oxygen 1s spectra show a large initial increase in intensity from 0 to 10 minutes as oxygen is incorporated into the film followed by further gradual increase with very little variation in peak position (figure 3.36e). There is a slight deviation to lower binding energies at 50 minutes but this is not retained through the remaining spectra and may therefore be due to a mishandled sample as the consistency of Zn 2p peaks eliminates the possibility of a systematic shift. The final binding energy is 532.6 eV. Binding energies involving oxygen have been reported at 535 ± 1 eV for water vapour, 533 ± 1 eV for C=O bonds [135] and 531 ± 1 eV for zinc oxide crystals [133] (table 3.1) thus it is not entirely clear in which form oxygen exists although water vapour can be dismissed. It is likely that oxygen exists in the form of both carbonyl groups and zinc oxide. From the survey spectra, the final Zn:O atomic ratio is 1/2, confirming that oxygen cannot be present solely in the form of zinc oxide. Yields of ZnO^+ ions from secondary ion mass spectrometry will be useful in determining whether zinc oxide has formed.

Zinc Tetraphenylporphyrin Following UV Treatment

XPS data for ZnTPP are shown in figure 3.37 for irradiation times of 0, 30, 60, 75, 90, 105, 120, 150 and 220 minutes with relevant peaks indicated in the survey spectra in addition to individual XPS spectra.

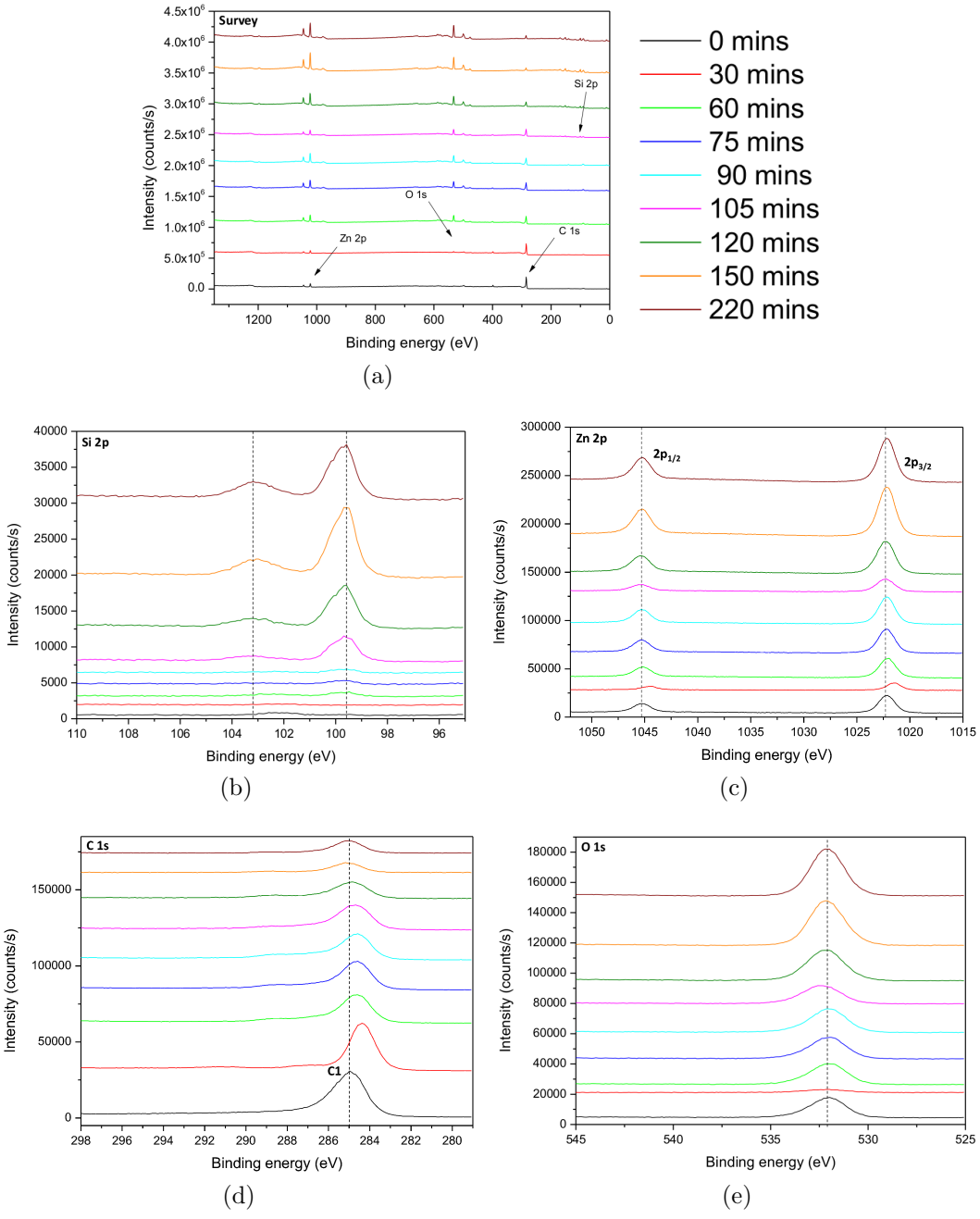

Figure 3.37: XPS spectra of UV treated ZnTPP for (a) survey, (b) silicon, (c) zinc, (d) carbon and (e) oxygen. The intensities are plotted as measured and are offset for presentation purposes

As with ZnPc, there is negligible silicon detected initially (figure 3.37b). After 120 minutes,

however, sufficient degradation has taken place to expose the substrate, whereas silicon was observed at 90 minutes in ZnPc. The Si 2p peak increases in intensity as further UV irradiation takes place. There is a significant peak at 103.1 eV in the spectra which are taken after 120 minutes, in contrast to ZnPc where a peak was only just visible at full degradation of the film. As UV treatment was carried out with ZnTPP for over twice the duration with ZnPc, once the substrate was exposed, there was an extended period in which the silicon could form its oxide which would produce a peak in a similar position [141].

The spectra for Zn 2p binding energies indicate an increasing percentage composition of zinc with no deviation in peak position as for ZnPc, with the exception of the sample exposed for 30 minutes. The peaks were shifted to lower binding energies for this sample from 1045.2 to 1044.5 eV and 1022.2 to 1021.5 eV, suggesting an error in recording the spectrum or a shift due to handling techniques as the difference in binding energies between the Zn $2p_{1/2}$ and Zn $2p_{3/2}$ peak was constant. As will be seen below, the 30 minute sample produced anomalous results for oxygen and should be disregarded as results suggest contamination of the surface.

The carbon spectra differ from ZnPc, mainly due to the ratios of peaks C2:C1 seen in the as-deposited films (figures 3.16,3.18). Even if the 30 minute sample is disregarded, there is a slight shift of the peak value to lower binding energies as the reaction time increases. As carbon is removed from the surface, the intensity decreases and the peak broadens towards higher energies. The normalised carbon 1s spectra for ZnTPP have been superimposed to allow further interpretation and are shown alongside those for ZnPc (figure 3.38).

With increasing UV irradiation, we can see more clearly that in the case of ZnPc, as the intensity of peak C1 decreases, there is a shift from 284.3 eV to higher binding energies, accompanied by increasing prominence of C2 (figure 3.38a). This agrees with the suggestion that aromatic carbon bonds are the first to react. What needs further explanation is the appearance of a peak, C4, in the region of 289.3 eV and a shoulder, C5, next to C2 at 286.6 eV. The difference between sp^2 and sp^3 bond energies is in the region of 0.9 eV [142] for amorphous carbon which suggests that a shift of aromatic to aliphatic bonds is responsible for the change in peak shape and the appearance of shoulder C5 as a result of damage to pyrollic carbon bonds not aromatic

bonds. The sp^3 bonds which would result from the peak, C1, would be expected to appear at approximately 285 eV and would therefore be difficult to distinguish from the spectra due to the presence of a satellite peak for C1 and the peak C2. However, peak C4 does not fall within the ranges for these bond energies. As it is possible that oxygen has reacted with carbon, evidence of this should also be sought in the spectra. Carbon 1s peaks have been reported at 286.7 eV for C-O bonds, 288.4 eV for C=O bonds and 289.7 eV for O-C-O bonds [143]. The latter of these corresponds most closely to the peak C4 at 289.3 eV.

Similarly for ZnTPP, the peak, C1, decreases in intensity, shifting from 284.3 eV to a higher binding energy of approximately 285 eV (figure 3.37d), with the appearance of a distinct peak, C4, at 288.7 eV marked in the normalised spectra for ZnTPP (figure 3.38b). The satellite for C1 appeared at 286.4 eV in as-deposited film but its presence here is obscured by broadening of the main peak which may be due to the shift from aromatic to aliphatic bonds as for ZnPc. Peak C4 may be due to either C=O bonds of energy 288.4 eV or O-C-O bonds with energy 289.7 eV [143]. Of these, the former, C=O bonds, seem more likely.

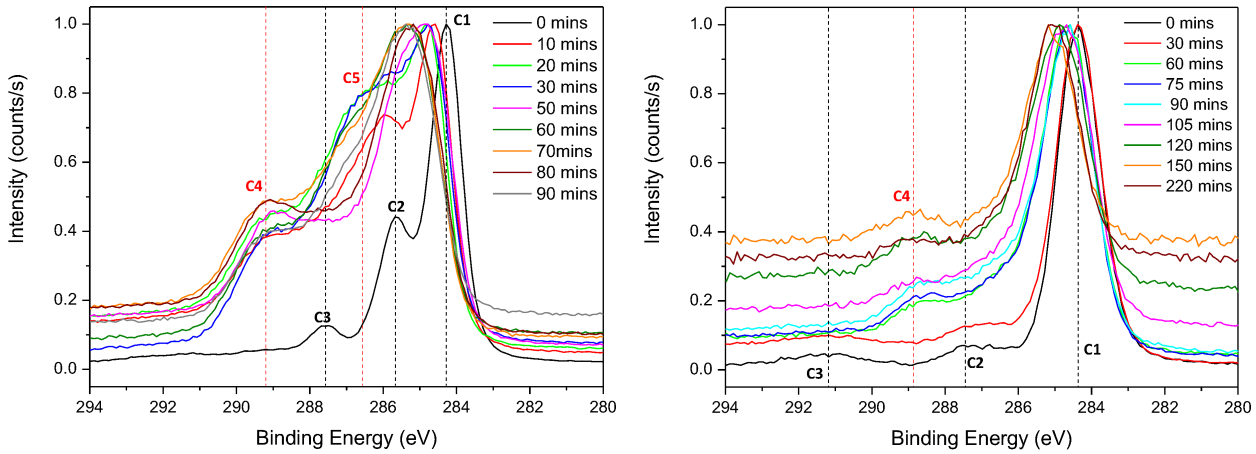

(a) (b)

Figure 3.38: Normalised XPS carbon 1s spectra superimposed for (a) ZnPc and (b) ZnTPP with peaks for as-deposited film and new peaks marked in black and red respectively

Finally, the oxygen 1s spectra for ZnTPP (figure 3.37e) exhibit peaks at approximately 532 eV, increasing in intensity as UV treatment progresses. The peaks are symmetrical and remain at the same binding energy with no perceptible broadening, with the exception of the sample for 30 minutes which exhibited an intensity lower than spectra taken after 0 and 60 minutes. As

mentioned earlier when analysing the results for zinc, this sample produced spectra which do not follow the trends shown by all other spectra and should be disregarded. Comparison with bond energies for water vapour (535 ± 1 eV), C=O bonds (533 ± 1 eV) and zinc oxide crystals (531 ± 1 eV) [135] (table 3.1) leads to the conclusion that oxygen may be present either in combination with zinc as zinc oxide or with carbon, with the peak arising from a C=O bond, as for ZnPc. Evidence of zinc oxide will be sought in SIMS data as significant detection of ZnO^+ ions will only occur beyond that produced by beam interaction if zinc oxide has indeed formed.

3.3.5 SIMS Depth Profiles

SIMS depth profiles were taken of UV treated films as for as-deposited films, using an O_2^+ primary sputter beam and a Bi_3^+ analysis beam with the same area parameters as in section 3.2.5.

Zinc Phthalocyanine Following UV Treatment

Figure 3.39 shows the SIMS depth profile for a ZnPc film irradiated for 90 minutes. Since the film homogeneity can no longer be relied upon and its composition is unknown, it would be meaningless to attempt a determination of sputter rate to show the variation of ion intensity with depth. Although the sputter rate cannot be quantified, the depth profile for fully reacted ZnPc does still give a very useful indication of the position of ions relative to depth within the film (figure 3.39). It is noteworthy that there is a high intensity of silicon from the outset suggesting that the substrate has been exposed through the development of pinholes as the UV process removes organic fragments from the film. This is consistent with XPS data showing the appearance of a silicon peak after 90 minutes of exposure and makes determination of the film/substrate interface difficult once the film is fully degraded. Silicon detection is accompanied by zinc ions at an intensity of over 10000 counts/s, a factor of five times higher than that for as-deposited film (figure 3.19). This represents a high concentration of zinc at the surface, a result of carbon and nitrogen removal with some increase in the zinc ion intensity due to enhancement

by the use of an oxygen primary beam in a metal oxide environment. In further evidence of material removal, the carbon intensity has dropped from 2000 to 700 counts/s although a further decrease to 500 counts/s at 21s implies that some ZnPc may remain unreacted on the substrate which is in agreement with the non-zero absorption seen in the UV-visible absorption spectrum after 90 minutes (figure 3.30a). The most significant change is the increase in ZnO^+ intensity from less than 10 counts/s to over 100. ZnO^+ ions present in as-deposited film were the product of sample-beam interaction and the levels of zinc oxide ions detected here far outweigh that which would therefore be attributable to interaction with the O_2^+ beam, confirming the formation of zinc oxide through the UV process.

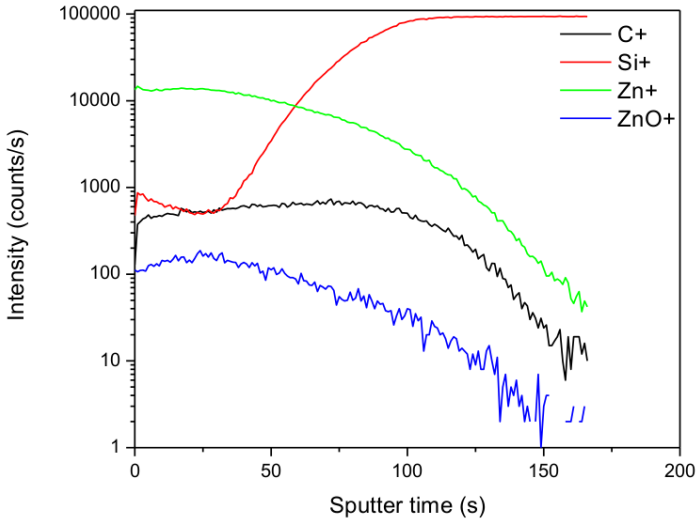

Figure 3.39: SIMS depth profile of 100 nm ZnPc after 90 minutes of UV treatment

Zinc Tetraphenylporphyrin Following UV Treatment

For comparison with ZnPc, the depth profile of ZnTPP after 105 minutes was chosen as XPS results indicted that the silicon substrate was detected from the outset at 90 minutes in ZnPc and 105 minutes in ZnTPP (figure 3.40).

As the concentration of zinc in ZnTPP is less than for ZnPc, it is expected that the yield for zinc ions would be lower in ZnTPP and the fall-off of Zn^+ intensity, beginning at 9000 counts/s once equilibrium is reached, does indeed show this, dropping to almost below 10 counts/s by 125s of sputter time, whereas the intensity of zinc ions in ZnPc is still at over 700 counts/s at

125s (figure 3.39). The intensity of ZnO^+ ions in as-deposited ZnTPP was below 5 counts/s (figure 3.20) and has risen to over 200 counts/s at the surface of irradiated film but drops rapidly to below 10 counts/s by 80s. Higher levels of zinc oxide ions were maintained in ZnPc until 150s.

The intensity of carbon was 1000 counts/s throughout the depth of as-deposited film and although carbon ions are still present on the surface after irradiation, the intensity has dropped very slightly to just under 1000 counts/s, rapidly decreasing to zero by 90s, so although the substrate has been reached during irradiation, all organic material has not been removed. The intensity of ZnO^+ ions has an initial value of 900 counts/s. As there was no zinc oxide detected in as-deposited film, this represents the formation of zinc oxide through UV exposure.

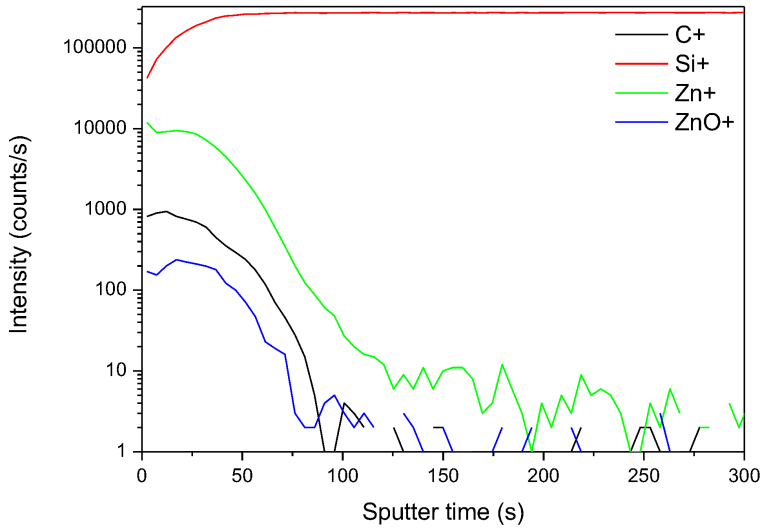

Figure 3.40: SIMS depth profile of 100 nm ZnTPP after 105 minutes of UV treatment

For further comparison between ZnPc and ZnTPP, the depth profiles were integrated to determine the total ion yield and are presented in table 3.3 where the zinc ion yield has been held constant at 1000 counts as no loss of zinc was anticipated. The total yield of C^+ ions decreases by a factor of 10 in ZnPc and by over a factor of 30 in ZnTPP from as-deposited films to 90 and 105 minutes respectively. As the UV process results in removal of organic fragments, a decrease was expected and the carbon content of ZnTPP is higher than that for ZnPc which results in a greater reduction of C^+ yield for ZnTPP. The increase in ZnO^+ yield confirms the formation of zinc oxide from both molecules with a higher increase in yield for ZnTPP. This

was not expected as the potential thickness of zinc oxide film which could be produced from 100 nm of precursor film is approximately 4 nm from ZnPc and 3 nm from ZnTPP. The discrepancy between expected and observed yields is likely to be a result of matrix effects or sample-beam interaction. As the composition of degraded films is not fully known and their homogeneity is not guaranteed, it is not possible to quantify any beam enhancements of positive ion yields.

Table 3.3: Total relative ion yield of ZnPc and ZnTPP before and after UV treatment with zinc ions normalised to 1000

	C^+	Zn^+	ZnO^+
ZnPc as-deposited	699	1000	5
ZnPc 90 minutes	68	1000	11
ZnTPP as-deposited	2800	1000	5
ZnTPP 105 minutes	88	1000	25

Despite the lack of information about film composition, Zn^+ and ZnO^+ ion yields of as-deposited films provide an upper limit for the ratio of Zn^+ to ZnO^+ ions, with the yields from a reference sample of zinc oxide deposited by pulsed laser deposition (PLD) giving a lower limit and indicating the degree of zinc oxide formation [144].

A sample of zinc oxide, 50 nm thick, was prepared using PLD by Dr Joseph Franklin of the Department of Materials at Imperial College London and a depth profile of the sample taken using the same conditions as for all other samples (figure 3.41). The zinc and zinc oxide ion intensities remain steady throughout the depth of the film, exhibiting a weak peak as the analysis beam reaches the substrate, as for ZnPc and ZnTPP. Silicon is detected at the outset but the intensity is below 100 counts/s, rising steeply as the substrate is reached. There is some surface contamination by carbon which is to be expected as the sample was not freshly made prior to depth profiling.

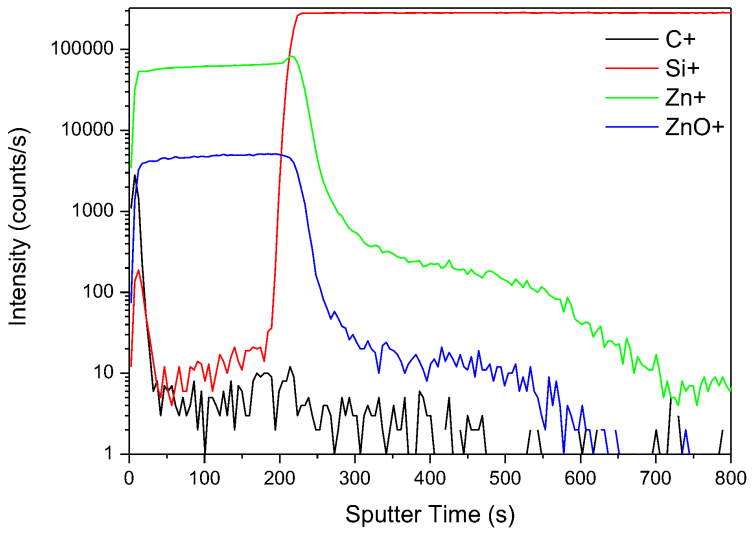

Figure 3.41: SIMS depth profile of 50 nm zinc oxide film produced by PLD

Ratios of Zn^+ ions to ZnO^+ ions in depth have been plotted for ZnPc and ZnTPP treated for 90 and 105 minutes respectively and for the reference sample of zinc oxide (figure 3.42).

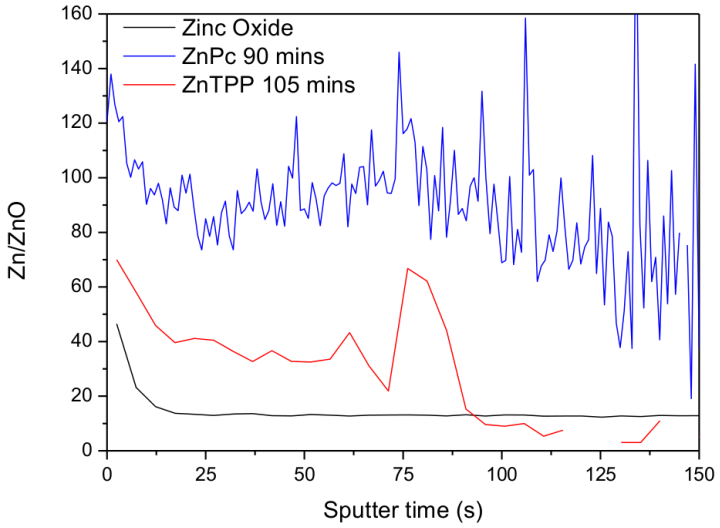

Figure 3.42: Ratio of zinc to zinc oxide ions against sputter time for a reference sample of zinc oxide, ZnPc treated for 90 minutes and ZnTPP treated for 105 minutes

In as-deposited films, the intensity of ZnO^+ ions is below 10 counts/s and often as low as zero, therefore, the Zn^+/ZnO^+ ratio was calculated from the average of its reciprocal through the depth of the film, giving 290 for ZnPc and 223 for ZnTPP, an upper limit for the Zn^+/ZnO^+ ratio which are similar to the ratios given by comparison of total ion yield in table 3.3. The ratio calculated from the average during the depth profile is likely to be more accurate as the

total ion yield does not include ions which have been driven into the substrate layer. Ratios for UV treated film are taken as averages through the regions where the ratio is most steady, approximately 15 - 60s. All ratios calculated thus are summarised in table 3.4, defining:

$$R_{ref} = \frac{[Zn^+]_{ref}}{[ZnO^+]_{ref}} \tag{3.5}$$

$$R_{PcUV} = \frac{[Zn^+]_{PcUV}}{[ZnO^+]_{UV}}, \qquad R_{TPPUV} = \frac{[Zn^+]_{TPPUV}}{[ZnO^+]_{TPPUV}} \tag{3.6}$$

$$R_{ZnPc} = \frac{[Zn^+]_{ZnPc}}{[ZnO^+]_{ZnPc}}, \qquad R_{ZnTPP} = \frac{[Zn^+]_{ZnTPP}}{[ZnO^+]_{ZnTPP}} \tag{3.7}$$

Table 3.4: Ratios of zinc to zinc oxide ions

Sample		Ratio $[Zn^+]/[ZnO^+]$
As deposited ZnPc	R_{ZnPc}	290
As deposited ZnTPP	R_{ZnTPP}	223
Zinc oxide reference sample	R_{ref}	14
ZnPc 90 mins UV	$R_{Pc\ UV}$	101
ZnTPP 105 mins UV	$R_{TPP\ UV}$	36

From figure 3.42, ratios of both ZnPc and ZnTPP are higher than that for the reference sample of ZnO, thereby demonstrating the presence of either unreacted precursor molecules or fragments thereof containing zinc.

Making the assumption that the lateral distribution of zinc and zinc oxide ions in the reference sample of zinc oxide is equal to that of zinc oxide formed from UV treated ZnPc and ZnTPP, it would be reasonable to expect that regions of ZnO formed from the precursor films would produce a ratio, Zn^+/ZnO^+, very close to the ratio, R_{ref} produced by the reference sample, neglecting any matrix effects caused by precursor fragments remaining in the environment of ZnO created. Making similar assumptions, the yields of ions from unreacted regions of ZnPc and ZnTPP would be expected to form ratios very close to those given by pristine films.

It is therefore possible to determine the proportion of zinc in the precursor film which has formed zinc oxide. Considering the intensities of zinc ions produced from as-deposited film and the resulting mixture of zinc oxide and unreacted precursor, if x is the proportion of zinc which forms zinc oxide, then for ZnPc:

$$[Zn^+]_{PcUV} = x[Zn^+]_{ZnO} + (1-x)[Zn^+]_{ZnPc}$$

and

$$x = \frac{[Zn^+]_{PcUV} - [Zn^+]_{ZnPc}}{[Zn^+]_{ZnO} - [Zn^+]_{ZnPc}} \tag{3.8}$$

From the assumptions made above regarding yields, equation 3.8 becomes:

$$x = \frac{[Zn^+]_{PcUV} - [Zn^+]_{ZnPc}}{R_{ref}[ZnO^+]_{ref} - [Zn^+]_{ZnPc}} \tag{3.9}$$

with a similar equation for ZnTPP. Using the total zinc ion yield within the first 10 second of UV treated films where the intensity is constant as $[Zn^+]_{Pc\ UV}$= 13600 and $[Zn^+]_{TPP\ UV}$= 9300 counts/s, the percentage of zinc converted to zinc oxide is

$$x_{ZnPc} = 19\%$$

$$x_{ZnTPP} = 14\%$$

These values are lower than the ratios given in table 3.4 would imply and are a consequence of the beam-enhanced yield of both zinc and zinc oxide from the reference sample. In particular, the yield of metal ions may increase by several orders of magnitude in the presence of an oxygen primary beam [109]. This would have the result of inflating the denominator in equation 3.9 and reducing the calculated yields as seen. The comparison of ratios remains a more useful

indication of the extent of oxide formation (table 3.4) and to establish that zinc oxide has been formed.

3.3.6 Identification of Zinc Oxide in Thick UV-Treated Precursor Films

Zinc oxide is known to be an absorber of ultraviolet light with transmission decreasing for wavelengths between 300 and 400 nm, whether the material is polycrystalline and deposited by spray pyrolysis [145] or sol-gel methods [146] or in the form of a single crystal [147] or nanoparticles [148]. As the yield of zinc oxide from ZnPc was not expected to exceed 4nm, a thicker film was employed to enable observation of UV absorption by zinc oxide. ZnPc films of 600 nm thickness were deposited by OMBD and exposed to UV treatment for 1000 minutes at the standard conditions described previously. As the films were very thick, transmission was close to zero over a wide range of wavelengths resulting in errors calculating the absorption, therefore, transmission spectra have been plotted for before and after 1000 minutes of UV treatment (figure 3.43)

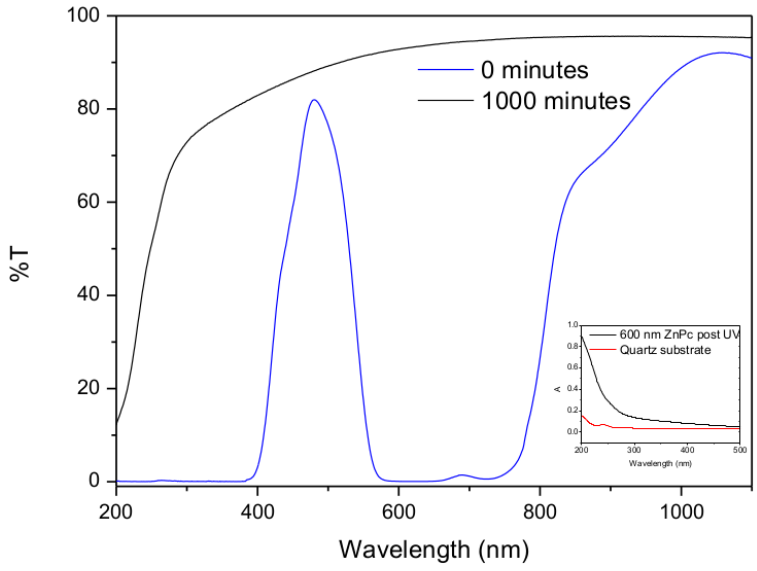

Figure 3.43: UV-visible transmission spectra of ZnPc before and after 1000 minutes of UV treatment. Inset shows absorbance for the UV treated film and the quartz substrate

The spectrum of as-deposited ZnPc shows high absorption in the regions occupied by the Soret

band and the Q band below 400 nm and between approximately 600 and 750 nm respectively (figure 3.43). After irradiation, there is very little absorption in the Q band but the transmission drops steeply from 300 nm which may be a result of absorption by zinc oxide. The inset shows the absorption for the UV treated film and the quartz substrate eliminating the possibility of substrate interference. With 600 nm of ZnPc precursor, it would be expected that approximately 24 nm of zinc oxide film would be formed if the precursor film reacted completely and no organic fragments remained. As the SIMS results demonstrate the formation of zinc oxide, it is likely that absorption in the UV region is due to the zinc oxide formed and the film remains transparent throughout the remainder of the spectrum. Zinc oxide was not detected by XRD, however and this is likely to be due to carbon residues and the minimum crystallite size required for detection.

3.4 Crystalline ZnTPP Deposited on KCl Substrates

The results using ZnPc and ZnTPP suggest that use of a crystalline precursor results in a higher rate of film degradation. To clarify the effect further, ZnTPP was grown on single crystal potassium chloride (KCl) substrates to form a crystalline film, reported to be a result of epitaxial alignment by the substrate [149]. Substrates were prepared as for previous films and 100 nm films of ZnTPP were deposited on silicon, quartz and KCl substrates. Following characterisation, the films were exposed to UV light for 120 minutes in standard conditions and properties re-examined. The results presented here for ZnTPP will not be directly comparable to those presented earlier in section 3.3, as the dose received from the xenon excimer lamp was significantly lower than in earlier sections due to a sudden reduction in performance, however, there is valuable information to be obtained by comparison of the influence of different substrates on the morphology and consequently on the rate of degradation as these samples were deposited, irradiated and characterised together.

Morphology

The amorphous films formed by ZnTPP have been characterised earlier in this chapter. AFM images of ZnTPP on KCl show crystalline films with an average crystallite diameter of approximately 45 nm. Crystallite size is non-uniform and the line profiles in figure 3.44b indicate hemispherical surfaces to the grains. In section 3.2.1, the roughness of ZnTPP was found to be 0.41 nm but here, the crystalline form has an increased roughness, $R_q = 7$ nm.

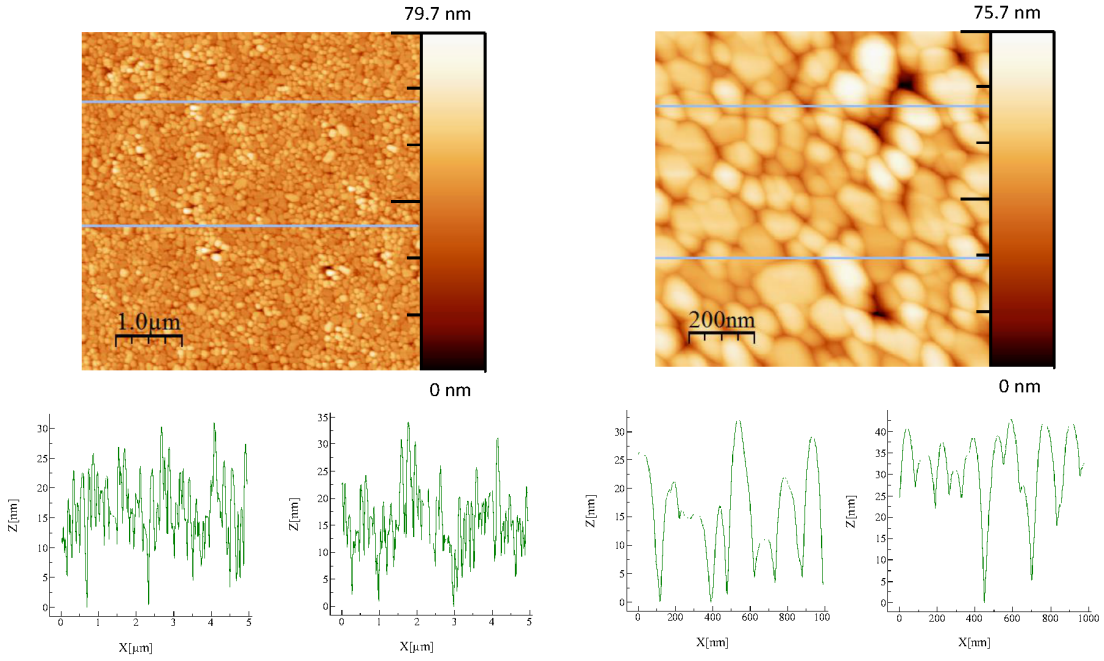

Figure 3.44: AFM images with line profiles of ZnTPP films grown on KCl substrates (a) 5 µm × 5 µm, roughness 7 nm, (b) 1 µm × 1 µm, roughness 9 nm

X-Ray Diffraction

X-ray diffractograms of ZnTPP deposited on KCl, the substrate and ZnTPP on KCl after 120 minutes of UV treatment were taken with a step size of 0.033 and a time/step of 300s (figure 3.45).

Peaks due to the substrate are clearly visible in the data for as-deposited film, although the peak present at 20.17° in the substrate has shifted slightly to 20.24° once the ZnTPP was deposited. The as-deposited film exhibits a peak at 20.42° which is close to the peak at

20.2° corresponding to the (12-2) plane seen in the powder diffraction pattern reported in the literature for the triclininc structure [4]. However, peaks are not likely to correspond directly to powder diffraction patterns due to influence of the KCl substrate resulting in a degree of epitaxial alignment [149]. The major peak in KCl at 25.6° has been shifted to the slightly higher angle of 25.7° after deposition of ZnTPP and remains at a higher angle once the film has been treated. This suggests that there may have been an instrumental error in the data.

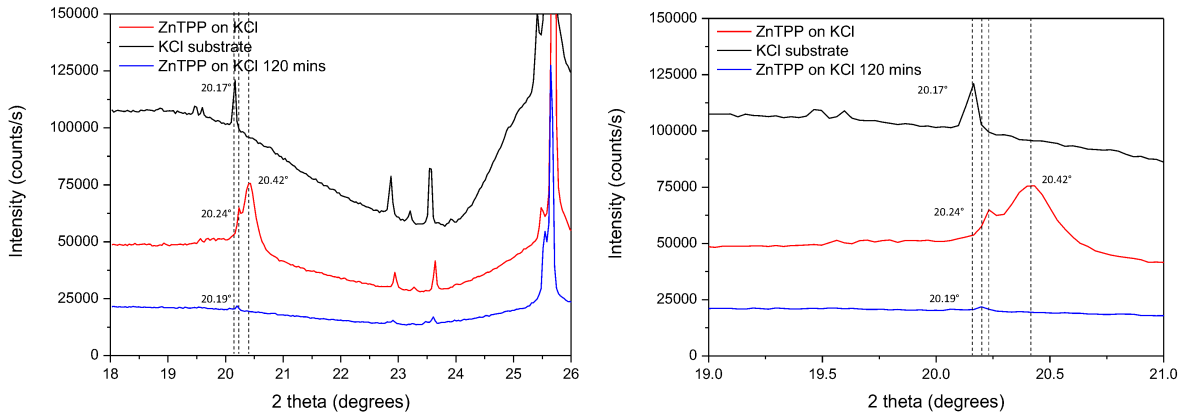

Figure 3.45: XRD scans for (a) ZnTPP on KCl as-deposited and after 120 minutes of UV treatment and the KCl substrate with (b) at a higher scale

Following UV treatment, the peak at 20.42° disappears, therefore, this peak can be attributed to ZnTPP. Furthermore, the peak seen at 20.24° has shifted to a slightly lower angle of 20.19° almost returning to the value given by the substrate. No new peaks were observed following UV treatment, therefore the XRD results showed a removal of crystalline ZnTPP within 120 minutes.

UV-Visible Absorption Spectra

Absorption spectra of ZnTPP deposited on glass, quartz and KCl substrates are shown with absorption spectra after 120 minutes of UV treatment (figure 3.46).

The absorption spectra showed a significant increase in degradation of ZnTPP on KCl compared to quartz with negligible reaction on glass. The percentage reduction in film thickness calculated

by integration of the Q band after correction for the substrate is summarised in table 3.5 with errors as calculated in section 3.2.3.

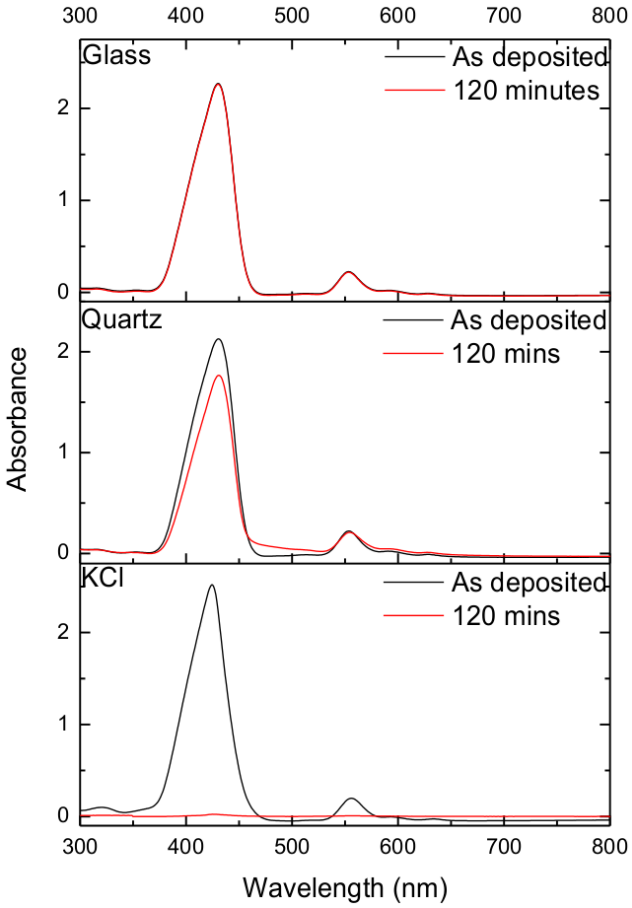

Figure 3.46: UV-visible absorption spectra of ZnTPP on glass, quartz and KCl substrates before and after UV irradiation

KCl substrates are minimally absorbing at 172 nm [150], however, they exhibit a reflectivity of approximately 15% in the same region [151] and this is likely to have some impact on the results. In comparison, fused quartz has a transmittance of approximately 88% and a reflectance of approximately 4% in the 172 nm region [152, 153].

Table 3.5: Percentage removal of ZnTPP film on quartz and KCl substrates

Substrate	Removal of ZnTPP film
Glass	$0 \pm 2\,\%$
Quartz	$25 \pm 1.5\,\%$
KCl	$90 \pm 1\,\%$

The XRD data demonstrate that very little crystalline ZnTPP remains after UV treatment when the films are grown on KCl (figure 3.45) and the absorption spectra confirm that degradation is increased by use of KCl substrates, compared to quartz and glass. The difference between the morphology of as-deposited films of ZnTPP on silicon (figure 3.5) and on KCl (figure 3.44) is likely to be a significant factor in the increase in reaction rate as ZnTPP forms amorphous films on non-interacting substrates such as silicon and glass [101] but crystalline films on KCl. As deposited films on silicon have a very low roughness of 0.41 nm with peak to trough distances of below 2 nm whereas films grown on KCl have a roughness of 9 nm with peak to trough distances of up to 30 nm, exceeding those of crystalline ZnPc. This difference in structure provides an additional route for oxygen assisted degradation of the film as the deep grain boundaries act as channels for diffusion of excited oxygen species.

From this, we can conclude that although there is degradation via photonic scission of bonds as shown by decreased absorption of irradiated film on quartz (where ZnTPP deposits as an amorphous film and is therefore subject initially to a greater effect from the UV-assisted mechanism), excited oxygen species greatly accelerate the reaction with the result that precursors forming crystalline films will degrade faster. In the specific case of KCl, a reflectivity of approximately 15% by the substrate may contribute to film degradation as ZnTPP is negligibly absorbing at 172 nm (section 3.1) and would allow much of the light to pass through. The substrate reflects a portion back into the film, however, 15% is not sufficient to explain the increase in film removal on KCl compared to quartz and the main factor must therefore be the crystalline morphology.

3.5 Conclusion

The use of two precursors forming films of contrasting morphology has been invaluable in determining the mechanism by which oxides form with UV light in the presence of oxygen. ZnPc forms crystalline films at room temperature in the α modification while ZnTPP forms amorphous films as confirmed by XRD data and AFM imaging. XRD data show a loss of

crystallinity in ZnPc as UV treatment progresses while AFM images reveal a gradual roughening of the surface from approximately 2 - 6 nm accompanied by an increase in average grain size from 9.3 - 11.8 nm and a reduction in the number of grains. Absorption spectra show that negligible ZnPc remains on the substrate after 90 minutes of irradiation and integration of the Q band demonstrated a linear film removal rate of 1.3 nm/minute, suggesting that the influence of oxygen assisted and photon assisted mechanisms remained constant throughout the 90 minutes. AFM images from ZnTPP films showed a dramatic change from a smooth, amorphous film with a roughness below 1 nm to a film with roughness of over 4 nm and the formation of grain-like features. Formation of grainy structures coincided with an acceleration in the rate of film degradation to 1.3 nm/minute between 75 - 90 minutes, as determined from absorption spectra, before returning to the previous, smooth film with an amorphous appearance and low initial roughness. As the grain like features were eroded, the rate of reaction decreased as shown by integration of the area under the Q band. Absorption spectroscopy detected no ZnTPP remaining after 150 minutes.

The photon assisted route is likely to affect only the regions of the film where the light is directly incident whereas the oxygen assisted reaction mechanism will also act within the depth of the film by diffusing between grain boundaries. As the morphology is largely retained throughout the degradation of ZnPc, these results suggest that both mechanisms act concurrently and the lack of change in morphology is reflected in the constant rate of film removal (figure 3.47a). In contrast, the initial rate with ZnTPP is much slower at 0.3 nm/minute, a consequence of the smooth surface of the film. At this point, the UV mechanism is likely to have the greatest impact and gradual degradation of the surface leads to roughening (figure 3.47b). Impurities and defects within the film may provide sites where oxygen species can have greater effect. This, in conjunction with the roughening caused by UV attack creates a grain-like structure by 7 - 90 minutes which allows further diffusion of oxygen within the film, resulting in the same rate of film removal seen in ZnPc. The rates are identical for both precursors at this point and suggest both mechanisms exert equal influence in both films.

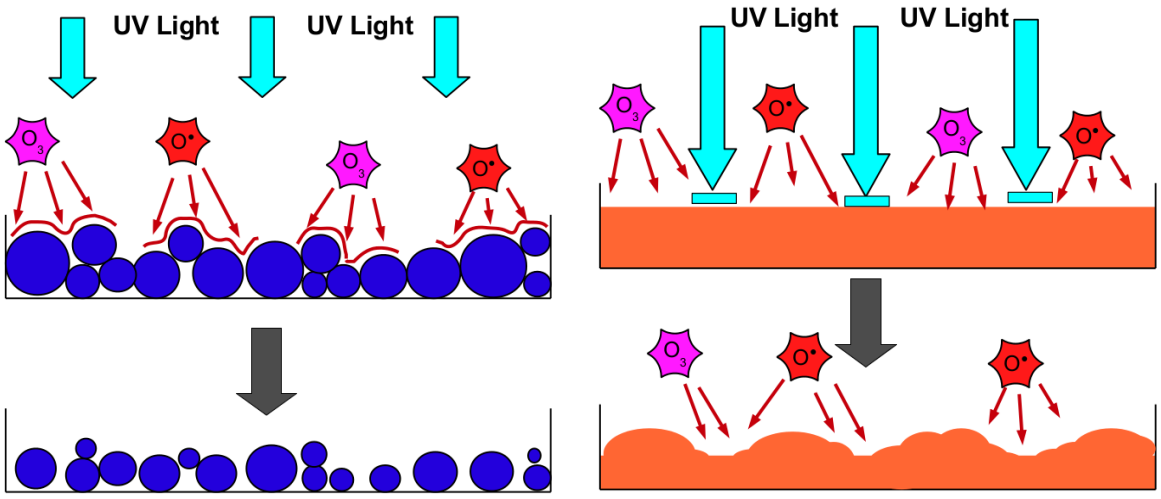

Figure 3.47: Schematic of action of UV assisted and oxygen assisted mechanisms in (a) ZnPc and (b) ZnTPP

This model is further validated by the near complete removal of crystalline ZnTPP film on KCl substrates and the significant amount of film remaining in ZnTPP films on quartz and glass substrates where ZnTPP forms amorphous films. It is clear that surface morphology and surface area are crucial in allowing the oxygen route to accelerate the reaction.

XPS studies of as-deposited precursors identified two C 1s peaks corresponding to aromatic and pyrollic carbons with accompanying satellite peaks. Spectra of treated films showed that aromatic carbon bonds were the first to be attacked, before those bonded to nitrogen atoms, as might be expected due to the location of aromatic carbons on the periphery of precursor molecules. Carbon and oxygen 1s spectra were instrumental in following the process and determining the incorporation of oxygen within the films. Together with SIMS results, the formation of zinc oxide has been established and the removal of the majority of organic fragments confirmed with some evidence of carbonyl and silicon dioxide formation. The presence of zinc oxide is further verified by the absorption in the UV region of a fully reacted thicker film of ZnPc.

Finally, the process required 90 minutes for full degradation of ZnPc, equivalent to a photon dose of 1.1×10^{20} photons/cm^2, to achieve a film containing zinc oxide, transparent in the visible region. ZnTPP required 150 minutes, equivalent to a photon dose of 1.9×10^{20} photons/cm^2.

Chapter 4

ZnPc and PTCDA as a Model for a Multi-layer Organic System

4.1 Introduction

Due to their versatility, metal phthalocyanines employed as active components contribute to a wide portfolio of organic electronic devices. Their charge transport properties make them particularly useful in organic thin film transistors (OFETs) [86], while their photoactivity makes them ideal candidates for use in solar cells where they form the benchmark small molecule photovoltaic heterojunctions with fullerenes such as C_{60} as an acceptor [154] and as hole transport layers in organic light emitting diodes (OLEDs) [85]. More recently, the magnetic properties of phthalocyanine complexes such as those of terbium and iron are being employed in the development of organic spintronic devices [87,155,156]. However, if the UV process is to prove a useful method for production of functional oxide films from metal phthalocyanines, it is important to determine the effect UV light and oxygen might have on any neighbouring organic layers within an organic electronic device.

Perylenetetracarboxylic-3,4,9,10-dianhydride (PTCDA) is a planar, polycyclic aromatic molecule with an extended π system which results in a regular stacking arrangement with the molecules lying nearly parallel to the substrate (figure 4.1). The extended π system results in inter-

molecular $\pi - \pi$ interactions responsible for a high anisotropic mobility in the region of 1.4 cm^2/Vs [157], leading to the use of PTCDA as an acceptor in conjunction with ZnPc as the donor in solar cells [103] and as a hole injection layer in OLEDs [104]. Its characteristics have has been extensively reported in the literature [158], making it an ideal molecule for investigations of thin films and in particular, for the effect of UV light and oxygen when forming oxide films.

On non-interacting substrates, PTCDA crystallises into its α or β polymorph, both monoclinic and falling within the $P2_1/c$ space group [158]. The molecules lie in the (10-2) plane with an intermolecular distance of 3.22 or 3.25Å for the α and β modifications respectively [106, 159] (figure 4.1).

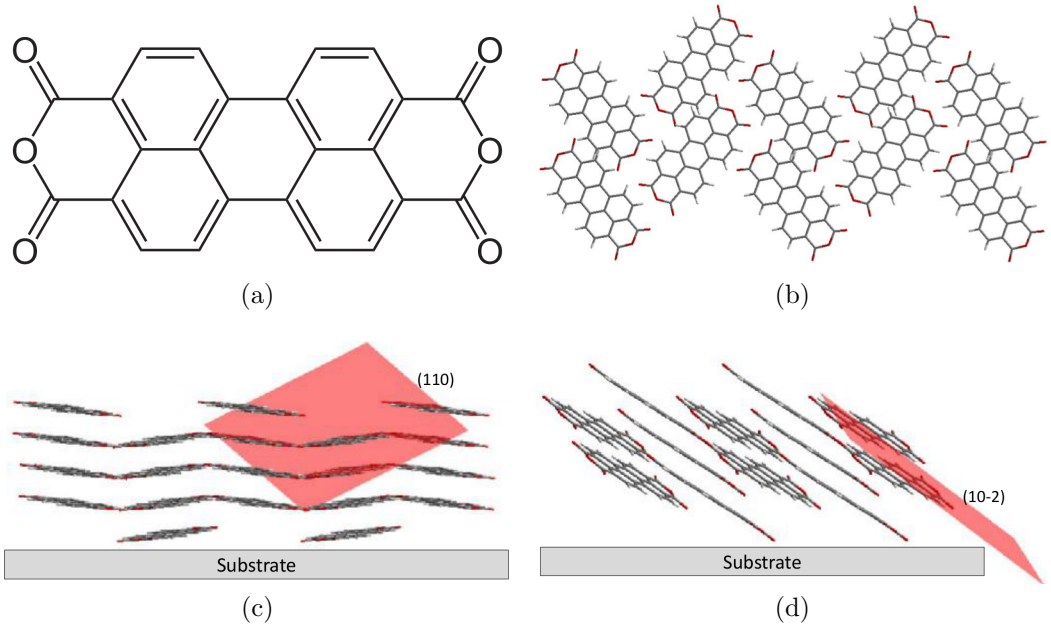

Figure 4.1: (a) Molecular structure of PTCDA, (b) top view of β-PTCDA with the (10-2) plane parallel to the substrate, (c) side view of β-PTCDA with the (10-2) plane parallel to the substrate with the (110) plane indicated in red and (d) side view of β-PTCDA with the (110) plane parallel to the substrate and the (10-2) indicated in red, according to crystallographic data reported in the literature [5, 6]

PTCDA grown by OMBD deposits with molecules lying flat, producing an X-ray diffraction peak at 27.2°, corresponding to the (10-2) plane but further deposition beyond 70 nm has shown the films also adopt a different orientation in the (110) plane resulting in an additional peak at 25.2° [160] (figure 4.1). This well-defined structure enables easy determination of the effect

of UV and oxygen assisted metal oxide film formation from ZnPc on a neighbouring layer of PTCDA.

In addition to easily identified X-ray diffraction peaks, the electronic absorption spectrum of PTCDA is well documented [16] with absorption regions largely separate from those of ZnPc, resulting in a reddish appearance for PTCDA whereas ZnPc appears blue, providing another method for observation of the effect of UV light and oxygen.

Finally, it is well-known that an initial layer of at least 15 nm of PTCDA will result in structural templating of subsequently deposited layers of phthalocyanine molecules, aligning the molecular plane parallel to the substrate and extending beyond a thickness of 300 nm (figure 4.2b) [161]. While ZnPc usually deposits with molecules nearly perpendicular to poorly interacting substrates such as glass or oxidised silicon, templating by PTCDA results in a complete change in orientation of approximately 90°, resulting in the observation of X-ray diffraction peaks at $2\theta = 26.6°$ and $27.6°$ corresponding to the (01-2) and (11-2) planes in the case of CuPc [19,160]. This effect has also been reported when depositing ZnPc on copper iodide substrates, resulting in the same orientations (figure 4.2a) [162]. Films of ZnPc on PTCDA will therefore also establish the effect of molecular orientation on oxide formation, information vital for application of the UV process in organic electronic devices where use may be made of the anisotropic mobility of molecules such as phthalocyanines by modification of molecular orientation, for example, in OFETs where a high conductivity parallel to the substrate is required and in OPV devices where conductivity orthogonal to the substrate is beneficial. If a subsequent layer of ZnPc is then subjected to UV treatment to form an oxide film, orientation may have an impact.

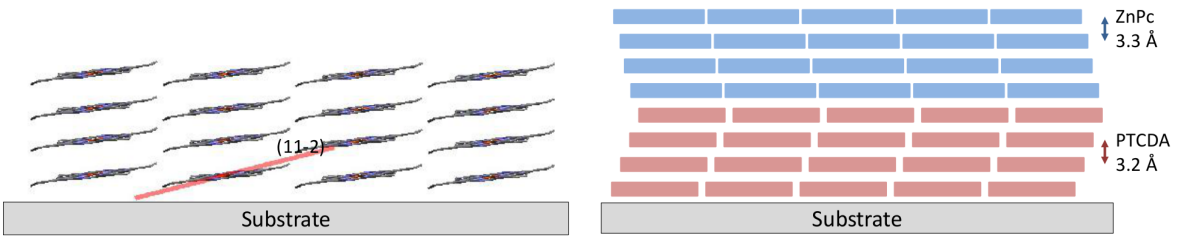

(a) (b)

Figure 4.2: (a) ZnPc deposited with the (01-2) plane parallel to the substrate with the (11-2) plane indicated in red and (b) schematic of templated ZnPc on PTCDA. Crystallographic data taken from the literature [3,6]

In order to establish the optimum combination of film thicknesses which would allow determination of the effect of UV light and oxygen on neighbouring organic layers and the effect of orientation on oxide formation, 20 nm and 100 nm films of ZnPc, PTCDA and permutations thereof were characterised by AFM, XRD and UV-visible absorption spectroscopy. As 100 nm films of ZnPc had been thoroughly investigated in chapter 3, 100 nm of ZnPc on PTCDA was considered the useful choice to allow comparison.

4.2 Characterisation of ZnPc and PTCDA Films

PTCDA and ZnPc were deposited individually as films of 20 and 100 nm and as heterostructures with the first layer either 20 or 100 nm of PTCDA. The X-ray diffraction data, AFM images and UV-visible absorption spectra were compared to determine the most useful combination.

4.2.1 Morphology - Atomic Force Microscopy

Topographical images were recorded using atomic force microscopy. All films had formed grains and showed little variation in morphology (figure 4.3).

ZnPc films grown on 20 nm PTCDA appeared to form smaller grains than those grown on 100 nm PTCDA and had a lower surface roughness (table 4.1). As these results will be compared to those from ZnPc films, it is interesting to note that all PTCDA and combined films appear less rough than the as-deposited ZnPc films (section 3.2.1), although the difference is not significant at 1.5 nm.

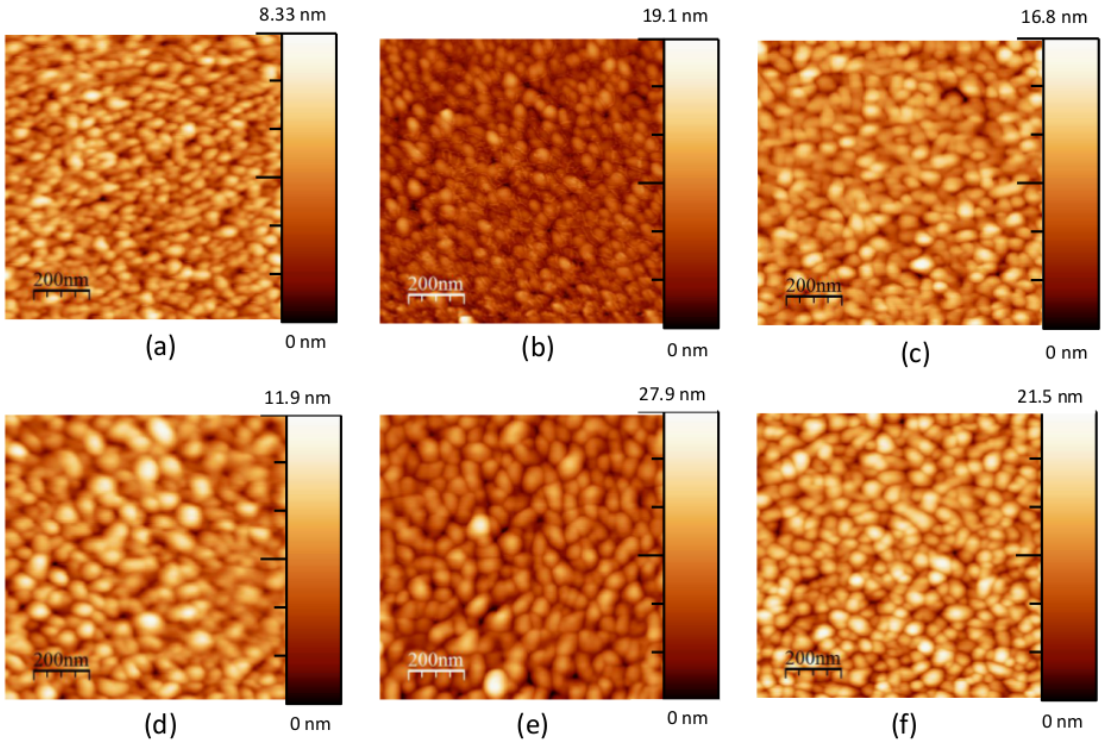

Figure 4.3: AFM images of (a) 20 nm PTCDA, (b) 20 nm ZnPc on 20 nm PTCDA, (c) 100 nm ZnPc on 20 nm PTCDA, (d) 100 nm PTCDA, (e) 20 nm ZnPc on 100 nm PTCDA and (f) 100 nm ZnPc on 100 nm PTCDA. All films were deposited on silicon.

Table 4.1: RMS Roughness of ZnPc and PTCDA films (nm)

20 nm PTCDA	20 nm ZnPc on 20 nm PTCDA	100 nm ZnPc on 20 nm PTCDA
1.04	1.60	2.12
100 nm PTCDA	20 nm ZnPc on 100 nm PTCDA	100 nm ZnPc on 100 nm PTCDA
1.63	3.19	3.11

4.2.2 X-Ray Diffraction

PTCDA Films

XRD scans of the 100 nm PTCDA film yielded a peak at $2\theta = 27.7°$ (figure 4.4), corresponding to the (10-2) plane reported in the literature for the β phase [6]. The 20 nm film, however, has only a very small peak at the same angle. A peak for PTCDA on glass has been reported at 25.5°,

arising from the (110) plane [107], however, there is no evidence here. It has been suggested that the α modification of PTCDA forms in lower thickness films and at higher substrate temperatures and that α and β PTCDA give rise to peaks at 27.6° and 27.5° respectively [163]. From the data shown, it is difficult to determine which phase the film has adopted although powder diffraction patterns from published crystallographic data suggest the film has deposited in the β phase [6]. However, both phases are quite similar, forming films with the (10-2) plane parallel to the substrate with equivalent orientations (figure 4.1b), it is likely to make very little difference to the templating of ZnPc or to the effect of UV light and oxygen.

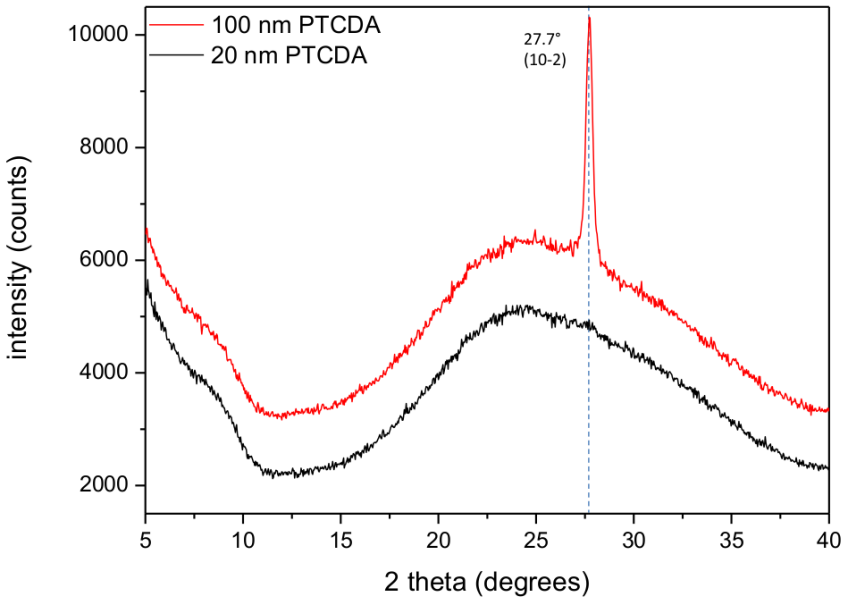

Figure 4.4: XRD scans of 20 nm and 100 nm PTCDA films on glass. Indexation based on [6]

20 nm ZnPc Deposited on PTCDA

Deposition of ZnPc on PTCDA results in the presence of diffraction peaks in the 25 - 30° region (figure 4.5), contrary to deposition on silicon and glass where peaks are observed at 7.08° (figures 3.6a and 3.27). These new peaks are most clearly seen in the sample with 100 nm ZnPc where diffraction is observed at 26.7° and 27.7°, in agreement with peaks seen for CuPc deposited in the α phase on PTCDA corresponding to the (01-2) and (11-2) planes respectively [19]. The presence of those peaks and the absence of peaks at lower angles indicates strong texturing with the ZnPc planes at 9° and 7.5° with respect to the substrate [19]. In par-

ticular, although a 20 nm film of PTCDA alone does not result in crystallite sizes large enough to produce diffraction peaks, the strong texturing effect evident in the 20 nm structurally templated ZnPc film does form crystallites of sufficient size to produce a diffraction peak. The sample with 20 nm ZnPc on 20 nm PTCDA has a shoulder at 27.4° to the main peak at 27.9°. The main peak is likely to be due to the sum of intensities from the (11-2) plane of ZnPc and the (10-2) plane of PTCDA. The additional shoulder has previously been attributed to the β modification of PTCDA [163, 164] but more recent investigations confirm that the β modification produces the higher peak detected here at 27.9° with the α modification yielding a peak at a slightly lower angle [5, 6]. It is interesting to note that although a 20 nm film of PTCDA does not show a clear diffraction peak (figure 4.4), it is still effective as a structural template.

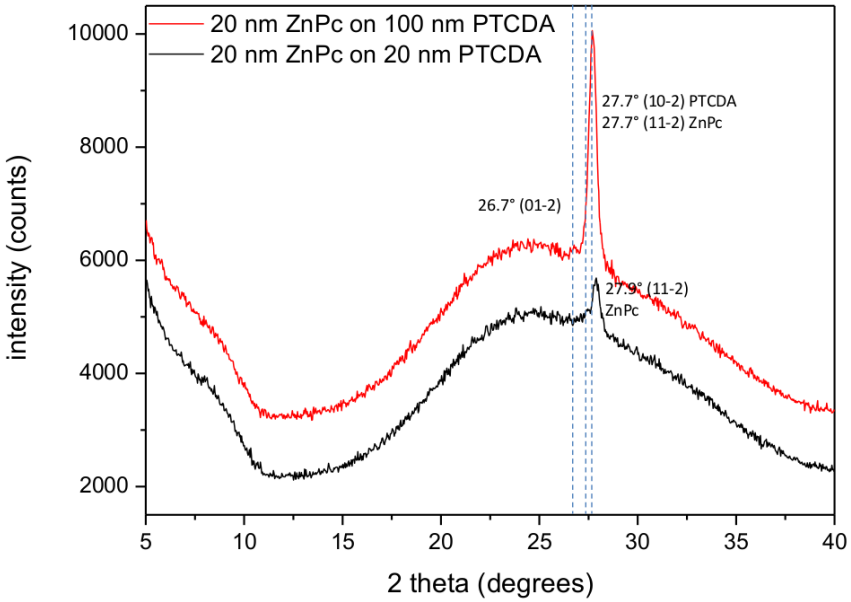

Figure 4.5: XRD scans of 20 nm ZnPc deposited on 20 and 100 nm PTCDA on glass. Indexation based on [6, 19]

100 nm ZnPc Deposited on PTCDA

Films of 100 nm ZnPc on 20 and 100 nm PTCDA show a number of differences to previous films (figure 4.6). The main peak at 27.9° in the 100 nm ZnPc on 100 nm PTCDA film has an intensity of approximately 130% of that for 100 nm PTCDA alone (figure 4.4) from which we can conclude that the peak is a sum of intensities from both the (10-2) plane of α-PTCDA and the (11-2) plane of α-ZnPc. This sample also produces a peak at 26.8° from the (01-2)

plane of templated α-ZnPc [19] and a new peak at 7.0° more commonly seen in non-templated ZnPc with diffraction from the (200) plane in the edge-on orientation [162]. This suggests that the templating effect may not have extended fully throughout the depth of ZnPc and is most likely a result of roughening of the PTCDA layer as it adopts the (110) orientation in addition to the (10-2) orientation as thickness increases (table 4.1) [107].

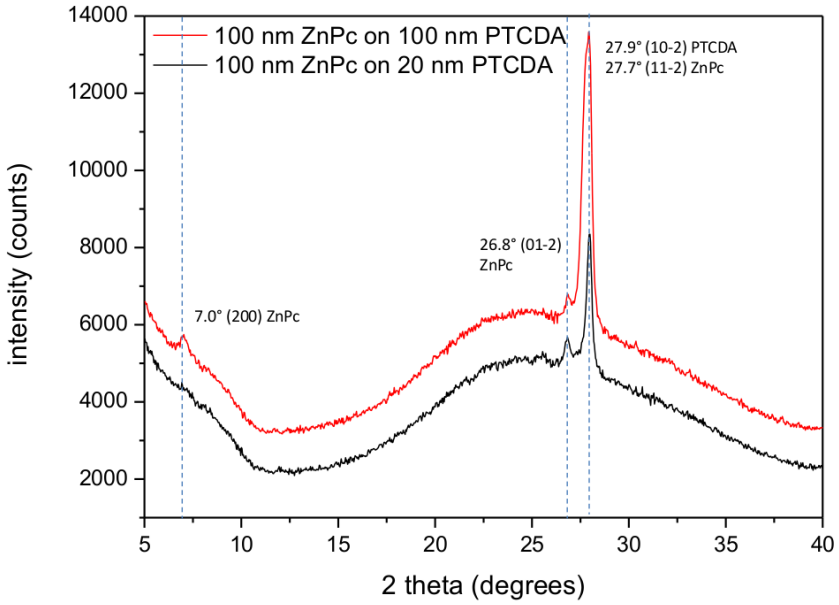

Figure 4.6: XRD scans of 100 nm ZnPc deposited on 20 and 100 nm PTCDA on glass. Indexation based on [6, 19]

From the XRD data for all films, it is clear that deposition of ZnPc on PTCDA does indeed have the effect of templating ZnPc molecules, orienting them parallel to the substrate. It is possible to monitor the removal of ZnPc film as irradiation with UV light progresses, however, it is not clear whether the peak at 27.7° may be used to determine when the PTCDA layer is affected. To provide some insight as to the contribution of PTCDA to this peak, films of 100 nm ZnPc on 20, 40 and 100 nm of PTCDA were compared.

100 nm ZnPc Deposited on 20, 40 and 100 nm PTCDA

Figure 4.7 shows the region between 24 - 30° where peaks due to the (01-2) and (11-2) planes of ZnPc and the (10-2) plane of β-PTCDA are easily seen. The ZnPc content of all films is 100 nm thus the increasing intensity and breadth of the peak at 27.9° can be attributed

to the increasing thickness of PTCDA. What is also apparent is an increasing asymmetry to the main peak with a shoulder on the lower angle side in the region of 27.7° due to the presence of the β modification of PTCDA. Peaks were therefore fitted with a Lorentzian profile following a removal of background intensity at 28.0°, 26.8° and 27.7° corresponding to angles for diffraction peaks produced by the (11-2) and (01-2) planes of ZnPc and the (10-2) plane of β-PTCDA respectively and intensities are displayed in table 4.2.

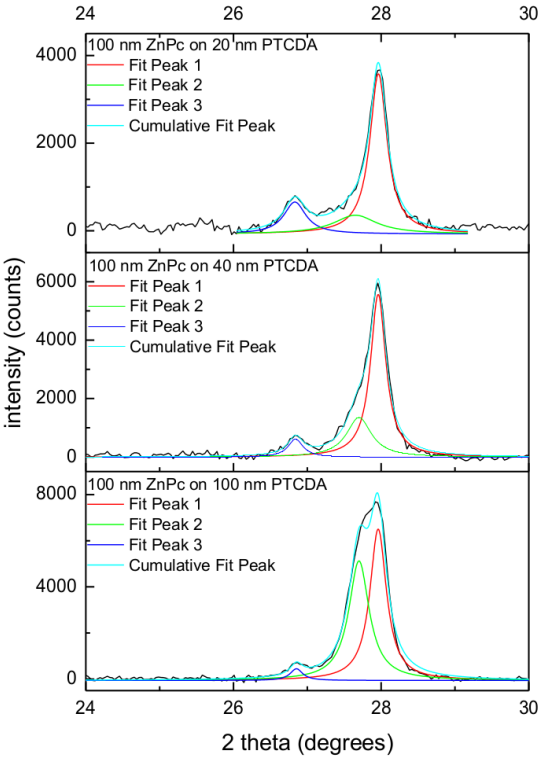

Figure 4.7: XRD scans of 100 nm ZnPc deposited on 20, 40 and 100 nm PTCDA on glass. Peak fitting using Lorentzian profiles.

Table 4.2: XRD peak intensities for films of 100 nm ZnPc on 20 nm PTCDA (100/20), 40 nm PTCDA (100/40) and 100 nm PTCDA (100/100) derived from peak fitting following removal of background intensity

Peak	2θ (deg)	100/20	100/40	100/100
1	28.0	1621 ± 41	2201 ± 44	2816 ± 67
2	27.7	478 ± 100	873 ± 60	2727 ± 77
3	26.8	415 ± 37	241 ± 27	165 ± 36

As expected, the intensity of peak 2 at 27.7° increases significantly with PTCDA thickness, whereas changes in intensities of the other two peaks is far less dramatic. The errors calculated

through fitting peaks, however, are not negligible. As the increase in the intensity of the main peak can only be caused by an increase in the thickness of PTCDA, comparison of intensities of peak 2 at 27.7° should correspond approximately to the change in PTCDA thickness. Similarly comparison between the intensities of peak 1, corresponding to the ZnPc (11-2) lattice plane for different samples should not vary significantly and neither should intensities of peak 3, corresponding to diffraction from the (01-2) plane in ZnPc. Ratios of peak intensities are summarised in table 4.3.

Table 4.3: Comparison of XRD peak intensities for films of 100 nm ZnPc on 20 nm PTCDA (100/20), 40 nm PTCDA (100/40) and 100 nm PTCDA (100/100) derived from peak fitting following removal of background intensity

Peak	2θ (deg)	(100/100)/ (100/20)	(100/100)/ (100/40)	(100/40)/ (100/20)
1	28.0	1.74 ± 0.06	1.28 ± 0.04	1.36 ± 0.04
2	27.7	6 ± 1	3.1 ± 0.2	1.8 ± 0.4
3	26.8	0.40 ± 0.09	0.7 ± 0.2	0.58 ± 0.08

The most relevant ratios here are those for peak 2 when comparing different thicknesses of film. It would be expected that the intensity of peak 2 for a film with 100 nm PTCDA would be approximately 5 times the intensity of that for a film with 20 nm PTCDA and this is indeed the case, with a ratio of 6 ± 1. Similarly films with 100 nm PTCDA and 40 nm PTCDA would be expected to yield a ratio of 2.5 which is close to the value of 3.1 ± 0.2 given in table 4.3. Finally, ratios of films with 40 nm and 20 nm PTCDA would yield a ratio of 2 and the value calculated is 1.8 ± 0.4. Peak 2 at 27.7° is indeed attributable to the diffraction from the (10-2) plane of β-PTCDA and comprises approximately $23 \pm 5\%$ of the total peak intensity of the main peak and diffraction from the (11-2) plane in ZnPc the remainder in films of 100 nm ZnPc on 20 nm PTCDA. Therefore, while the third peak at 26.8° may be used to identify when ZnPc has been fully degraded, the combined intensity of peaks 1 and 2 may only be used as a qualitative indicator of the presence of PTCDA once the ZnPc reaction nears completion.

From the XRD data, templating of ZnPc is achieved by a 20 nm layer of PTCDA and a 100 nm thick layer of ZnPc is easily detected by XRD at 26.7°, whereas 20 nm ZnPc produces a

peak of limited intensity. The peak at 27.7° may be used as indication of PTCDA remaining from which 100 nm ZnPc on 20 nm PTCDA is the sensible choice for the heterostructure. As the optical absorption regions of ZnPc and PTCDA only overlap slightly, electronic absorption spectroscopy will be extremely useful identifying the amount of film remaining during the UV process.

4.2.3 UV-Visible Absorption Spectroscopy

Electronic absorption spectra have been one of the key signatures for determining the relative influence of ultraviolet light and oxygen on oxide formation (chapter 3) and if appropriate, will also be employed here to evaluate the effect of the UV process on neighbouring organic layers.

Absorption spectra of 100 nm films of ZnPc have already been described in section 3.2.3. The absorption spectrum of 20 nm PTCDA on glass is presented in figure 4.8. Peaks at 361, 374, 484, 554 nm closely match reported values [16]. The highest wavelength peak at 554 nm corresponds to a transition by a charge transfer state, CT, due to aggregate states resulting in $\pi - \pi$ overlap between stacked molecules. While the peak itself is due exclusively to free charge transfer states, the long tail towards higher wavelengths is an indication of self-trapping of excitons caused by strong exciton-phonon coupling, an interaction between the exciton and the excited vibrational modes within a molecular crystal. The peak at 484 nm arises from the S1(0-2) transition from the first excited singlet state to a different vibronic state and the breadth of this band is due to transitions to several vibronic states ν_n [16]. Peaks at wavelengths below 400 nm correspond to transitions from deeper HOMO levels to the LUMO level or from the HOMO level to higher LUMO levels [165]. It is notable that there is minimal absorption above 600 nm.

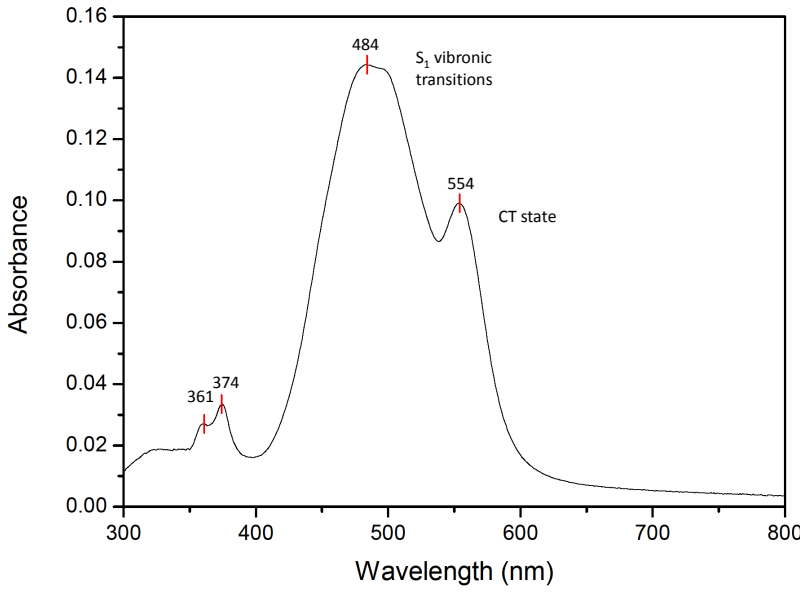

Figure 4.8: Absorption spectrum of 20 nm PTCDA on glass, corrected for substrate contribution

Absorption spectra of 20 nm PTCDA, 100 nm ZnPc and 100 nm ZnPc on 20 nm PTCDA have been plotted together to determine the value of absorption spectroscopy as a technique to measure the effect of the UV process on PTCDA (figure 4.9).

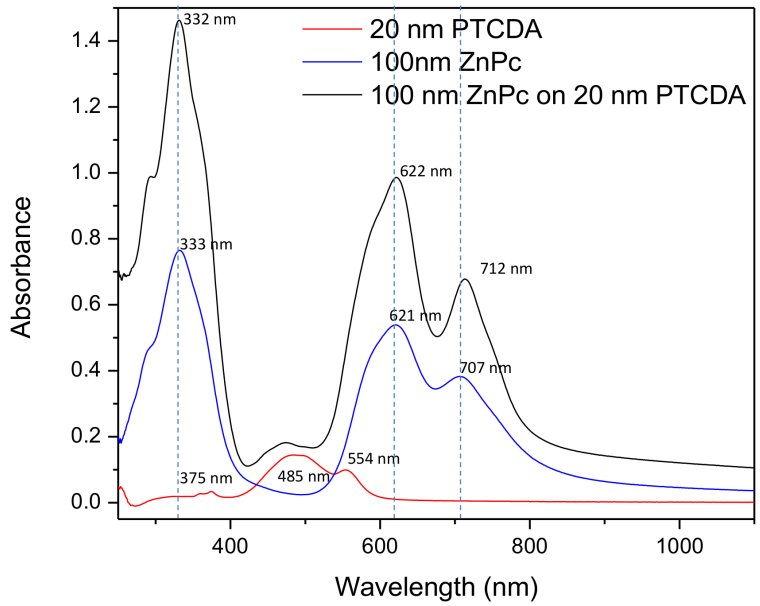

Figure 4.9: Absorption spectra of 20 nm PTCDA, 100 nm ZnPc and 100 nm ZnPc on 20 nm PTCDA on glass, corrected for substrate contribution

The spectrum for pure ZnPc is as measured in section 3.2.3, however, the peak at 707 nm attributed to $\pi - \pi*$ transitions shifts to a higher wavelength of 712 nm when deposited on

PTCDA, with no change in any higher energy peaks. This must be due to the change in orientation of stacking axis from parallel to normal to the substrate as PTCDA itself is non-absorbing in that region. This effect has also been observed in CuPc templated by PTCDA and attributed to an increase in the HOMO energy level, measured by ultra-violet photoelectron spectroscopy [166]. As an increased HOMO level results in a lower HOMO-LUMO energy difference, we can infer the same conclusion here, leading to a lower energy $\pi - \pi*$ transition and consequently an increase in the wavelength measured.

The highest wavelength peak at 707 nm in the absorption spectrum of ZnPc is considered representative of the monomer character of the film whereas the lower wavelength peak at 622 nm relates to aggregated molecules [167]. The Q band regions have been normalised to allow comparison of the structure of the ZnPc film when deposited alone and on PTCDA (figure 4.10) and show that the degree of aggregation has not decreased upon templating and has, in fact, increased slightly, suggesting that the films are more ordered, resulting in higher levels of intermolecular interactions, maintaining their one-dimensional stacking nature with a change in orientation.

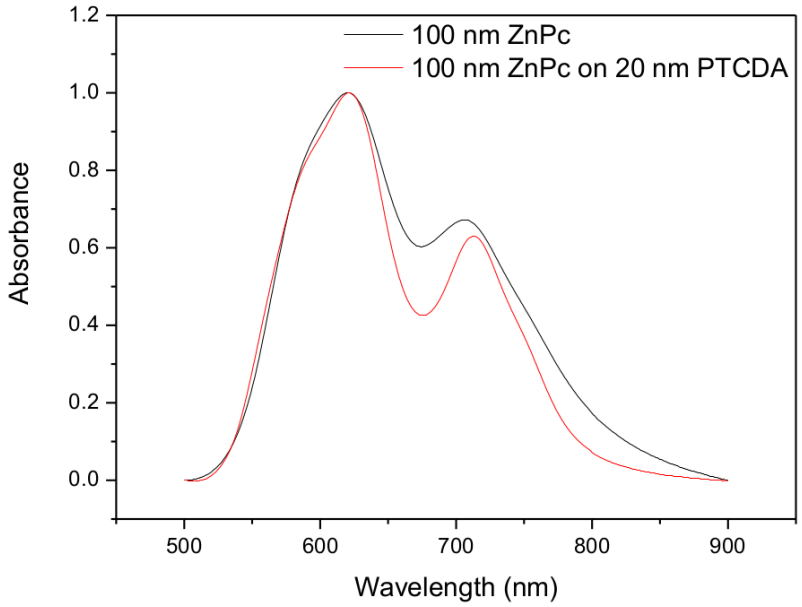

Figure 4.10: Normalised absorption spectra in the Q band region of 100 nm ZnPc film and 100nm ZnPc on 20 nm PTCDA film on glass, corrected for substrate contribution

From the spectra of individual component films and that of ZnPc on PTCDA (figure 4.8),

it appears that templating increases the absorbance of the film beyond that expected and comparison of the absorption spectrum of 100 nm ZnPc on 20 nm PTCDA with the linear sum of the individual absorption spectra of the component films confirms that increased absorption is a result of templating (figure 4.11). There is negligible change in the region between 400 - 500 nm where PTCDA absorbs. As the increased absorption occurs above 500 nm and PTCDA is non-absorbing in this region, we can infer that orientation affects absorption and alignment of the phthalocyanine molecules parallel to the substrate leads to enhanced absorption. When measuring the absorption spectra, light is incident normal to the sample with its electric field vector, $\vec{E}$, parallel to the plane of templated ZnPc molecules and it is the alignment of the molecular electronic dipole moment with the electric field that leads to increased absorption (figure 4.12b). In non-templated films, the molecular planes are oriented nearly orthogonal to the electric field with the consequence of reduced absorption (figure 4.12a). The molecular plane in templated films will therefore also be in alignment with the electric field, $\vec{E}$, of the UV light produced by the excimer lamp and increased absorption would be expected to reduce the time taken for zinc oxide to form and the film to be removed. This is explored later.

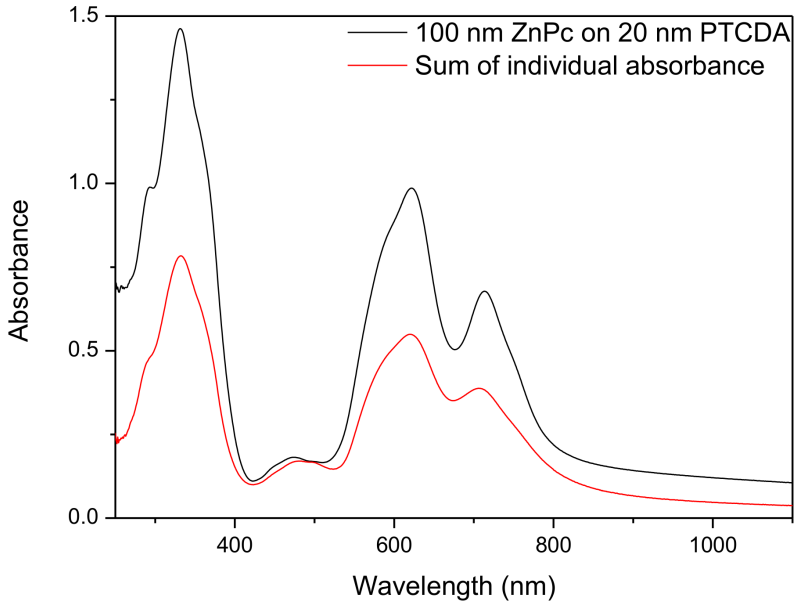

Figure 4.11: Absorption spectra of 100nm ZnPc on 20 nm PTCDA film and the linear sum of the individual films on glass, corrected for substrate contribution

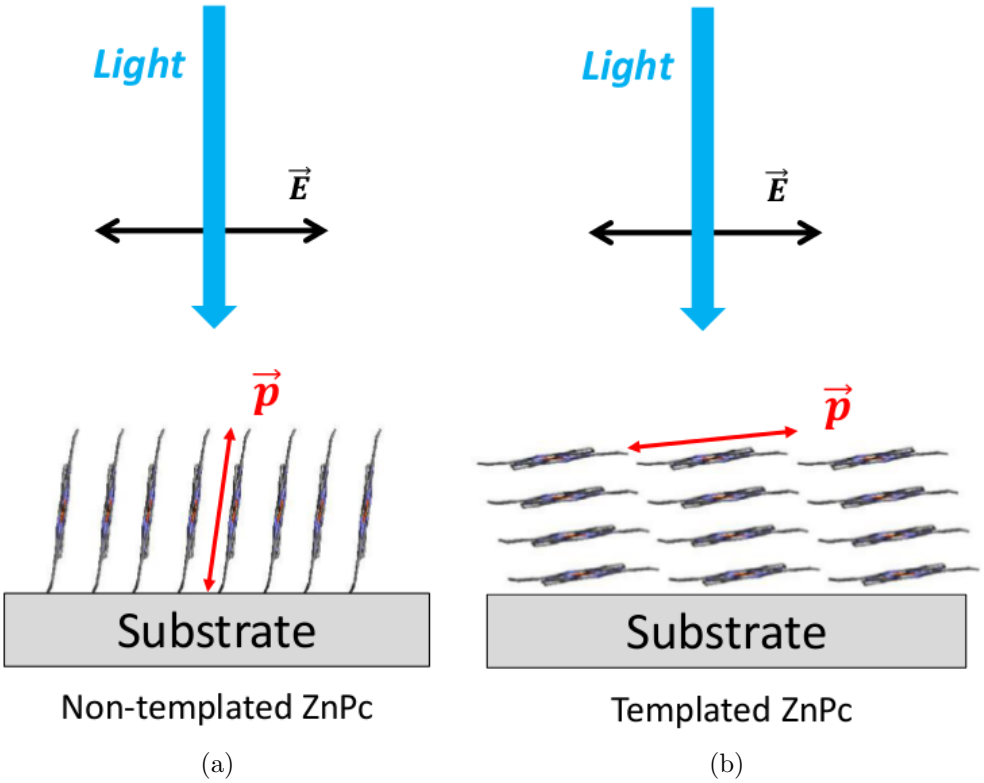

Figure 4.12: Schematic showing relative orientation of the electric field vector, $\vec{E}$, with the molecular dipole moment, $\vec{p}$, in (a) non-templated ZnPc and (b) templated ZnPc

In previous studies using ZnTPP and ZnPc, the percentage of film remaining was determined by integration of the region within the Q band. Here, there is a slight overlap with the absorption of PTCDA which requires modification of the this method, thus the Q band region above 600 nm will be used. As stated in chapter 3, reflectance of films will be neglected.

4.2.4 X-Ray Photoelectron Spectroscopy

XPS data for 100 nm ZnPc on 20 nm PTCDA were recorded as for section 3.2.4.

Binding energies arising from carbon, nitrogen, oxygen and zinc are clearly identified in the survey spectrum (figure 4.13a) and intensity counts yield ratios of C:N:Zn of 18:3:1 which differ from the ratio of 32:8:1 expected from the chemical formula. The C:N ratio is 6 which is close to the expected value of 4. However, the intensity of zinc is far greater than expected. As the survey spectrum is the sum of only three passes, the resolution and accuracy are limited.

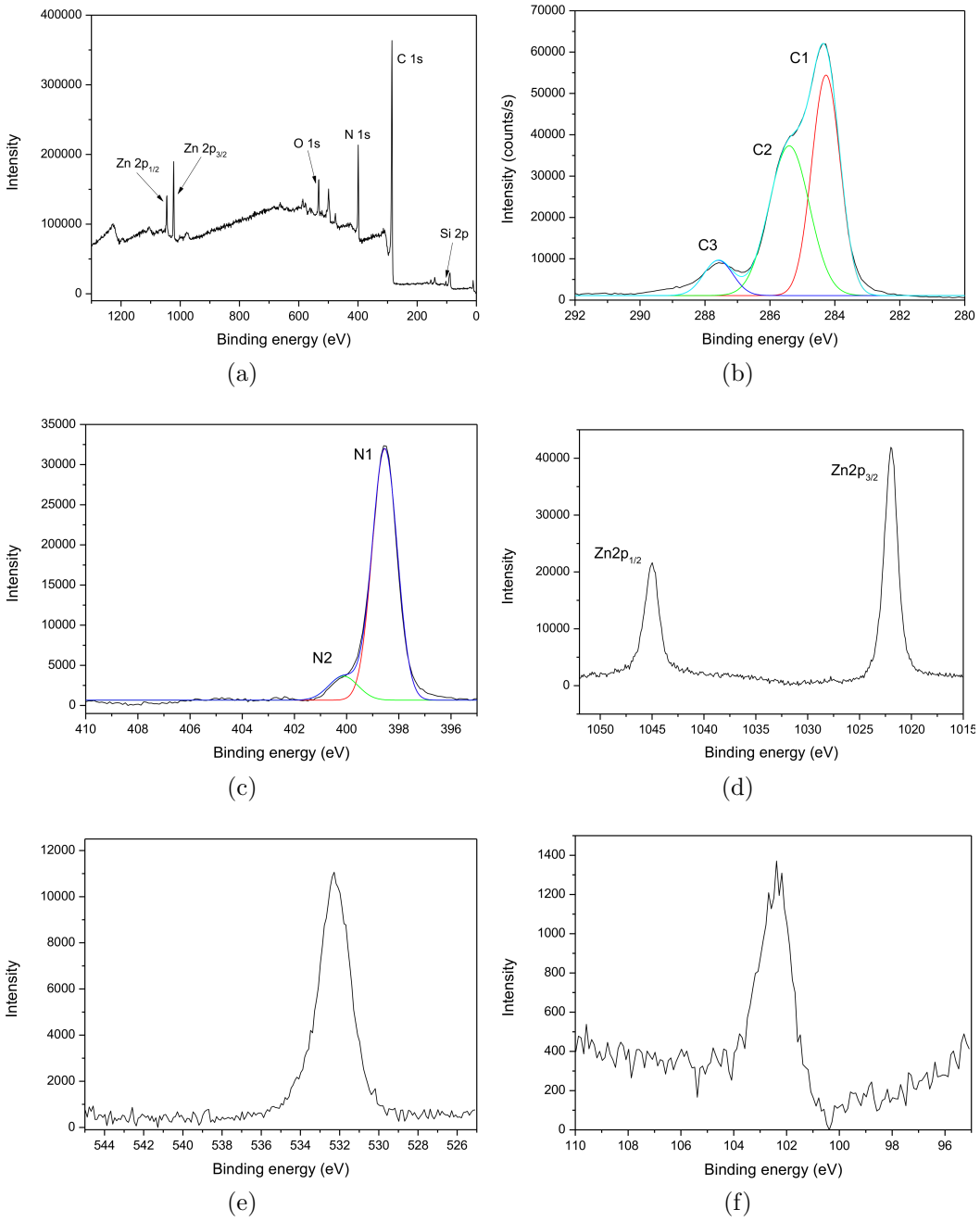

Figure 4.13: XPS spectra of as-deposited 100 nm ZnPc on 20 nm PTCDA: (a) survey, (b) carbon, (c) nitrogen, (d) zinc, (e) oxygen and (f) silicon. The intensities are plotted as measured in black and fitted curves in colour

Peaks C1, C2 and satellite C3 in the carbon 1s spectrum at binding energies of 284.3, 285.4 and 287.6 eV respectively (figure 4.13b) are in agreement with values found for as-deposited ZnPc in chapter 3 (figure 3.16) and with the literature [128–130]. The ratio of areas of peaks C1 to C2 is again not 3:1 as the satellite peak for C1 is difficult to distinguish and therefore alters the result. The overall shape differs from that in chapter 3 where the peaks C1 and C2

were more easily identified but here, they are only revealed by fitting Gaussian peaks to values already known from earlier experiments. Comparison between figures 3.16b and 4.13b show an increase in intensity of peak C2 with respect to C1 from a ratio of 22/9 to 1, an approximate doubling of the intensity of C2. As XPS samples at a depth of up to 10 nm below the surface, the initial layer of PTCDA cannot be responsible for this change in intensity nor can a change of orientation as the molecules themselves are only 13Å in length and with both templated and non-templated ZnPc, XPS will probe multiple layers of molecules. Surface contamination is one possible factor, although peak profiles of other elements have not been affected to this extent.

The two peaks at binding energies of 398.5 eV and 400.1 eV in the N1s spectrum (figure 4.13c) correspond to the same nitrogen peak seen in as-deposited ZnPc and its satellite peak (figure 3.16), in agreement with values quoted in the literature [128, 132]

Binding energies recorded in the zinc 2p spectrum at 1045.0 and 1022.0 eV (figure 4.13d) are within 0.1 eV of previous measurements (figure 3.16) and in agreement with binding energies measured for ZnPc on copper substrates [128]

A peak is observed at an energy of 532.3 eV in the spectrum for oxygen (figure 4.13e), very close to the broad, poorly defined peak seen at 532.3 eV in figure 3.16 for as-deposited ZnPc. Oxygen forms less than 4% of atomic composition and is likely to be due to surface contamination.

Finally, there is evidence of a small amount of surface contamination from handling techniques in the silicon 2p spectrum (figure 4.13f) as was also observed in figure 3.16 for as-deposited ZnPc.

4.3 Irradiated Films of ZnPc on PTCDA

Films of 20 nm PTCDA were grown by OMBD on prepared quartz, silicon and glass substrates before subsequent deposition of a 100 nm layer of ZnPc. The samples were placed on a sample holder in the vacuum chamber at a distance of 8.5 cm from the excimer lamp and irradiated

for periods between 0 - 90 minutes in 10 minute intervals as for ZnPc films (section 3.3). The films were characterised using atomic force microscopy, absorption spectroscopy, X-ray diffractometry and X-ray photoelectron spectroscopy.

4.3.1 Morphology - Atomic Force Microscopy

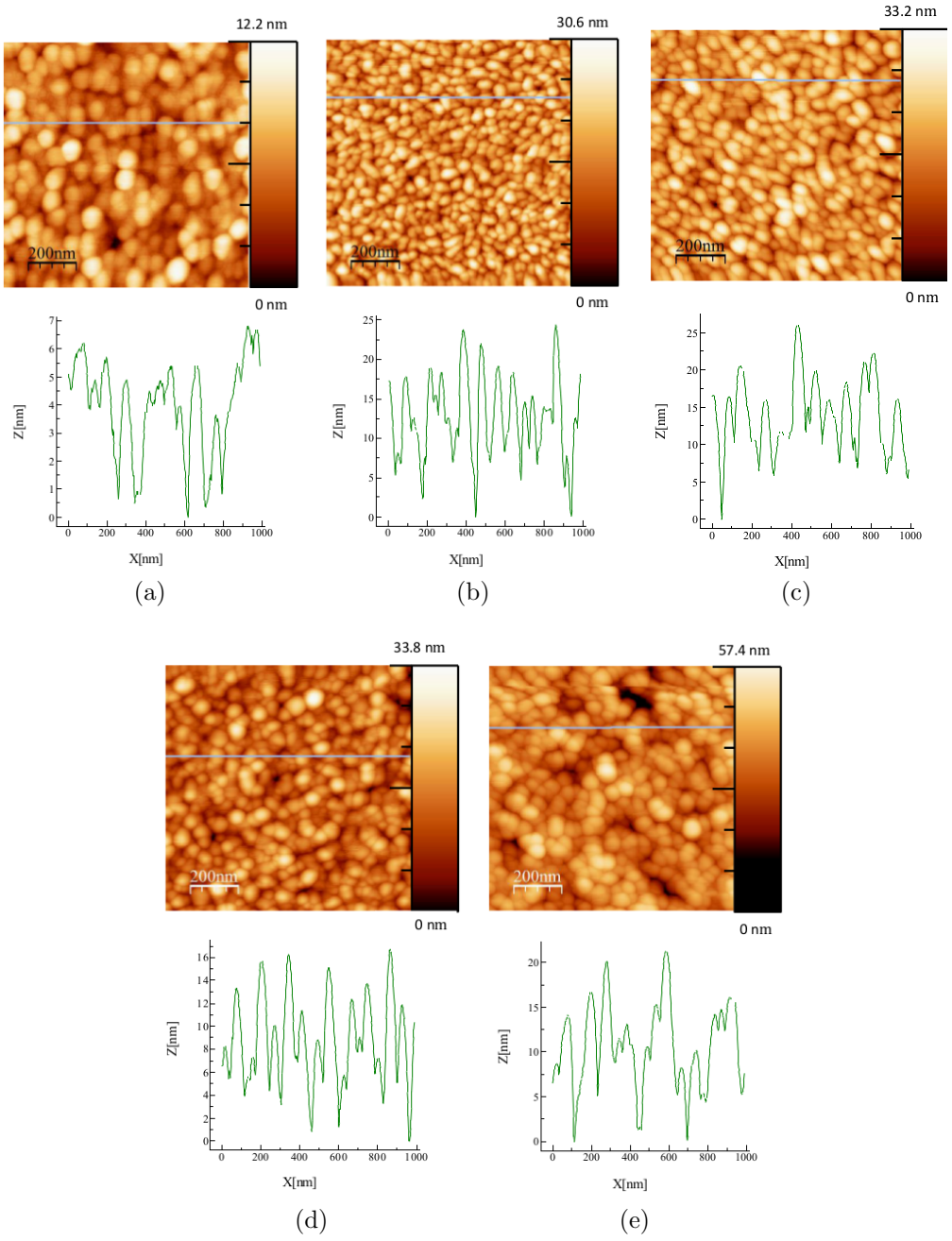

Figure 4.14: AFM images and line profiles of films of 100 nm ZnPc on PTCDA on silicon, irradiated with UV light in oxygen (a) 0, (b) 20, (c) 40, (d) 60 and (e) 80 minutes

AFM images of films irradiated for 0, 20, 40, 60 and 80 minutes show that the crystalline appearance is maintained throughout UV treatment (figure 4.14). As the UV irradiation time is increased, material is removed and deeper troughs become visible as the increasing z-scale, a measure of average peak-to-trough distance, shows.

RMS roughness was compared (figure 4.15) and a grain analysis carried out (figure 4.16) as for ZnPc (figure 3.23) in section 3.3 and data regarding grain size and number summarised in table 4.4.

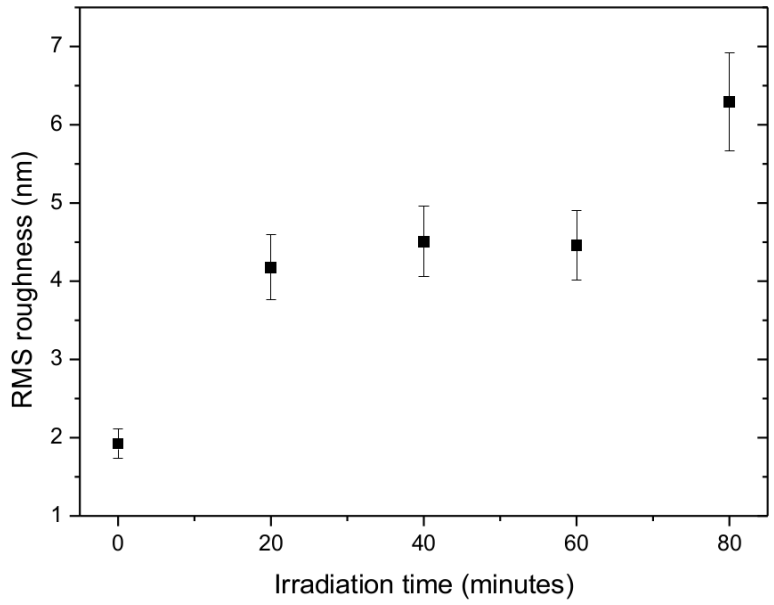

Figure 4.15: RMS roughness of films of 100 nm ZnPc on 20 nm PTCDA after UV irradiation

Roughness increases steeply from approximately 2 nm to 4 nm during the first 20 minutes of UV treatment and then again from 4.5 nm to over 6 nm between 60 and 80 minutes. However, between 20 and 60 minutes, there is very little change. Overall, once the film has been fully removed, the total increase in surface roughness is approximately 4 nm, as for films of ZnPc alone.

Grain analyses of the AFM data show that grains with radii in the region of 1 nm make up the majority of those identified in as-deposited film with very few grains of radius over 5 nm (figure 4.16) and although the distribution is skewed to smaller radii, the range of sizes measured extends to particles of 20 nm radius.

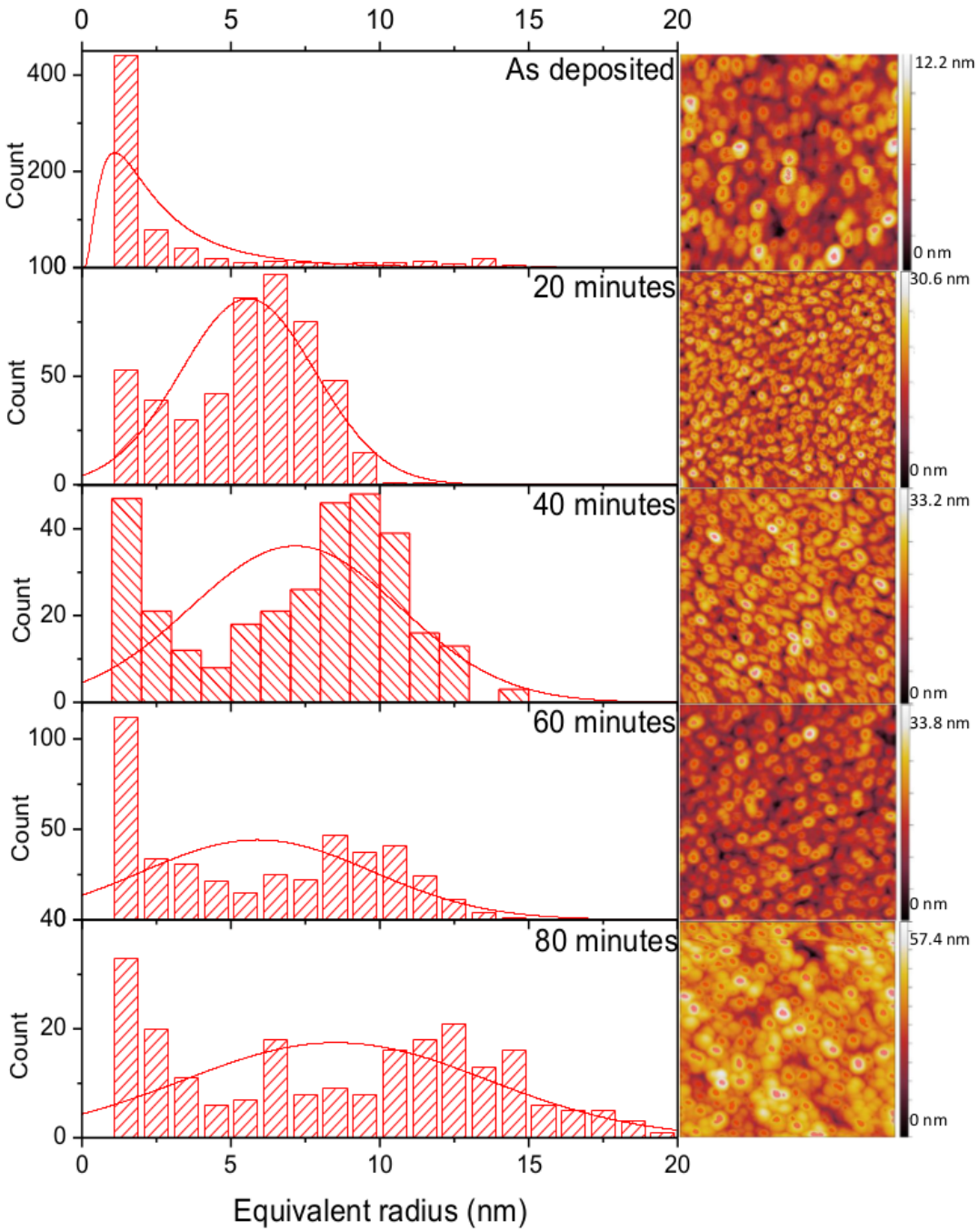

Figure 4.16: Grain analysis of films of 100 nm ZnPc on 20 nm PTCDA after UV irradiation

With increasing UV treatment time, there is a decrease in the number of particles at the extrema of the range while particles with radii in the region of 50 nm increase in number. As the film reacts under the influence of UV light and oxygen, the smallest grains will be the first to fully degrade and all grains will suffer some degree of removal of material. As morphology has been shown to be integral in the rate of oxide formation and oxygen has been shown to have a greater influence than photonic degradation, diffusion of excited oxygen species within grain

boundaries will affect smaller grains to a higher extent. This and the amalgamation of smaller grains as molecules diffuse laterally results in the particle size distribution seen (figure 4.16). The sample exposed to UV light for 80 minutes shows a large increase in roughness from 60 minutes, concomitant with the increase in peak to trough distance and this was also the case in samples from 0 to 20 minutes of UV irradiation.

Table 4.4: Data from grain analysis of UV treated films of ZnPc on PTCDA

UV treatment time (minutes)	0	20	40	60	80
Number of grains	695	487	318	425	224
Average of equivalent disc diameter (nm)	6.2	11.2	14.3	11.8	17.0

Comparison with ZnPc films deposited directly onto silicon shows that for both films, average grain size increased and the total number of grains decreased (tables 4.4 and 3.2). The roughness increased linearly with time for non-templated ZnPc films whereas figure 4.15 suggests that there was either a change in the relative influence of the photon-assisted and oxygen-assisted mechanisms or that the PTCDA layer affected the rate of change in roughness. The peak to trough distances showed very little variation in ZnPc films, unlike the heterostructures where initial distances increased by a factor of three. It is possible that the orientation of ZnPc molecules may affect the change in morphology and may also increase the rate of reaction as expected from the alignment of molecules with the electric field vector of incident light. This is explored further in the results from asborption spectroscopy (section 4.3.3).

4.3.2 X-Ray Diffraction

X-ray diffraction scans were recorded for samples of ZnPc deposited on PTCDA which had been treated in UV light for 0 - 90 minutes. Samples irradiated for 0 - 70 minutes show diffraction peaks from the (11-2) plane in ZnPc at approximately 27.9° with some contribution from the (10-2) plane in PTCDA and at 26.8° from the (01-2) plane in ZnPc (figure 4.17a) [6, 19]. No peaks are visible after 70 minutes. Although there is some overlap of the peak due to ZnPc in

the (11-2) orientation with the peak at 27.7° from PTCDA diffracting from the (10-2) plane, it was demonstrated in section 4.2 that the contribution to the total intensity from PTCDA was less than 23%.

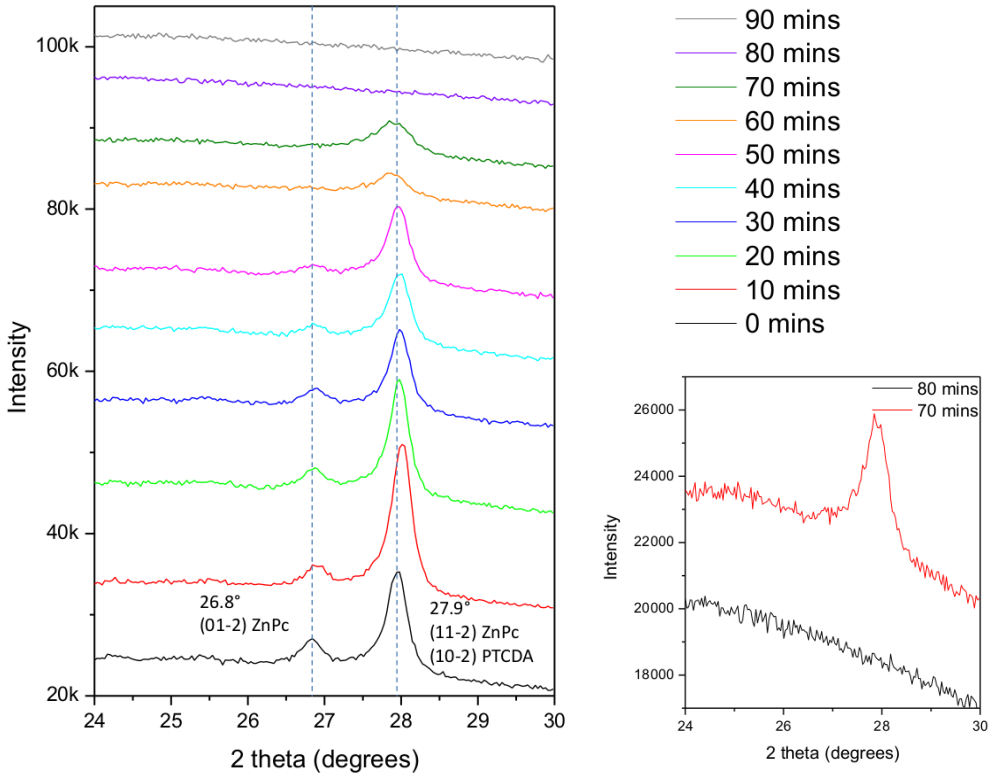

(a) (b)

Figure 4.17: XRD diffractograms of (a) films of 100 nm ZnPc on 20 nm PTCDA irradiated with UV light for 0 - 90 minutes in 10 minute intervals and (b) enlarged diffractograms of films irradiated for 70 and 90 minutes. Indexation based on [6, 19]

The disappearance of the peak at 26.8°, corresponding to ZnPc, within 60 minutes of UV irradiation suggests that the ZnPc crystallites are too small to be detected by XRD at least 20 minutes before ZnPc can no longer be detected in non-templated films (figure 3.27). Following 70 minutes, neither ZnPc or PTCDA remain intact, however, as the peak at 26.8° is solely due to the presence of ZnPc and approximately 77% of the peak at 27.9° is due to the presence of ZnPc, the fact that diffraction from the (01-2) plane in ZnPc is no longer seen could be taken as an indication that ZnPc has been removed and that any remaining intensity in the peak at 27.9° arises from the presence of PTCDA. If this is the case, PTCDA is removed within the next 20 minutes of irradiation. Furthermore, this would coincide with the appearance of deep troughs in the AFM images (figure 4.14e), perhaps attributable to the degradation of the PTCDA layer.

Confirmation of this is possible by examination of absorption spectra (section 4.3.3).

4.3.3 UV-Visible Absorption Spectroscopy

AFM and XRD data show that the film including both the ZnPc and PTCDA layers are removed by 80 minutes, 10 minutes earlier than for ZnPc alone where some residual ZnPc remained after 90 minutes. These results are confirmed by the absorption spectra of ZnPc films deposited on PTCDA (figure 4.18) which show negligible evidence of ZnPc or PTCDA after 80 minutes. This increased reaction rate may be a result of the change in orientation of ZnPc molecules, the presence of PTCDA which itself contains oxygen or a combination of the two. If orientation is responsible for the acceleration of film removal, ZnPc may be similarly templated by copper iodide [162] and should demonstrate an equally increased rate of film removal. If, however, the presence of PTCDA affects the rate by supplying oxygen from below the ZnPc film, then depositing multiple alternating layers of ZnPc and PTCDA should increase the rate further. A multilayer heterostructure was deposited and results are described later (section 4.4). Deposition on copper iodide will be included in further work.

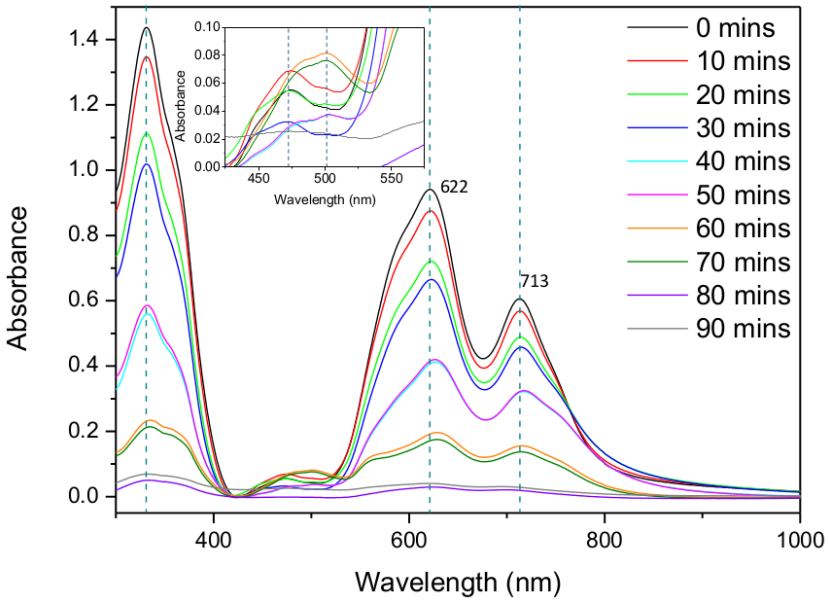

Figure 4.18: Absorption spectra of 100 nm ZnPc films grown on 20 nm PTCDA on glass, irradiated for 0 - 90 minutes in 10 minute intervals. Inset shows region corresponding to absorption by PTCDA

Looking more closely at the absorption spectra, peak positions remain largely stable throughout UV irradiation. As UV exposure time increases from 50 minutes, a shoulder becomes visible on the higher energy side of the peak at 621 nm, at a wavelength of approximately 560 nm. A peak at 567 nm (2.19 eV) in ZnPc has been reported and broadening of the Q band attributed to Davydov or excitonic splitting [97] but without explanation for this transition itself, however, this shoulder is likely to contain some contribution from the charge transfer transition of PTCDA observed at 554 nm in as-deposited PTCDA (figure 4.8). Absorption by PTCDA in the region between 400 - 550 nm experiences a bathochromic shift as UV irradiation increases, noticeable at 50 minutes, which is roughly in agreement with the point at which XRD results suggest UV light begins to affect the PTCDA layer. The shift of almost 27 nm within the PTCDA absorption region is much greater than that seen in the ZnPc $\pi - \pi*$ transition at 713 nm. As the peak at 554 nm in the absorption spectrum of PTCDA corresponds to a charge transfer transition and those at lower wavelengths to $\pi - \pi*$ and vibronic transitions [16], the change in the spectra seen suggests that intramolecular transitions are the first to be disrupted when the PTCDA layer is reached, which is somewhat counter-intuitive.

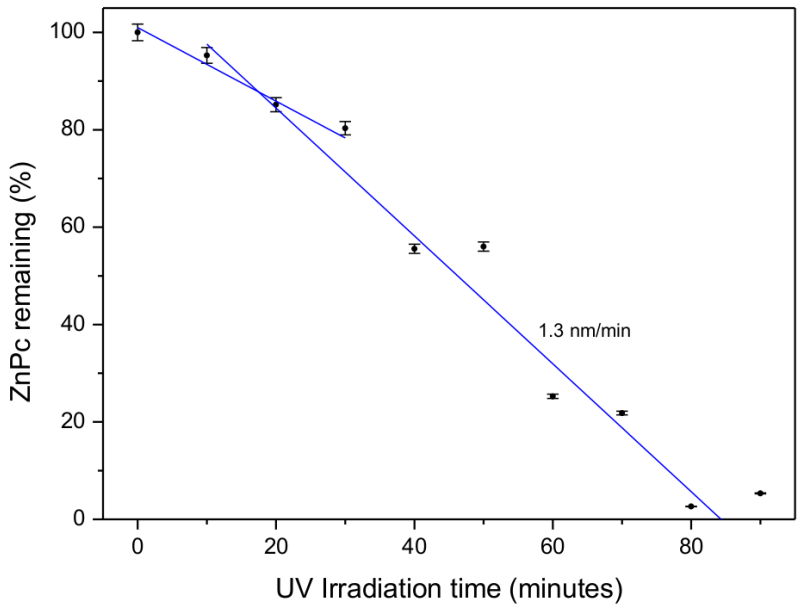

Figure 4.19: Area under Q band of absorption spectra of ZnPc on PTCDA films integrated to relate absorption to percentage of ZnPc film remaining

Unlike the absorption spectra for UV irradiated ZnPc films, the spectra here are not equally spaced, implying a non-linear rate of film removal, in agreement with AFM roughness data.

To further examine film removal, the area under the Q band was integrated, as for ZnPc and ZnTPP films in section 3.3.3 but integrating from 600 - 900 nm to avoid any contribution from PTCDA (figure 4.19).

As the film is crystalline, it would be expected that the kinetics of film removal would be similar to those for ZnPc films, however, the rate increases until 20 - 30 minutes when the rate becomes linear with a film removal rate of 1.3 nm/minute as for ZnPc only films. The as-deposited AFM image shows larger grains than for subsequent samples (figure 4.14) which would result in an initially slower degradation, with an increasing rate of film removal in as-deposited film once initial degradation allows further oxygen diffusion. Considering the as-deposited grain analyses for both ZnPc films (figure 3.23) and ZnPc on PTCDA films, (figure 4.16), many grains may have been identified more than once in the templated films and the peak to trough distance is higher than for non-templated films. This may have the effect of an inaccurate assessment of grain number or distribution and grains may be far fewer than given by the algorithm used. With a significantly lower number of grains, the initial rate of film removal would not be expected to reach 1.3 nm/minute and this is borne out in the rates seen from integration of the Q band. Although the initial rate is lower than for ZnPc only films, the reaction is completed earlier in templated films than in ZnPc only films as there is no residual ZnPc after 80 minutes.

From the orientation of ZnPc molecules in templated film and the consequential increased absorption seen in as-deposited spectra, it was expected that the reaction would proceed at a faster rate than for ZnPc films alone. However, once the reaction has progressed beyond 20 minutes, the rates are equivalent with the implication that the oxygen assisted mechanism exerts a far greater influence than photon-assisted, as was concluded from studies in chapter 3. The crucial difference with templated films appears to be the complete removal of film which may be attributed to the presence of oxygen-containing PTCDA below the ZnPc layer whereas a residual film of approximately 7% remained after 90 minutes of irradiation in non-templated ZnPc films. As the AFM images show, deep fissures develop in the film after 60 minutes of UV irradiation which may allow the initiation of PTCDA degradation before the film is fully exposed, thereby providing excited oxygen species to layers of ZnPc that have not yet been uncovered and completing the reaction.

As for non-templated ZnPc, it was necessary to ascertain the validity of using absorbance to determine the thickness of film remaining. Reflectance measurements show values of up to 30% in the IR region which may affect absorption values (figure 4.20). It is interesting that reflectance in this region drops significantly at 60 minutes, once the underlying PTCDA layer begins to degrade. Reflection will occur not only from the surface of the heterostructure and from the substrate, but also from the interface between ZnPc and PTCDA. The drop in reflectance at 60 minutes therefore is in agreement with the view that degradation of the ZnPc/PTCDA interface will reduce reflection from this interface

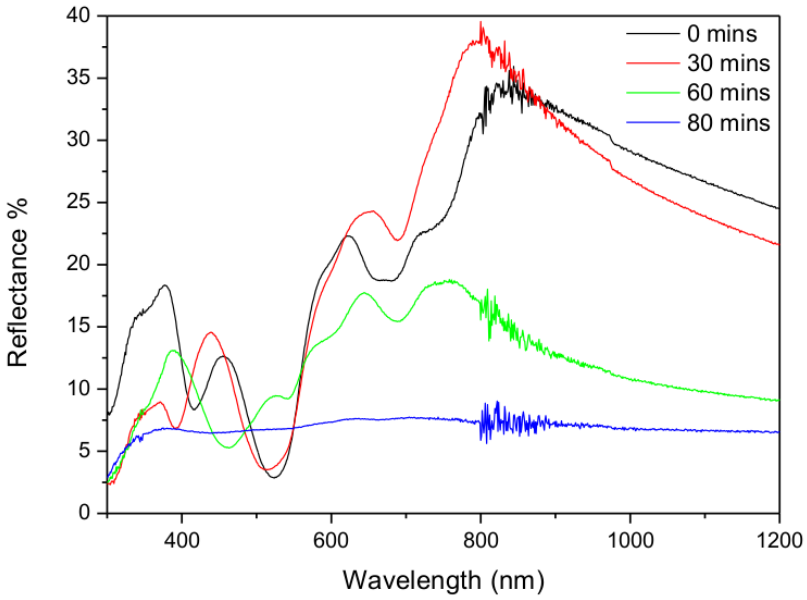

Figure 4.20: Reflectance measurements for films of ZnPc on PTCDA irradiated for 0, 30, 60 and 80 minutes

Comparison of absorbance and absorptance demonstrate the effect of reflectance on absorbance which is non-zero in the infra-red region, whereas absorptance accounts for reflectance in calculations (figure 4.21). Integration of the Q band for both sets of spectra, avoiding the contribution from PTCDA, gives results which lie within 6% of each other (figure 4.22). The percentage of film remaining as determined from absorptance follows the same profile as for percentages calculated from absorbance. Therefore, use of absorbance to determine the thickness of film remains a valid method, even for ZnPc/PTCDA heterostructures.

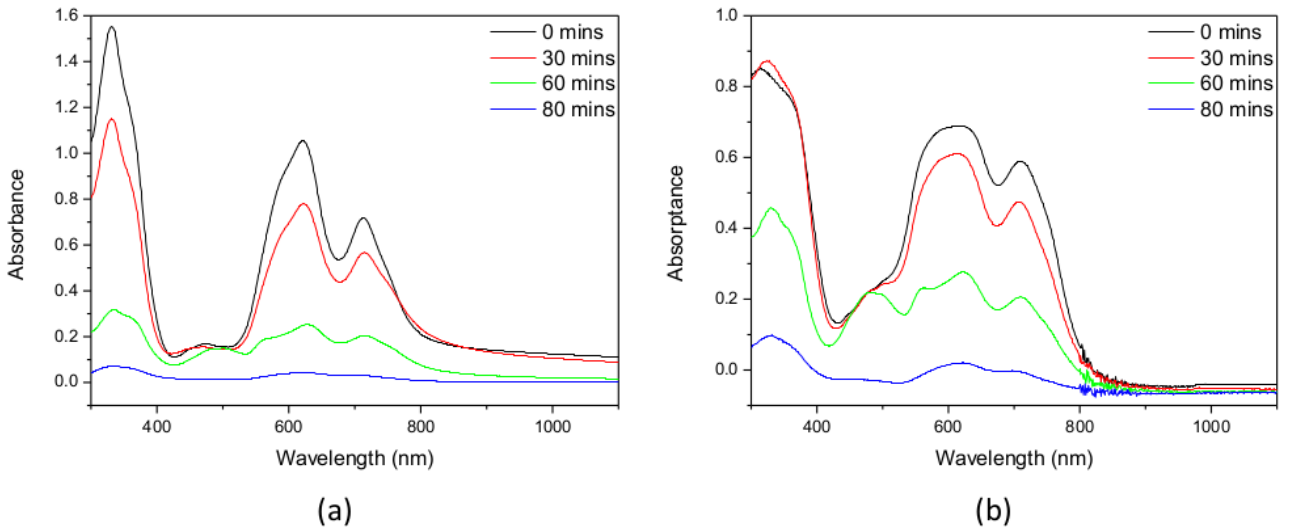

Figure 4.21: (a) Absorbance and (b) absorptance spectra for films of ZnPc on PTCDA irradiated for 0, 30, 60 and 80 minutes

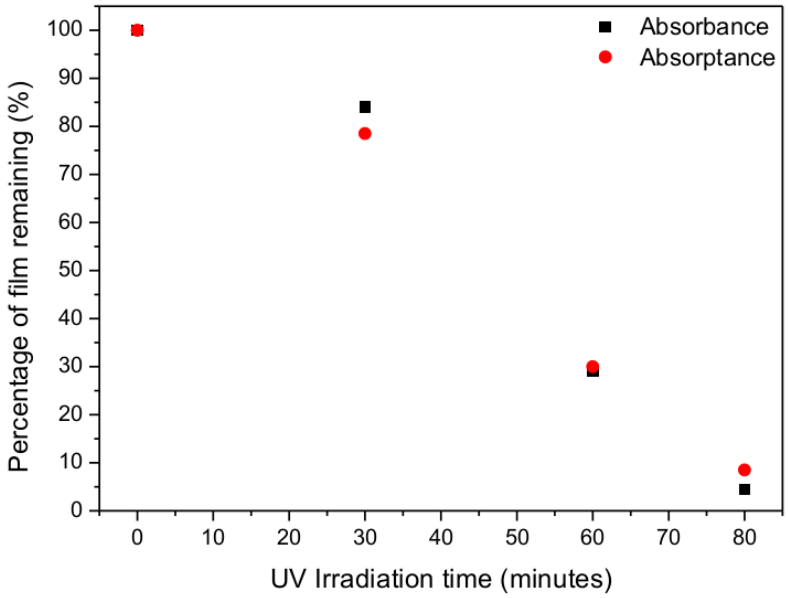

Figure 4.22: Percentage of ZnPc film remaining calculated by integration of the Q band of absorbance and absorptance, avoiding any contribution from PTCDA

4.3.4 X-Ray Photoelectron Spectroscopy

XPS data were recorded for samples of ZnPc on PTCDA irradiated for 0, 20, 40, 60 and 80 minutes. The percentage composition of the films showed a reduction of carbon content from 80% to 30% and nitrogen content from 13% to 4% with an increase in zinc content from 5% to 21% and oxygen content from 4% to 28% (figure 4.23). There was no change in silicon

content until the last sample which had been irradiated for 80 minutes. As PTCDA is highly unlikely to affect the XPS spectra until the ZnPc layer is close to being fully removed, the atomic composition of samples treated with UV light within 0 - 60 minutes arises from the degradation of the ZnPc film with associated removal of organic fragments and the incorporation of oxygen with formation of zinc oxide. The initial ratio of zinc to oxygen by percentage composition is 1.2 in as-deposited film, dropping to 0.55 after 20 minutes as oxygen is incorporated into the film. After 40 minutes, the ratio reaches 0.69 and stabilises at 0.73 for the remaining samples. As carbon and nitrogen are removed, a higher proportion of surface material will be zinc and the decreasing ratio of zinc to oxygen is an indication of a successful reaction with oxygen.

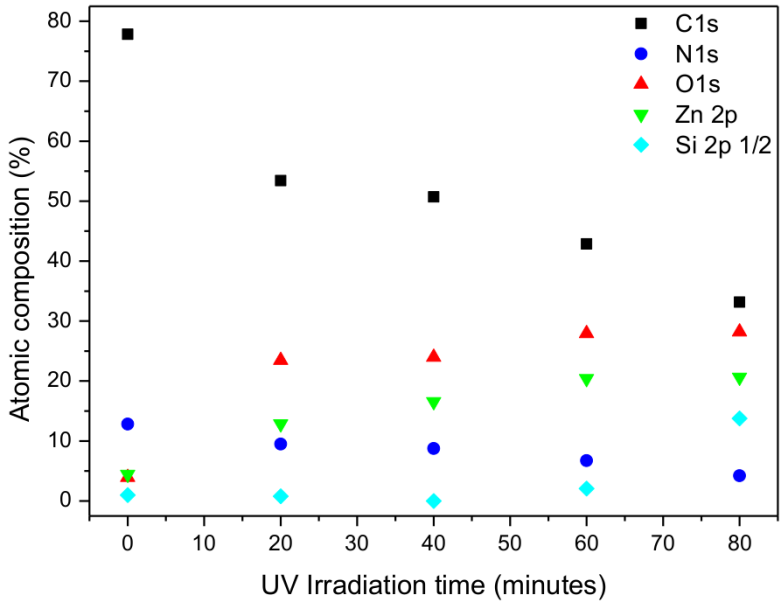

Figure 4.23: Atomic composition of UV treated films of ZnPc on PTCDA, determined by X-ray photoelectron spectroscopy

Higher resolution spectra of carbon 1s binding energies show a decreasing intensity of peak C1, corresponding to aromatic carbon atoms within benzene rings [128, 129], with a gradual shift to higher binding energies as the overall shape broadens (figure 4.24). As UV irradiation time increases, the intensity of peak C1 does not decrease to the same extent as for ZnPc films (figure 3.36) which may be due to the presence of PTCDA which has 24 carbon atoms in each molecule, 20 of which are aromatic but not bonded to oxygen. The broadening of the peak profile is a result of carbon in the film reacting with oxygen to form C=O bonds with binding energies in the region of 289 eV and may also be due to detection of carbon atoms within

carbonyl groups in PTCDA once 50 minutes of irradiation time have elapsed [143, 168].

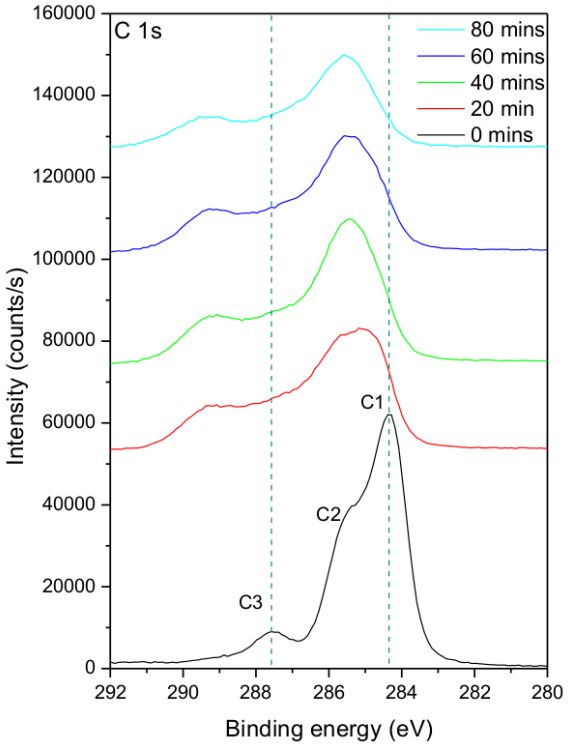

Figure 4.24: XPS spectra of carbon for films of ZnPc on PTCDA, irradiated in UV light for 0 - 80 minutes in intervals of 20 minutes, offset for presentation purposes

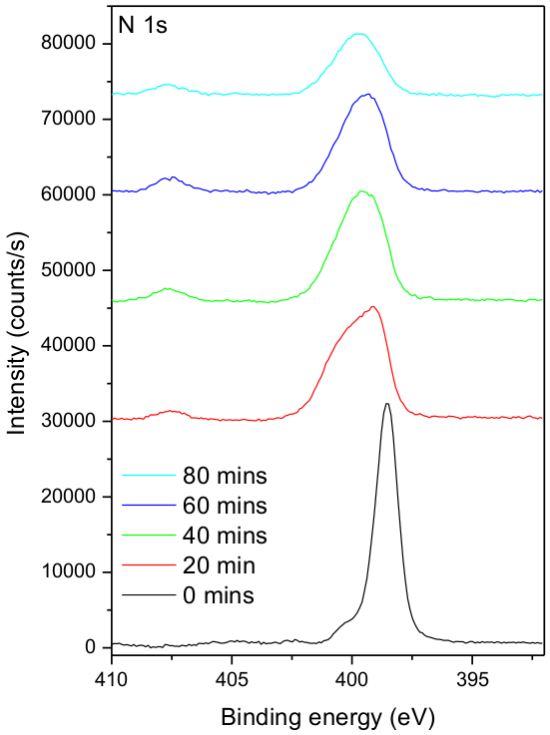

Figure 4.25: XPS spectra of nitrogen for films of ZnPc on PTCDA, irradiated in UV light for 0 - 80 minutes in intervals of 20 minutes, offset for presentation purposes

Higher resolution spectra of nitrogen 1s binding energies show a removal of nitrogen in agreement with atomic composition data (figures 4.25,4.23).

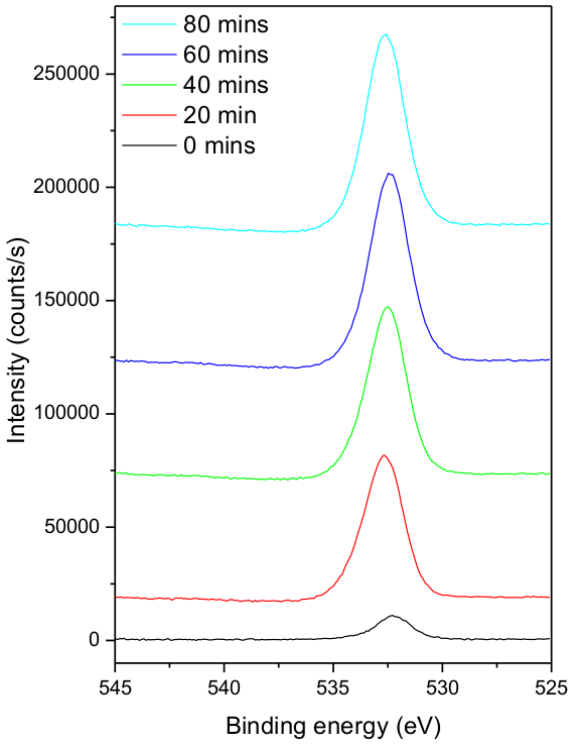

Figure 4.26: XPS spectra of oxygen for films of ZnPc on PTCDA, irradiated in UV light for 0 - 80 minutes in intervals of 20 minutes, offset for presentation purposes

The position of the oxygen 1s peak does not change significantly as UV irradiation time increases (figure 4.26). As the oxygen 1s binding energy in a C=O bond is 533 eV [135] and in a Zn-O bond 531 eV [133], the binding energies recorded here could be due to either or both. The XPS spectra of UV treated ZnPc films had similar well-defined peaks with a stable binding energy (figure 3.36) and the formation of zinc oxide was confirmed by SIMS. As the only change in ZnPc itself in the templated film is that of orientation, it is likely that the O 1s peaks seen here also include a contribution from Zn-O bonds. However, PTCDA also contains oxygen whose binding energies have been reported at 532.2 eV and 534 eV for the carbonyl and anhydride oxygen atoms respectively [168]. The spectra taken for ZnPc on PTCDA show only one peak which is closer to the carbonyl binding energy and this is the case even in the film which has been irradiated for 80 minutes, by which time the PTCDA layer has been reached. This suggests that the anhydride bonds must break too rapidly when exposed to either UV light or

excited oxygen species and are therefore not detected in the oxygen spectra.

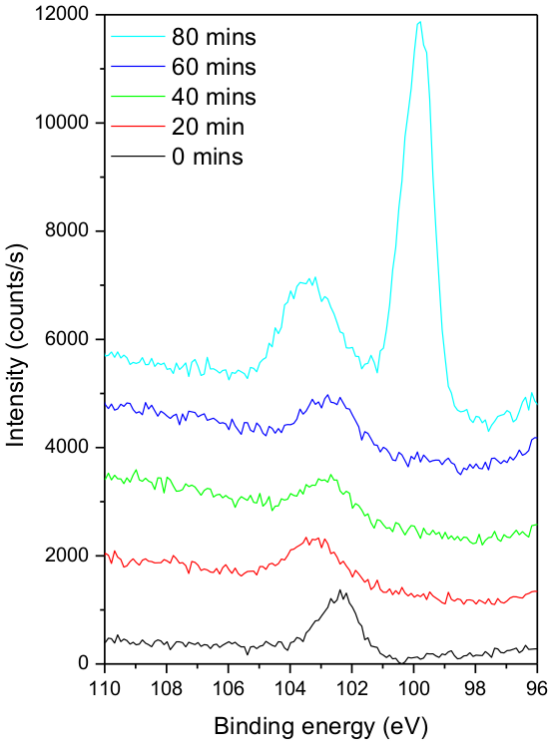

Figure 4.27: XPS spectra of silicon for films of ZnPc on PTCDA, irradiated in UV light for 0 - 80 minutes in intervals of 20 minutes, offset for presentation purposes

The Si 2p spectra show a peak at binding energy 102.5 eV which gradually shifts to higher binding energies of up to 104 eV as UV treatment time increases and a new peak appears at a binding energy of 99.8 eV (figure 4.27). This new peak is only present in the film which has been irradiated for 80 minutes and is a consequence of sufficient removal of material to expose the substrate, whereas the peak at 102.5 eV is due to surface contamination. The Si 2p peak was not seen in ZnPc only films at this intensity and was only recorded at 99.8 eV once 90 minutes of irradiation had elapsed.

4.4 Multilayer Structures Employing PTCDA to Assist in the Formation of Oxide

As PTCDA may enhance the rate at which ZnPc degrades, multilayers of ZnPc and PTCDA were deposited, beginning with an initial templating film of 20 nm of PTCDA, followed by 10 nm of ZnPc then alternating 10 nm of PTCDA with 10 nm ZnPc until the total depth of ZnPc deposited amounted to 100 nm, finishing with ZnPc (figure 4.28). As PTCDA contains oxygen, the aim was to determine whether layering ZnPc with a comparatively oxygen rich layer would reduce the irradiation time required to degrade ZnPc and form zinc oxide.

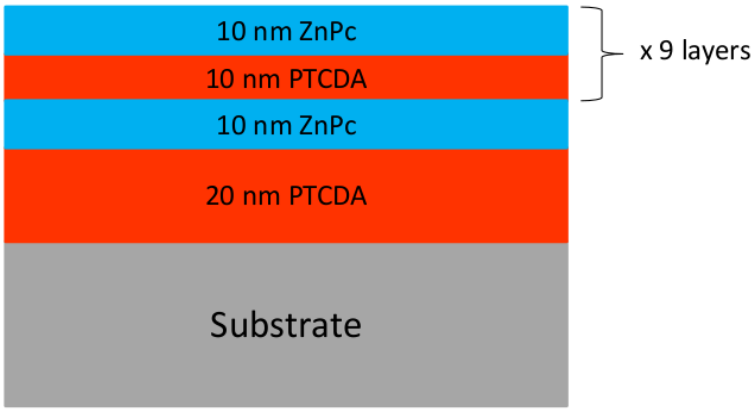

Figure 4.28: Schematic showing construction of multilayer structure with a total of 100 nm of ZnPc and 110 nm PTCDA

The films were irradiated for 0, 20, 40, 60 and 90 minutes using the standard conditions specified in earlier sections. In addition, one sample was irradiated in an atmosphere of nitrogen only, at 3.0 mbar to allow determination of the extent to which PTCDA contributes oxygen. Absorption spectroscopy and XRD were used to analyse the results.

4.4.1 UV-Visible Absorption Spectroscopy

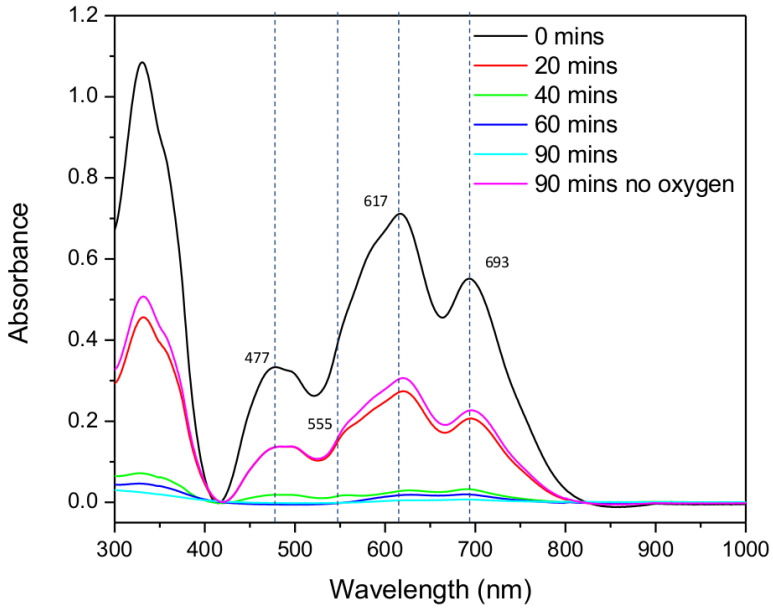

Figure 4.29: Absorption spectra of ZnPc/PTCDA multilayer films irradiated in UV light

From the absorption spectra of as-deposited film in figure 4.29, it is possible to identify contributions from both PTCDA and ZnPc by comparison with spectra of individual component films. The charge transfer exciton transition observed at 554 nm in PTCDA (figure 4.8) can be seen as a shoulder to the higher energy peak at 621 nm in the Q band of ZnPc observed previously (figure 3.30a). As there is now a total of 110 nm of PTCDA in the multilayer film, the contribution to absorption in this region will be significant and overlap with the absorption by a transition at 567 nm reported in ZnPc [97]. Vibronic transitions within PTCDA are responsible for the broad peak at 477 nm, a lower energy than the 484 nm previously measured for a 20 nm film (figure 4.8) and the breadth of the peak is due coexistence of both α and β modifications of PTCDA as the peaks in the absorption spectra of these phases differs slightly in energy [163]. Both peaks in the Q band of ZnPc demonstrate hypsochromic shifts from non-templated ZnPc films (figure 3.30a), contrary to shifts observed in the film of 100 nm ZnPc on 20 nm PTCDA (figure 4.9), where wavelengths for both peaks increased slightly.

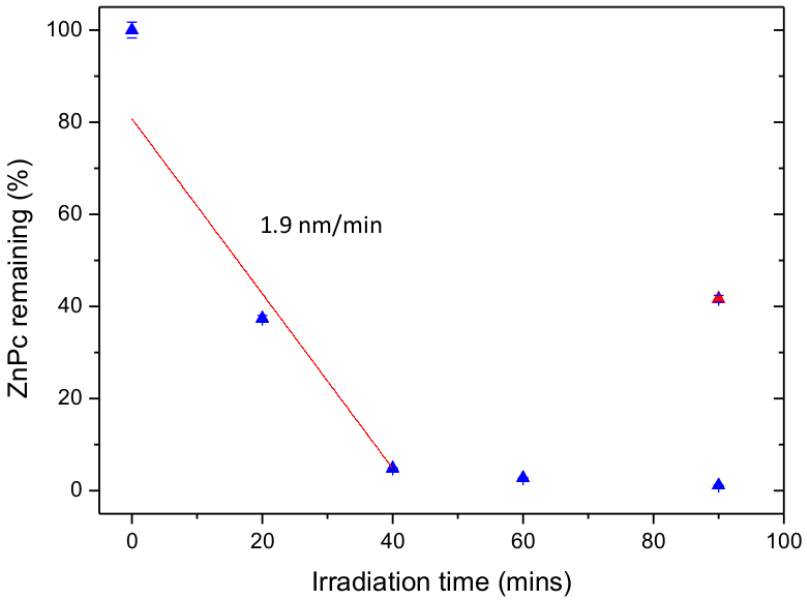

Figure 4.30: Area under the Q band integrated from 600 - 900 nm to determine percentage of ZnPc film remaining in multilayer films. Red data point correspond to film irradiated without oxygen

From the absorption spectra, it is clear that layering ZnPc with PTCDA significantly accelerates the rate of film removal, with minimal absorption due to ZnPc visible after 40 minutes of irradiation (figure 4.29). As the impact of templating was found to affect the rate of film removal to a limited extent earlier, this increase in reaction rate is due to the oxygen content within PTCDA molecules rather than a change in orientation of ZnPc. This is verified by the absorption spectrum of the film which was irradiated for 90 minutes in nitrogen only as degradation occurred to the same extent as for a multilayer film irradiated for 20 minutes in standard conditions with a partial pressure of oxygen of 1.8 mbar. Integration of the area under the Q band between 600 - 900 nm to avoid PTCDA contributions confirms the impact of PTCDA (figure 4.30), indicating the rapid removal of nearly all the ZnPc within 40 minutes, in comparison with ZnPc only films which require 90 minutes of irradiation to achieve the same effect and ZnPc films deposited on PTCDA which require the slightly lower time of 80 minutes. Without oxygen in the chamber, ZnPc degradation still exceeds 50%. In the case of ZnPc only films, it was demonstrated that the presence of oxygen in the chamber greatly increased the rate of the reaction, also contributing oxygen for the formation of zinc oxide (figure 3.29). As the presence of PTCDA alone, without oxygen in the chamber, results in only a slightly higher

percentage of film removal than for ZnPc in nitrogen, the presence of excited oxygen species are clearly vital for the reaction, regardless of oxygen containing molecules in the film.

4.4.2 X-Ray Diffraction

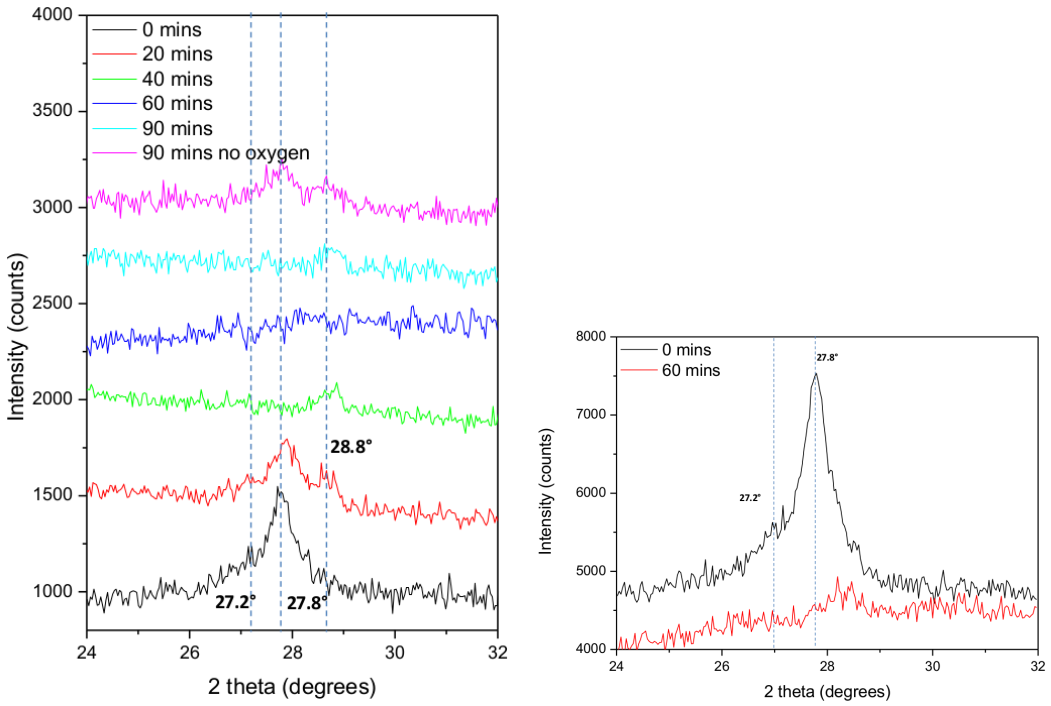

Figure 4.31: (a) X-Ray diffractograms of multilayer films irradiated for 0, 20, 40, 60, 90 minutes in standard conditions and 90 minutes in nitrogen offset for presentation purposes and (b) higher resolution X-ray diffractograms of multilayer film as-deposited and irradiated for 60 minutes, offset for presentation purposes

XRD data were recorded for an as-deposited multilayer film and for a film irradiated for 20, 40, 60 and 90 minutes in standard conditions and for 90 minutes in nitrogen (figure 4.31a). The data for the pristine film shows a broad peak at 27.8° corresponding to diffraction from the (11-2) plane of ZnPc and the (10-2) plane of β-PTCDA. However, the shoulder at 27.2° suggests that a proportion of PTCDA exists in the α modification. This is expected as the absorption spectrum showed a broadening of the peak corresponding to vibronic transitions in PTCDA as a result of the coexistence of both phases. The intensity of the peak in as-deposited film is only approximately 500 counts in contrast with films of 100 nm ZnPc deposited on 20 nm PTCDA where the diffraction peak intensity reaches over 7000 counts (figure 4.6) and is

a consequence of the reduced average crystallite size. Deposition of alternating layers of 10 nm thickness prevents the development of larger grain sizes and the broadening of the peak is an indication of a reduced ordering. Irradiated films show progressively less evidence of either ZnPc or PTCDA. The broad peak resolves into separate peaks at 27.8° and 28.8° after 20 minutes of UV treatment and the peak at the higher angle is still visible in the 40 minute and 90 minute samples.

The high resolution data for a multilayer film irradiated for 60 minutes shows no evidence of either PTCDA or ZnPc remaining in agreement with absorption spectra which showed a near-complete removal of film at 40 minutes (figure 4.31b). Furthermore, the XRD data for the film irradiated for 90 minutes in nitrogen shows a degree of degradation similar to that for the film irradiated for 20 minutes in oxygen, also in agreement with data from absorption spectra

4.5 Conclusions

PTCDA was combined with ZnPc to create a simple model system for multi layer organic devices. As a molecule frequently employed for electronic purposes, its well-researched properties and characteristics made it an ideal choice to determine the effect on organic layers below the precursor layer in a device. Furthermore, deposition of metal phthalocyanines on an initial layer of PTCDA result in the templating of the precursor layer, with a change in molecular orientation from normal to parallel to the substrate and this effect provides an opportunity to investigate the impact of orientation on film degradation. Lastly, the UV method for oxide formation employs UV light and oxygen to fragment the organic macrocycle resulting with the formation of metal oxide and removal of carbon and nitrogen. Use of an oxygen containing molecule such as PTCDA may provide an additional route for oxide formation. Comparison of the effect of the UV process on these heterostructures with the results in chapter 3 will shed light on the questions posed above.

Templated films of ZnPc on PTCDA have been fully characterised using XRD, AFM, XPS and absorption spectroscopy and indexed correctly for the first time to examine the effect on

previously deposited organic layers. Throughout the UV treatment of these bilayer films, the crystalline appearance was retained, as for ZnPc films. Roughness increased, to the same extent as for ZnPc films but initially at a slower rate due to a slightly larger grain size presenting fewer grain boundaries for diffusion of excited oxygen species. As the reaction with heterostructures neared completion, initiation of PTCDA degradation created deep troughs and a corresponding steep increase in roughness.

XRD results detected no ZnPc after 60 minutes, whereas for ZnPc only films, the precursor was still visible at 80 minutes. The PTCDA layer remained intact until shortly before full ZnPc removal, when a decrease in intensity of the peak corresponding to the (10-2) plane indicated the onset of PTCDA degradation which was completed within 80 minutes. These observations regarding PTCDA were mirrored by XPS data which showed a reduction of carbon and zinc content by 60 - 70% and an increase in oxygen content by over a factor of 7. Aromatic carbon atoms in ZnPc were the first to react, with some subsequently forming carbonyl bonds as inferred from the carbon 1s spectra. The lack of observed binding energies in the oxygen 1s spectra corresponding to anhydride groups contained in PTCDA support the view that PTCDA was rapidly removed once ZnPc had degraded and suggest that it was these bonds which reacted first. The deep troughs seen in AFM images are likely to be a consequence of PTCDA removal and are the origin of the silicon peak measured at 99.8 eV upon exposure of the substrate.

The rate of ZnPc removal in bilayer films determined by integration of the Q band of absorption spectra was equal to the rate for ZnPc films once a linear regime had been reached. Therefore, oxygen within the chamber exerts a major influence in the formation of zinc oxide and removal of organic fragments as determined in chapter 3 regardless of templating. From the absorption spectra, it was clear that PTCDA remained largely unaffected until 40 minutes of irradiation had elapsed, at which point approximately 50% of ZnPc remained. This suggests that the effect of UV light and oxygen is manifested 50 nm below the surface of a film of ZnPc and does not occur following a layer-by-layer process. The impact of surface roughness was explored in chapter 3 and confirmed that the reaction took place within the depth of the film. Although approximately 18% of incident UV light will penetrate through 50 nm of ZnPc (figure 3.3), it is the diffusion of oxygen which results in film degradation and oxide formation. From this, we

are able to construct a model for the reaction which is depicted in figure 4.32.

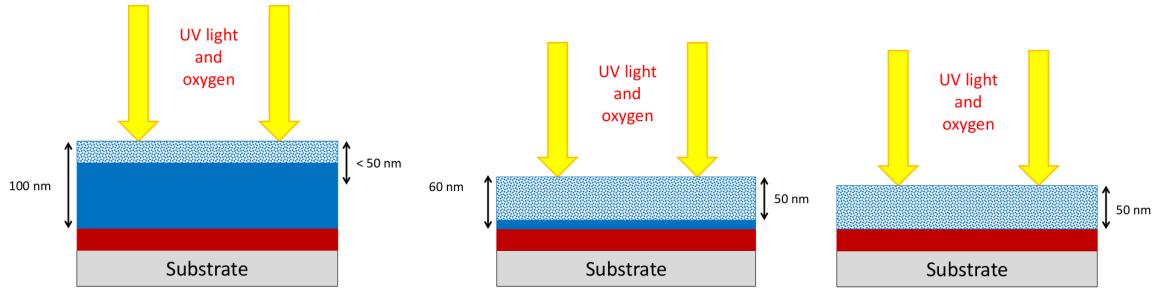

Figure 4.32: Schematic of action of UV light and oxygen on templated ZnPc films on PTCDA (a) at 0 minutes, UV light and oxygen affect the uppermost layers of the ZnPc film, (b) at 40 minutes, the effect of UV light and oxygen is manifest throughout a depth of 50 nm and is approaching the PTCDA layer and (c) at 50 minutes the PTCDA layer is affected

The minimal amount of ZnPc remaining following UV irradiation of heterostructure films compared to residual levels in ZnPc films may be attributed to the degradation of PTCDA following the removal of the majority of precursor film, allowing another route for oxygen diffusion, thereby completing ZnPc removal in a shorter time than for ZnPc films. This effect was further explored in the multilayer film in which 100 nm of ZnPc and at least 80 nm of PTCDA were fully removed within 40 minutes, demonstrating a greatly accelerated rate of degradation and the potential for optimising the UV process by careful choice of oxygen-containing precursors.

Templated and non-templated ZnPc films have been shown to degrade at equivalent rates once the linear regime has been reached from which we can conclude that orientation does not affect film removal, despite the alignment of the molecular electronic dipole with the electric field of incident light in the case of templated films as oxygen is the major factor in the process.

Summarising, the use of PTCDA with ZnPc as a model for a multi layer organic system has been successful in demonstrating that the integrity of neighbouring layers is maintained until the precursor film is approximately 50% degraded. Templating has been shown to have minimal effect on the rate with which the UV process is completed and this method may therefore be reliably applied regardless of orientation. The inclusion of oxygen containing molecules such as PTCDA significantly increases the rate of film degradation and provides the opportunity to exploit room temperature UV assisted oxide formation by a judicious choice of molecule to be

codeposited or alternately deposited with the precursor.

Chapter 5

Combining Nanosphere Lithography with the UV Process

The work in this chapter was carried out in association with Masters student Lucille Chambon and the majority of AFM data was collected by Dr Victoria Bemmer.

The oxygen assisted UV process results in the formation of metal oxides from metalorganic precursors and offers an opportunity to employ differences between the precursor material and the end product for a variety of purposes. Here, we investigate the possibility of creating nanostructured arrays of ZnPc, zinc oxide and air via nanosphere lithography (NSL), for exploitation of changes in optical characteristics to produce photonic structures.

Lithographic techniques include photolithography, where an optical source is used to pattern light sensitive chemicals to form a mask, allowing formation of patterns on the material underneath. Frequently employed for production of integrated circuits, it is an inexpensive route to large area patterning only suitable for thinner structures. Electron beam lithography allows the creation of structures with resolution as little as 10 nm but does not lend itself to large area production due to expense [169, 170]. Dip-pen nanolithography uses an AFM tip and the capillary action of chemicals to write patterns with a linewidth resolution of approximately 30 nm but is also not suitable for larger areas [171]. Other nanostructure fabrication methods include focussed ion beam micromachining and deposition which use liquid metal ion sources

such as those employed in SIMS to provide control down to 10 nm [172]. Nanosphere, or colloidal, lithography, however, is a versatile, inexpensive method applicable to larger areas. First used to create a platinum template for contact imaging [173], it relies on the self-assembly of colloidal nanospheres (NS) to form a mask through which material is deposited.

NSL may be used as a method to produce structures employable as outcouplers for OLEDS to decrease the light lost through total internal reflection and waveguiding in substrates [174], as solar concentrators in solar cells and for optical coatings such as antireflection films but has the disadvantage of introducing defects into an array in the form of dislocations, aggregations, multilayers and voids in nanosphere monolayers. The method used here minimises the formation of these defects [175].

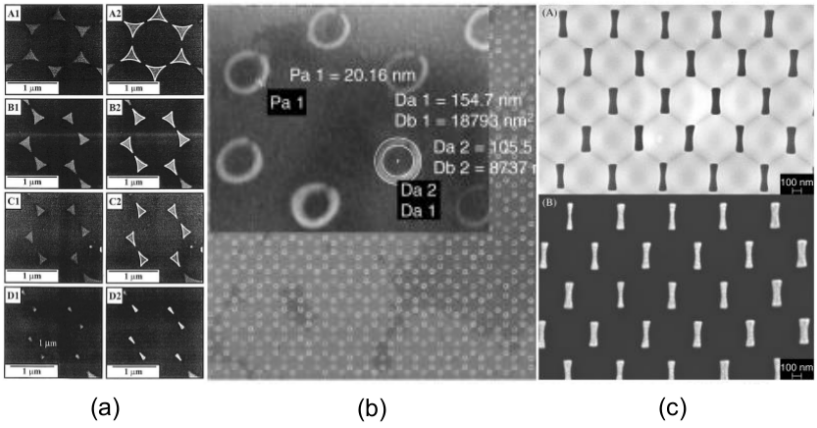

Figure 5.1: Examples of nanostructures possible using nanosphere lithography (a) Field emission scanning electron micrographs of angle resolved NSL-fabricated nanoparticle arrays (A1 - D1) and images with simulated geometry superimposed (A2 - D2) at 40k magnification [20], scanning electron microscope pictures of (a) ordered iron nanorings evaporated over an annealed 540nm PS latex mask and (c) rodlike apertures in stretched and subsequently annealed 540nm PS latex mask (A), and hcp-ordered iron nanorods evaporated through this mask (B) [21].

Typically, NSL involves the deposition of polystyrene (PS) or silica nanospheres as two dimensional hexagonal close-packed (hcp) arrays, forming a mask through which material is deposited to create nanostructured arrays. Deposition of material through the interstitials of the nanospheres from a direction normal to the mask will produce arrays of nanosized triangular structures. The orientation of deposition angle may be varied and the mask heated to effect a change in morphology to create crescents or rings [20, 21] and the method may be combined with other techniques, photolithography, for example [176], to widen the potential further to

include an almost limitless range of nanostructures (figure 5.1). The nanosphere mask may be modified not only by heating [21] but also by etching or by oxygen plasma treatment to induce changes in nanosphere size or profile [177,178]. The impact of this on nanostructure formation using UV light and oxygen is discussed later in this chapter.

Deposition of metal nanostructures has great importance in the field of plasmonics as the size and distribution of arrays may be tuned to select specific wavelengths of light with which surface resonance effects are produced. At its simplest, electrons within metal nanospheres redistribute upon the application of an external electric field in the form of light. The size and distance of the metal spheres determines which wavelengths are absorbed and which are scattered. Combination with fluorophores (fluorescent chemical compounds) results in metal enhanced fluorescence [179]. Application of NSL to create metal nanoparticle arrays linked with fluorophores to be used as biosensors is a highly active area of research [180].

The method employed here is water buffer based transfer NSL, a modification of a procedure reported in the literature [175]. A 10% w/v solution of polystyrene (in deionised water with sodium azide and surfactant sodium dodecyl sulphate, purchased from Bangs Laboratories Inc., USA) is mixed with an equal volume of ethanol to facilitate suspension of the nanospheres on water and sonicated briefly. Silicon wafer substrates used to transfer nanospheres and substrates for subsequent deposition of nanospheres are first cleaned in a UV ozone chamber for 30 minutes to increase the surface energy, favouring monolayer formation. Drops of the NS solution are applied to the transfer wafers, held above deionised water, at an angle slightly greater than normal to the meniscus with the lower end slightly submerged in the water. As the drops slide down the silicon towards the water, the increased surface energy of the silicon results in the drop spreading laterally over a greater area, promoting the formation of NS monolayers over aggregated clusters on the surface of the wafer. The NS coated silicon is allowed to dry before gently immersing in fresh deionised water where monolayers are transferred from the wafer to the water surface and aggregated nanospheres and multiple layers sink to the bottom. The wafer is fully submerged in the water and carefully brought out on the other side of a buffer bar. The buffer bar is simply a sleeving of rubber mounted on a rod and placed at the surface of the water to prevent the transfer of disturbances to monolayers when the wafer is extracted.

This process is repeated until the monolayer on the surface of the water is sufficiently large and well formed.

Prior to deposition of nanosphere monolayers on substrates, approximately 2-4 µl of a 2% w/v solution of sodium dodecyl sulphate solution, a surfactant, is added around the edges of the container in which the monolayers have formed. This reduces the surface tension, encouraging any separate regions of monolayers to coalesce, forming one single monolayer. A cleaned substrate is inserted into the water on the opposite side of the buffer bar before gently manoeuvring it under the monolayers and gradually removing it from the water, maintaining a nearly horizontal orientation. The substrates are left to dry overnight at a 45° angle. Removal of nanospheres is by either sonication in ethanol, ozone treatment or with adhesive tape. The latter is the method used here as ZnPc will dissolve in ethanol and ozone is likely to affect results.

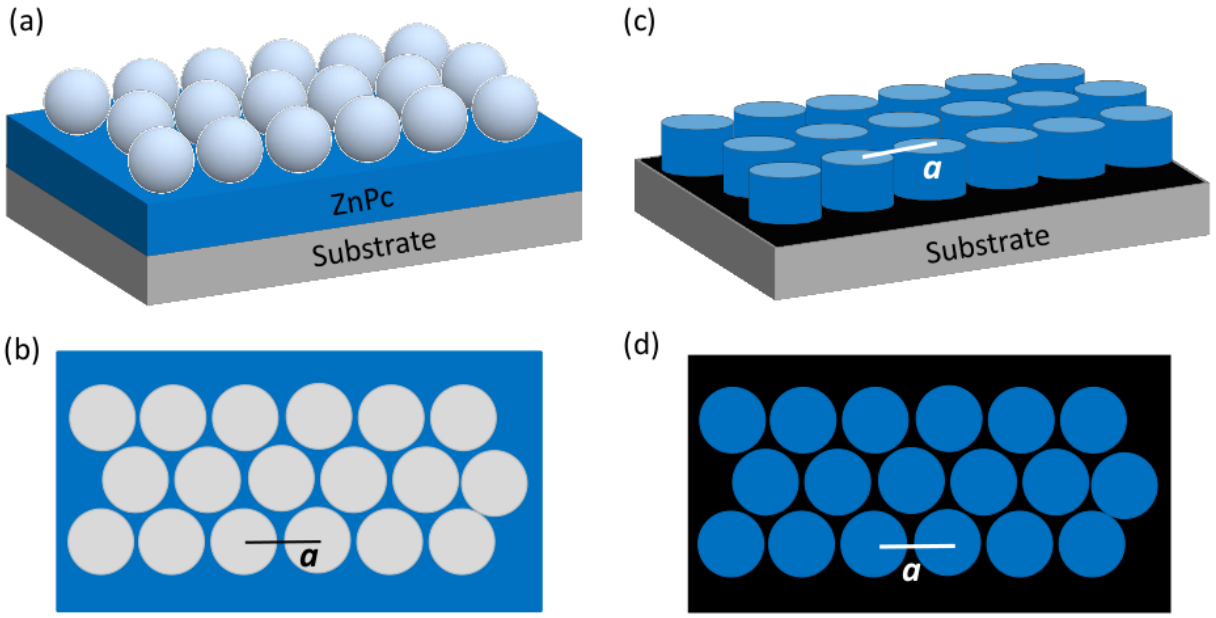

Figure 5.2: Schematic of nanosphere lithography on ZnPc films (a) deposition of nanospheres on a film of ZnPc, (b) top view, (c) pillars of ZnPc surrounded by a layer of zinc oxide formed after UV irradiation and removal of nanospheres, (d) top view. Distance a is expected to be 200 nm, 500 nm and 800 nm for 200, 500 and 800 nm nanospheres respectively

There are several possible routes which may be used to create nanostructured arrays using NSL with ZnPc, the first of which is deposition of nanospheres on a film of ZnPc, followed by UV irradiation in oxygen and subsequent removal of the nanosphere mask (figure 5.2). The

expected result would be cylinders of ZnPc surrounded by a thinner layer of zinc oxide.

The dimensions of features expected to form is easily determined from the geometry of the nanosphere array (figure 5.3). For nanospheres of diameter, d, the perpendicular height, h, of the triangular structures is given by

$$h = \frac{3}{2}\left(\sqrt{3} - 1 - \frac{1}{\sqrt{3}}\right) d \approx 0.233d \tag{5.1}$$

The distance between the nanoparticles formed, d_{np}, is given by

$$d_{np} = \frac{1}{\sqrt{3}} d \approx 0.577d \tag{5.2}$$

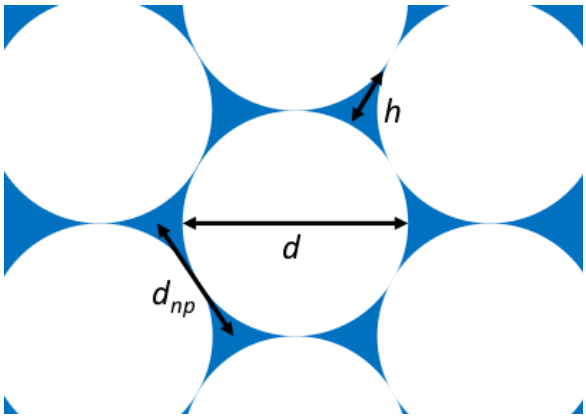

Figure 5.3: Dimensions of triangular nanostructures formed using NSL

Another route is the deposition of ZnPc over a monolayer of nanospheres followed by removal of the NS mask (figure 5.4). In contrast to deposition of the mask on top of ZnPc, this method would be expected to create an array of triangular ZnPc nanostructures in air.

Both these options are explored in this chapter, firstly establishing the suitability of ZnPc films for nanosphere lithography before assessing the quality of nanosphere monolayers formed on glass for a selection of NS diameters. As oxygen plasma is frequently used to modify the morphology of NS masks, the effect of UV light and oxygen on PS nanospheres is determined before choosing a single size of NS to create the nanostructured arrays. Scanning electron microscopy

and atomic force microscopy are used to examine morphological changes and absorption spectroscopy to determine the amount of ZnPc remaining following removal of the mask, neglecting any effects of reflectance.

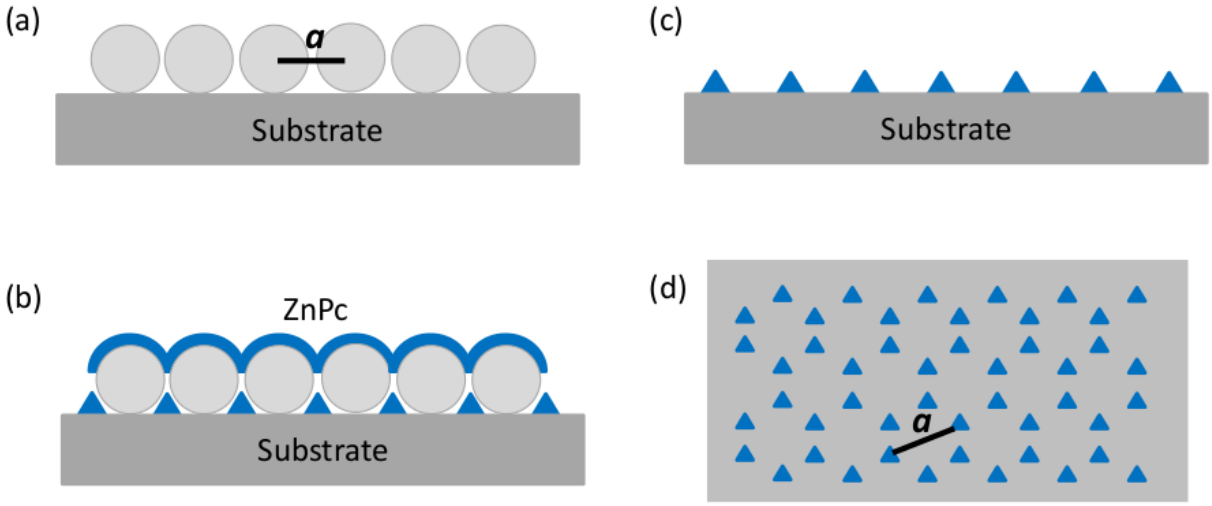

Figure 5.4: Schematic of nanosphere lithography directly onto the substrate (a) deposition of nanospheres on the substrate, (b) subsequent deposition of ZnPc film, (c) triangular nanostructures formed by removal of nanospheres, (d) top view showing array of triangular ZnPc nanostructures. Distance a is expected to be 200 nm, 500 nm and 800 nm for 200, 500 and 800 nm nanospheres respectively

5.1 Results: Feasibility Studies for the use of Nanosphere Lithography with ZnPc and the UV Process

NSL is routinely carried out on silicon, glass and mica substrates but has so far not been tried on ZnPc films which may be too hydrophobic to allow adherence of a monolayer of nanospheres. The hydrophobicity is assessed by measurement of contact angle. Nanospheres of different sizes are deposited on glass and irradiated with UV light in the presence of oxygen to determine the optimum combination of NS size and ZnPc film thickness.

5.1.1 Suitability of ZnPc for Nanosphere Lithography

If ZnPc films exhibit a high contact angle with water, it may not be possible to deposit nanospheres on the film. Contact angle measurements of 100nm and 200 nm films of ZnPc were taken using a Dataphysics Contact Angle System OCA 15Pro (table 5.1).

Table 5.1: Contact angle measurements of ZnPc film

ZnPc film thickness (nm)	Contact angle (°)
100	86 ± 2
200	99 ± 5

Native silicon dioxide layers on silicon substrates have a contact angle very close to zero [181] whereas the slides used in our experiments, VWR soda-glass slides, have a contact angle between 5 - 30°, depending on the cleaning method used [182]. Both these angles are considerably less than that measured for ZnPc, even the 100 nm film which has contact angle of 86°, lower than that of a 200 nm film. ZnPc films are therefore far less hydrophilic than silicon or glass substrates and this may cause problems when attempting to form monolayers of nanospheres.

5.1.2 Monolayer Formation on Glass

Monolayers of 200, 500 and 800 nm nanospheres were deposited on glass and scanning electron microscopy used to assess the quality of the monolayers formed (figure 5.5). The 200 nm nanospheres have formed small monolayer domains with many voids and areas with multiple layers. The 800 nm nanospheres do have much larger domains of monolayers but the 500 nm NS have formed the greatest areas of close-packed nanospheres.

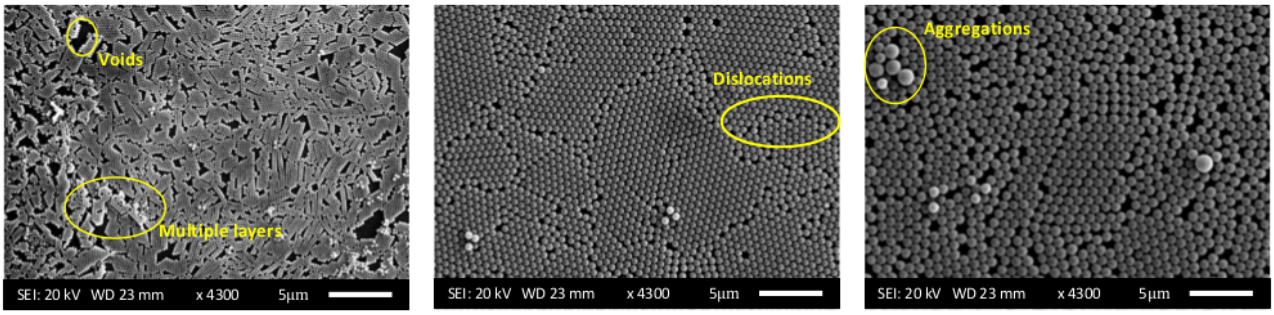

Figure 5.5: Monolayers on glass: (a) 200 nm NS, (b) 500 nm NS and (c) 800 nm NS. Defects such as voids, dislocations and aggregations are indicated

Higher magnification SEM images of the monolayers show the regular hcp arrangement expected (figure 5.6), however, the sample with 200 nm spheres contains a high number of defects. Assuming full coverage of the substrate with a monolayer of hexagonally close-packed spheres (equivalent to a monolayer of cubic close packed spheres), only 21.5% of the ZnPc film will be exposed to UV irradiation, providing a guideline for assessment of the extent of ZnPc degradation during the UV process.

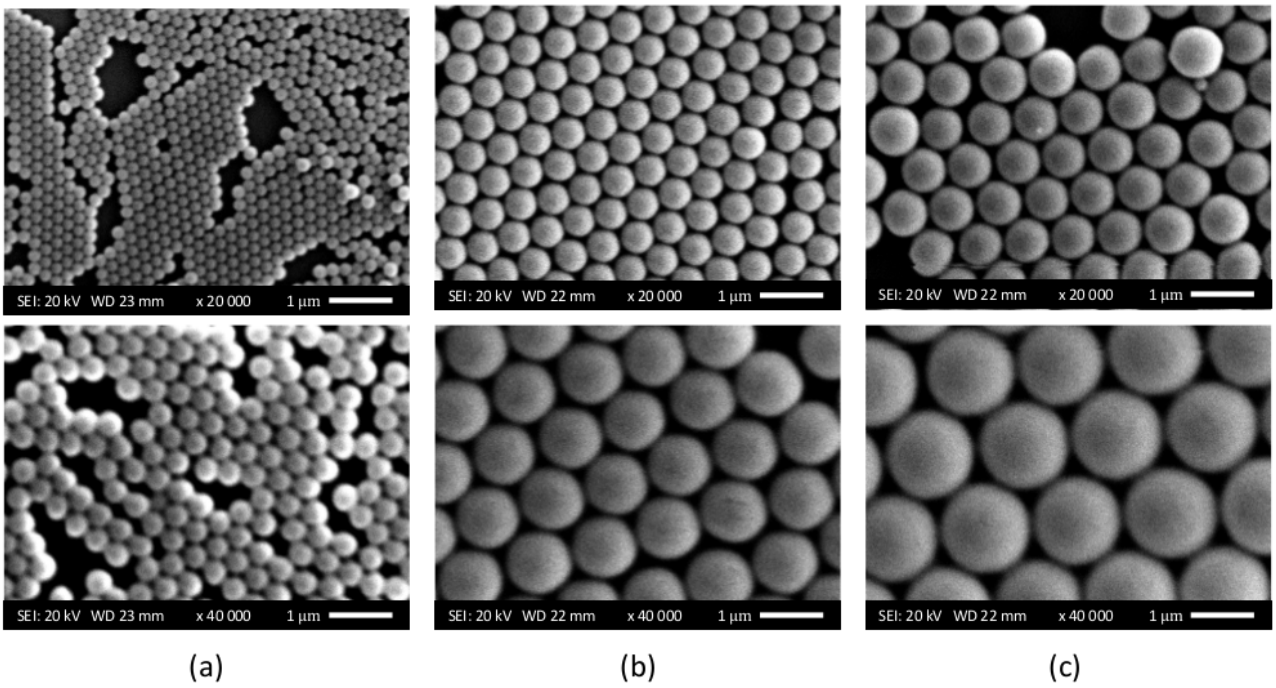

Figure 5.6: SEM images of monolayers on glass: (a) 200 nm NS, (b) 500 nm NS and (c) 800 nm NS

UV-visible absorption spectra of the monolayers on glass were recorded (figure 5.7). 200 nm

spheres show very little absorption, apart from in the UV region below 300 nm. The 500 nm spheres, however, exhibit absorption maxima at 338, 531 and 665 nm with maxima at 414, 458 and 929 nm for the 800 nm spheres. The regular array of spheres acts a two dimensional photonic structure with transmittance and absorbance at preferential wavelengths.

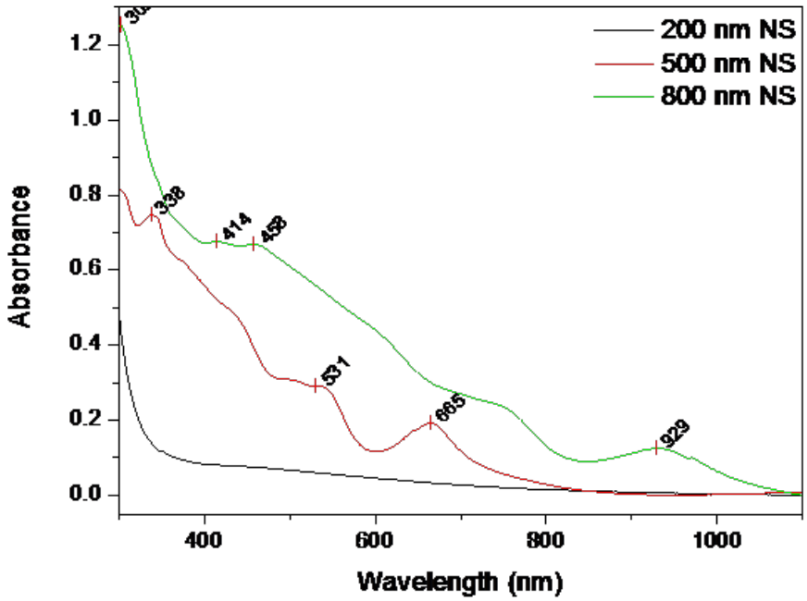

Figure 5.7: Absorption spectra of 200nm, 500 nm and 800 nm nanospheres deposited on glass

The interaction with light is dependent on the effective refractive index, n_{eff}. For our films with 500 nm spheres, n_{eff} may be calculated using the volume fractions of components, i, in the film:

$$n_{eff}^2 = \sum_{n=i} n_i^2 \phi_i \tag{5.3}$$

giving an effective refractive index of $n_{eff} = 1.46$ for our close packed polystyrene spheres ($\phi_i = 0.74$) with a refractive index of 1.59 for polystyrene [183], regardless of sphere radius. The irregularity of monolayer distributions in the film will result in not only broadening of absorption peaks but also a shift in the effective refractive index. A sparser distribution of spheres would have the effect of blue shifting peaks.

5.1.3 The effect of UV Light and Oxygen on Polystyrene Nanospheres

Oxygen plasma is routinely used to modify PS masks through reaction with O_2^+, O_2^-, O_3, ionised ozone, free electrons and other excited oxygen species [178, 184]. Furthermore, irradiation of PS with VUV light at 172 nm in air results in photolysis of the polymer backbone and oxidation of the surface [185].The morphology of the NS monolayer is therefore likely to be affected during UV treatment which results in the formation of similar excited oxygen species (equations 3.2a,3.2b) and the choice of NS used will depend on the extent to which it is affected by UV light and oxygen. Monolayers of 200, 500 and 800 nm nanospheres on glass were irradiated in oxygen for 60, 80 and 100 minutes respectively in 20 minute intervals and any erosion of the polystyrene evaluated using SEM.

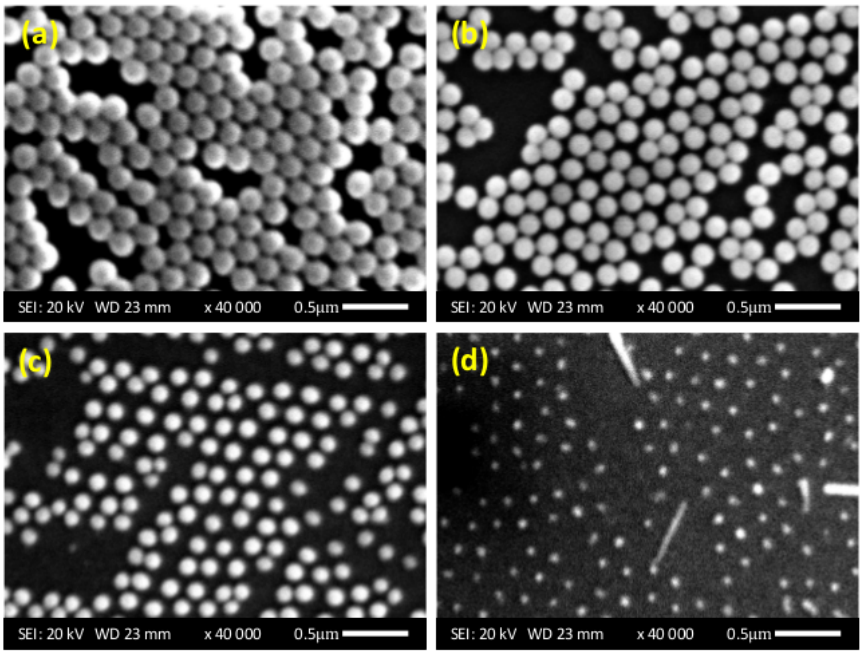

Figure 5.8: SEM images of monolayers of 200 nm spheres on glass, irradiated in standard conditions for: (a) 0 minutes, (b) 20 minutes, (c) 40 minutes and (d) 60 minutes

The 200 nm spheres suffer heavy erosion of material during UV treatment. As full reaction of 100 nm ZnPc requires 80 - 90 minutes, the sensitivity of PS to UV light and oxygen makes these nanospheres unsuitable for use other than for comparison. 500 nm and 800 nm spheres show less impact from degradation of the polymer due to their larger initial diameter (figure 5.9, 5.10). For all sizes, there is a gradual removal of material of the spheres. As the size decreases

with increasing UV irradiation time, some material appears to form links between the spheres. For 200 nm spheres, this occurs between 20 - 40 minutes, between 40 - 60 minutes with 500 nm spheres and between 40 - 60 minutes with 800 nm spheres. The formation of links continues until the spheres are too far apart. Particle diameters were measured using ImageJ, an open source image processing program. This was only possible if the nanospheres were clearly defined with no linkages in which case, measurements taken manually. The variation of particle diameter with UV treatment time is shown in figure 5.11a.

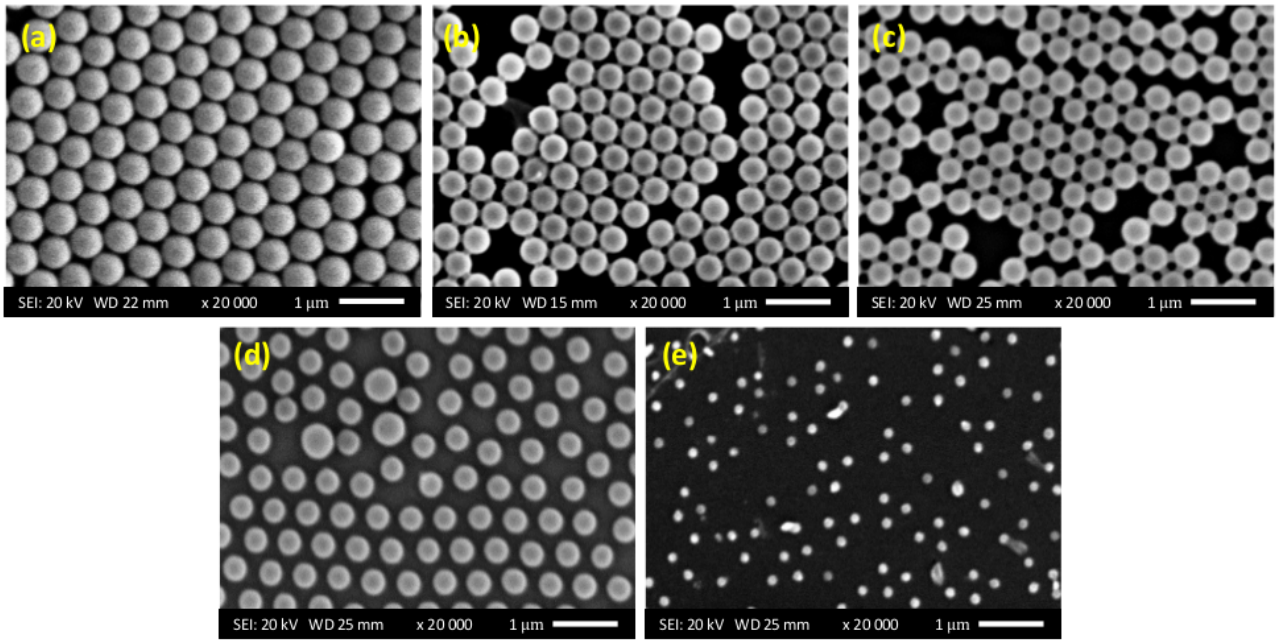

Figure 5.9: SEM images of monolayers of 500 nm spheres on glass, irradiated in standard conditions for: (a) 0 minutes, (b) 20 minutes, (c) 40 minutes, (d) 60 minutes and (e) 80 minutes

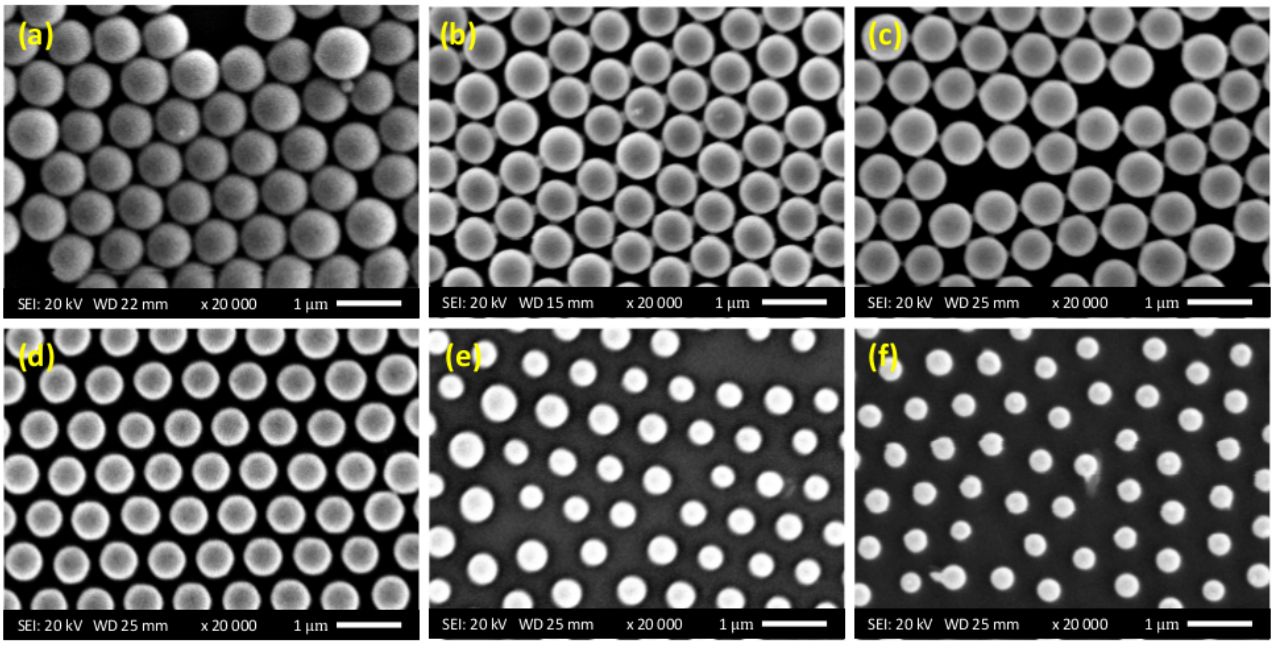

Figure 5.10: SEM images of monolayers of 800 nm spheres on glass, irradiated in standard conditions for: (a) 0 minutes, (b) 20 minutes, (c) 40 minutes, (d) 60 minutes, (e) 80 minutes and (f) 100 minutes

The SEM images demonstrate a significant decrease in the coverage of film by 500 nm NS by 60 minutes UV irradiation time and by 80 minutes for 800 nm spheres. The area of ZnPc film remaining masked by the spheres is plotted in figure 5.11b and shows that although 500 nm spheres suffer a decrease in size, the proportion of area remaining covered is higher than for 800 nm spheres. Furthermore, 500 nm spheres have been shown to form larger domains of monolayers and are therefore the most promising candidates for NSL. However, as the polystyrene will not withstand extended periods of irradiation in oxygen, the formation of arrays of ZnPc and zinc oxide nanostructures is more likely to be achieved using a thinner film which requires less irradiation time. ZnPc films of 50 nm are therefore used. From data collected in chapter 3, a 100 nm film of ZnPc will take approximately 80 minutes to fully react, therefore, the 50 nm film would be expected to degrade within approximately 40 minutes, assuming no change in the UV lamp output. Coverage by 500 nm spheres will drop from 65% to 45% during this time. Hereafter, all ZnPc films referred to are of 50 nm thickness unless otherwise stated.

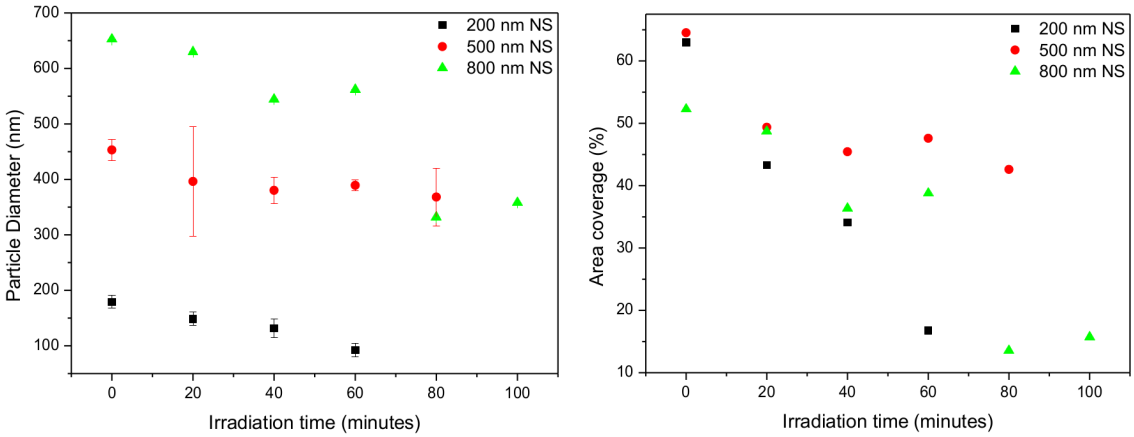

(a) (b)

Figure 5.11: Effect of UV irradiation on nanosphere size at standard conditions: (a) variation of particle diameter and (b) impact on coverage of ZnPc film

Absorption spectra of 500 nm spheres before and after irradiation for 40 minutes do indeed show a blue shift in peak positions for the two peaks at higher wavelengths, as expected from equation 2.2, despite reflectance contributions being disregarded (figure 5.12). This is not the case for the peak at 338 nm which is shifted to longer wavelengths. Interestingly, absorbance has increased in the region below 500 nm, coinciding with the B band in the absorption spectrum of ZnPc.

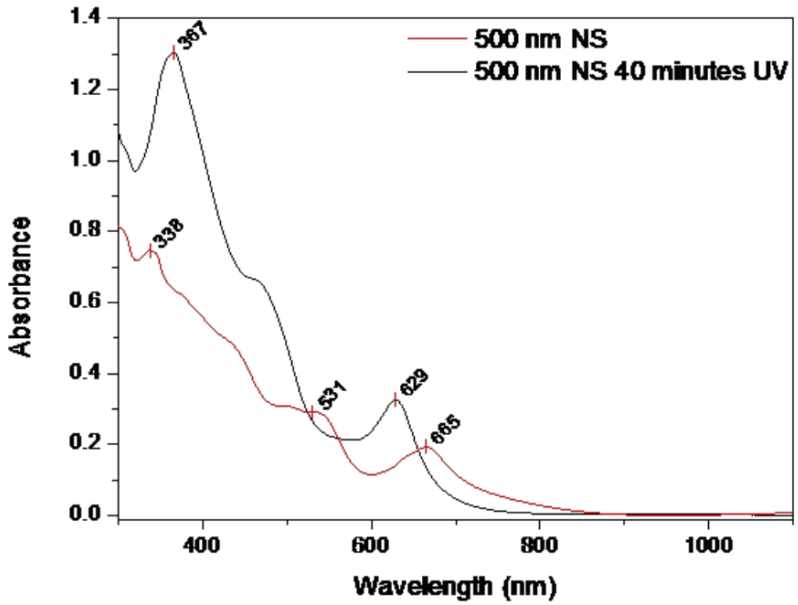

Figure 5.12: Absorption spectra of 500 nm NS monolayer films before and after irradiation in standard conditions for 40 minutes

Finally, SEM images of 200 nm NS after 40 minutes of irradiation were taken from the sample edge to provide a side view of the spheres (figure 5.13) and show that UV treatment has resulted in a flattened profile. This may affect the diffusion of oxygen into ZnPc shielded by nanospheres, however, the profile is still sufficiently raised to allow removal of the mask using adhesive tape.

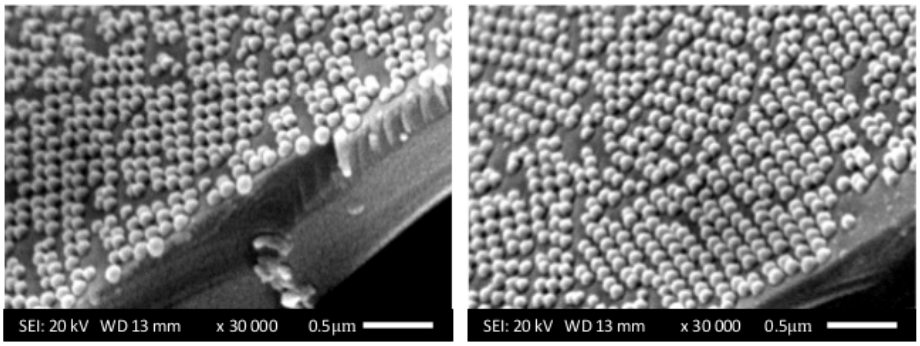

Figure 5.13: SEM images of monolayers of 200 nm spheres on glass, irradiated in standard conditions for 40 minutes, taken from the side to highlight the modified profile of the spheres

5.2 Results: Arrays Formed by Deposition of ZnPc on Nanosphere Monolayers

To create arrays of triangular ZnPc nanostructures, 50 nm films of ZnPc were grown on monolayers of 200, 500 and 800 nm nanospheres on glass.

5.2.1 Atomic Force Microscopy Imaging of ZnPc Deposited on Nanosphere Monolayers

Once ZnPc has been deposited on the monolayers, the gaps observed between nanospheres in monolayers on glass (figure 5.25) are no longer distinguishable (figure 5.14, 5.15). The nanospheres are regularly arranged and line profiles taken from samples of ZnPc on 200 nm nanospheres indicate a distance of approximately 40 nm from peak to trough between the spheres. Although the spheres themselves are 200 nm in diameter, much of the space between the spheres has been filled by deposition of ZnPc

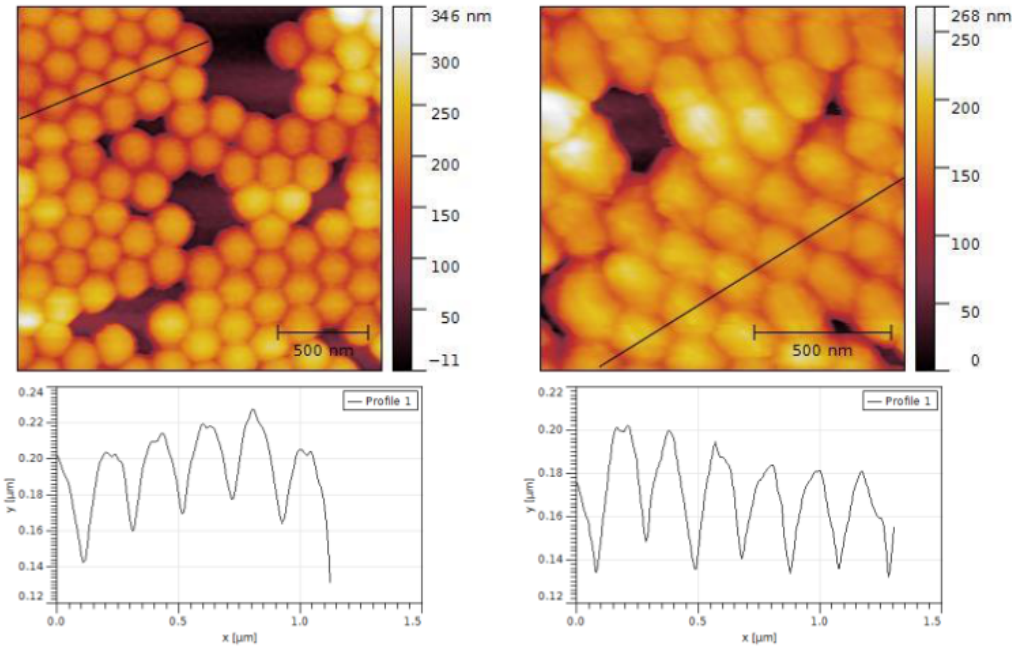

Figure 5.14: AFM images of ZnPc deposited on monolayers of 200 nm nanospheres with line profiles taken as indicated on the images

A line profile taken from the AFM image of ZnPc on 800 nm nanospheres gives a peak to trough distance of approximately 130 nm, considerably smaller than the nanosphere height (figure 5.15). The single nanosphere shown has a height of 250 nm. As only 50 nm of ZnPc are deposited on top of the nanospheres, this suggests that the spaces between the spheres are not filled with ZnPc before the gap between spheres accumulates enough ZnPc to close. Grains of crystalline ZnPc are just distinguishable on the surface of the nanosphere. What is particularly noticeable in this film is the hexagonal appearance spheres have taken on upon deposition of ZnPc as a result of the smallest gaps between spheres becoming occluded. A vacancy has been highlighted in red and the ZnPc has deposited, unevenly though the void. The spheres themselves cast a shadow on the areas beneath them and ZnPc has deposited between the spheres surrounding a void, without accumulating directly below them, resulting in the uneven film growth seen, as shown in the schematic below (figure 5.16). Line profiles taken across the void yield a depth of approximately 80 nm.

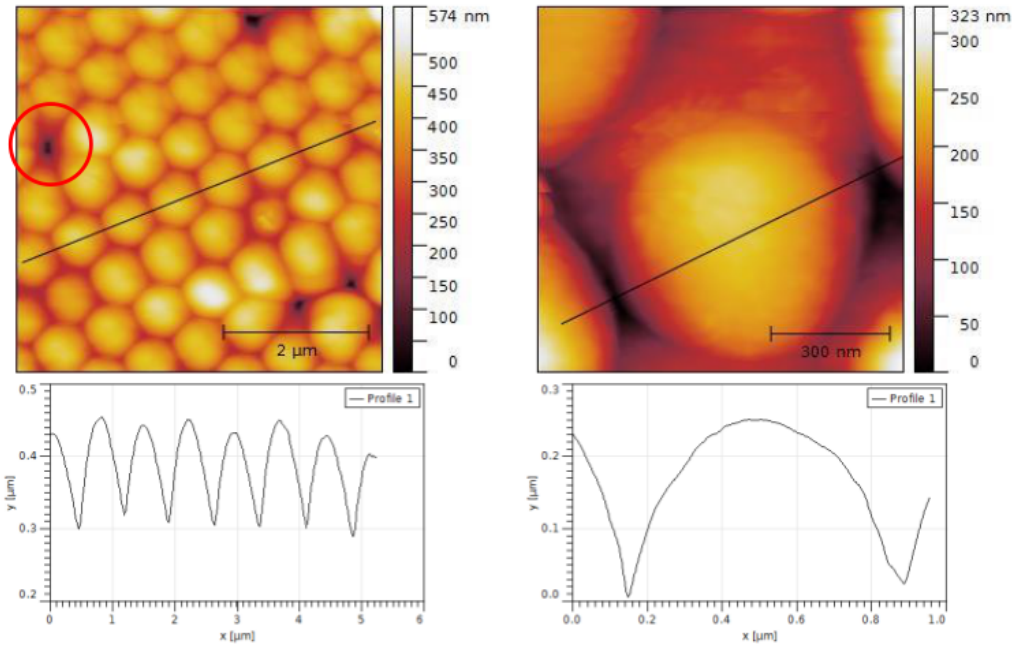

Figure 5.15: AFM images of ZnPc deposited on monolayers of 800 nm nanospheres with line profiles taken as indicated on the images and a void left by an absent nanosphere indicated in red

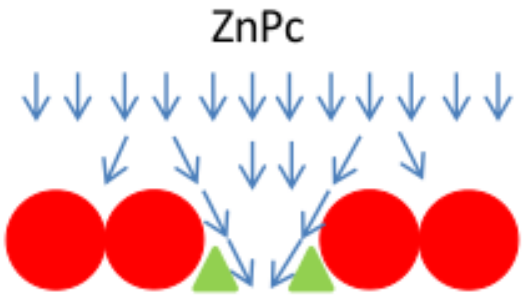

Figure 5.16: Schematic to show deposition of ZnPc into a void created by absence of a nanosphere

5.2.2 Atomic Force Microscopy Imaging Following Removal of Nanosphere Monolayers

AFM images were taken of ZnPc films deposited on monolayers of 200, 500 and 800 nm nanosphere monolayers following removal of the nanospheres.

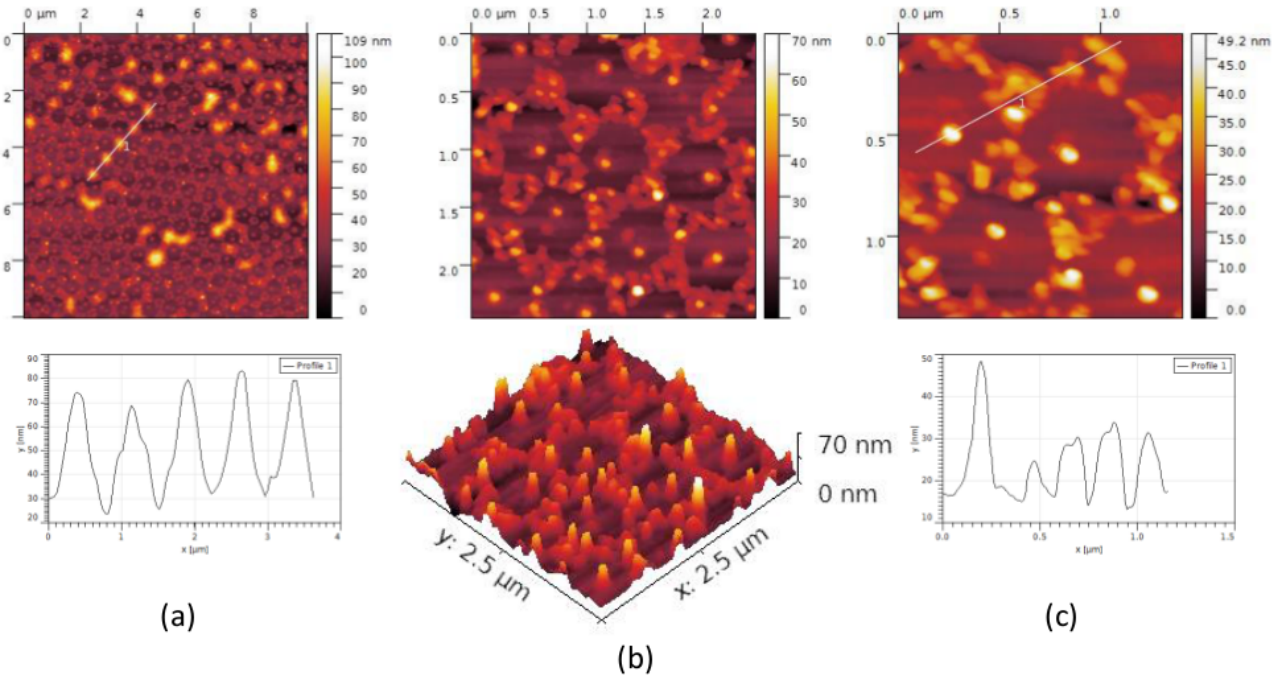

Figure 5.17: AFM images of ZnPc deposited on monolayers of 800 nm nanospheres and the nanospheres removed: (a) a 10 µm image and a line profile taken where indicated, (b) a 2.5 µm image showing triangular structures and a 3D view and (c) a 1.5 µm image with a line profile taken as shown

Removal of the 800 nm nanospheres left a regular hexagonal array of dark circles, easily identified in figure 5.17a. These are areas which were shielded from ZnPc deposition by nanospheres subsequently removed, as is clear from the topography in the region and the line profile taken across a row of raised features. The height of these prominent features is between 40 - 50 nm and is therefore a result of ZnPc deposition in voids where there were no nanospheres present during deposition. Other features are more clearly observed in higher resolution images. Surrounding each circular region bare of ZnPc are 6 roughly triangular structures which are the ZnPc nanostructures expected to form at the interstices of the nanosphere array. The average distance between neighbouring triangular structures is 430 ± 20 nm which is very close to the distance $d_{np} = 462$ nm given by equation 5.2 confirming that these triangular structures are indeed those we aimed to create. At the centre of each circle is a raised point which may be due to residual polystyrene remaining at the point of contact between the nanosphere and substrate when the mask was removed. The distances between these raised points is approximately 800 nm, corresponding well to the sphere diameter. The 3D view shows the relative positions and

heights of PS residue and triangular nanostructures more clearly.

The diameter of circles left bare by nanospheres was expected to be 800 nm, however, they measure 570 ± 40 nm, demonstrating that the nanospheres do not effectively shield the region below during deposition of ZnPc and diffusion of ZnPc occurs beneath the spheres. Assuming that ZnPc was effectively deposited between the spheres, the height of triangular nanostructures would be 50 nm. Measurement of a range of line profiles as shown in figure 5.17c yields an average height of 24 ± 11 nm which may be due to the increased width as a result of ZnPc diffusion laterally below the spheres. Interestingly, the triangular structures have a dimple at the centre which suggests that either ZnPc deposits preferentially on silicon and polystyrene, rather than itself or that the aperture through which ZnPc must flow is small enough to affect the flow direction.

AFM images of structures observed after removal of 500 nm spheres repeat findings from AFM images from 800 nm monolayer films (figure 5.18). There are some very prominent features visible on the left of the image in figure 5.18a with a height of 510 ± 20 nm and these are clearly 500 nm spheres which have not been removed. As for results from 800 nm nanospheres, this image also has evidence of voids in which ZnPc has deposited, giving a height greater than the majority of the film once the nanospheres are removed. The morphology of the triangular structures is much clearer with 500 nm nanospheres and measurement across those in figure 5.18b gives a height of 12 ± 4 nm, much smaller than those measured in the previous images. Furthermore, the dimple seen in the centre of the triangular structures is far more conspicuous from which it may be inferred that the flow of ZnPc is indeed disrupted by a narrow aperture through the interstices of the hexagonal nanosphere array as the effect is enhanced as the vertical height of the triangles, h, as shown in figure 5.3 decreases from 186 nm with 800 nm nanospheres to 117 nm with 500 nm nanospheres (equation 5.1).

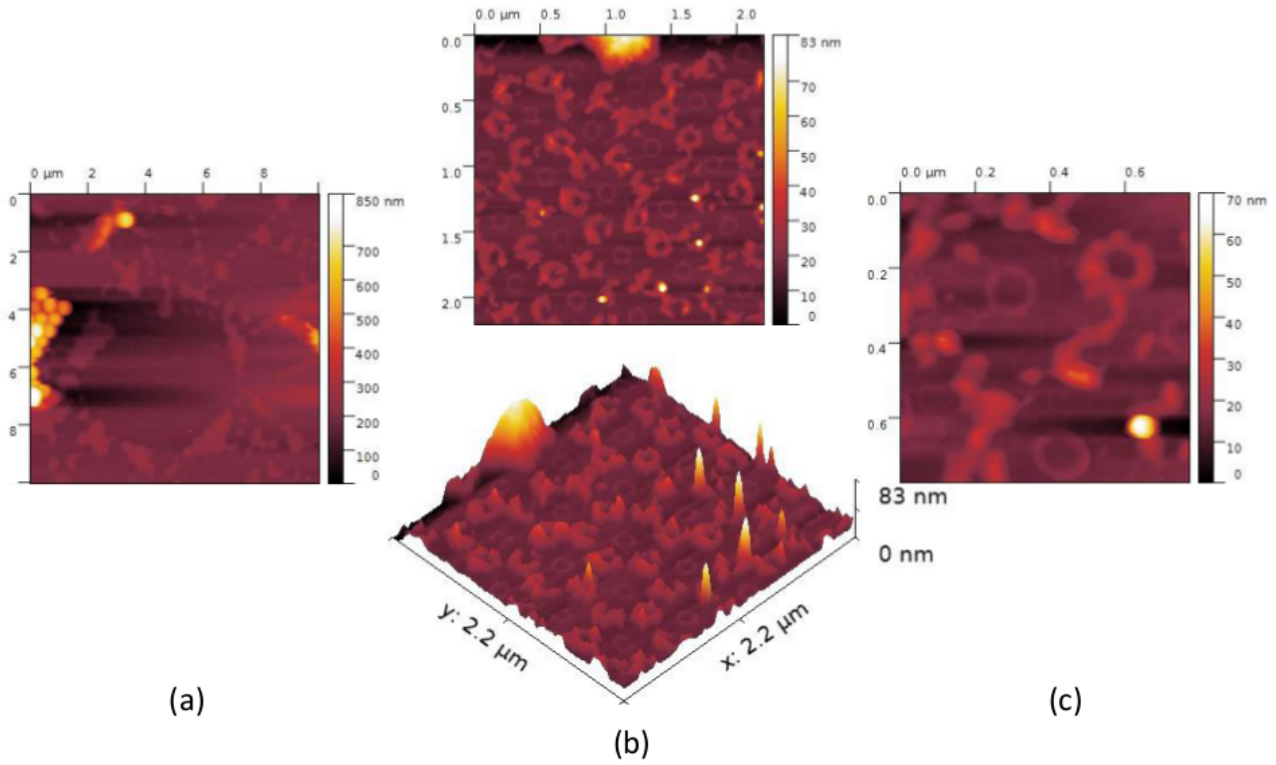

Figure 5.18: AFM images of ZnPc deposited on monolayers of 500 nm nanospheres and the nanospheres removed: (a) a 10 µm image with polystyrene nanospheres remaining, (b) a 2.25 µm image showing triangular structures and a 3D view and (c) a 0.8 µm image focusing on the structures formed around one nanosphere

Measurement of several circles bare of ZnPc in figure 5.18b gives an average diameter of 380±40 nm which is again less than the diameter of the nanospheres used. The distance measured between neighbouring triangular features is 280 ± 10 nm, very close indeed to the distance, d_{np} = 289 nm predicted by equation 5.2. The 3d view highlights the regularity of the array of features and with figure 5.18c shows clearly the effect of a narrow aperture on deposition of ZnPc between spheres as the dimples in the triangular structures is very well-defined, with an appearance similar to hollow cylinders. Interestingly, the features considered to be polystyrene residue observed in films after removal of 800 nm spheres (figure 5.17) are not reproduced faithfully here. The region exposed by removal of 500 nm spheres now contains a ring, rather than a spot. This suggests that the ring is in fact an accumulation of ZnPc at the base of the sphere and that little polystyrene remained on the surface after nanosphere removal. The reason for this is unclear but the distances separating the rings are approximately equal to 500 nm, the diameter of spheres used.

Images of structures formed by deposition of ZnPc on 200 nm nanosphere monolayers following removal of the spheres show far less regularity than with either 500 or 800 nm nanospheres (figure 5.19). Many areas where nanospheres remain are visible in figure 5.19a and line profiles such as that shown at the bottom of the image indicate a height in excess of 70 nm which confirms that these features are the result of residual nanospheres and not from deposition of ZnPc in voids. Such voids are more clearly seen in figure 5.19b where a line has been drawn through a row on the right hand side of the image. The height of these features is between 20 - 30 nm. It was not possible to image any circular or triangular features due to the poor regularity of the films and the high number of nanospheres and voids.

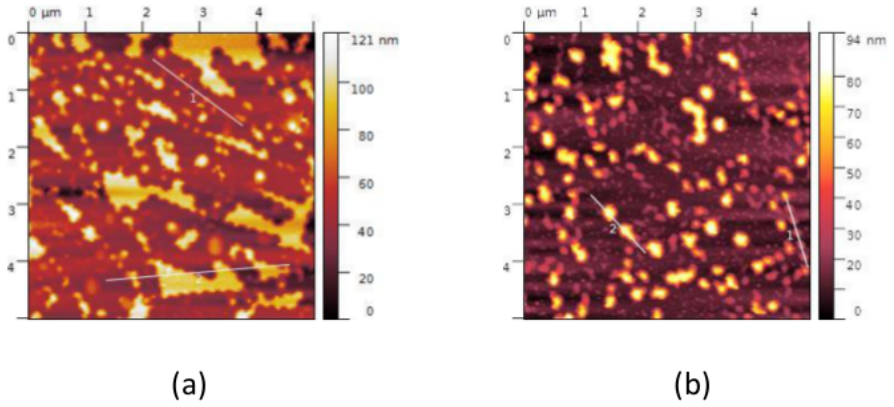

Figure 5.19: AFM images of ZnPc deposited on monolayers of 200 nm nanospheres and the nanospheres removed: (a) a 5 µm image with polystyrene nanospheres remaining and (b) a 5 µm image with ZnPc deposited in voids highlighted by line profile 1

5.2.3 Absorption Spectra of ZnPc Deposited on Nanosphere Monolayers

Absorption spectra of ZnPc deposited on nanosphere monolayers were recorded and compared to those of constituent films and of nanospheres deposited on ZnPc (figure 5.20).

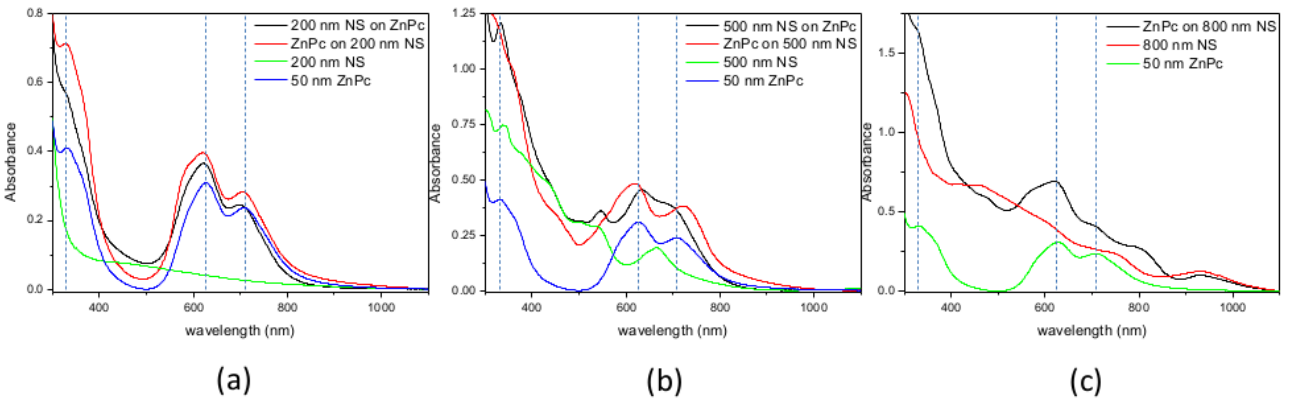

Figure 5.20: Absorption spectra of films of (a) 200 nm NS monolayers on ZnPc and ZnPc deposited on 200 nm NS monolayers, (b) 500 nm NS monolayers on ZnPc and ZnPc deposited on 500 nm NS monolayers, (c) ZnPc deposited on 800 nm NS monolayers and constituent components. Guides to the eye drawn at wavelengths corresponding to absorption peaks of ZnPc

ZnPc deposited on 200 nm NS displays more characteristics arising from the absorption spectrum of ZnPc than when nanospheres are deposited on ZnPc (figure 5.20), in particular, the peak in the B band of ZnPc is visible in the spectrum of ZnPc on nanospheres. This is not repeated in the spectra with 500 nm or 800 nm nanospheres as the proportion of ZnPc relative to polystyrene is reduced (figure 5.20b,c). What is noticeable with 500 nm nanospheres is that the lower intensity peak in the Q band has been shifted to a higher wavelength when ZnPc is deposited on the nanospheres, compared to when nanospheres are deposited on ZnPc. Although this could be explained by an increase in effective refractive index (equations 5.3,2.2), the same cannot be said for the higher intensity peak in the Q band of ZnPc which has been shifted to lower wavelengths when ZnPc is deposited on 500 nm nanospheres. It is possible that deposition of ZnPc on a monolayer affects the reflectance and this will affect the absorbance.

Following removal of the nanosphere mask, the percentage of ZnPc remaining was calculated by integration of the Q band region in the absorption spectra (figure 5.21) and is given in table 5.2.

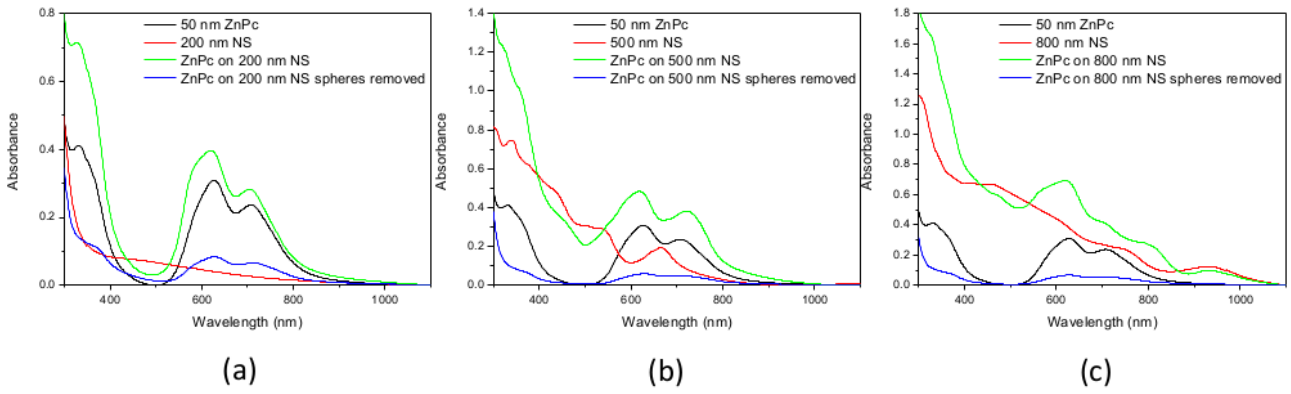

Figure 5.21: Absorption spectra of films before and after removal of nanospheres: (a) ZnPc deposited on 200 nm NS monolayers, (b) ZnPc deposited on 500 nm NS monolayers, (c) ZnPc deposited on 800 nm NS monolayers

Table 5.2: Percentage of ZnPc film remaining following removal of nanospheres

Film	Percentage of ZnPc remaining
ZnPc on 200 nm NS	31
ZnPc on 500 nm NS	22
ZnPc on 800 nm NS	26

As a perfect monolayer of nanospheres will cover 78.5% of the substrate, if ZnPc was deposited between the nanospheres to a thickness of 50 nm, it would be expected that 21.5% of ZnPc would remain following removal of nanospheres. The values for 200 and 800 nm nanospheres given in table 5.2 are both higher than this, but the amount of film remaining after removal of 500 nm nanospheres is as expected. As AFM images of ZnPc deposited on monolayers showed (figures 5.14,5.15), there were areas where no nanospheres had adhered. This was further confirmed in AFM images taken after removal of nanospheres (figures 5.19,5.18,5.17) in which raised areas were observed where ZnPc had deposited and remained when the nanospheres were removed. This will have the effect of increasing the absorption due to ZnPc and had resulted in a higher percentage of film remaining on the surface. The spectra themselves have lost all characteristics seen in nanosphere spectra, indicating that a high proportion were removed, despite observation of some remaining nanospheres in the 500 nm sample (figure 5.18).

5.3 Results: Nanosphere Lithography on ZnPc Films

5.3.1 Absorption Spectroscopy of Nanosphere Monolayers on ZnPc Films

Prior to deposition of nanospheres on ZnPc, absorption spectra of 50 nm thick films of ZnPc were taken, as-deposited and after 40 minutes of UV treatment (figure 5.22). Peaks identifying transitions in the Q band and B band at 626 nm and 331 nm respectively agree with spectra measured in previous chapters (sections 3.2.3,) and with the literature [96].

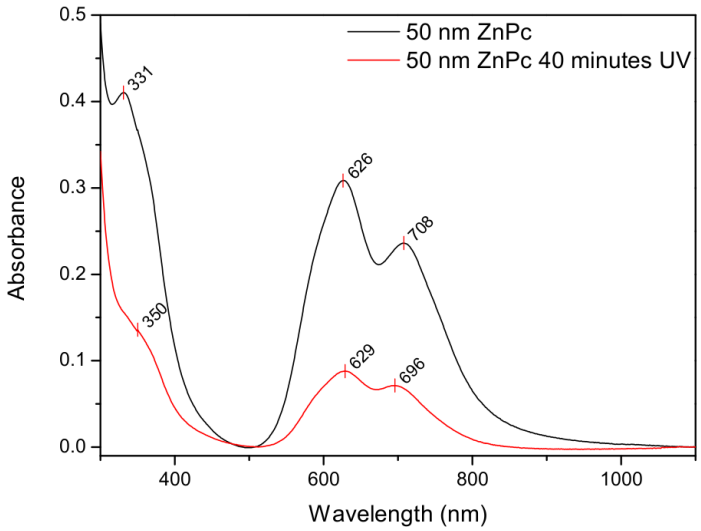

Figure 5.22: Absorption spectra of 50 nm films of ZnPc, as-deposited and after irradiation in standard conditions for 40 minutes

As a 100 nm film degraded in 80 minutes, it would be expected that these 50 nm ZnPc films would be fully degraded in 40 minutes, however, integration of the Q band shows that 24% of ZnPc film remains, equivalent to approximately 12 nm. The output of the excimer lamp does decrease with continual use and at this point, the lamp was nearing the end of its life, having been in use for several years. However, all UV irradiation was taken within a relatively short period, avoiding superfluous lamp use and the output is therefore unlikely to vary significantly over the samples irradiated in this chapter.

Monolayer coverage shields 78.5% of the film from UV light and 21.5% of the ZnPc film is directly illuminated by UV light. Therefore, neglecting the effect of diffusion of excited oxygen

species, 21.5% of film following UV treatment would have a thickness of 12 nm and the remainder would still be 50 nm. We would therefore expect irradiation of NS monolayers on ZnPc to result in removal of at least 16.3% of ZnPc. The actual amount removed is likely to be higher due to oxygen assisted degradation affecting ZnPc shielded by the nanospheres and due to the gradual decrease in sphere diameter. The features produced by this process are also likely to be modified by these factors.

Despite the hydrophobicity of ZnPc, demonstrated by its high contact angle, polystyrene nanospheres were successfully deposited on ZnPc films, an achievement which has not been reported prior to this. 200 nm and 500 nm nanospheres deposited on 50 nm ZnPc result in composite films with absorbance largely composed of a superposition of individual component films (figure 5.23). The 200 nm NS layer on ZnPc is simply the sum of the individual absorbances as any diffraction modes are outside the range of wavelengths measured, although there is a very slight shift of up to 6 nm to lower wavelengths. Similarly for 500 nm NS on ZnPc, however, here there are resonance modes at 535 and 330 nm where absorption has been enhanced slightly beyond mere superposition of absorbance. The films were irradiated for 40 minutes and absorption spectra taken before and after removal of nanospheres then compared to those for as-deposited films (figure 5.24).

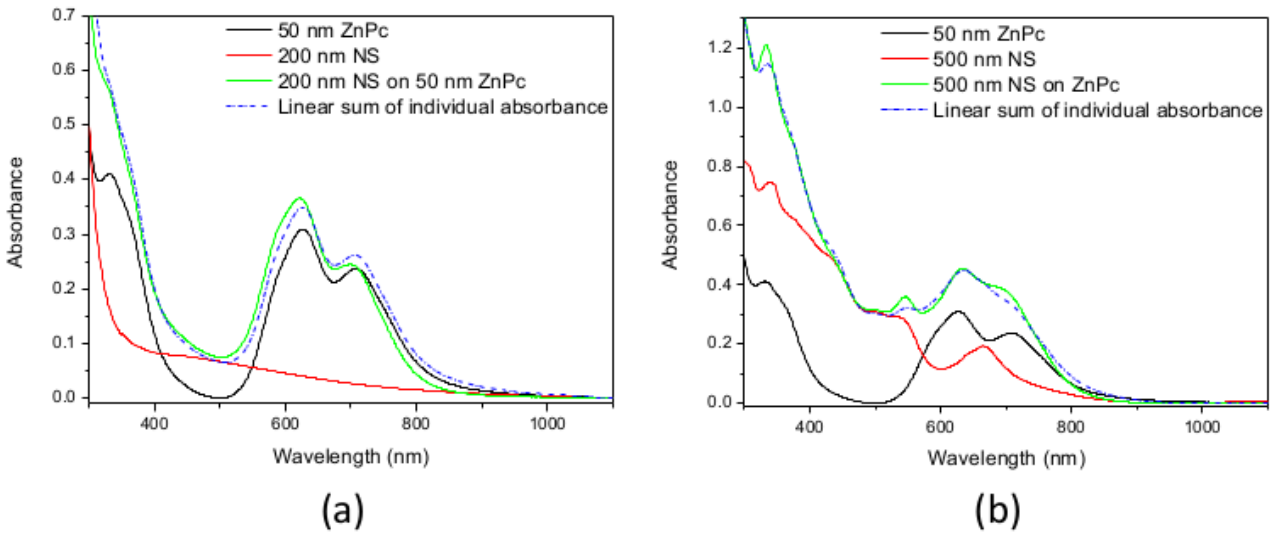

Figure 5.23: Absorption spectra of (a) 200 nm nanosphere monolayers and (b) 500 nm nanosphere monolayers on 50 nm films of ZnPc, with spectra for nanospheres on glass and the linear sum of individual absorbances for comparison

ZnPc coated with 200 nm NS shows a decrease in absorption upon radiation with little change after removal of the nanosphere mask. It is possible that some nanospheres remain on the surface but the most likely reason for little change after removal of nanospheres is that much of the polystyrene has been degraded during the process. Integration of the Q band after NS removal shows that 14% of the ZnPc film has been removed which is lower than the expected value of 16%. ZnPc coated with monolayers of 500 nm NS showed an increased absorption after UV irradiation with peaks at wavelengths of 356 and 623 nm, similar to the increase seen in 500 nm nanospheres after UV treatment, where peaks were observed at 367 and 629 nm (figure 5.12). Much of the absorption is due to the NS as shown by the spectrum obtained after removal of the 500 nm NS. Integration of the Q band gives a value of 24% for the amount of ZnPc removed which is greater than the minimum film removal expected. As the polystyrene is gradually eroded during the UV process, a larger area of ZnPc film is exposed to UV light. This, in combination with oxygen-assisted degradation results in greater film removal.

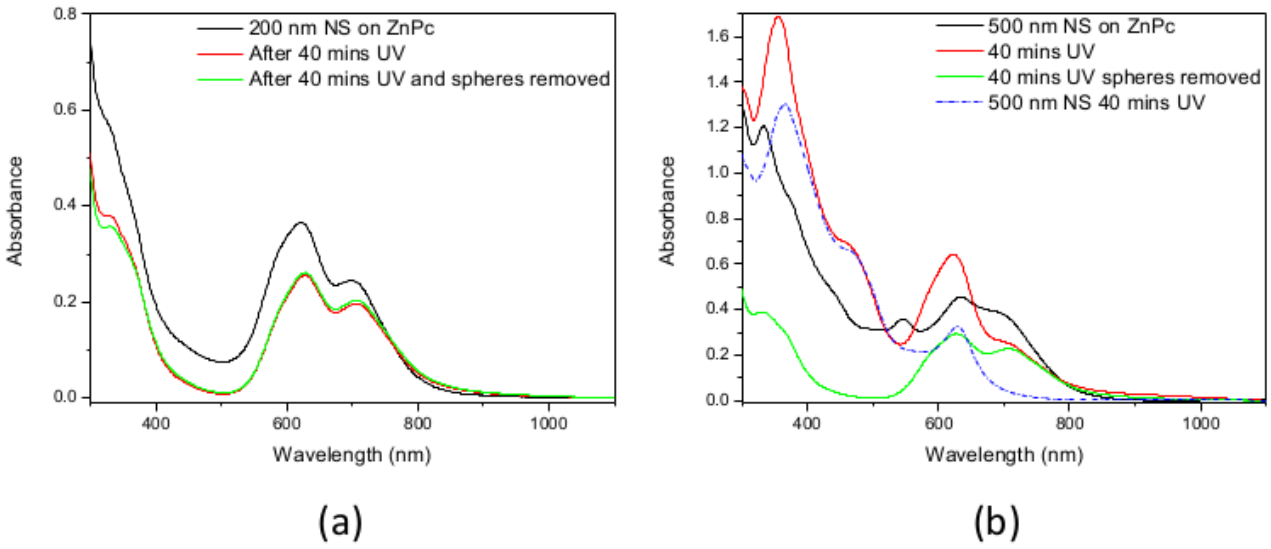

Figure 5.24: Absorption spectra after 40 minutes of UV treatment, before and after removal of the nanosphere mask: (a) 200 nm nanosphere monolayers and (b) 500 nm nanosphere monolayers on 50 nm films of ZnPc, with spectra for as-deposited nanospheres on ZnPc

5.3.2 Scanning Electron Microscopy Images of Nanosphere Monolayers on ZnPc Films

SEM images of monolayers on ZnPc demonstrate the effect of hydrophobicity on nanosphere adhesion (figure 5.25). 200 nm nanospheres deposited on ZnPc form domains of monolayers with far less regularity than when deposited on glass with frequent clustering of spheres (figure 5.25a,b). The 500 nm nanospheres do still form larger areas of monolayers than the 200 nm nanospheres, but the impact of the hydrophobic nature of ZnPc is evident in the smaller domain size and greater prevalence of voids and dislocations (figure 5.25c,d). Despite this, 500 nm nanospheres on ZnPc form monolayers covering the majority of the surface and the results of NSL will be observable. Films with monolayers of 200 and 500 nm NS were both irradiated for 40 minutes in standard conditions.

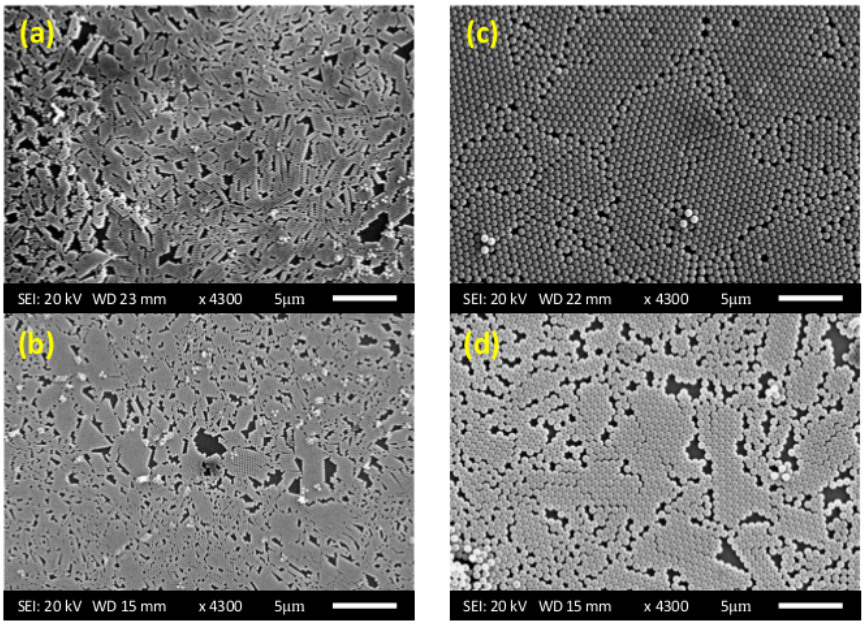

Figure 5.25: Scanning electron microscopy images of nanosphere monolayers: (a) 200 nm nanospheres on glass, (b) 200 nm nanospheres on ZnPc, (c) 500 nm nanospheres on glass and (d) 500 nm nanospheres on ZnPc

SEM images of irradiated nanosphere monolayers on ZnPc show a large removal of mask material from the 200 nm NS on ZnPc (figure 5.26a,b), whereas 500 nm NS on ZnPc still retain a masking effect (figure 5.26c,d).

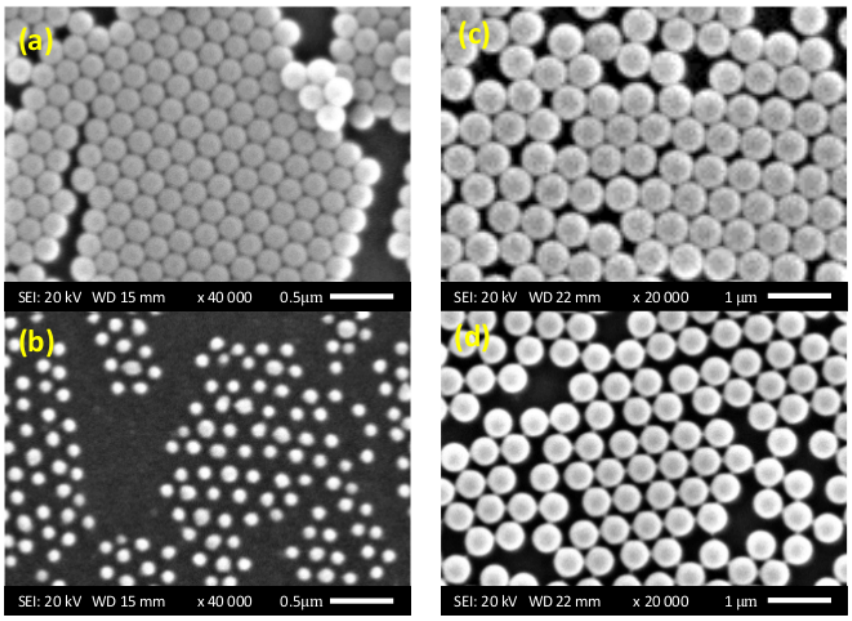

Figure 5.26: Scanning electron microscopy images of nanosphere monolayers: (a) 200 nm nanospheres on ZnPc, (b) 200 nm nanospheres on ZnPc after 40 minutes of UV irradiation in standard conditions, (c) 500 nm nanospheres on ZnPc and (d) 500 nm nanospheres on ZnPc after 40 minutes of UV irradiation in standard conditions

Following removal of the nanospheres using adhesive tape, the samples were analysed using atomic force microscopy.

5.3.3 Atomic Force Microscopy Imaging of Films Following Removal of Nanospheres

As the nanosphere diameter is reduced by interaction with UV light and oxygen, the profile of features created by the masking effect of the nanospheres is unlikely to be cylindrical and is more likely to take the form of a truncated cone. Similarly, the triangular arrays of zinc oxide are likely to exhibit a concave surface as the centre will have been irradiated for longer than the edges more recently exposed by erosion of the nanospheres. AFM images of monolayers of 200 nm NS on ZnPc films following UV irradiation and removal of the mask are shown in figure 5.27.

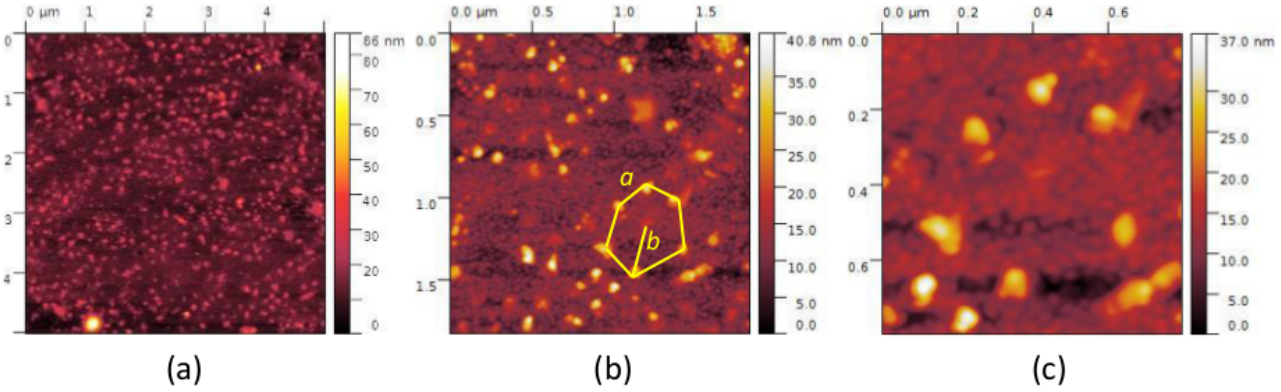

Figure 5.27: AFM images of 200 nm NS on ZnPc, following irradiation for 40 minutes and removal of nanospheres: (a) 5 µm image, (b) 2 µm image with a hexagonal arrangement of features identified and (c) higher resolution 0.8 µm image of the hexagonal arrangement

The lower resolution AFM image after removal of 200 nm NS shows a few areas of regularly arranged ZnPc features (figure 5.27a). The expected hcp arrangement of truncated cones is difficult to identify and the final size of nanostructures formed is small, as indicated by the height scale of the highest resolution image (figure 5.27c). One set of ZnPc structures arranged as a hexagon have been highlighted in figure 5.27b. The average distance from the centre of the hexagon to its vertices (b) is 240 ± 40 nm and the average length of the sides of the hexagon, a, is 260 ± 60 nm. From the diameter of the nanospheres, the expected value for both a and b is 200 nm and this arrangement is highly likely to be seven ZnPc nanostructures remaining after NS removal. In the background of these structures, residual ZnPc crystallites are clearly visible with inter-grain distances of approximately 40 nm as was observed for as-deposited ZnPc in chapter 3.

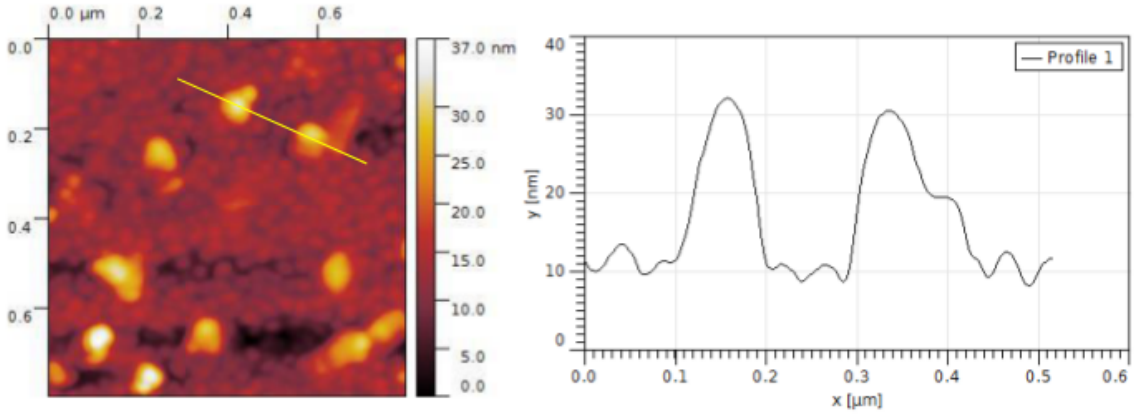

Figure 5.28: AFM image of ZnPc coated with a monolayer of 200 nm nanospheres, irradiated and nanospheres removed, with a line profile taken across two features as indicated

A line profile taken across two of the structures within the hexagonal arrangement yields a height of approximately 21 nm for the two taller structures with heights of approximately 3 - 4 nm for the ZnPc grains in the background. The expected height for ZnPc nanostructures from absorption spectroscopy (section 5.3.1) is 38 nm and the effect of erosion of the 200 nm nanospheres has been to reduce the final height of the ZnPc pillars.

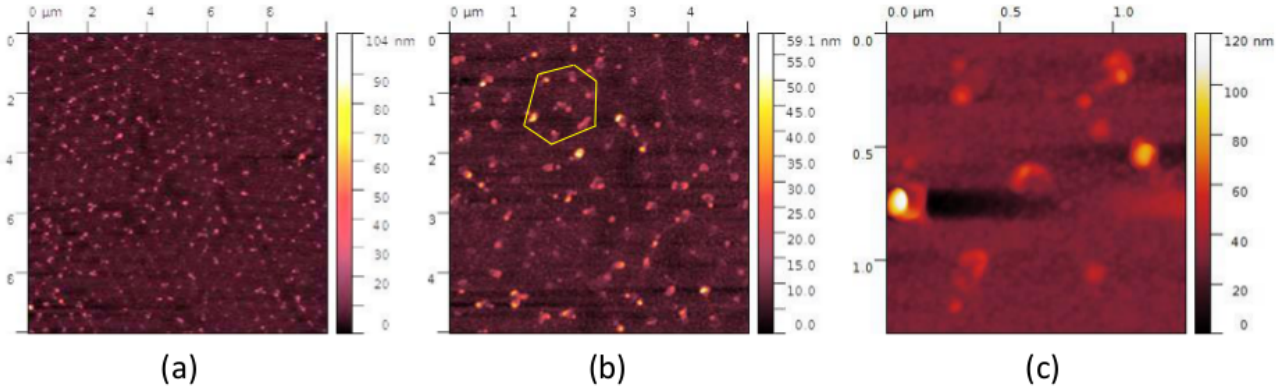

Figure 5.29: AFM images of 500 nm NS on ZnPc, following irradiation and removal of nanospheres: (a) 10 µm image, (b) 5 µm image with a hexagonal arrangement of features identified and (c) higher resolution 1.5 µm image of the hexagonal arrangement

A far more regular arrangement of nanostructures is visible in the image of ZnPc film with 500 nm nanospheres removed (figure 5.29a) and many more take the hcp arrangement expected. One such arrangement has been highlighted in figure 5.29b in which the average distance between the nanostructures is 600 ± 90 nm, very close to the 500 nm expected. As for 200 nm nanospheres, polystyrene erosion and oxygen diffusion have an impact which is confirmed not only by absorption spectroscopy which indicated removal of 24% of ZnPc (section 5.3.1), but also by examining the line profile of features seen in figure 5.29c.

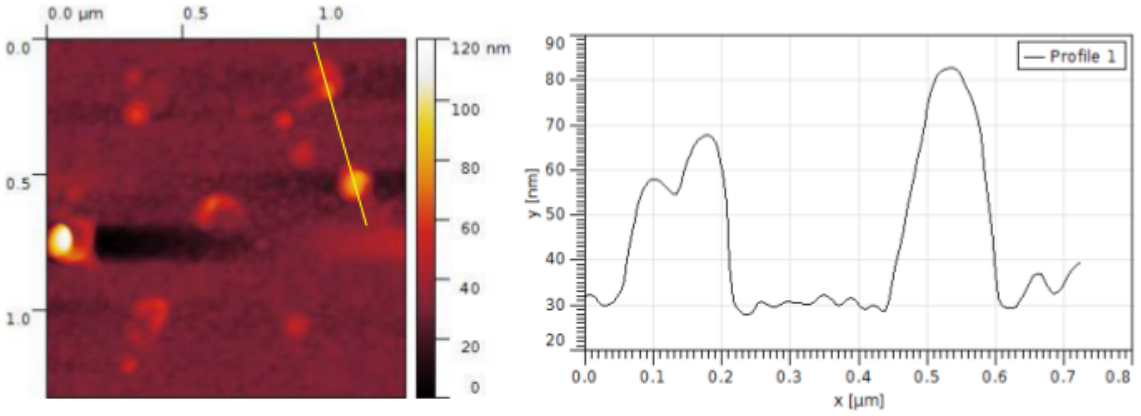

Figure 5.30: AFM image of ZnPc coated with a monolayer of 500 nm nanospheres, irradiated and nanospheres removed, with a line profile taken across two features as indicated

The line profile in figure 5.30 gives a pillar height of 40 - 50 nm with a width of 180 - 200 nm. The expected height and width were 38 and 500 nm respectively but that was calculated by taking no account of nanosphere erosion or the impact of oxygen-assisted degradation which have both clearly affected the final size of features. Although irradiation for 40 minutes was not quite sufficient for all the exposed ZnPc to degrade and form zinc oxide, monolayers of 500 nm nanospheres do produce an array of ZnPc nanostructures.

5.4 Conclusion

Nanosphere lithography applied to ZnPc films and combined with the UV and oxygen assisted degradation of the film through the mask to form zinc oxide is partially successful as a technique to create patterned arrays of nanostructures. Careful choice of nanosphere size to allow conversion of ZnPc to oxide without excessive loss of polystyrene due to degradation by UV light produces truncated cones of ZnPc surrounded by zinc oxide and any unreacted ZnPc with cones appearing in a hexagonal array of spacing equivalent to the size of nanosphere used. The width of ZnPc pillars formed after UV irradiation and subsequent removal of the mask is smaller than the nanosphere size due to the effect of oxygen assisted degradation which affects the periphery of ZnPc shielded from UV light by the nanospheres. The polystyrene mask is almost completely removed by a simple technique using adhesive tape.

Absorption spectra are largely a superposition of individual component spectra and are used to determine the percentage of ZnPc remaining. Values of ZnPc removed exceed those expected, confirming an erosion of nanosphere resulting in reduced masking and therefore an increase in ZnPc degraded by UV light.

Deposition of ZnPc on monolayers of nanospheres followed by subsequent removal of the nanosphere mask successfully creates an array of triangular nanostructures in positions corresponding to interstices of the hexagonally arranged nanospheres. The nanostructures are regularly spaced at a distance given by the geometry of hexagonal close packed spheres. Although some ZnPc diffuses to deposit under the edges of the nanospheres, no ZnPc is present in the majority of the circular region screened by the spheres. Removal of spheres is successful but a residue of polystyrene remains in the centre of each bare circle. The narrow aperture of interstitial sites results in a disruption to the flow of ZnPc to the substrate, an effect which increases with decreasing nanosphere size. An unexpected consequence is a scarcity of ZnPc in the centre of the triangular nanostructure. Combined with diffusion of ZnPc beneath the spheres, disruption of ZnPc flow results in the formation of centrally vacant triangular structures similar to hollow cylinders. Deposition of ZnPc on the surfaces of the spheres results in a narrowing of the aperture and an eventual obstruction of flow with the consequence that the nanostructures formed have a height lower than expected.

Absorption spectra of ZnPc on nanospheres are not simply a superposition of individual spectra as deposition of ZnPc between spheres results in a higher effective refractive index and in the case of 800 nm nanospheres, this is observed as a shift of transmission peaks to higher wavelength. The peaks for 500 nm nanospheres, however, overlap the electronic transitions of ZnPc making it difficult to distinguish the impact of a raised effective refractive index.

As polystyrene is sensitive to oxygen and UV light when combined, the use of silica nanospheres would improve results substantially by the creation of features with higher definition if cylindrical pillars are required. The photonic effects of an array of nanostructures in a matrix depend on the difference between the refractive indices of the material the nanostructures are composed of and the matrix itself. In addition, the dimensions and arrangement of the nanostructures are

also important. As degradation of a 50 nm film of ZnPc will produce a film of zinc oxide only a few nm thick, we have essentially created arrays of two types of ZnPc nanostructure surrounded by air. Modification of spacing is easily effected by choice of nanosphere, thus photonic effects would be dependent on the relative refractive indices of air and ZnPc.

Chapter 6

Conclusion

6.1 The Mechanism of Oxide Formation

Comparison of two similar molecules forming films with contrasting morphology has been used to determine the relative influence of the two mechanisms involved in the formation of zinc oxide from metal organic precursors using UV light and oxygen. The process can proceed either through direct scission of organic bonds upon absorption of UV light or through bond breakage by excited oxygen species produced by the interaction of oxygen with UV light.

XRD scans and AFM imaging of α-ZnPc showed that a crystalline morphology was maintained throughout ZnPc degradation with the diffraction peak corresponding to the α modification decreasing in intensity as the film was removed. This was accompanied by a linear increase in surface roughness and increasing grain size. ZnTPP, however, was initially amorphous, developing a grain like structure under UV treatment which coincided with an increase in roughness, then returning to the original smooth, featureless surface of the as-deposited film once ZnTPP was removed. Absorption spectra revealed differences in the kinetics of degradation in the precursor films, with ZnPc exhibiting a linear rate of film removal at 1.3 nm/minute and ZnTPP two separate regimes, the first at 0.3 nm/minute but the second, a linear rate equal to that for ZnPc and occurring only when the morphology of ZnTPP had taken on a grainy structure. Overall, the time taken for ZnTPP to fully react was significantly longer than for the

crystalline film of ZnPc. From these results, it was inferred that morphology was fundamental in determining the rate of film removal. The acceleration in degradation for ZnTPP from 0.3 to 1.3 nm/minute upon formation of a grainy structure implied an increased effect due to the diffusion of excited oxygen species between features which had minimal impact when the film was pristine and smooth. The oxygen assisted route was therefore far more significant in the conversion of precursor to metal oxide than the UV assisted route.

This deduction was confirmed by UV treatment of crystalline ZnTPP, formed by deposition on KCl substrates. The initial grain size and surface roughness both exceeded those of ZnPc, as determined by AFM, producing channels for oxygen diffusion from the outset of UV irradiation. Absorption spectra showed a complete removal of crystalline ZnTPP film earlier than for amorphous ZnTPP. Although KCl reflects approximately 15% of light back into the film, this is not sufficient to explain the rapid reaction compared to that for ZnTPP on quartz and glass carried out simultaneously and is therefore a direct result of morphology, reinforcing the conclusion that the oxygen assisted route is the primary process by which the film is removed and zinc oxide formed.

Analysis of XPS and SIMS data demonstrated conclusively the formation of zinc oxide, with a conversion ratio of zinc to zinc oxide of 0.19 for ZnPc and 0.14 for ZnTPP determined by ion yields in SIMS. Zinc oxide formation was further supported by absorption in the UV region of a UV treated 600 nm thick ZnPc film. XPS data also provided a description of the order in which the reaction occurred with bonds involving carbon atoms in aromatic rings being the first to break, followed by those bonded to nitrogen. This was the case for both precursors. The silicon XPS spectra provided further evidence of roughening of the surface leading to exposure of the substrate during UV irradiation.

6.2 Heterostructures

Deposition of ZnPc on PTCDA resulted in a complete change in the orientation of ZnPc molecules from perpendicular to the PTCDA film to nearly parallel as a result of $\pi - \pi$ in-

teractions between PTCDA and ZnPc molecules, with ZnPc presenting a grains size slightly larger than for non-templated ZnPc. XRD scans were used to identify the ZnPc molecular planes aligned orthogonal to the substrate for the first time as the (01-2) and (11-2) planes, with interplanar distances of 3.3Å and 3.2Å respectively. Templating was effected with a 20 nm thick film of PTCDA and the new arrangement of ZnPc maintained through most of a 100 nm thick film with XRD evidence of some relaxation of structure to the more ubiquitous (100) orientation.

There was no discernible impact of molecular orientation on the degradation of ZnPc, despite favourable alignment of the molecular electronic dipole with the electric field of light, in agreement with the conclusion from chapter 3 that the oxygen assisted route was the major factor in zinc oxide formation using oxygen and UV light. However, the kinetics of templated ZnPc differed in that the reaction began slowly at first, due to the larger grain size, before proceeding at 1.3 nm/minute as for non-templated ZnPc. The total degradation times were equal as the underlying layer of ZnPc provided additional oxygen, completing the reaction more efficiently than for non-templated ZnPc alone. XPS spectra for carbon yielded the same order of bond breakage as for non-templated ZnPc, with bonds involving carbon atoms in aromatic rings breaking first and no influence of molecular orientation.

PTCDA was employed as a model for a multilayer organic system to determine any effect of the UV process on organic layers adjacent to the ZnP precursor film. The underlying PTCDA layer was only affected once 50 nm of ZnPc had been removed from which it was concluded that when UV degradation is proceeding in the linear regime, the influence of the oxygen assisted route is manifest at a depth of 50 nm below the film surface as a result of film morphology permitting diffusion of oxygen. The film roughness, in particular peak to trough distances, further support this conclusion.

Deposition of an underlying layer containing oxygen provides an additional route for oxygen assisted film degradation and raised the possibility of substantially decreasing the processing time by layering alternately with precursor films. A multilayer structure alternating 10 nm films of PTCDA and ZnPc such that the film contained a total of 100 nm of ZnPc reduced

the time taken for ZnPc to fully degrade by half. UV degradation carried out in the absence of oxygen for a 100 nm thick ZnPc film and the multilayer structure results in degradation of 48% and 60% of ZnPc respectively, due to the contribution of oxygen by PTCDA. For the multilayer film, this also involves the removal of at least 50 nm of PTCDA, reinforcing the view that inclusion of an oxygen-containing molecule accelerates degradation.

6.3 Nanosphere Lithography

We aim to exploit the differences in optical properties of ZnPc and ZnO to form photonic structures by applying nanosphere lithography to UV-assisted zinc oxide formation from ZnPc films.

Monolayers of polystyrene nanospheres may be successfully applied to ZnPc films using a facile, water based technique without affecting the initially deposited organic layer. The nanospheres assemble to form a hexagonally close packed array of monolayer thickness although quality was not equal that of monolayers formed on glass due to the hydrophobicity of ZnPc, as determined by SEM imaging. 500 and 800 nm spheres form acceptable monolayers whereas 200 nm spheres generate large numbers of faults. The combined absorption spectra are similar to a simple addition of individual spectra.

UV irradiation of ZnPc through the polystyrene mask to create arrays of ZnPc pillars surrounded by triangles of zinc oxide results in gradual erosion of nanospheres with 200 nm spheres suffering the greatest damage. Consequently, truncated cones of ZnPc are formed instead of pillars with a reduced width as determined by AFM. Excited oxygen species formed upon UV absorption by oxygen in the chamber diffuse below the nanospheres also contributing to a decrease in nanostructure diameter. Use of polystyrene which is sensitive to UV light limits the total irradiation time which may be applied and the ZnPc film is not fully degraded. Therefore, conical nanostructures of ZnPc are formed in a regular hexagonal array with spacing corresponding to nanosphere size and are surrounded by a film of zinc oxide and ZnPc.

An alternative approach for photonic structure formation without the need to rely on the

formation of ZnO with UV light involved deposition of ZnPc onto monolayers of nanospheres on glass before removal of the nanosphere mask to form regularly arranged triangular ZnPc structures on glass. AFM images taken prior to mask removal showed obstruction of the interstitial gaps by ZnPc and subsequent removal of nanospheres revealed triangular structures whose height had been limited by the reduced flow of ZnPc through narrowing apertures. The spacing of the triangular nanostructures, measured using AFM, corresponded directly to distances between interstices in the hexagonal arrangement taken by the nanospheres for both 500 and 800 nm spheres. The centre of each circular region shielded from ZnPc deposition by nanospheres was bare of ZnPc but a residue of polystrene from nanosphere removal remained at the very centre of the circle. Alterations in the flow of ZnPc between nanospheres resulted in deposition close to the spheres, leaving the centre of each triangular structure relatively free of ZnPc and an overall shape approximately that of a hollow cylinder6. This effect was amplified when reducing nanosphere size from 800 to 500 nm.

Deposition of ZnPc on polystyrene nanospheres resulted in a modification of the transmission of polystyrene as a consequence of a new, higher effective refractive index, redshifting the transmission peaks.

6.4 Implications and Future Work

Elucidation of the mechanism by which metal oxide is formed from metalorganic precursors using UV light and oxygen has demonstrated the importance of the oxygen-assisted route. Precursor films may be deposited to take advantage of this by exploiting the benefit of crystalline morphology. For example, altering deposition conditions to form smaller crystallites increases the number grain boundaries which were shown to result in a faster rate of film degradation. Other options to exploit the oxygen assisted route would be patterning of the precursor film.

Initially, the UV process affects the surface layer and only the regions accessible from grain boundaries already present, however, once underway, diffusion of oxygen increases the depth at which the process acts to a maximum of 50 nm in a film of initial thickness 100 nm. Control

of precursor thickness will prevent damage to underlying layers as might the inclusion of a protecting amorphous layer.

UV assisted metal oxide formation is a technique which may be applied regardless of molecular orientation as the interaction of the precursor molecule with UV light is of minor influence compared to that of excited oxygen species. Therefore, the process has potential for use within production of any device, irrespective of the direction of charge transport required, for example, OFETs and OPV devices require transport properties arising from the orthogonal and parallel orientation of the phthalocyanine molecular plane respectively. Although the studies here have been carried out on ZnPc and ZnTPP, the UV process is not limited to these molecules and careful choice of precursor would allow an increase in yield or efficiency. To determine more precisely the effect of orientation, comparison of ZnPc deposited on CuI substrates and on PTCDA, both resulting in ZnPc depositing with the (01-2) and (11-2) planes parallel to the substrate, will allow isolation of the impact of orientation from the effect of inclusion of an oxygen containing molecule.

The UV process may be further improved by codeposition of oxygen containing molecules to facilitate degradation of the film and subsequent oxide formation. Zinc acetate, for example, is a precursor commonly employed for zinc oxide production by thermal decomposition. Codeposition with ZnPc may have a beneficial effect on yield and degradation rate and would not demand the high temperatures normally required for oxide formation from zinc acetate, ensuring the process remains feasible at room temperature for plastic electronic purposes. Although PTCDA has been shown to increase the rate of film degradation, the ideal oxygen-containing molecule would have minimal carbon composition and would also contain zinc, thereby increasing yield and providing additional oxygen without leaving residual carbon deposits.

The novel combination of nanosphere lithography with UV assisted oxide formation may be significantly improved by the use of silica nanospheres which are unaffected by UV light and oxygen and would permit precursor films to fully degrade. In order to create an alternating array of ZnPc and zinc oxide nanostructures rather than an array of ZnPc pillars surrounded by a film of zinc oxide and unreacted ZnPc, using silica nanospheres would allow repeated cycles of

ZnPc deposition followed by UV irradiation to gradually increase the thickness of oxide formed. Although time-consuming, this process is carried out at room temperature.

Finally, reflectance has been shown to affect absorption by ZnPc and ZnTPP films, although quantifying film thickness by integration of the Q band remains a valid method due the minimal impact reflectance has. However, the same may not be true for ZnPc films combined with nanolithography. It would be interesting to measure both specular and diffuse reflectance of nanosphere monolayers on ZnPc and of ZnPc deposited on monolayer films to determine the effect of a change in effective refractive index on transmission.

As a technique for oxide formation, the UV assisted methodology functions at room temperature and may be easily integrated into the production of organic electronic devices. The technique is equally applicable to other metal phthalocyanines such as VOPc and FePc to create their respective oxides and may easily be used to form mixed oxides by codeposition of the precursors without risk of phase separation. Facile and versatile, it offers many avenues for potential improvement via modification of morphology, precursor choice and method of application.

Bibliography

[1] T. Minami, "Transparent conducting oxide semiconductors for transparent electrodes," *Semiconductor Science and Technology* **20** (apr, 2005) S35–S44. http://iopscience.iop.org/article/10.1088/0268-1242/20/4/004.

[2] M. Ashida, "The Orientation Overgrowth of Metal-phthalocyanines on the Surface of Single Crystals. II. Vacuum-condensed Films of Copper-phthalocyanine on Alkali Halides," *Bulletin of the Chemical Society of Japan* **39** (mar, 1966) 2632–2638. https://www.jstage.jst.go.jp/article/bcsj1926/39/12/39{_}12{_}2632/{_}article.

[3] A. Hoshino, Y. Takenaka, and H. Miyaji, "Redetermination of the crystal structure of α-copper phthalocyanine grown on KCl," *Acta Crystallographica Section B Structural Science* **59** (jun, 2003) 393–403. http://scripts.iucr.org/cgi-bin/paper?bk0130http://scripts.iucr.org/cgi-bin/paper?S010876810300942X.

[4] W. R. Scheidt, J. U. Mondal, C. W. Eigenbrot, A. Adler, L. J. Radonovich, and J. L. Hoard, "Crystal and molecular structure of the silver(II) and zinc(II) derivatives of meso-tetraphenylporphyrin. An exploration of crystal-packing effects on bond distance," *Inorganic Chemistry* **25** (mar, 1986) 795–799. http://dx.doi.org/10.1021/ic00226a014.

[5] . Tojo and J. Mizuguchi, "Refinement of the crystal structure of α-3,4:9,10-perylenetetracarboxylic dianhydride, C24H8O6, at 223 ," *Zeitschrift für Kristallographie - New Crystal Structures* **217** (jan, 2002) 253–254.

http://www.degruyter.com/view/j/ncrs.2002.217.issue-1/ncrs.2002.217.1.253/ncrs.2002.217.1.253.xml?rskey=kV6I6z{&}result=19.

[6] . Tojo and J. Mizuguchi, "Refinement of the crystal structure of β-3,4:9,10-perylenetetracarboxylic dianhydride, C24H8O6, at 223 ," *Zeitschrift für Kristallographie - New Crystal Structures* **217** (jan, 2002) 255–256. http://www.degruyter.com/view/j/ncrs.2002.217.issue-jg/ncrs.2002.217.jg.255/ncrs.2002.217.jg.255.xml.

[7] W. E. U. Kogelschatz, B. Eliasson, "Dielectric-barrier discharges. principle and applications,".

[8] M. Friedrich, *Bluelight Compact excimer UV system 172/120Z.* Hereus Noblelight GmbH, 2014.

[9] K. P. Gentry, T. Gredig, and I. K. Schuller, "Asymmetric grain distribution in phthalocyanine thin films," *Physical Review B* **80** (nov, 2009) 174118. http://journals.aps.org/prb/abstract/10.1103/PhysRevB.80.174118{#}fulltext.

[10] J. H. Sharp and M. Lardon, "Spectroscopic characterization of a new polymorph of metal-free phthalocyanine," *The Journal of Physical Chemistry* **72** (sep, 1968) 3230–3235. http://dx.doi.org/10.1021/j100855a024.

[11] L. Edwards and M. Gouterman, "Porphyrins," *Journal of Molecular Spectroscopy* **33** (feb, 1970) 292–310. http://www.sciencedirect.com/science/article/pii/0022285270900408.

[12] S. Senthilarasu, S. Velumani, R. Sathyamoorthy, G. Canizal, P. Sebastian, J. Chavez, R. Perez, A. Subbarayan, and J. Ascencio, "Characterization of zinc phthalocyanine (ZnPc) for photovoltaic applications," *Applied Physics A: Materials Science & Processing* **77** (aug, 2003) 383–389. http://link.springer.com/10.1007/s00339-003-2184-7.

[13] S. Senthilarasu, "Thermally evaporated ZnPc thin filmsband gap dependence on thickness," *Solar Energy Materials and Solar Cells* **82** (may, 2004) 179–186. http://www.sciencedirect.com/science/article/pii/S092702480400025X.

[14] L. Edwards, D. Dolphin, M. Gouterman, and A. Adler, "Porphyrins XVII. Vapor absorption spectra and redox reactions: Tetraphenylporphins and porphin," *Journal of Molecular Spectroscopy* **38** (apr, 1971) 16–32. http://www.sciencedirect.com/science/article/pii/0022285271900907.

[15] S. Funakura, K. Nakatani, H. Misawa, N. Kitamura, and H. Masuhara, "Absorption Microspectroscopy of Zinc Tetraphenylporphyrin in an Individual Droplet in Water," *The Journal of Physical Chemistry* **98** (mar, 1994) 3073–3075. http://dx.doi.org/10.1021/j100063a003.

[16] V. Bulović, P. Burrows, S. Forrest, J. Cronin, and M. Thompson, "Study of localized and extended excitons in 3,4,9,10-perylenetetracarboxylic dianhydride (PTCDA) I. Spectroscopic properties of thin films and solutions," *Chemical Physics* **210** (oct, 1996) 1–12. http://www.sciencedirect.com/science/article/pii/0301010496001140.

[17] "Veeco dimension 3100 atomic force microscope users manual." http://nist.gov/cnst/nanofab/upload/Veeco_Dimension3100_AFM_USERMANUAL_v1.pdf.

[18] *Agilent Diffuse reflectance accessory (external) user manual.*

[19] M. Warner, S. Mauthoor, S. Felton, W. Wu, J. A. Gardener, S. Din, D. Klose, G. W. Morley, A. M. Stoneham, A. J. Fisher, G. Aeppli, C. W. M. Kay, and S. Heutz, "Spin-based diagnostic of nanostructure in copper phthalocyanine-C60 solar cell blends.," *ACS nano* **6** (dec, 2012) 10808–15. http://dx.doi.org/10.1021/nn304156e.

[20] Christy L. Haynes, Adam D. McFarland, Matthew T. Smith, John C. Hulteen, and R. P. V. Duyne, "Angle-Resolved Nanosphere Lithography: Manipulation of Nanoparticle Size, Shape, and Interparticle Spacing,". http://pubs.acs.org/doi/full/10.1021/jp013570{%}2B.

[21] A. Kosiorek, W. Kandulski, H. Glaczynska, and M. Giersig, "Fabrication of nanoscale rings, dots, and rods by combining shadow nanosphere lithography and annealed polystyrene nanosphere masks.," *Small (Weinheim an der Bergstrasse, Germany)* **1** (apr, 2005) 439–44. http://www.ncbi.nlm.nih.gov/pubmed/17193469.

[22] S. Shockley, "Circuit element utilizing semiconductive material," Sept. 25, 1951. https://www.google.com/patents/US2569347. US Patent 2,569,347.

[23] T. Tsutsui and K. Fujita, "The Shift from Hard to Soft Electronics," *Advanced Materials* **14** (jul, 2002) 949–952. http://onlinelibrary.wiley.com/doi/10.1002/1521-4095%2820020705%2914:13/14%3C949::AID-ADMA949%3E3.0.CO;2-9/abstract.

[24] S. R. Forrest, "The path to ubiquitous and low-cost organic electronic appliances on plastic.," *Nature* **428** (apr, 2004) 911–8. http://dx.doi.org/10.1038/nature02498.

[25] W. C. Dash and R. Newman, "Intrinsic Optical Absorption in Single-Crystal Germanium and Silicon at 77K and 300K," *Physical Review* **99** (aug, 1955) 1151–1155. http://journals.aps.org/pr/abstract/10.1103/PhysRev.99.1151.

[26] D. E. Carlson and C. R. Wronski, "Amorphous silicon solar cell," *Applied Physics Letters* **28** (aug, 1976) 671. http://scitation.aip.org/content/aip/journal/apl/28/11/10.1063/1.88617.

[27] A. Facchetti, "π-Conjugated Polymers for Organic Electronics and Photovoltaic Cell Applications ," *Chemistry of Materials* **23** (feb, 2011) 733–758. http://dx.doi.org/10.1021/cm102419z.

[28] M. A. Green, "Silicon solar cells: state of the art.," *Philosophical transactions. Series A, Mathematical, physical, and engineering sciences* **371** (aug, 2013) 20110413. http://rsta.royalsocietypublishing.org/content/371/1996/20110413.

[29] B. Azzopardi, C. J. M. Emmott, A. Urbina, F. C. Krebs, J. Mutale, and J. Nelson, "Economic assessment of solar electricity production from organic-based photovoltaic modules in a domestic environment," *Energy & Environmental Science* **4** (sep, 2011) 3741. http://pubs.rsc.org/en/Content/ArticleHTML/2011/EE/C1EE01766G.

[30] D. D. Eley, "Phthalocyanines as Semiconductors," *Nature* **162** (nov, 1948) 819–819. http://adsabs.harvard.edu/abs/1948Natur.162..819E.

[31] D. Kearns and M. Calvin, "Photovoltaic Effect and Photoconductivity in Laminated Organic Systems," *The Journal of Chemical Physics* **29** (aug, 1958) 950. http://scitation.aip.org/content/aip/journal/jcp/29/4/10.1063/1.1744619.

[32] C. W. Tang, "Two-layer organic photovoltaic cell," *Applied Physics Letters* **48** (1986) no. 2, 183. http://link.aip.org/link/APPLAB/v48/i2/p183/s1{&}Agg=doi.

[33] C. W. Tang and S. A. VanSlyke, "Organic electroluminescent diodes," *Applied Physics Letters* **51** (sep, 1987) 913. http://scitation.aip.org/content/aip/journal/apl/51/12/10.1063/1.98799.

[34] J. H. Burroughes, D. D. C. Bradley, A. R. Brown, R. N. Marks, K. Mackay, R. H. Friend, P. L. Burns, and A. B. Holmes, "Light-emitting diodes based on conjugated polymers," *Nature* **347** (1990) no. 6293, 539–541. http://www.nature.com/physics/looking-back/burroughes/.

[35] N. S. Sariciftci, L. Smilowitz, A. J. Heeger, and F. Wudl, "Photoinduced electron transfer from a conducting polymer to buckminsterfullerene.," *Science (New York, N.Y.)* **258** (nov, 1992) 1474–6. http://science.sciencemag.org/content/258/5087/1474.abstract.

[36] H. Shirakawa, E. J. Louis, A. G. MacDiarmid, C. K. Chiang, and A. J. Heeger, "Synthesis of electrically conducting organic polymers: halogen derivatives of polyacetylene, (CH) x," *Journal of the Chemical Society, Chemical Communications* (jan, 1977) 578. http://pubs.rsc.org/en/Content/ArticleLanding/1977/C3/C39770000578.

[37] J. You, L. Dou, K. Yoshimura, T. Kato, K. Ohya, T. Moriarty, K. Emery, C.-C. Chen, J. Gao, G. Li, and Y. Yang, "A polymer tandem solar cell with 10.6% power conversion efficiency.," *Nature communications* **4** (jan, 2013) 1446. http://dx.doi.org/10.1038/ncomms2411.

[38] Apr, 2016. http://www.heliatek.com/en/heliafilm/technical-data.

[39] S. Ishibashi, "Low resistivity indiumtin oxide transparent conductive films. II. Effect of sputtering voltage on electrical property of films," *Journal of Vacuum Science & Technology A: Vacuum, Surfaces, and Films* **8** (may, 1990) 1403. http://scitation.aip.org/content/avs/journal/jvsta/8/3/10.1116/1.576890.

[40] D. S. Hecht, L. Hu, and G. Irvin, "Emerging transparent electrodes based on thin films of carbon nanotubes, graphene, and metallic nanostructures.," *Advanced materials (Deerfield Beach, Fla.)* **23** (apr, 2011) 1482–513. http://www.ncbi.nlm.nih.gov/pubmed/21322065.

[41] B. G. Lewis and D. C. Paine, "Applications and Processing of Transparent Conducting Oxides," *MRS Bulletin* **25** (jan, 2011) 22–27. http://journals.cambridge.org/abstract{_}S0883769400027135.

[42] A. Argun, A. Cirpan, and J. Reynolds, "The First Truly All-Polymer Electrochromic Devices," *Advanced Materials* **15** (aug, 2003) 1338–1341. http://doi.wiley.com/10.1002/adma.200305038.

[43] S. Kirchmeyer and K. Reuter, "Scientific importance, properties and growing applications of poly(3,4-ethylenedioxythiophene)," *Journal of Materials Chemistry* **15** (may, 2005) 2077. http://pubs.rsc.org/en/Content/ArticleHTML/2005/JM/B417803N.

[44] T. Dürkop, S. A. Getty, E. Cobas, and M. S. Fuhrer, "Extraordinary Mobility in Semiconducting Carbon Nanotubes," *Nano Letters* **4** (jan, 2004) 35–39. http://dx.doi.org/10.1021/nl034841q.

[45] A. D. Pasquier, H. E. Unalan, A. Kanwal, S. Miller, and M. Chhowalla, "Conducting and transparent single-wall carbon nanotube electrodes for polymer-fullerene solar cells," *Applied Physics Letters* **87** (2005) no. 20, 203511. http://link.aip.org/link/APPLAB/v87/i20/p203511/s1{&}Agg=doi.

[46] K. S. Novoselov, A. K. Geim, S. V. Morozov, D. Jiang, Y. Zhang, S. V. Dubonos, I. V. Grigorieva, and A. A. Firsov, "Electric field effect in atomically thin carbon

films.," *Science (New York, N.Y.)* **306** (oct, 2004) 666–9. http://science.sciencemag.org/content/306/5696/666.abstract.

[47] Q. Zhang, X. Wan, F. Xing, L. Huang, G. Long, N. Yi, W. Ni, Z. Liu, J. Tian, and Y. Chen, "Solution-processable graphene mesh transparent electrodes for organic solar cells," *Nano Research* (may, 2013) . http://link.springer.com/10.1007/s12274-013-0325-7.

[48] Y. Liu, Q. Chang, and L. Huang, "Transparent, flexible conducting graphene hybrid films with a subpercolating network of silver nanowires," *Journal of Materials Chemistry C* **1** (apr, 2013) 2970. http://pubs.rsc.org/en/Content/ArticleHTML/2013/TC/C3TC30178H.

[49] J. Wu, H. a. Becerril, Z. Bao, Z. Liu, Y. Chen, and P. Peumans, "Organic solar cells with solution-processed graphene transparent electrodes," *Applied Physics Letters* **92** (2008) no. 26, 263302. http://link.aip.org/link/APPLAB/v92/i26/p263302/s1{&}Agg=doi.

[50] B. OConnor, C. Haughn, K.-H. An, K. P. Pipe, and M. Shtein, "Transparent and conductive electrodes based on unpatterned, thin metal films," *Applied Physics Letters* **93** (dec, 2008) 223304. http://scitation.aip.org/content/aip/journal/apl/93/22/10.1063/1.3028046.

[51] D. S. Ghosh, L. Martinez, S. Giurgola, P. Vergani, and V. Pruneri, "Widely transparent electrodes based on ultrathin metals," *Optics Letters* **34** (jan, 2009) 325. http://www.osapublishing.org/viewmedia.cfm?uri=ol-34-3-325{&}seq=0{&}html=true.

[52] J.-Y. Lee, S. T. Connor, Y. Cui, and P. Peumans, "Solution-processed metal nanowire mesh transparent electrodes.," *Nano letters* **8** (feb, 2008) 689–92. http://dx.doi.org/10.1021/nl073296g.

[53] M.-G. Kang, H. Joon Park, S. Hyun Ahn, and L. Jay Guo, "Transparent Cu nanowire mesh electrode on flexible substrates fabricated by transfer printing and its application

in organic solar cells," *Solar Energy Materials and Solar Cells* **94** (jun, 2010) 1179–1184. http://www.sciencedirect.com/science/article/pii/S0927024810000929.

[54] A. Suzuki, T. Matsushita, N. Wada, Y. Sakamoto, and M. Okuda, "Transparent Conducting Al-Doped ZnO Thin Films Prepared by Pulsed Laser Deposition," *Japanese Journal of Applied Physics* **35** (jan, 1996) L56–L59. http://iopscience.iop.org/article/10.1143/JJAP.35.L56.

[55] H.-Y. Park, D. Lim, K.-D. Kim, and S.-Y. Jang, "Performance optimization of low-temperature-annealed solution-processable ZnO buffer layers for inverted polymer solar cells," *Journal of Materials Chemistry A* **1** (may, 2013) 6327. http://pubs.rsc.org/en/Content/ArticleHTML/2013/TA/C3TA10637C.

[56] V. Shrotriya, G. Li, Y. Yao, C.-W. Chu, and Y. Yang, "Transition metal oxides as the buffer layer for polymer photovoltaic cells," *Applied Physics Letters* **88** (feb, 2006) 073508. http://scitation.aip.org/content/aip/journal/apl/88/7/10.1063/1.2174093.

[57] L. Zhang, H. Zhang, Y. Bai, J. W. Ma, J. Cao, X. Jiang, and Z. L. Zhang, "Enhanced performances of ZnO-TFT by improving surface properties of channel layer," *Solid State Communications* **146** (jun, 2008) 387–390. http://www.sciencedirect.com/science/article/pii/S0038109808001737.

[58] H.-H. Huang, S.-Y. Chu, P.-C. Kao, Y.-C. Chen, M.-R. Yang, and Z.-L. Tseng, "Enhancement of hole-injection and power efficiency of organic light emitting devices using an ultra-thin ZnO buffer layer," *Journal of Alloys and Compounds* **479** (jun, 2009) 520–524. http://www.sciencedirect.com/science/article/pii/S0925838809000048.

[59] T. Minami, K. Oohashi, S. Takata, T. Mouri, and N. Ogawa, "Preparations of ZnO:Al transparent conducting films by d.c. magnetron sputtering," *Thin Solid Films* **193-194** (dec, 1990) 721–729. http://www.sciencedirect.com/science/article/pii/0040609090902242.

[60] H. Agura, A. Suzuki, T. Matsushita, T. Aoki, and M. Okuda, "Low resistivity transparent conducting Al-doped ZnO films prepared by pulsed laser deposition," *Thin Solid Films* **445** (dec, 2003) 263–267. http://www.sciencedirect.com/science/article/pii/S0040609003011581.

[61] T. Maruyama and J. Shionoya, "Zinc oxide thin films prepared by chemical vapour deposition from zinc acetate," *Journal of Materials Science Letters* **11** (jan, 1992) 170–172. http://www.springerlink.com/content/nv11710824423548/.

[62] C. Mazon, J. Muci, A. Sa-Neto, A. Ortiz-Conde, and F. Garcia, "Spray pyrolysis of ZnO thin films for photovoltaic applications: effect of gas flow rate and solute concentration," in *The Conference Record of the Twenty-Second IEEE Photovoltaic Specialists Conference - 1991*, pp. 1156–1161. IEEE, 1991. http://ieeexplore.ieee.org/lpdocs/epic03/wrapper.htm?arnumber=169392.

[63] T. Ohgaki, N. Ohashi, H. Kakemoto, S. Wada, Y. Adachi, H. Haneda, and T. Tsurumi, "Growth condition dependence of morphology and electric properties of ZnO films on sapphire substrates prepared by molecular beam epitaxy," *Journal of Applied Physics* **93** (jan, 2003) 1961. http://scitation.aip.org/content/aip/journal/jap/93/4/10.1063/1.1535256.

[64] Z. R. Khan, M. S. Khan, M. Zulfequar, and M. Shahid Khan, "Optical and Structural Properties of ZnO Thin Films Fabricated by Sol-Gel Method," *Materials Sciences and Applications* **02** (may, 2011) 340–345. http://www.scirp.org/journal/PaperInformation.aspx?PaperID=4774{&}{#}abstract.

[65] B. N. Illy, A. C. Cruickshank, S. Schumann, R. Da Campo, T. S. Jones, S. Heutz, M. A. McLachlan, D. W. McComb, D. J. Riley, and M. P. Ryan, "Electrodeposition of zno layers for photovoltaic applications: controlling film thickness and orientation," *J. Mater. Chem.* **21** (2011) 12949–12957. http://dx.doi.org/10.1039/C1JM11225B.

[66] T. Bintsis, E. Litopoulou-Tzanetaki, and R. K. Robinson, "Existing and potential applications of ultraviolet light in the food industry - a critical review," *Journal of the*

Sci-

ence of Food and Agriculture **80** (may, 2000) 637–645. http://doi.wiley.com/10.1002/{%}28SICI{%}291097-0010{%}2820000501{%}2980{%}3A6{%}3C637{%}3A{%}3AAID-JSFA603{%}3E0.CO{%}3B2-1.

[67] A. L. Santos, V. Oliveira, I. Baptista, I. Henriques, N. C. M. Gomes, A. Almeida, A. Correia, and Â. Cunha, "Wavelength dependence of biological damage induced by UV radiation on bacteria.," *Archives of microbiology* **195** (jan, 2013) 63–74. http://www.ncbi.nlm.nih.gov/pubmed/23090570.

[68] C. Auner, U. Palfinger, H. Gold, J. Kraxner, A. Haase, T. Haber, M. Sezen, W. Grogger, G. Jakopic, J. Krenn, G. Leising, and B. Stadlober, "Residue-free room temperature UV-nanoimprinting of submicron organic thin film transistors," *Organic Electronics* **10** (dec, 2009) 1466–1472. http://www.sciencedirect.com/science/article/pii/S1566119909002316.

[69] S. H. Ahn and L. J. Guo, "High-Speed Roll-to-Roll Nanoimprint Lithography on Flexible Plastic Substrates," *Advanced Materials* **20** (jun, 2008) 2044–2049. http://doi.wiley.com/10.1002/adma.200702650.

[70] F. Moulis and J. Krýsa, "Photocatalytic degradation of several VOCs (n-hexane, n-butyl acetate and toluene) on TiO2 layer in a closed-loop reactor," *Catalysis Today* **209** (jun, 2013) 153–158. http://www.sciencedirect.com/science/article/pii/S0920586112007377.

[71] T. N. Obee and R. T. Brown, "TiO2 Photocatalysis for Indoor Air Applications: Effects of Humidity and Trace Contaminant Levels on the Oxidation Rates of Formaldehyde, Toluene, and 1,3-Butadiene.," *Environmental science & technology* **29** (may, 1995) 1223–31. http://dx.doi.org/10.1021/es00005a013.

[72] S. Rentenberger, A. Vollmer, E. Zojer, R. Schennach, and N. Koch, "UVozone treated Au for air-stable, low hole injection barrier electrodes in organic electronics," *Journal of*

Applied Physics **100** (sep, 2006) 053701.
http://www.osti.gov/scitech/biblio/20884695.

[73] C. C. Wu, C. I. Wu, J. C. Sturm, and A. Kahn, "Surface modification of indium tin oxide by plasma treatment: An effective method to improve the efficiency, brightness, and reliability of organic light emitting devices," *Applied Physics Letters* **70** (mar, 1997) 1348.
http://scitation.aip.org/content/aip/journal/apl/70/11/10.1063/1.118575.

[74] C.-M. Chan, T.-M. Ko, and H. Hiraoka, "Polymer surface modification by plasmas and photons," *Surface Science Reports* **24** (may, 1996) 1–54.
http://www.sciencedirect.com/science/article/pii/0167572996800033.

[75] Y.-J. Kim, Y. Taniguchi, K. Murase, Y. Taguchi, and H. Sugimura, "Vacuum ultraviolet-induced surface modification of cyclo-olefin polymer substrates for photochemical activation bonding," *Applied Surface Science* **255** (jan, 2009) 3648–3654.
http://www.sciencedirect.com/science/article/pii/S0169433208021363.

[76] J. R. Vig, "UV/ozone cleaning of surfaces," *Journal of Vacuum Science & Technology A: Vacuum, Surfaces, and Films* **3** (may, 1985) 1027.
http://scitation.aip.org/content/avs/journal/jvsta/3/3/10.1116/1.573115.

[77] D. H. Chen, X. Ye, and K. Li, "Oxidation of PCE with a UV LED Photocatalytic Reactor," *Chemical Engineering & Technology* **28** (jan, 2005) 95–97.
http://doi.wiley.com/10.1002/ceat.200407012.

[78] M. Mori, A. Hamamoto, A. Takahashi, M. Nakano, N. Wakikawa, S. Tachibana, T. Ikehara, Y. Nakaya, M. Akutagawa, and Y. Kinouchi, "Development of a new water sterilization device with a 365 nm UV-LED.," *Medical & biological engineering & computing* **45** (dec, 2007) 1237–41. http://www.ncbi.nlm.nih.gov/pubmed/17978842.

[79] B. Eliasson and U. Kogelschatz, "UV excimer radiation from dielectric-barrier discharges," *Applied Physics B Photophysics and Laser Chemistry* **46** (aug, 1988) 299–303. http://link.springer.com/10.1007/BF00686452.

[80] N. Ohta and M. Gomi, "Photochemical Decomposition of Co Phthalocyanine Films Using Ultraviolet Excimer Lamp," *Japanese Journal of Applied Physics* **39** (jul, 2000) 4195–4197. http://iopscience.iop.org/article/10.1143/JJAP.39.4195.

[81] J. A. Gardener, I. Liaw, G. Aeppli, I. W. Boyd, R. J. Chater, T. S. Jones, D. S. McPhail, G. Sankar, A. M. Stoneham, M. Sikora, G. Thornton, and S. Heutz, "A novel route for the inclusion of metal dopants in silicon," *Nanotechnology* **21** (2010) no. 2, 025304. http://stacks.iop.org/0957-4484/21/i=2/a=025304.

[82] R. Linstead, "212. phthalocyanines. part i. a new type of synthetic colouring matters," *Journal of the Chemical Society (Resumed)* (1934) 1016–1017.

[83] M. G. Walter, A. B. Rudine, and C. C. Wamser, "Porphyrins and phthalocyanines in solar photovoltaic cells," *Journal of Porphyrins and Phthalocyanines* **14** (jan, 2010) 759. http://www.worldscientific.com/doi/abs/10.1142/S1088424610002689.

[84] M. Bouvet, G. Guillaud, A. Leroy, A. Maillard, S. Spirkovitch, and F.-G. Tournilhac, "Phthalocyanine-based field-effect transistor as ozone sensor," *Sensors and Actuators B: Chemical* **73** (feb, 2001) 63–70. http://www.sciencedirect.com/science/article/pii/S0925400500006821.

[85] J. Blochwitz, M. Pfeiffer, T. Fritz, and K. Leo, "Low voltage organic light emitting diodes featuring doped phthalocyanine as hole transport material," *Applied Physics Letters* **73** (aug, 1998) 729. http://scitation.aip.org/content/aip/journal/apl/73/6/10.1063/1.121982.

[86] O. A. Melville, B. H. Lessard, and T. P. Bender, "Phthalocyanine-Based Organic Thin-Film Transistors: A Review of Recent Advances.," *ACS applied materials & interfaces* **7** (jun, 2015) 13105–18. http://dx.doi.org/10.1021/acsami.5b01718.

[87] M. Serri, W. Wu, L. R. Fleet, N. M. Harrison, C. F. Hirjibehedin, C. W. M. Kay, A. J. Fisher, G. Aeppli, and S. Heutz, "High-temperature antiferromagnetism in molecular semiconductor thin films and nanostructures.," *Nature communications* **5** (jan, 2014)

3079.
http://www.nature.com/ncomms/2014/140121/ncomms4079/full/ncomms4079.html.

[88] B. Bott and T. Jones, "A highly sensitive NO2 sensor based on electrical conductivity changes in phthalocyanine films," *Sensors and Actuators* **5** (jan, 1984) 43–53. http://www.sciencedirect.com/science/article/pii/0250687484870055.

[89] M.-S. Liao and S. Scheiner, "Electronic structure and bonding in metal phthalocyanines, metal=fe, co, ni, cu, zn, mg," *The Journal of Chemical Physics* **114** (2001) no. 22, 9780–9791. http://scitation.aip.org/content/aip/journal/jcp/114/22/10.1063/1.1367374.

[90] P. Erk, H. Hengelsberg, M. F. Haddow, and R. van Gelder, "The innovative momentum of crystal engineering," *CrystEngComm* **6** (oct, 2004) 474. http://pubs.rsc.org/en/content/articlehtml/2004/ce/b409282a.

[91] N. Uyeda, M. Ashida, and E. Suito, "Orientation Overgrowth of Condensed Polycyclic Aromatic Compounds Vacuum-Evaporated onto Cleaved Face of Mica," *Journal of Applied Physics* **36** (1965) no. 4, 1453. http://scitation.aip.org/content/aip/journal/jap/36/4/10.1063/1.1714329.

[92] T. Kobayashi, Y. Fujiyoshi, F. Iwatsu, and N. Uyeda, "High-resolution TEM images of zinc phthalocyanine polymorphs in thin films," *Acta Crystallographica Section A* **37** (Sep, 1981) 692–697. http://dx.doi.org/10.1107/S0567739481001563.

[93] J. C. Buchholz and G. A. Somorjai, "The surface structures of phthalocyanine monolayers and vapor-grown films: A low-energy electron diffraction study," *The Journal of Chemical Physics* **66** (aug, 1977) 573. http://scitation.aip.org/content/aip/journal/jcp/66/2/10.1063/1.433979.

[94] M. Hara, H. Sasabe, A. Yamada, and A. F. Garito, "Epitaxial Growth of Organic Thin Films by Organic Molecular Beam Epitaxy," *Japanese Journal of Applied Physics* **28** (feb, 1989) L306–L308. http://iopscience.iop.org/article/10.1143/JJAP.28.L306.

[95] "Structure and electrical conduction properties of phthalocyanine thin films," *Coordination Chemistry Reviews* **156** (dec, 1996) 237–274. http://www.sciencedirect.com/science/article/pii/S0010854596012386.

[96] M. El-Nahass, H. Zeyada, M. Aziz, and N. El-Ghamaz, "Structural and optical properties of thermally evaporated zinc phthalocyanine thin films," *Optical Materials* **27** (dec, 2004) 491–498. http://www.sciencedirect.com/science/article/pii/S0925346704001971.

[97] A. T. Davidson, "The effect of the metal atom on the absorption spectra of phthalocyanine films," *The Journal of Chemical Physics* **77** (jul, 1982) 168. http://link.aip.org/link/?JCPSA6/77/168/1.

[98] H. Yoshida, Y. Tokura, and T. Koda, "Charge-transfer excitation bands in electro-absorption spectra of metal (Co, Ni, Cu, Zn)-phthalocyanine films," *Chemical Physics* **109** (nov, 1986) 375–382. http://www.sciencedirect.com/science/article/pii/0301010486870665.

[99] Q. Sun, L. Dai, X. Zhou, L. Li, and Q. Li, "Bilayer- and bulk-heterojunction solar cells using liquid crystalline porphyrins as donors by solution processing," *Applied Physics Letters* **91** (dec, 2007) 253505. http://scitation.aip.org/content/aip/journal/apl/91/25/10.1063/1.2823586.

[100] H. Imahori, T. Umeyama, and S. Ito, "Large pi-aromatic molecules as potential sensitizers for highly efficient dye-sensitized solar cells.," *Accounts of chemical research* **42** (nov, 2009) 1809–18. http://dx.doi.org/10.1021/ar900034t.

[101] C. Trinh, M. T. Whited, A. Steiner, C. J. Tassone, M. F. Toney, and M. E. Thompson, "Chemical Annealing of Zinc Tetraphenylporphyrin Films: Effects on Film Morphology and Organic Photovoltaic Performance," *Chemistry of Materials* **24** (jul, 2012) 2583–2591. http://dx.doi.org/10.1021/cm3012777.

[102] G. D. Dorough, J. R. Miller, and F. M. Huennekens, "Spectra of the Metallo-derivatives of α,β,γ,δ-Tetraphenylporphine," *Journal of the American Chemical Society* **73** (sep, 1951) 4315–4320. http://dx.doi.org/10.1021/ja01153a085.

[103] H. Derouiche and V. Djara, "Impact of the energy difference in LUMO and HOMO of the bulk heterojunctions components on the efficiency of organic solar cells," *Solar Energy Materials and Solar Cells* **91** (aug, 2007) 1163–1167. http://www.sciencedirect.com/science/article/pii/S0927024807001171.

[104] V. Bulovic, P. Tian, P. E. Burrows, M. R. Gokhale, S. R. Forrest, and M. E. Thompson, "A surface-emitting vacuum-deposited organic light emitting device," *Applied Physics Letters* **70** (jun, 1997) 2954. http://scitation.aip.org/content/aip/journal/apl/70/22/10.1063/1.119260.

[105] J. R. Ostrick, A. Dodabalapur, L. Torsi, A. J. Lovinger, E. W. Kwock, T. M. Miller, M. Galvin, M. Berggren, and H. E. Katz, "Conductivity-type anisotropy in molecular solids," *Journal of Applied Physics* **81** (may, 1997) 6804. http://scitation.aip.org/content/aip/journal/jap/81/10/10.1063/1.365238.

[106] M. Möbus, N. Karl, and T. Kobayashi, "Structure of perylene-tetracarboxylic-dianhydride thin films on alkali halide crystal substrates," *Journal of Crystal Growth* **116** (feb, 1992) 495–504. http://www.sciencedirect.com/science/article/pii/0022024892906586.

[107] A. J. Lovinger, S. R. Forrest, M. L. Kaplan, P. H. Schmidt, and T. Venkatesan, "Structural and morphological investigation of the development of electrical conductivity in ion-irradiated thin films of an organic material," *Journal of Applied Physics* **55** (jan, 1984) 476. http://scitation.aip.org/content/aip/journal/jap/55/2/10.1063/1.333049.

[108] M. Hennessy, Z. Soos, R. Pascal, and A. Girlando, "Vibronic structure of PTCDA stacks: the excitonphonon-charge-transfer dimer," *Chemical Physics* **245** (jul, 1999)

199–212.
http://www.sciencedirect.com/science/article/pii/S0301010499000828.

[109] J. C. Vickerman and I. S. Gilmore, *Surface Analysis: The Principal Techniques*. John Wiley & Sons Ltd, 2009.

[110] H. Kim, C. M. Gilmore, J. S. Horwitz, A. Pique, H. Murata, G. P. Kushto, R. Schlaf, Z. H. Kafafi, and D. B. Chrisey, "Transparent conducting aluminum-doped zinc oxide thin films for organic light-emitting devices," *Applied Physics Letters* **76** (jan, 2000) 259. http://scitation.aip.org/content/aip/journal/apl/76/3/10.1063/1.125740.

[111] X. Jiang, F. L. Wong, M. K. Fung, and S. T. Lee, "Aluminum-doped zinc oxide films as transparent conductive electrode for organic light-emitting devices," *Applied Physics Letters* **83** (aug, 2003) 1875. http://scitation.aip.org/content/aip/journal/apl/83/9/10.1063/1.1605805.

[112] D. C. Olson, J. Piris, R. T. Collins, S. E. Shaheen, and D. S. Ginley, "Hybrid photovoltaic devices of polymer and ZnO nanofiber composites," *Thin Solid Films* **496** (feb, 2006) 26–29. http://www.sciencedirect.com/science/article/pii/S0040609005014148.

[113] S.-H. Liao, H.-J. Jhuo, P.-N. Yeh, Y.-S. Cheng, Y.-L. Li, Y.-H. Lee, S. Sharma, and S.-A. Chen, "Single junction inverted polymer solar cell reaching power conversion efficiency 10.31% by employing dual-doped zinc oxide nano-film as cathode interlayer.," *Scientific reports* **4** (jan, 2014) 6813. http://www.nature.com/srep/2014/141029/srep06813/full/srep06813.html.

[114] T. Hirao, M. Furuta, H. Furuta, T. Matsuda, T. Hiramatsu, H. Hokari, M. Yoshida, H. Ishii, and M. Kakegawa, "Novel top-gate zinc oxide thin-film transistors (ZnO TFTs) for AMLCDs," *Journal of the Society for Information Display* **15** (2007) no. 1, 17. http://doi.wiley.com/10.1889/1.1828693.

[115] S. W. Benson, "III - bond energies," *Journal of Chemical Education* **42** (1965) no. 9, 502, http://dx.doi.org/10.1021/ed042p502.
http://dx.doi.org/10.1021/ed042p502.

[116] M.-S. Liao and S. Scheiner, "Electronic structure and bonding in metal porphyrins, metal=Fe, Co, Ni, Cu, Zn," *The Journal of Chemical Physics* **117** (jun, 2002) 205. http://scitation.aip.org/content/aip/journal/jcp/117/1/10.1063/1.1480872.

[117] R. E. Huffman, "Absorption cross-sections of atmospheric gases for use in aeronomy," *Canadian Journal of Chemistry* **47** (1969) no. 10, 1823–1834.

[118] B. Eliasson and U. Kogelschatz, "Ozone generation with narrowband uv radiation," *Ozone: Science & Engineering* **13** (1991) no. 3, 365–373, http://dx.doi.org/10.1080/01919519108552472.
http://dx.doi.org/10.1080/01919519108552472.

[119] J. A. Gardener, I. Liaw, G. Aeppli, I. W. Boyd, S. Fiddy, G. Hyett, T. S. Jones, S. Lauzurica, R. G. Palgrave, I. P. Parkin, G. Sankar, M. Sikora, A. M. Stoneham, G. Thornton, and S. Heutz, "Oxide Nanoparticle Thin Films Created Using Molecular Templates," *The Journal of Physical Chemistry C* **115** (jul, 2011) 13151–13157. http://pubs.acs.org/doi/abs/10.1021/jp200567r.

[120] M. Wojdya, B. Derkowska, Z. ukasiak, and W. Baa, "Absorption and photoreflectance spectroscopy of zinc phthalocyanine (ZnPc) thin films grown by thermal evaporation," *Materials Letters* **60** (dec, 2006) 3441–3446. http://www.sciencedirect.com/science/article/pii/S0167577X06003302.

[121] B. Schechtman and W. Spicer, "Near infrared to vacuum ultraviolet absorption spectra and the optical constants of phthalocyanine and porphyrin films," *Journal of Molecular Spectroscopy* **33** (jan, 1970) 28–48. http://www.sciencedirect.com/science/article/pii/0022285270900500.

[122] S. Dahmane, A. Lasia, and Y. Zhao, "Thermal, Optical and Electrochemical Properties of Side-Chain Azopyridine Polymers Complexed with

Metalloporphyrins," *Macromolecular Chemistry and Physics* **207** (aug, 2006) 1485–1491. http://doi.wiley.com/10.1002/macp.200600143.

[123] S. C. Abrahams and J. L. Bernstein, "Remeasurement of the structure of hexagonal ZnO," *Acta Crystallographica Section B Structural Crystallography and Crystal Chemistry* **25** (jul, 1969) 1233–1236. http://scripts.iucr.org/cgi-bin/paper?a06799.

[124] S. Major and K. Chopra, "Indium-doped zinc oxide films as transparent electrodes for solar cells," *Solar Energy Materials* **17** (aug, 1988) 319–327. http://www.sciencedirect.com/science/article/pii/0165163388900147.

[125] S. Senthilarasu, Y. B. Hahn, and S.-H. Lee, "Structural analysis of zinc phthalocyanine (ZnPc) thin films: x-ray diffraction study," *J. Appl. Phys.* **102** (2007) no. Copyright (C) 2012 American Chemical Society (ACS). All Rights Reserved., 043512/1–043512/6.

[126] C. J. Brown, "Crystal structure of beta-copper phthalocyanine," *Journal of the Chemical Society A: Inorganic, Physical, Theoretical* (jan, 1968) 2488. http://pubs.rsc.org/en/Content/ArticleLanding/1968/J1/J19680002488.

[127] J. E, S. Kim, E. Lim, K. Lee, D. Cha, and B. Friedman, "Effects of substrate temperature on copper(II) phthalocyanine thin films," *Applied Surface Science* **205** (jan, 2003) 274–279. http://www.sciencedirect.com/science/article/pii/S0169433202011157.

[128] Y. Niwa, "X-ray photoelectron spectroscopy of tetraphenylporphin and phthalocyanine," *The Journal of Chemical Physics* **60** (aug, 1974) 799. http://scitation.aip.org/content/aip/journal/jcp/60/3/10.1063/1.1681153.

[129] K. Nilson, P. Palmgren, J. Åhlund, J. Schiessling, E. Göthelid, N. Mårtensson, C. Puglia, and M. Göthelid, "STM and XPS characterization of zinc phthalocyanine on InSb(001)," *Surface Science* **602** (2008) no. 2, 452–459. http://www.sciencedirect.com/science/article/pii/S0039602807010801.

[130] L. Zhang, H. Peisert, I. Biswas, M. Knupfer, D. Batchelor, and T. Chassé, "Growth of zinc phthalocyanine onto ZnS film investigated by synchrotron radiation-excited X-ray photoelectron and near-edge absorption spectroscopy," *Surface Science* **596** (2005) no. 1, 98–107. http://www.sciencedirect.com/science/article/pii/S003960280500960X.

[131] Y. Niwa, H. Kobayashi, and T. Tsuchiya, "X-ray photoelectron spectroscopy of azaporphyrins," *Inorganic Chemistry* **13** (dec, 1974) 2891–2896. http://dx.doi.org/10.1021/ic50142a024.

[132] H. Höchst, A. Goldmann, S. Hüfner, and H. Malter, "X-Ray Photoelectron Valence Band Studies on Phthalocyanine Compounds," *physica status solidi (b)* **76** (aug, 1976) 559–568. http://doi.wiley.com/10.1002/pssb.2220760215.

[133] L. G. Mar, P. Y. Timbrell, and R. N. Lamb, "An XPS study of zinc oxide thin film growth on copper using zinc acetate as a precursor," *Thin Solid Films* **223** (feb, 1993) 341–347. http://www.sciencedirect.com/science/article/pii/004060909390542W.

[134] J. Kim, H. Marzouk, P. Reucroft, and C. Hamrin, "Characterization of high quality c axis oriented ZnO thin films grown by metal organic chemical vapor deposition using zinc acetate as source material," *Thin Solid Films* **217** (sep, 1992) 133–137. http://www.sciencedirect.com/science/article/pii/004060909290619M.

[135] A. Wilson and R. A. Collins, "GasSurface Reactions on Phthalocyanine Thin Films," *physica status solidi (a)* **98** (dec, 1986) 633–644. http://doi.wiley.com/10.1002/pssa.2210980238.

[136] D. H. Karweik and N. Winograd, "Nitrogen charge distributions in free-base porphyrins, metalloporphyrins, and their reduced analogs observed by x-ray photoelectron spectroscopy," *Inorganic Chemistry* **15** (oct, 1976) 2336–2342. http://dx.doi.org/10.1021/ic50164a003.

[137] A. Kretschmann, M.-M. Walz, K. Flechtner, H.-P. Steinrück, and J. M. Gottfried, "Tetraphenylporphyrin picks up zinc atoms from a silver surface.," *Chemical*

communications (Cambridge, England) (feb, 2007) 568–70. http://pubs.rsc.org/en/Content/ArticleHTML/2007/CC/B614427F.

[138] M. L. Yu, "Chemical enhancement effects in SIMS analysis," *Nuclear Instruments and Methods in Physics Research Section B: Beam Interactions with Materials and Atoms* **15** (apr, 1986) 151–158. http://www.sciencedirect.com/science/article/pii/0168583X86902739.

[139] Virginia Semiconductor, 1501 Powhatan Street, Fredericksburg, VA 22401-4647 USA, *The General Properties of Si, Ge, SiGe, SiO_2 and Si_3N_4*, June, 2002.

[140] W. R. Scheidt and W. Dow, "Molecular stereochemistry of phthalocyanatozinc(II)," *Journal of the American Chemical Society* **99** (feb, 1977) 1101–1104. http://dx.doi.org/10.1021/ja00446a021.

[141] J. Finster, D. Schulze, F. Bechstedt, and A. Meisel, "Interpretation of XPS core level shifts and structure of thin silicon oxide layers," *Surface Science* **152-153** (apr, 1985) 1063–1070. http://www.sciencedirect.com/science/article/pii/0039602885905217.

[142] J. Díaz, G. Paolicelli, S. Ferrer, and F. Comin, "Separation of the sp 3 and sp 2 components in the C1 s photoemission spectra of amorphous carbon films," *Physical Review B* **54** (sep, 1996) 8064–8069. http://journals.aps.org/prb/abstract/10.1103/PhysRevB.54.8064.

[143] C.-T. Hsieh and H. Teng, "Influence of oxygen treatment on electric double-layer capacitance of activated carbon fabrics," *Carbon* **40** (apr, 2002) 667–674. http://www.sciencedirect.com/science/article/pii/S0008622301001828.

[144] L. G. Arellano, J. K. Bhamrah, J. Yang, J. B. Gilchrist, D. W. McComb, M. P. Ryan, and S. Heutz, "Room temperature routes for the creation of zinc oxide films from molecular precursors," *ACS Applied Materials and Interfaces* (2016) .

[145] C. GÜMÜS, O. M. OZKENDIR, H. KAVAK, and Y. UFUKTEPE, "Structural and optical properties of zinc oxide thin films prepared by spray pyrolysis method," *Journal*

of optoelectronics and advanced materials **8** no. 1, 299–303. http://cat.inist.fr/?aModele=afficheN{&}cpsidt=17571816.

[146] Y. Natsume and H. Sakata, "Zinc oxide films prepared by sol-gel spin-coating," *Thin Solid Films* **372** (sep, 2000) 30–36. http://www.sciencedirect.com/science/article/pii/S0040609000010567.

[147] V. Srikant and D. R. Clarke, "On the optical band gap of zinc oxide," *Journal of Applied Physics* **83** (may, 1998) 5447. http://scitation.aip.org/content/aip/journal/jap/83/10/10.1063/1.367375.

[148] S. Talam, S. R. Karumuri, and N. Gunnam, "Synthesis, Characterization, and Spectroscopic Properties of ZnO Nanoparticles," *ISRN Nanotechnology* **2012** (2012) 1–6. http://www.hindawi.com/isrn/nanotechnology/2012/372505/.

[149] T. Djuric, T. Ules, S. Gusenleitner, N. Kayunkid, H. Plank, G. Hlawacek, C. Teichert, M. Brinkmann, M. Ramsey, and R. Resel, "Substrate selected polymorphism of epitaxially aligned tetraphenyl-porphyrin thin films.," *Physical chemistry chemical physics : PCCP* **14** (jan, 2012) 262–72. http://pubs.rsc.org/en/content/articlehtml/2012/cp/c1cp22299f.

[150] J. E. Eby, K. J. Teegarden, and D. B. Dutton, "Ultraviolet Absorption of Alkali Halides," *Physical Review* **116** (dec, 1959) 1099–1105. http://journals.aps.org/pr/abstract/10.1103/PhysRev.116.1099.

[151] G. Baldini and B. Bosacchi, "Optical Properties of Alkali-Halide Crystals," *Physical Review* **166** (feb, 1968) 863–870. http://journals.aps.org/pr/abstract/10.1103/PhysRev.166.863.

[152] E. W. J. Mitchell and E. G. S. Paige, "CXI. The optical effects of radiation induced atomic damage in quartz," *Philosophical Magazine* **1** (dec, 1956) 1085–1115. http://www.tandfonline.com/doi/abs/10.1080/14786435608238193.

[153] B. K. Johnson, "Reflecting-power measurements in the spectral region 2000 A. to 1300 A," *Proceedings of the Physical Society* **53** (may, 1941) 258–264. http://iopscience.iop.org/article/10.1088/0959-5309/53/3/308.

[154] B. P. Rand, J. Genoe, P. Heremans, and J. Poortmans, "Solar cells utilizing small molecular weight organic semiconductors," *Progress in Photovoltaics: Research and Applications* **15** (dec, 2007) 659–676. http://doi.wiley.com/10.1002/pip.788.

[155] L. Malavolti, L. Poggini, L. Margheriti, D. Chiappe, P. Graziosi, B. Cortigiani, V. Lanzilotto, F. Buatier de Mongeot, P. Ohresser, E. Otero, F. Choueikani, P. Sainctavit, I. Bergenti, V. A. Dediu, M. Mannini, and R. Sessoli, "Magnetism of TbPc2 SMMs on ferromagnetic electrodes used in organic spintronics.," *Chemical communications (Cambridge, England)* **49** (dec, 2013) 11506–8. http://pubs.rsc.org/en/Content/ArticleHTML/2013/CC/C3CC46868B.

[156] C. Isvoranu, B. Wang, K. Schulte, E. Ataman, J. Knudsen, J. N. Andersen, M. L. Bocquet, and J. Schnadt, "Tuning the spin state of iron phthalocyanine by ligand adsorption.," *Journal of physics. Condensed matter : an Institute of Physics journal* **22** (dec, 2010) 472002. http://iopscience.iop.org/article/10.1088/0953-8984/22/47/472002.

[157] S. R. Forrest, M. L. Kaplan, and P. H. Schmidt, "Organic-on-inorganic semiconductor contact barrier diodes. II. Dependence on organic film and metal contact properties," *Journal of Applied Physics* **56** (jul, 1984) 543. http://scitation.aip.org/content/aip/journal/jap/56/2/10.1063/1.333944.

[158] S. R. Forrest, "Ultrathin Organic Films Grown by Organic Molecular Beam Deposition and Related Techniques," *Chemical Reviews* **97** (oct, 1997) 1793–1896. http://dx.doi.org/10.1021/cr941014o.

[159] C. Rompf, D. Ammermann, and W. Kowalsky, "Deposition and characterisation of crystalline organic semiconductors for photonic devices," *Materials Science and*

Technology (jul, 2013) .
http://www.tandfonline.com/doi/abs/10.1179/mst.1995.11.8.845.

[160] D. Hong, Y. R. Do, H. T. Kwak, and S. Yim, "Structural templating and growth behavior of copper phthalocyanine thin films deposited on a polycrystalline perylenetetracarboxylic dianhydride layer," *Journal of Applied Physics* **109** (mar, 2011) 063507.
http://scitation.aip.org/content/aip/journal/jap/109/6/10.1063/1.3553884.

[161] S. Heutz, R. Cloots, and T. S. Jones, "Structural templating effects in molecular heterostructures grown by organic molecular-beam deposition," *Applied Physics Letters* **77** (2000) no. 24, 3938. http://adsabs.harvard.edu/abs/2000ApPhL..77.3938H.

[162] B. P. Rand, D. Cheyns, K. Vasseur, N. C. Giebink, S. Mothy, Y. Yi, V. Coropceanu, D. Beljonne, J. Cornil, J.-L. Brédas, and J. Genoe, "The Impact of Molecular Orientation on the Photovoltaic Properties of a Phthalocyanine/Fullerene Heterojunction," *Advanced Functional Materials* **22** (jul, 2012) 2987–2995.
http://doi.wiley.com/10.1002/adfm.201200512.

[163] M. Leonhardt, O. Mager, and H. Port, "Two-component optical spectra in thin PTCDA films due to the coexistence of α- and β-phase," *Chemical Physics Letters* **313** (nov, 1999) 24–30.
http://www.sciencedirect.com/science/article/pii/S0009261499010519.

[164] C. Ludwig, B. Gompf, W. Glatz, J. Petersen, W. Eisenmenger, M. Mbus, U. Zimmermann, and N. Karl, "Video-STM, LEED and X-ray diffraction investigations of PTCDA on graphite," *Zeitschrift fr Physik B Condensed Matter* **86** (oct, 1992) 397–404. http://link.springer.com/10.1007/BF01323733.

[165] N. U. Zhanpeisov, S. Nishio, and H. Fukumura, "Density functional theory study of vibrational properties of the 3,4,9,10-perylene tetracarboxylic dianhydride (PTCDA) molecule: IR, Raman, and UV-vis spectra," *International Journal of Quantum Chemistry* **105** (2005) no. 4, 368–375. http://doi.wiley.com/10.1002/qua.20712.

[166] B. E. Lassiter, R. R. Lunt, C. K. Renshaw, and S. R. Forrest, "Structural templating of multiple polycrystalline layers in organic photovoltaic cells.," *Optics express* **18 Suppl 3** (sep, 2010) A444–50. http://www.osapublishing.org/viewmedia.cfm?uri=oe-18-S3-A444{&}seq=0{&}html=true.

[167] P. Sullivan, T. S. Jones, A. J. Ferguson, and S. Heutz, "Structural templating as a route to improved photovoltaic performance in copper phthalocyanine/fullerene (C[sub 60]) heterojunctions," *Applied Physics Letters* **91** (dec, 2007) 233114. http://scitation.aip.org/content/aip/journal/apl/91/23/10.1063/1.2821229.

[168] H. Derouiche, "Optimization of the properties of bulk heterojunctions obtained by coevaporation of Zn-phthalocyanine/perylene," *Dyes and Pigments* **63** (dec, 2004) 277–289. http://www.sciencedirect.com/science/article/pii/S0143720804000476.

[169] C. Vieu, F. Carcenac, A. Pépin, Y. Chen, M. Mejias, A. Lebib, L. Manin-Ferlazzo, L. Couraud, and H. Launois, "Electron beam lithography: resolution limits and applications," *Applied Surface Science* **164** (sep, 2000) 111–117. http://www.sciencedirect.com/science/article/pii/S0169433200003524.

[170] A. Tseng, C. Chen, and K. Ma, "Electron beam lithography in nanoscale fabrication: recent development," *IEEE Transactions on Electronics Packaging Manufacturing* **26** (apr, 2003) 141–149. http://ieeexplore.ieee.org/lpdocs/epic03/wrapper.htm?arnumber=1236879.

[171] R. D. Piner, ""Dip-Pen" Nanolithography," *Science* **283** (jan, 1999) 661–663. http://science.sciencemag.org/content/283/5402/661.abstract.

[172] S. Davies and B. Khamsehpour, "Focused ion beam machining and deposition for nanofabrication," *Vacuum* **47** (may, 1996) 455–462. http://www.sciencedirect.com/science/article/pii/0042207X95002359.

[173] U. C. Fischer, "Submicroscopic pattern replication with visible light," *Journal of Vacuum Science and Technology* **19** (nov, 1981) 881. http://scitation.aip.org/content/avs/journal/jvst/19/4/10.1116/1.571227.

[174] S. Moller and S. R. Forrest, "Improved light out-coupling in organic light emitting diodes employing ordered microlens arrays," *Journal of Applied Physics* **91** (mar, 2002) 3324. http://scitation.aip.org/content/aip/journal/jap/91/5/10.1063/1.1435422.

[175] F. Xie, A. Centeno, M. R. Ryan, D. J. Riley, and N. M. Alford, "Au nanostructures by colloidal lithography: from quenching to extensive fluorescence enhancement," *J. Mater. Chem. B* **1** (dec, 2013) 536–543. http://pubs.rsc.org/en/Content/ArticleHTML/2013/TB/C2TB00278G.

[176] Y.-C. Chang, S.-C. Lu, H.-C. Chung, S.-M. Wang, T.-D. Tsai, and T.-F. Guo, "High-throughput nanofabrication of infra-red and chiral metamaterials using nanospherical-lens lithography.," *Scientific reports* **3** (jan, 2013) 3339. http://www.nature.com/srep/2013/131128/srep03339/full/srep03339.html.

[177] A. Plettl, F. Enderle, M. Saitner, A. Manzke, C. Pfahler, S. Wiedemann, and P. Ziemann, "Non-Close-Packed Crystals from Self-Assembled Polystyrene Spheres by Isotropic Plasma Etching: Adding Flexibility to Colloid Lithography," *Advanced Functional Materials* **19** (oct, 2009) 3279–3284. http://doi.wiley.com/10.1002/adfm.200900907.

[178] W.-G. Yan, X.-T. Kong, Z.-B. Li, and J.-G. Tian, "Nanostructure Fabricated by Nanosphere Lithography Assisted with O¡SUB¿2¡/SUB¿ Plasma Treatment," *Journal of Nanoscience and Nanotechnology* **13** (jun, 2013) 4311–4315. http://www.ingentaconnect.com/content/asp/jnn/2013/00000013/00000006/art00088.

[179] A. Centeno and F. Xie, "An Electromagnetic Study of Metal Enhanced Fluorescence Due to Immobilized Nanoparticle Arrays on Glass Substrates," *Materials Today:*

Proceedings **2** (2015) no. 1, 94–100.
http://www.sciencedirect.com/science/article/pii/S2214785315000140.

[180] C. L. Haynes and R. P. Van Duyne, "Nanosphere Lithography: A Versatile Nanofabrication Tool for Studies of Size-Dependent Nanoparticle Optics," *The Journal of Physical Chemistry B* **105** (jun, 2001) 5599–5611.
http://dx.doi.org/10.1021/jp010657m.

[181] R. Williams, "Wetting of thin layers of SiO2 by water," *Applied Physics Letters* **25** (oct, 1974) 531.
http://scitation.aip.org/content/aip/journal/apl/25/10/10.1063/1.1655297.

[182] J. Cras, C. Rowe-Taitt, D. Nivens, and F. Ligler, "Comparison of chemical cleaning methods of glass in preparation for silanization," *Biosensors and Bioelectronics* **14** (dec, 1999) 683–688.
http://www.sciencedirect.com/science/article/pii/S0956566399000433.

[183] "Polybead polystyrene microspheres, technical data sheet 238," May, 2013.

[184] N. Vogel, S. Goerres, K. Landfester, and C. K. Weiss, "A Convenient Method to Produce Close- and Non-close-Packed Monolayers using Direct Assembly at the Air-Water Interface and Subsequent Plasma-Induced Size Reduction," *Macromolecular Chemistry and Physics* **212** (aug, 2011) 1719–1734.
http://doi.wiley.com/10.1002/macp.201100187.

[185] J. López Gejo, N. Manoj, S. Sumalekshmy, H. Glieman, T. Schimmel, M. Wörner, and A. M. Braun, "Vacuum-ultraviolet photochemically initiated modification of polystyrene surfaces: morphological changes and mechanistic investigations.," *Photochemical & photobiological sciences : Official journal of the European Photochemistry Association and the European Society for Photobiology* **5** (oct, 2006) 948–54.
http://pubs.rsc.org/en/Content/ArticleHTML/2006/PP/B611874G.